Structural Health Monitoring of Thick Composites using Ultrasonic Guided Waves

Tianyi Feng

Department of Aeronautics

Imperial College London

Supervisor:

Professor M. H. Ferri Aliabadi

A thesis submitted in partial fulfilment of the requirements for the degree of Doctor of Philosophy and the Diploma of Imperial College

January 2022

满腔热血，砥砺航空强国之志。奋然无悔，力践民族振兴之行。愿山河无恙，国泰民安。誓以吾辈之青春，捍卫盛世之中华！

公元 *2021* 年 *12* 月 *13* 日

I would like to strive forward the aspiration of a strong country in aviation with full of enthusiasm. I will make great efforts to achieve national rejuvenation with no regrets. May the mountains and the rivers be safe, and may the country and the people be safe. I swear to defend prosperous China with the youth of my generation!

13 Dec 2021

Acknowledgements

I would like to express my deepest appreciation to my supervisor Professor M.H. Ferri Aliabadi and co-supervisor Reader Zahra Sharif Khodaei for their precious guidance and efficient support to complete my PhD research. Without their guidance and help, I would lose the direction of my research. The same appreciation is also to Dr Omar Bacarreza Nogales for his technical support of my research.

In addition, I would like to thank the postdocs and the graduated PhD students in the group of Structural Integrity and Health Monitoring in alphabetical order: Dr Aldy Hami Seno, Dr Dimitrios Bekas, Dr Florian Lambinet, Dr Hailing Fu, Dr Jun Li, Dr Ifan Dafydd, Dr Ilias Giannnakeas and Dr Nan Yue. My research would not finish in time without their technical assistance and encouragement. I would also like to thank the support staff in the Department of Aeronautics in alphabetical order: Franco Giammaria, Frank Gommer, Gary Senior, Jonathan Cole, Joseph Meggyesi, Keith Wolstenholme. Thanks for all their assistance that my experimental work could be finished in time, especially during the pandemic of Covid-19 in 2020.

Furthermore, I would like to thank the headquarter of Aviation Industry Corporation of China, Ltd. (AVIC), AVIC General Huanan Aircraft Industry Co. Ltd., and the China Scholarship Council (CSC) for the three-year funding of my PhD research. I would also like to thank Imperial College London to support me with extra three-month funding during the Covid-19 lockdown. As a staff funded by AVIC and CSC, I will work harder to better serve the company and my country in the future.

Finally, I would like to thank my parents who have been unconditionally supporting me all the time. It was a tough decision that I decided to stay in the UK to finish the rest experimental work before the outbreak of Covid-19 in the UK. My mother worried me for a whole year during that time, and she got ovarian cancer when I came back to China. I was told about her illness until I almost finished my PhD thesis. It was extremely miserable for me when I knew her illness and I had to pretend to be stronger and more optimistic in front of her. Her health became worse after the next day I finished the thesis and she passed away 17 days later since then. I am extremely regretful that she would not see the day I graduated and the day I get married. I really do not want to lose her and she knows how much I love her. She is no longer in pain, and she will live in my heart forever.

Looking back on the past four years as a PhD student at Imperial College London, I clearly remember that I insisted on my novel experimental plan when I had a different opinion from a post-doc in our group in my early first academic year. I was glad that I insisted that because my experimental work improved the stability and the accuracy of the fabrication level in our research group. I could still remember clearly that I was immune to sleep and was walking in

circuits to find solutions in my studio in late-night. Nearly two-thirds of my hair was lost during this time.

With the outbreaks, ongoing spread and the evolution of the Covid-19 in the UK since the start of Mar 2020, I had to overcome the fear, despair, and loneliness and fight against the coronavirus every day. After easing the first restriction from the end of June 2020, I had to spend two and half hours walking to and back to the college (a total of 15 km) in the safest way and took about 10 hours in the lab to do the experiments every day (wearing the face mask all day). Nearly a total of 1209 km was shown on my cellphone's app record after finishing my experiments (5 months). I strongly believe that all these will be valuable experiences in my life.

In loving memory of my mom!

11 Nov 2018, Westminster, London, UK

Declaration of Originality

I hereby declare that this thesis and the work reported herein was composed by and originated entirely from myself. Information obtained from the work of others has been properly acknowledged in the text and references are given in the list of sources.

Tianyi Feng
December 2021

Copyright declaration

Abstract

This thesis systematically evaluates the influence of composite thickness on properties of ultrasonic guided waves (UGW) under varying temperatures for damage detection using surface-mounted and embedded lead zirconate titanate (PZT) transducers for Structural Health Monitoring (SHM) purposes.

First, a novel edge cut-out method for embedding diagnostic films with PZT transducers based on the circuit-printed technique will be proposed. The use of thin diagnostic films with printed circuits instead of traditional cables was shown to significantly reduce the weight of composite structures. In addition, the novel edge cut-out method allowed edge trimming possible which can be used in industrial mass manufacturing for the next higher assembly.

Then the structural integrity of the composites with the embedded diagnostic film and PZT transducers will be assessed. Initially, the effect of fatigue tests on the electro-mechanical impedance (EMI) properties of PZT transducers under different loading cycles (up to 1 million) was studied. In addition, the effect of fatigue tests on active sensing behaviours based on UGW under different loading cycles was investigated. Finally, the tensile and compressive tests were conducted to assess the effect of the novel embedding technique on the elastic modulus of the composite materials.

After that, the peak amplitude and the group velocity of the S_0 and the A_0 modes and temperature influence through different thicknesses of composites actuated by surface-mounted and embedded PZT transducers will be investigated. The interactions of UGW with the surface-mounted artificial damage and the impact damage were studied by laser Doppler vibrometer (LDV) using surface-mounted and embedded PZT transducers. Finally, damage detection and localization for the surface-mounted artificial damage and the impact damage were investigated by surface-mounted and embedded PZT transducers. The influence of the embedded position of PZT transducers on UGW was also numerically and experimentally studied. The reversibility of the peak amplitude of the first wave packet of UGW actuated/received by PZT transducers in different positions was compared.

In the end, the possibility of monitoring the debonding and the simulated damage of the composite bonded by a repair structure using a smart repair patch will be investigated. First, the EMI method was used to verify the bonding properties of PZT transducers. Second, the damage index (DI) correlation coefficient and the delay-and-sum (DAS) algorithm were used to detect and locate the artificial delamination and the surface-mounted artificial damage, respectively.

Table of Contents

List of Figures

List of Tables

Chapter 1

1. Introduction

1.1. Background

Advanced high-performance composites are now the prominent material in modern commercial airframe aircraft [1, 2]. These types of composites have a superior strength-to-weight ratio, higher tensile strength and stiffness, good properties of corrosion/fatigue resistance, and higher thermal stability [1-5]. For instance, the usage of using composites has saved 50% weight (Boeing Dreamliner 787) [2]. A key consideration for composites is their susceptibility to the low-velocity impact damage which is not detectable by the naked eye, commonly referred to as barely visible impact damage (BVID) [1, 6, 7]. This damage will reduce stiffness and durability of the structure due to fibre breakage and internal delamination [8, 9]. These initial damages may propagate during the service and cause the failure of the part [10-12]. Failure to detect such damages may lead to unexpected failures, and therefore, their early detection is of great interest within the aeronautics sector.

Thick composites as primarily load-carrying structural components are extensively used especially in large aircraft structures (Boeing Dreamliner 787 and Airbus 350 XWB) [13, 14]. Generally, the layup and the part thickness depend on the service loading and the residual strength evaluation of components given the likelihood of a certain damage size. As the result, the fuselage, wing box and their internal parts such as stiffeners, frames and spares are manufactured to different thicknesses. The internal defects in composites are complex, consisting of multimode damage and the extent of the impact damage normally spreads across the thickness under the impacted surface. The characterization of the BVID in different thickness composites is complicated and differs for each composite structure depending on its layup, material and thickness [15].

In thin composite structures, matrix cracking is caused by the impact generated from the lowest ply layer because of the bending stress. In addition, a reverse pine-tree pattern is formed since intra-ply cracks and interface delamination propagated from the lowest surface to the impact surface [16]. In thick composite structures, the damage propagates away from the impact location in the shape of a cone and forms a pine-tree pattern [16]. It is also demonstrated that thicker composite structures have higher bending stiffness and have higher compression after the impact strength [15].

Structural Health Monitoring (SHM) can play an important role in the early detection of the BVID. These inspection techniques are developed to detect damage, hence allowing the real-time health of the structure (e.g., the size and the location of the damage) and analyzing the load history of the aircraft [17-21]. Figure 1.1a shows the schematic of non-destructive inspect-

ion (NDI) requirements for the aircraft from Airbus. The application of the SHM technique in the aeronautic industry is still under development [22, 23], so the schematic of the concept of the smart aircraft based on the SHM techniques is shown in Figure 1.1b. Ultrasonic guided waves (UGW) are widely used to monitor composite structures due to their low attenuation to propagate long distances [24-26]. Generally, guided waves consist of the symmetric (S_i) and the anti-symmetric (A_i) modes with different phase and group velocities [7]. Different modes are excited depending on the frequency and the thickness of the composites, each with different dispersion and propagation properties, making each suitable for detecting different damage sizes and types [27, 28].

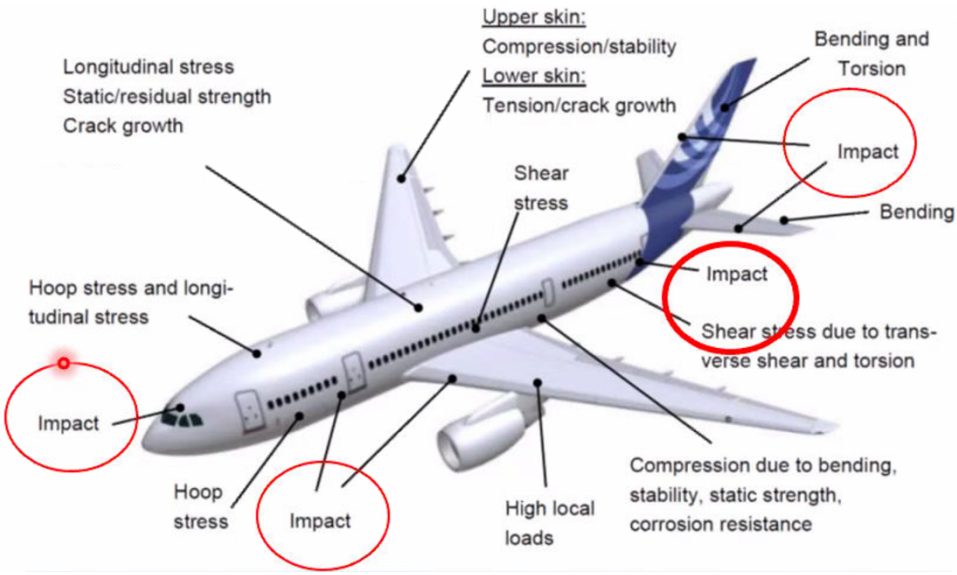

(a)

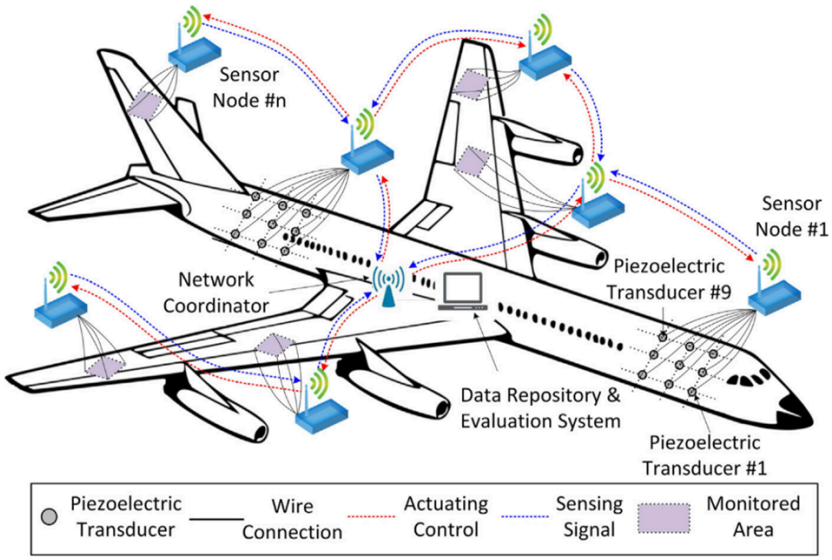

(b)

Figure 1.1. Schematics of **(a)** non-destructive inspection (NDI) requirements for the aircraft from Airbus [29] and **(b)** the concept of the smart aircraft based on the SHM techniques [30].

Piezoelectric lead zirconate titanate (PZT) transducers and fibre-optic sensors (FOS) are two main types of sensors used for guided wave identification. The advantages of PZT transducers are high mechanical strength with a wide frequency range, good coupling capacity which is particularly suitable for embedding, low price and small sizes [31, 32]. In addition, they can simultaneously exhibit actuator/sensor behaviours, which allows for both passive and active detections [33-35]. Furthermore, the guided wave signal actuated by PZT transducer can have desirable amplitude, frequency and waveform to suit different cases, and the number of actuators/sensors can reduce to half due to their actuator/sensor behaviours [32]. Figure 1.2 shows a schematic of damage detection and localization using PZT transducers.

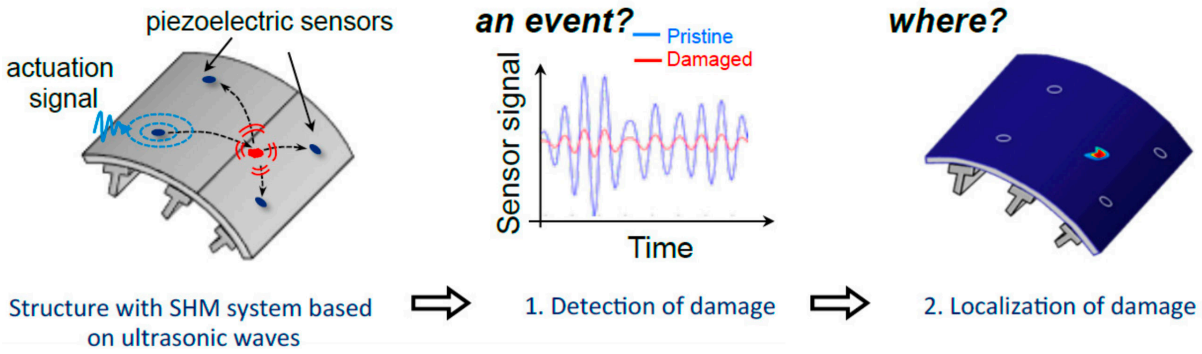

Figure 1.2. Schematic of active sensing for damage detection and localization using PZT transducers [36].

Fibre-optic sensors (FOS) are super-light, small in size, sensitive, durable, lower consumption, immune to electromagnetic interferences/corrosion and have high bandwidth that one optic fibre can have multiplexing sensors [31, 32, 37-40]. Generally, one FOS has five modalities: (i) scattering-based sensors including Rayleigh, Raman and Brillouin principles, (ii) intensity-based sensors (microbend sensors), (iii) polarization-based sensors, (iv) phase-based sensors based on the principle of interferometry and (v) wavelength based sensors such as fibre Bragg gratings (FBG) [41]. The modality based on FBG has been widely used for sensing static/dynamic strains in SHM applications. Figure 1.3 shows the working principle of FBG sensors. By comparing guided wave signals captured by PZT transducers and FBG sensors, PZT transducers can capture the 'integrated' signals in the entire covered area, while FBG sensors are directional dependent [32]. In addition, PZT transducers are sensitive to both the S_0 and the A_0 modes, while FBG sensors are less sensitive to the A_0 mode [32]. Furthermore, the amplitude of the guided wave signal is linear to the in-plane area of PZT transducers and the grating length of FBG sensors [32].

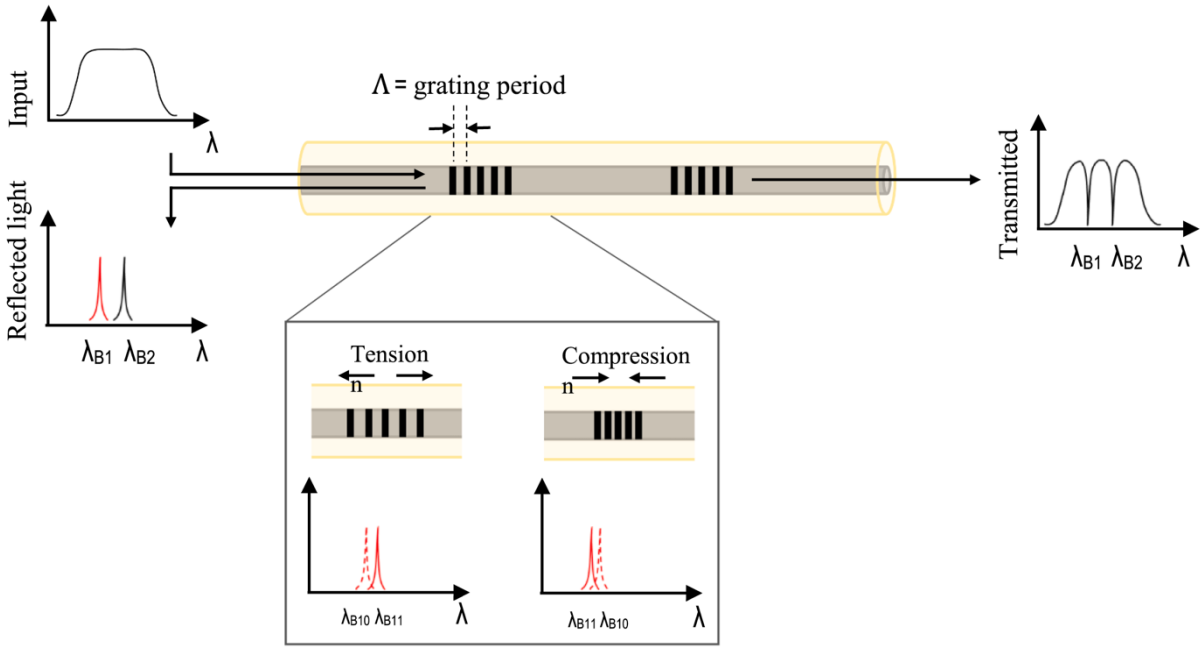

Figure 1.3. Schematic of the working principles for FBG sensors [31].

Acoustic emission (AE) as a passive SHM technique has been successfully used in the aeronautic industry due to its sensitivity, and capability of detecting various types of composite damage [42]. The theory of the AE can be described as a rapid energy release that an elastic stress wave generated by permanent internal changes propagating in a material [38, 43-46]. Many mechanisms can cause the AE which include crack initiation and propagation, friction, fretting, impact damage, plastic deformation, delamination, matrix cracking and fibre breakage [38, 42, 43, 46]. The structural health integrity of the composite structure thus can be assessed using the acoustic waves captured by PZT transducers and FBG sensors [43, 46]. The schematic of the AE detection theory can be seen in Figure 1.4. In the thin-walled plate-like structures, these acoustic signals can propagate as UGW with the symmetric or the antisymmetric modes [44].

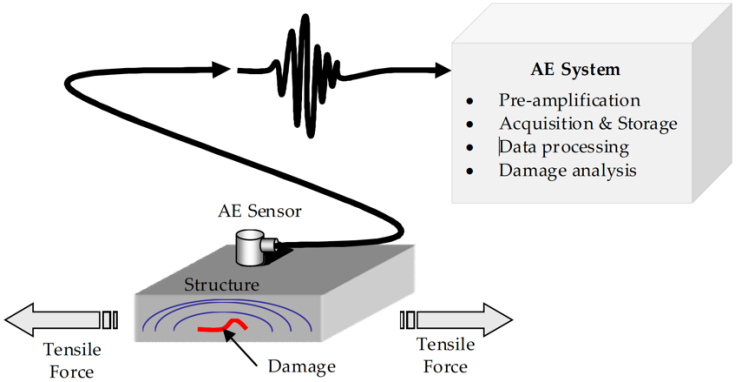

Figure 1.4. Schematic of the AE detection theory [42].

1.2. Motivation

For diagnostic purposes based on the SHM techniques, UGW should ideally be non-dispersive, low attenuative and high sensitive to the BVID which requires the optimum wave mode to be selected [7]. However, often this information is not known, therefore it is important that during the design and development phase of any SHM system, a detailed investigation is carried out to choose the optimum parameters of the UGW (frequency, amplitude and mode) which will interact with the probable damage types in the plate and enable a reliable damage detection. Many studies have been carried out to capture the guided wave propagation properties in composite structures of different layup, material, complexity and size, numerically, since experimental investigations are often timely and expensive to allow a deeper understanding of the wave/damage interaction to optimize the parameters of the SHM system, towards condition-based maintenance concept.

There is extensive research focusing on studying the dispersive properties of the S_0 and the A_0 modes and the relationship between central frequency, thickness, and material properties for thin composites. De Luca A. *et al.* [47] used the finite element method (FEM) to simulate the guided wave propagation in a thin double-curvatures winglet made by glass fibre reinforced polymers (GFRP) with foam core (five layers sandwich structure). The study showed a good agreement between the FEM and experiments and the simulated signals were able to detect and locate the BVID accurately. Wandowski T. *et al.* [48] used the numerical analysis based on the time domain spectral element method (SEM) to study the guided wave (the S_0 and the A_0 modes) conversion and interaction with the impact damage for glass fibre reinforced polymer (GFRP) laminates with a thickness of 2 mm. In their study, the damping parameters were difficult to calibrate and the damage detection results had a good agreement between the SEM and laser Doppler vibrometer (LDV) measurements.

In addition, Mei H. *et al.* [49] used the semi-analytical finite element (SAFE) method to present the dispersion curves and guided wave propagation (the S_0 and the A_0 modes) actuated by a PZT transducer in damped composite laminates (1.8 mm thickness). A good match for the attenuation of the S_0 and the A_0 modes due to the damping was obtained between the SAFE simulation and the experiments (LDV measurements). Their further studies also used the SAFE [50] and the FEM [51] methods to study the wave propagation and interaction with damages, dispersion curves and damage detection and localization of the BVID. There were good agreements between the simulation and experiments. Other studies related the guide wave propagation with wave modes, dispersion curves and phase/group velocities in thin composite structures can be found in [5, 16, 25, 27, 28, 52-58].

However, there are limited studies focused on UGW in thick composite structures. James R. *et al.* [59] compared the BVID size resulting from different impact energy and force for the coupons with different thicknesses. They demonstrated that the impact damage propagates through the thickness for the 2 mm and the 4 mm coupons but not for the 6 mm coupons (thick composites). In addition, the controlled impact size was more difficult to obtain for the thick composite coupon compared to the thin composite coupon. Moreover, the indentation shape

for the thicker composite coupon was flatter than that of the thinner one given the hemispherical tip of the tup for the impactor. However, their study did not include any guided wave or wave/damage interaction investigation for different thickness composites. Abetew AD. *et al.* [60] used a pulse-echo laser ultrasonic system to inspect thick composite structures (thicknesses of 8 mm and 10.3 mm). They found that a larger laser beam size can increase the bigger peak-to-peak amplitude of guided waves which significantly increased the propagation depth of UGW into the structure and can improve the capability of inspecting thick composite structures.

Furthermore, Duan M. *et al.* [15] numerically studied and experimentally validated low-velocity impact tests and frequency-sweep vibration tests for thick composite laminate. They showed a good agreement between the simulation and the experiments and found that the damage occurred at the outer plies first for thick composite laminates. The main reason for the matrix damage was the high contact stress and laminate bending deformation under impact load. The delamination happened at the upper plies and propagated to the inner plies due to the high contact stress and formed a pine-type damage pattern in the thickness direction. With increasing the impact energy, a larger bigger damage area was obtained, and the damage shape changed from an ellipse to a 'peanut' shape to an irregular shape in the end. Andreades C. *et al.* [61] proposed a novel nonlinear ultrasonic localization method for the BVID in thick composites (thicknesses of 6 mm and 13 mm). This method did not require the signal transmission frequency, nor the time-of-flight of guided waves and no need to obtain the baseline state of the composite structures either. Their experiment results showed that the BVID can be accurately located.

However, none of the above studies investigated the guided wave propagation (wave modes and propagation velocities) through thick composite structures in detail and under different environmental conditions. Due to the anisotropic behaviour and complex BVID scenarios [47, 50] and extremally high attenuation [60] of thick composite structures, it is always a challenge to successfully detect thick composite structures based on the SHM techniques. Monitoring the BVID is a key to the advanced application of composite materials in the aeronautic industry for SHM purposes. In addition, temperature change affects UGW in two ways: change in phase and change in amplitude which both can significantly compromise the reliability of the diagnosis if not compensated [62]. There are several detailed investigations on the effect of temperature on the guided wave signals for thick composite plates [63], however, no research has reported the temperature effect in thick composites and whether there is any dependency on the thickness. This effect could be taken into include via temperature compensation algorithms. Therefore, the temperature effect on the peak amplitude of the first wave packet of guided wave signals would need to be evaluated.

Furthermore, the repair of in-service composite parts plays an important role in the sustainability of composite airframes due to the recent increase in the utilisation of composite structures in modern aircraft. In certain practical cases, the repair of composite structures according to the Structural Repair Manual (SRM) can reduce the cost of replacement without compromising the mechanical of composite structures [64-66]. However, the strength and the

durability of the repaired area still need to be considered since the stress transfer at the interface is under the service load with different environmental conditions [67]. The mechanical properties of the exposed thermosetting adhesives and the resin of bonded area will absorb the moisture, which will affect the durability [68-71]. The defects will be also generated near stress concentrations and initial fatigue cracks when the repaired structure subjecting to cycled loadings [72-74]. In addition, the failures occur due to the inconsistent processing methods and human errors which will degrade the mechanical properties between the repair patch and the composite bondline and generate a stress concentration [67, 75]. Therefore, it is important to monitor the integrity of the bonded repair area of composite structures.

1.3. Thesis Outline

This thesis studies ultrasonic guided waves (UGW) and temperature influences through-thickness of the composite laminates and investigates thickness effects on damage detection and localization based on active sensing SHM techniques.

Chapter 2 introduces the fundamentals of UGW, the phase and the group velocities, and dispersive properties. In addition, theories of PZT transducers including the polarization, the piezoelectricity, the electro-mechanical impedance (EMI) properties and the finite element modelling (FEM) have been reviewed. Furthermore, the signal actuation and the postprocessing are introduced, followed by theories of the damage index (DI) - correlation coefficient for damage detection, the delay-and-sum algorithm for damage localization and the laser Doppler vibrometry for damage identification.

Chapter 3 reviews the state-of-the-art of embedding techniques into composites and proposes a novel edge cut-out embedding technique, which allows edge trimming possible and can be used for mass manufacturing for the next higher assembly. The structural integrity has also been assessed by mechanical tests including fatigue, tensile and compressive tests.

Chapter 4 compares explicit and implicit dynamic analyses of the FEM for surface-mounted PZT transducers. Three modelling strategies are proposed to find the optimum solution for embedding PZT transducers into composite transducers and structural damping properties will be investigated. Finally, interactions of UGW with the surface-mounted artificial damage and the impact damage will be studied.

Chapter 5 studies the amplitude and the group velocity of the S_0 and the A_0 modes of UGW and temperature influences through different thicknesses of composites by surface-mounted PZT transducers. Interactions of UGW with the surface-mounted artificial damage and the impact damage will be evaluated by laser Doppler vibrometer (LDV) measurements. In addition, damage detection and localization for the surface-mounted artificial damage and the impact damage are also investigated.

Chapter 6 studies UGW through different thicknesses of composites by embedded PZT transducers under varying temperatures. Interactions of UGW with the surface-mounted artificial damage and the impact damage are studied by LDV measurements. The surface-

mounted artificial damage and the impact damage are detected by the damage index (DI) and localized using the delay-and-sum (DAS) algorithm. UGW actuated/received by PZT transducers embedded in different composite layers are also numerically and experimentally studied.

Chapter 7 introduces the fabrication of a composite smart repair patch using the embedded diagnostic film with PZT transducers. The EMI method is used to verify the bonding qualities of embedded PZT transducers. The DI and the DAS algorithm are used to detect and localize the artificial defects – the delamination and the surface-mounted artificial damage.

Chapter 8 reviews and concludes the thesis, followed by future work in this specific field.

1.4. Contributions

The main contributions related to this research and the corresponding publications are listed below:

(1) Proposed a novel embedding technique, which allows for edge trimming possible after composite curing, and studied the temperature influence on UGW and damage interactions with UGW actuated by the embedded and surface-mounted PZT transducers for thick composites:

- T. Feng, D. Bekas, M. Aliabadi, Active Health Monitoring of Thick Composite Structures by Embedded and Surface-Mounted Piezo Diagnostic Layer, Sensors 20(12) (2020) 3410.

(2) For the first time accessed the structural integrity of composite coupons with embedded PZT transducers using the novel embedding technique, investigated the EMI properties and active sensing performance under fatigue tests and evaluated the effect of embedding on the elastic modulus of thick composite coupons:

- T. Feng, M.H.F. Aliabadi, Structural Integrity Assessment of Composites Plates with Embedded PZT Transducers for Structural Health Monitoring, Materials 14(20) (2021) 6148.

(3) For the first time manufactured a composite smart repair patch with embedded PZT transducers using the novel embedding technique and investigated the abilities to detect and locate the artificial defects.

- T. Feng, M.H.F. Aliabadi, Smart Patch for Structural Health Monitoring of Composite Repair, Applied Sciences 12(10) (2022) 4916.

(4) For the first time systematically studied the influences of the thickness and the temperature on the amplitude and the group velocity of UGW actuated by surface-mounted PZT transducers and investigated the thickness effect on damage interaction, detection and localization by surface-mounted PZT transducers.

- T. Feng, Z. Sharif Khodaei, M. Aliabadi, Influence of Composite Thickness on Ultrasonic Guided Wave Propagation for Damage Detection. Smart Materials and Structures. (Under Review)

(5) For the first time systematically studied the influences of the thickness and the temperature on the amplitude and the group velocity of UGW actuated by embedded PZT transducers and investigated the thickness effect on damage interaction, detection and localization by embedded PZT transducers.

- T. Feng, M. Aliabadi, Structural Health Monitoring with Ultrasonic Guided Waves Actuated by embedded PZT transducers for Thick composites. (Under Preparation)

(6) For the first time numerically and experimentally investigated the effect of the embedded positions on UGW through different thicknesses of composites.

- T. Feng, M. Aliabadi, Numerical and Experimental Study of Effects of Embedding Position of PZT Transducers on Thick Composites Using Ultrasonic Guided Waves. (Under Preparation)

Chapter 2

2. Fundamentals of SHM Techniques

2.1. Introduction

Ultrasonic guided waves (UGW) have proved to be a popular SHM approach due to their ability to travel long distances with relatively low attenuations [24, 76, 77] and sensitivity to various types of damage for carbon fibre reinforced polymer (CFRP) composite structures [78-85]. Lead zirconate titanate (PZT) transducer is widely used in UGW based on the SHM systems for damage detection and localization of composites due to its low cost with high curing temperature, [86, 87]. It can exhibit both actuator and sensor behaviours, which allows for both passive and active detection [33-35]. The actuator can activate guided waves to travel along the surface of solid media with minimal energy loss using piezoelectric properties [33].

This chapter will introduce the fundamentals of SHM which are of relevance to the remaining chapters. First, the theories of UGW will be introduced, which include Lamb wave modes, phase/group velocities, and dispersion curves. Second, the theory of the polarization and the piezoelectric properties for the PZT transducer will be presented, which includes the fundamentals of the piezoelectricity used for ABAQUS implicit dynamic analysis, the electrical-mechanical impedance (EMI) techniques. Furthermore, the theory of the finite element modelling for dynamic problems in the time domain will be introduced, which includes explicit and implicit time integration methods, and modelling of the disk PZT actuator and sensor for the explicit dynamic analysis. Then the signal processing will also be reviewed, followed by the theories of the damage index for damage detection and the delay-and-sum algorithm for damage localization. Finally, the general background of laser Doppler vibrometer (LDV) will be described.

2.2. Ultrasonic Guided Waves (UGW)

2.2.1. Guided Wave in Isotropic Plates

In a thin isotropic and homogeneous plate shown in Figure 2.1, the governing equation of Lamb waves can be expressed in Cartesian tensor notation as [32]

$$\mu \cdot u_{i,jj} + (\lambda + \mu) \cdot u_{i,jj} + \rho \cdot f_i = \rho \cdot \ddot{u}_i, (i, j = 1, 2, 3) \quad where\ \lambda = \frac{2\mu \cdot v}{1 - 2v} \tag{2.1}$$

where μ, v and ρ are the shear modulus, Poisson's ratio and the density of the plate respectively, u_i and f_i are the components displacement and the force in the x_i direction.

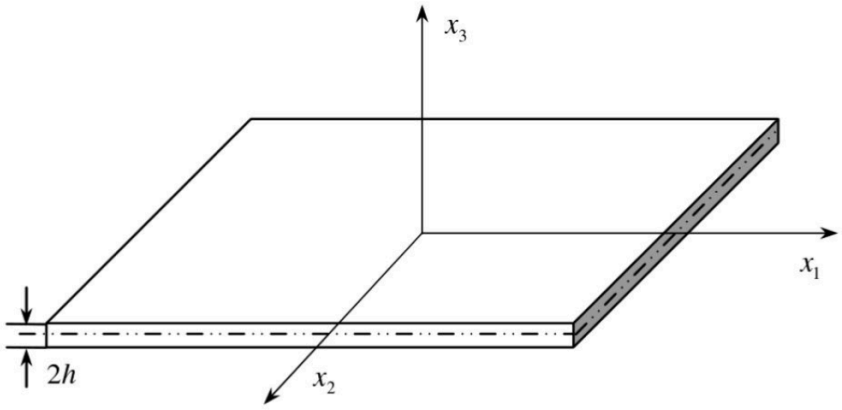

Figure 2.1. Schematic of an isotropic plate with a thickness of $2h$ [32].

The displacement potential method based on the Helmholtz decomposition is used to decompose (2.1) into two uncoupled parts under the plane strain condition [32, 88-91]:

$$\begin{aligned} &\frac{\partial^2 \Phi}{\partial x_1^2}+\frac{\partial^2 \Phi}{\partial x_3^2}=\frac{1}{c_L^2}\cdot\frac{\partial^2 \Phi}{\partial t^2} && \text{governing longitudianl waves} \\ &\frac{\partial^2 \Psi}{\partial x_1^2}+\frac{\partial^2 \Psi}{\partial x_3^2}=\frac{1}{c_T^2}\cdot\frac{\partial^2 \Psi}{\partial t^2} && \text{governing shear waves} \end{aligned} \tag{2.2}$$

where

$$\begin{aligned} \Phi &= [A_1 \sin(px_3) + A_2 \cos(px_3)] \cdot \exp[i(kx_1 - \omega t)] \\ \Psi &= [B_3 \sin(px_3) + B_2 \cos(qx_3)] \cdot \exp[i(kx_1 - \omega t)] \end{aligned} \tag{2.3}$$

where constants A_1, A_2, B_1 and B_2 are determined by boundary conditions. $p^2 = \frac{\omega^2}{c_L^2} - k^2, q^2 = \frac{\omega^2}{c_T^2} - k^2, k = \frac{2\pi}{\lambda_{wave}}$. k, ω and λ_{wave} are the wavenumber, the circular frequency and the wavelength of the wave respectively. c_L and c_T are the longitudinal velocities and the transverse velocities respectively, defined by

$$c_L = \sqrt{\frac{E(1-\nu)}{\rho(1+\nu)(1-\nu)}} = \sqrt{\frac{2\mu(1-\nu)}{\rho(1-2\nu)}}, \qquad c_T = \sqrt{\frac{E}{2\rho(1+\nu)}} = \sqrt{\frac{\mu}{\rho}} \tag{2.4}$$

where E is Young's modulus of the plate.

The displacement propagating in the x_1 direction and the normal direction x_3 as a result of the strain condition (Figure 2.1) can be defined as:

$$u_1 = \frac{\partial \Phi}{\partial x_1} + \frac{\partial \Psi}{\partial x_3}, u_2 = 0, u_3 = \frac{\partial \Phi}{\partial x_3} + \frac{\partial \Psi}{\partial x_1} \tag{2.5}$$

The stress given Hook's law can be defined as:

$$\sigma_{31} = \mu \cdot \left(\frac{\partial u_3}{\partial u_1} + \frac{\partial u_1}{\partial u_3}\right) = \mu \cdot \left(\frac{\partial^2 \Phi}{\partial x_1 \partial x_3} - \frac{\partial^2 \Psi}{\partial x_1^2} + \frac{\partial^2 \Psi}{\partial x_3^2}\right)$$
$$\sigma_{33} = \lambda \cdot \left(\frac{\partial u_1}{\partial u_1} + \frac{\partial u_3}{\partial u_3}\right) + 2\mu \cdot \frac{\partial u_3}{\partial u_3} = \lambda \cdot \left(\frac{\partial^2 \Phi}{\partial x_1^2} + \frac{\partial^2 \Psi}{\partial x_3^2}\right) + 2\mu \cdot \left(\frac{\partial^2 \Phi}{\partial x_3^2} + \frac{\partial^2 \Psi}{\partial x_1 \partial x_3}\right) \tag{2.6}$$

The equation of the Lamb wave can be obtained by applying boundary conditions for free upper and lower surfaces

$$\begin{aligned} &u(x,t) = u_0(x,t) && \text{(displacement)} \\ &t_i = \sigma_{ji} n_j && \text{(traction)} \\ &\sigma_{31} = \sigma_{33} = 0 \quad at \quad x_3 = \pm d/x = \pm h \end{aligned} \tag{2.7}$$

to (2.6) and substitute into (2.3)

$$\frac{\tan(qh)}{\tan(ph)} = \frac{4k^2 qpu}{(\lambda k^2 + \lambda p^2 + 2\mu p^2)(k^2 - p^2)} \tag{2.8}$$

Given the (2.8) has a trigonometric function tangent defined with sine and cosine, the (2.8) can be substituted in the symmetric and the anti-symmetric properties [32]:

$$\begin{aligned} &\frac{\tan(qh)}{\tan(ph)} = -\frac{4k^2 qp}{(k^2 - p^2)^2} && \text{for sysmmetric modes} \\ &\frac{\tan(qh)}{\tan(ph)} = -\frac{(k^2 - p^2)^2}{4k^2 qp} && \text{for antisysmmetric modes} \end{aligned} \tag{2.9}$$

(2.9) are also known as *Rayleigh-Lamb equations*. Generally, the symmetric modes (S_i modes) are in-plane modes whilst the anti-symmetric modes (A_i modes) are out-of-plane modes. Figure 2.2 shows the schematics of the symmetric and the anti-symmetric modes respectively. However, their solutions are only possible using numerical methods.

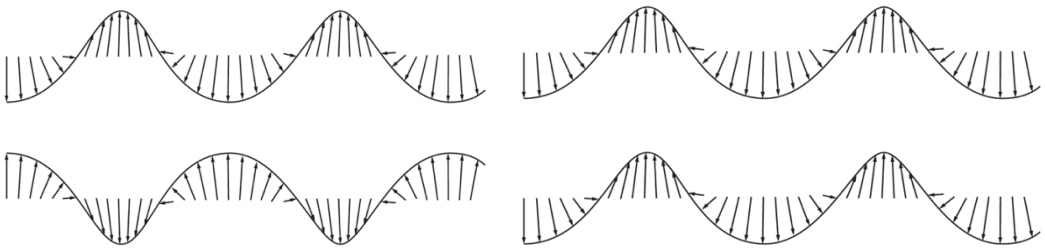

(a) **(b)**

Figure 2.2. Schematics of **(a)** the symmetric and **(b)** the anti-symmetric modes [90].

2.2.2. Guided Wave in Layered Structures

Given the plate with multiple layers, the guided wave propagation inside the plate not only includes the scattering of the upper and the bottom surface but also includes the reflection and the refraction of the layers. The anisotropic property of multi-layer panels can cause different wave speeds and the group velocities in different directions. Therefore, by expanding the (2.1), the Lamb wave propagating in a N-layered plate (shown in Figure 2.3) can be defined as its displacement filed u within each layer satisfying the Navier's displacement equations [32].

$$\mu^n \nabla^2 u^n + (\lambda^n + \mu^n)\nabla(\nabla \cdot u^n) = \rho^n \frac{\partial^2 u^n}{\partial t^2} \quad (n = 1, 2, \cdots, N) \tag{2.10}$$

where $\nabla = \frac{\partial}{\partial x_1} + \frac{\partial}{\partial x_2} + \frac{\partial}{\partial x_3}$, $\nabla^2 = \frac{\partial^2}{\partial {x_1}^2} + \frac{\partial^2}{\partial {x_2}^2} + \frac{\partial^2}{\partial {x_2}^2}$ and u is the displacement.

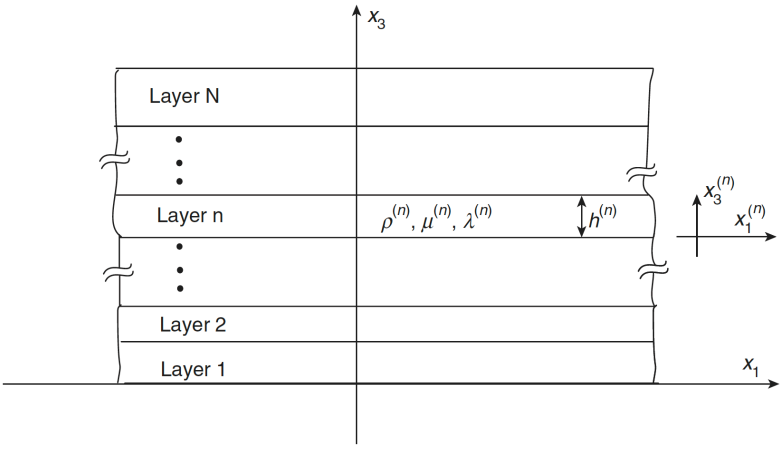

Figure 2.3. Schematic of the Lamb wave propagating in an N-layered plate [90].

2.2.3. Phase Velocity and Group Velocity

The phase (c_p) and the group (c_g) velocities are key characters for Lamb wave propagation. The phase velocity is the propagation speed of the wave phase at a certain frequency, which can be defined as [32]:

$$c_p = (\omega/2\pi) \cdot \lambda_{wave} \tag{2.11}$$

where λ_{wave} is the wavelength.

The group velocity can be defined as the velocity of the envelope wave at any constant phase point [32]:

$$c_g = \frac{d\omega}{dk} \tag{2.12}$$

The relationship between the wavenumber k, the circular frequency ω and the phase velocity c_p is defined by the below equation [32]:

$$k = \frac{\omega}{c_p}, \text{ where } \omega = 2\pi f \text{ and } c_p = f\lambda_{wave} \tag{2.13}$$

After substituting (2.13) into (2.12), the group velocity can be re-written by [32, 90-92]:

$$c_g = d\omega\left[d\left(\frac{\omega}{c_p}\right)\right]^{-1} = d\omega\left[\frac{d\omega}{c_p} - \omega\frac{dc_p}{{c_p}^2}\right]^{-1} = {c_p}^2\left[c_p - \omega\frac{dc_p}{d\omega}\right]^{-1}$$

$$= {c_p}^2\left[c_p - (fd)\frac{dc_p}{d(fd)}\right]^{-1} \tag{2.14}$$

Where f denotes the central frequency of the wave and fd is the frequency times thickness. The actual group velocity can be measured in experiments.

2.2.4. Dispersion Curves

Lamb waves are dispersive in nature that the wave velocity depends on excitation frequency and the structural geometry (plate thickness). Dispersion curves can be used to analyse and predict relationships between the frequency, the group velocity and the thickness. The time-harmonic factor $exp[i(kx - \omega t)]$ is an important physical characteristic of the dispersion curve. It has been concluded that only real values can represent the structural propagation

modes. Hence, for an isotropic plate, the dispersion equations can be rewritten in (2.9) to get real values of the wavenumbers k [32, 88-95]

$$\begin{aligned} &\frac{\tan(qh)}{q}+\frac{4k^2p\tan(ph)}{(k^2-p^2)^2}=0 && \text{for symmetric modes} \\ &q\tan(qh)+\frac{(k^2-p^2)^2\tan(ph)}{4k^2p}=0 && \text{for anti}-\text{symmetric modes} \end{aligned} \tag{2.15}$$

The numerical solutions of the above equations can be referred to [32] which includes obtaining a root via the frequency-thickness product $(fd)_0$ choosing and the phase velocity (c_p) searching. The root-finding algorithm must be reapplied because multiple modes always exist at the same fd product. Once the roots at all other fd products of interest are found, the dispersion curves can be plotted.

For an N-layered laminate with free upper and lower surfaces, the general solution has four unknown constants C_1^n, C_2^n, C_3^n and C_4^n (n =1, 2, ⋯, N) for each layer to the (2.10). By applying the boundary conditions at the $N-1$ interface and two free surfaces, there is a total of $4N$ equations for the whole laminate:

$$\begin{bmatrix} A_{11} & A_{12} & \cdots & A_{2(4N)} \\ A_{21} & A_{22} & \cdots & A_{2(4N)} \\ \vdots & \vdots & \ddots & \vdots \\ A_{(4N)1} & A_{(4N)2} & \cdots & A_{(4N)(4N)} \end{bmatrix} \cdot \begin{bmatrix} C_1^1 \\ C_2^1 \\ \vdots \\ C_4^N \end{bmatrix} = \begin{bmatrix} 0 \\ 0 \\ \vdots \\ 0 \end{bmatrix} \tag{2.16}$$

[A] is the coefficient matrix and must be 0 to make the above equation generally tenable, *i.e.*,

$$|A(\omega, k, \lambda^n, \mu^n, d_n)| = 0 \tag{2.17}$$

(2.17) is an implicit equation that the circular frequency ω and the wavenumber k are related to the effective material properties (λ^n, μ^n) and the thickness d_n of the individual layer. The captured Lamb waves often present much complexity due to their dispersive nature. Many works have been done to investigate the inherent properties of Lamb waves, including global matrix method (GMM), transfer matrix method (TMM) and semi-analytical finite element (FAME), the theories of the above methods can be referred to [64].

2.3. Lead Zirconate Titanate (PZT) Transducers

2.3.1. Polarization

Polarization refers to the separation of positive and negative charges at different ends of a dielectric material under the action of an applied electric field, as is shown in Figure 2.4.

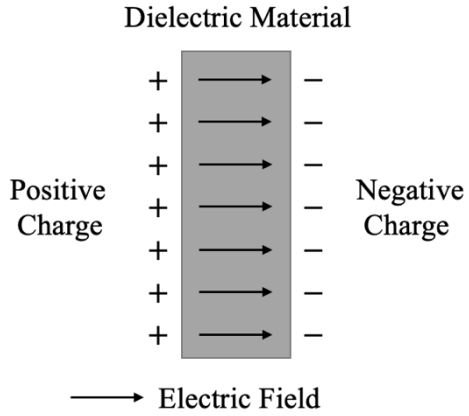

Figure 2.4. Schematic of the polarization in an applied electric field [96].

The level and the direction of the polarization can be defined by the electric displacement vector *D* as [96]:

$$D = \varepsilon E + P \tag{2.18}$$

where ε, εE, P denote the dielectric permittivity, the polarization induced by an applied electric field, and the permanent polarization respectively. The process of generating permanent polarization in a material is known as poling.

2.3.2. Piezoelectricity

The piezometric transducers can convert electrical energy into mechanical energy, or vice versa. Figure 2.5 shows the schematics of the direct and the converse piezoelectric effects.

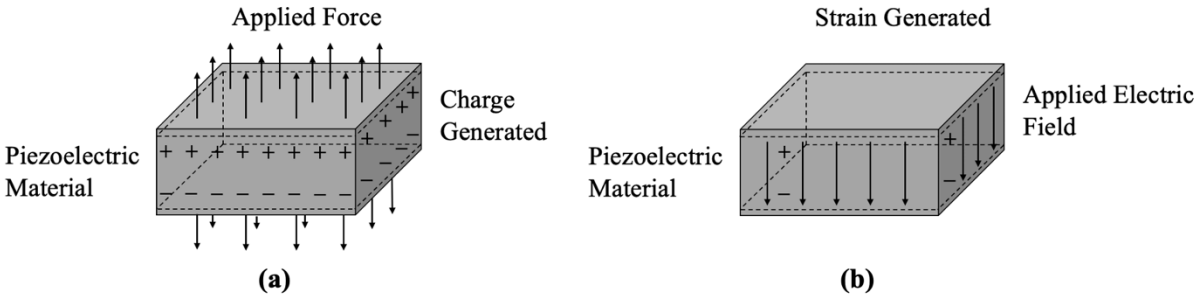

Figure 2.5. Schematics of **(a)** the direct and **(b)** the converse piezoelectric effects [96].

The general form of the piezoelectric matrix can be defined as [96]:

$$\begin{Bmatrix} S_1 \\ S_2 \\ S_3 \\ S_4 \\ S_5 \\ S_6 \\ D_1 \\ D_2 \\ D_3 \end{Bmatrix} = \begin{bmatrix} s_{11}^E & s_{12}^E & s_{13}^E & 0 & 0 & 0 & 0 & 0 & d_{31} \\ s_{11}^E & s_{22}^E & s_{23}^E & 0 & 0 & 0 & 0 & 0 & d_{32} \\ s_{13}^E & s_{23}^E & s_{33}^E & 0 & 0 & 0 & 0 & 0 & d_{33} \\ 0 & 0 & 0 & s_{44}^E & 0 & 0 & 0 & d_{24} & 0 \\ 0 & 0 & 0 & 0 & s_{55}^E & 0 & d_{15} & 0 & 0 \\ 0 & 0 & 0 & 0 & 0 & s_{66}^E & 0 & 0 & 0 \\ 0 & 0 & 0 & 0 & d_{15} & 0 & \varepsilon_{11}^T & 0 & 0 \\ 0 & 0 & 0 & d_{24} & 0 & 0 & 0 & \varepsilon_{22}^T & 0 \\ d_{31} & d_{32} & d_{33} & 0 & 0 & 0 & 0 & 0 & \varepsilon_{33}^T \end{bmatrix} \begin{Bmatrix} T_1 \\ T_2 \\ T_3 \\ T_4 \\ T_5 \\ T_6 \\ E_1 \\ E_2 \\ E_3 \end{Bmatrix} \tag{2.19}$$

For an orthotropic material, the compliance matrix $[s^E]$ can be expressed as a function of the engineering constants E_i, v_{ij} and G_{ij} [96]:

$$[s^E] = \begin{bmatrix} \frac{1}{E_x} & -\frac{v_{yx}}{E_y} & -\frac{v_{zx}}{E_z} & 0 & 0 & 0 \\ -\frac{v_{xy}}{E_x} & -\frac{1}{E_y} & -\frac{v_{zy}}{E_{yz}} & 0 & 0 & 0 \\ -\frac{v_{xz}}{E_x} & -\frac{v_{yz}}{E_y} & -\frac{1}{E_z} & 0 & 0 & 0 \\ 0 & 0 & 0 & \frac{1}{G_{yz}} & 0 & 0 \\ 0 & 0 & 0 & 0 & \frac{1}{G_{xz}} & 0 \\ 0 & 0 & 0 & 0 & 0 & \frac{1}{G_{xy}} \end{bmatrix} \tag{2.20}$$

where x and y are aligned with the poling direction 1 and 2, and z with the direction 3. Due to the matrix is symmetric, so

$$\frac{v_{yz}}{E_y} = \frac{v_{xy}}{E_x}, \quad \frac{v_{zy}}{E_z} = \frac{v_{xz}}{E_x}, \quad \frac{v_{zy}}{E_z} = \frac{v_{yz}}{E_y} \tag{2.21}$$

For a thin disk piezoelectric ceramic, it has transversely isotropic properties that the material properties are the same in the plane perpendicular to the direction of polarization. Hence, the compliance matrix can be reduced to:

$$[s^E] = \begin{bmatrix} \frac{1}{E_p} & -\frac{v_p}{E_p} & -\frac{v_{zp}}{E_z} & 0 & 0 & 0 \\ -\frac{v_p}{E_p} & -\frac{1}{E_p} & -\frac{v_{zp}}{E_z} & 0 & 0 & 0 \\ -\frac{v_{pz}}{E_p} & -\frac{v_{pz}}{E_p} & -\frac{1}{E_z} & 0 & 0 & 0 \\ 0 & 0 & 0 & \frac{1}{G_{zp}} & 0 & 0 \\ 0 & 0 & 0 & 0 & \frac{1}{G_{zp}} & 0 \\ 0 & 0 & 0 & 0 & 0 & \frac{1}{G_p} \end{bmatrix} \tag{2.22}$$

and since the matrix is symmetric, so:

$$\frac{v_{zp}}{E_z} = \frac{v_{pz}}{E_p} \tag{2.23}$$

where the subscript p denotes the in-plane properties. The piezoelectric coefficients matrix is [96]:

$$[d] = \begin{bmatrix} 0 & 0 & 0 & 0 & d_{15} & 0 \\ 0 & 0 & 0 & d_{15} & 0 & 0 \\ d_{31} & d_{31} & d_{33} & 0 & 0 & 0 \end{bmatrix} \tag{2.24}$$

and the dielectric permittivity is [96]:

$$[\varepsilon^T] = \begin{bmatrix} \varepsilon_{11}^T & 0 & 0 \\ 0 & \varepsilon_{11}^T & 0 \\ 0 & 0 & \varepsilon_{33}^T \end{bmatrix} \tag{2.25}$$

The coupling coefficients for each piezoelectric mode is [96]:

$$k_{31} = \sqrt{\frac{d_{31}^2}{\varepsilon_{33}^T s_{11}^E}}, \quad k_{33} = \sqrt{\frac{d_{33}^2}{\varepsilon_{33}^T s_{33}^E}}, \quad k_{15} = \sqrt{\frac{d_{15}^2}{\varepsilon_{11}^T s_{55}^E}}, \quad g_{31} = \frac{d_{31}}{\varepsilon_{33}^T}, \quad g_{33} = \frac{d_{33}}{\varepsilon_{33}^T} \tag{2.26}$$

For a thin disk piezoelectric ceramic, the coupling coefficient k_p can be expressed by

$$k_p = \sqrt{\frac{2k_{31}^2}{1+\frac{s_{12}^E}{s_{11}^2}}} \tag{2.27}$$

The mechanical engineering constants E_p, E_z, G_p and G_{zp} can be defined as:

$$E_p = \frac{1}{s_{11}^E}, \quad E_z = \frac{1}{s_{33}^E}, \quad G_p = \frac{E_p}{2(1+v_p)}, \quad G_{zp} = \frac{1}{s_{55}^E} \tag{2.28}$$

where s_{55}^E is:

$$s_{55}^E = \frac{d_{15}^2}{\varepsilon_{11}^T k_{15}^2} \tag{2.29}$$

The Poisson's ratio v_p is:

$$v_p = -E_p s_{12}^E \tag{2.30}$$

where s_{12}^E is:

$$s_{12}^E = -s_{11}^E + 2\frac{d_{31}^2}{k_p^2 \varepsilon_{33}^T} \tag{2.31}$$

2.3.3. Electro-Mechanical Impedance

The electro-mechanical impedance (EMI) method based on active sensing (normally embed or surface mount PZT transducers into/on the host structure) is one of the most promising methods in SHM technology. The theory of the EMI method is based on the piezoelectric effect that a PZT transducer can generate the strain conversed by applying a harmonic voltage [97]. This method not only can evaluate the local damage severities but also can detect the bonding conditions between the PZT transducer and its host structure. Sharif-Khodaei *et al.* [97] experimentally and numerically evaluated the barely visible impact damage (BVID) and the debonding on a composite panel, and further numerically applied the EMI technique to a complicated stiffened composite panel. The BVID and the debonding were detected when values of the root mean square deviation (RMSD) of the impedance were higher than normal ones. In addition, Zou *et al.* [98] used the EMI technique to numerically study the debonding detection of the aluminium substrate based on the boundary element method (BEM) and also experimentally validated the BEM results. The damage indexes (DI) – RMSD, the mean absolute percentage deviation (MAPD) and the correlation coefficient deviation (CCD) were

used to evaluate the debonding in this paper. It was found that the frequency range of 70-85 kHz could be used for detecting the damage using the MAPD and the CCD values.

In addition, the EMI technique can also be used for accessing transducers fractures, degradation of mechanical/electrical properties of the transducers, and the integrity of bonding properties between the PZT transducer and its host structure [99, 100]. Previous research had found that any change in the host structure would change its vibration behaviour and indirectly affect the admittance properties of the PZT transducer [101, 102]. The admittance change in the imaginary part will determine the integrity structure between the transducer and its host structure and that change in the real part will determine the damage distance from the PZT transducer [97]. Park *et al.* [100] accessed the integrity of the bonding properties by comparing the slope of the imaginary part of the admittance for surface-mounted PZT transducers by using different bonding materials. Voutetaki *et al.* [103] pointed out that different bonding situations between the embedded and surface-mounted PZT transducers would cause shifts in the slope of the imaginary part of the admittance.

The tensorial piezoelectric constitutive equations coupled with the electrical and the mechanical effects can be defined as

$$S_i = s_{ij}^E T_j + d_{mi} E_m$$
$$D_m = d_{mi} T_i + \varepsilon_{mk}^T E_k \tag{2.32}$$

where S denotes the mechanical strain, s denotes the mechanical compliance, T denotes the mechanical stress, d denotes the piezoelectric coupling constant, E denotes the electric field, D denotes the charge density, ε is the dielectric constant of the PZT transducer, and subscripts i and j are the directions of the stress, subscripts m and k are the directions of the strain and the electric field. Both the electric field E and the mechanical stress T are measured at zero electric fields and zero stress respectively

For a one-dimensional situation, the total electric current I flowing through the PZT transducer can be expressed when $T = 0$,

$$I = i\omega \iint D_3 dxdy = i\omega \iint \varepsilon_{33}^T (1 - \delta) E_3 dxdy \tag{2.33}$$

where ω is the angular frequency, δ is the dielectric loss tangent of the PZT transducer, and x and y denote the coordinates of the PZT transducer.

The formula of electrical admittance for a free-free boundary condition PZT transducer $Y_{free}(\omega)$ is given in [100]

$$Y_{free}(\omega) = \frac{I}{V} = \omega \frac{wl}{t_c} (\varepsilon_{33}^T (1 - i\delta)) \tag{2.34}$$

where V denotes the applied voltage, w, l and t_c denote the width, the length, and the thickness of the PZT transducer respectively.

For a surface-mounted PZT transducer, the formula of the electrical admittance $Y_{surface}(\omega)$ is shown in [100]

$$Y_{surface}(\omega) = i\omega \frac{wl}{t_c}(\varepsilon_{33}^{T}(1-i\delta) - d_{31}^{2}\hat{Y}_{P}^{E} + \frac{Z_a(\omega)}{Z_a(\omega)+Z_s(\omega)})d_{31}^{2}\hat{Y}_{P}^{E}(\frac{\tan kl}{kl})) \tag{2.35}$$

where d_{31} is piezoelectric strain constant, $\hat{Y}_P^E$ is the complex Young's modulus of the PZT at zero electric field, $Z_a(\omega)$ and $Z_s(\omega)$ are the mechanical impedance of the host structure and that of the PZT transducer respectively, k is the wavenumber of the PZT transducer, which is defined as

$$k = \omega\sqrt{\frac{\rho}{\hat{Y}_P^E}} \tag{2.36}$$

where ρ denotes the mass density of the PZT transducer.

Mathematical expressions for the embedded PZT transducer largely depend on the manufacturing conditions of embedding. A 3D model of the electrical admittance $Y_{embedded}(\omega)$ which is suitable for embedding PZT transducers into concrete was proposed by [101].

2.4. Finite Element Modelling – Dynamic Analysis in the Time Domain

Wave propagation is a dynamic problem in the time domain, which needs to be solved by numerical calculation methods. The governing equation of the finite element modelling (FEM) for the dynamic problem can be considered as generalized Newton's second law, which can be defined as [90]:

$$[\mathbf{M}]\{\ddot{\mathbf{d}}\} + [\mathbf{C}]\{\dot{\mathbf{d}}\} + [\mathbf{K}]\{\mathbf{d}\} = \{\mathbf{F}\} \tag{2.37}$$

where $[\mathbf{M}]$, $[\mathbf{C}]$ and $[\mathbf{K}]$ are the mass matrix, the damping matrix and the Global stiffness matrix, respectively. $\{\mathbf{d}\}$ and $\{\mathbf{F}\}$ are the Nodal displacement vector and the Equivalent load vector, respectively. In addition, $\{\dot{\mathbf{d}}\} = d\{\mathbf{d}\}/dt$ and $\{\ddot{\mathbf{d}}\} = d^2\{\boldsymbol{d}\}/dt^2$ denote the velocity vector and the acceleration vector.

For the Rayleigh damping, the damping matrix is the linear combination of the mass matrix and the stiffness matrix [90]:

$$[\mathbf{C}] = \alpha[\mathbf{M}] + \beta[\mathbf{K}]$$

(2.38)

where α and β can be acquired from experiments. Since α has little effect on high-frequency problems in ultrasonic guided waves, the governing equation can be expressed by [90]

$$[\mathbf{M}]\{\ddot{\mathbf{d}}\} + \beta[\mathbf{K}]\{\dot{\mathbf{d}}\} + [\mathbf{K}]\{\mathbf{d}\} = \{\boldsymbol{F}\} \tag{2.39}$$

The most popular numerical approach is the direct integration method which is a finite difference method obtaining the derivation of the time t from Taylor's polynomial to calculate the time domain response [104]. The explicit and implicit algorithms are widely used for the direct time-integration methods in the numerical calculation [104]. In addition, For larger models, the explicit algorithm is more computationally efficient than the implicit algorithm [105].

2.4.1. Explicit Time Integration

The explicit algorithm is only conditionally stable that the equilibrium state at the time step $t + \Delta t$ entirely depends on the results of the previous time step t [104]. The most widely used explicit direct integration method is the central difference method. In the central difference method, the velocity and the acceleration at the time step n can be estimated as [90]

$$\{\dot{\mathbf{d}}\}_n = \frac{d}{dt}[\mathbf{d}]_n = \frac{1}{2\Delta t}(\{\mathbf{d}\}_{n+1} - \{\mathbf{d}\}_{n-1})$$
$$\{\ddot{\mathbf{d}}\}_n = \frac{d}{dt^2}[\mathbf{d}]_n = \frac{1}{\Delta t^2}(\{\mathbf{d}\}_{n+1} - 2\{\mathbf{d}\}_n - \{\mathbf{d}\}_{n-1}) \tag{2.40}$$

For the direct integration method, the value of the initial displacement, the velocity and the acceleration of the host structure shall be provided to solve the problem [90].

2.4.2. Implicit Time Integration

The implicit algorithm is unconditionally stable in that the increments size of the time step Δt only depends on the frequency range and the accuracy requirement [104]. The representative implicit direct integration method is the Newmark method. In the Newmark method, the velocity and the displacement at the time step n can be estimated as [90]

$$\{\dot{\mathbf{d}}\}_{n+1} = \{\dot{\mathbf{d}}\}_n + \Delta t(1-\gamma)\{\ddot{\mathbf{d}}\}_n + \gamma\{\ddot{\mathbf{d}}\}_{n+1}), \quad (0.5 \ll \gamma \ll 1)$$

$$\{\mathbf{d}\}_{n+1} = \{\mathbf{d}\}_n + \Delta t\{\mathbf{d}\}_n + \frac{\Delta t^2}{2}((1-2\beta)\{\ddot{\mathbf{d}}\}_n + 2\beta\{\ddot{\mathbf{d}}\}_{n+1}), \quad (0.5 \ll 2\beta \ll 1)$$

(2.41)

2.4.3. Modelling Coupled PZT Actuator – Explicit Method

Figure 2.6 shows an actuator's polar coordinate system ($r-\theta-Z$) given the absence of an in-plane electric field (*i.e.*, $K_1 = K_2 = 0$) and an out-of-plane electric field K_3. For a thin disk PZT actuator with a radius of R and the thickness of h, the in-plane radial strain ε_{r-PZT} and the in-plane tangential strain $\varepsilon_{\theta-PZT}$ can be given [32] when applying an external voltage V_{inp}:

$$\varepsilon_{r-PZT} = \varepsilon_{\theta-PZT} = d_{31}K_3 = \frac{d_{31}}{h_{PZT}} \cdot V_{inp} \tag{2.42}$$

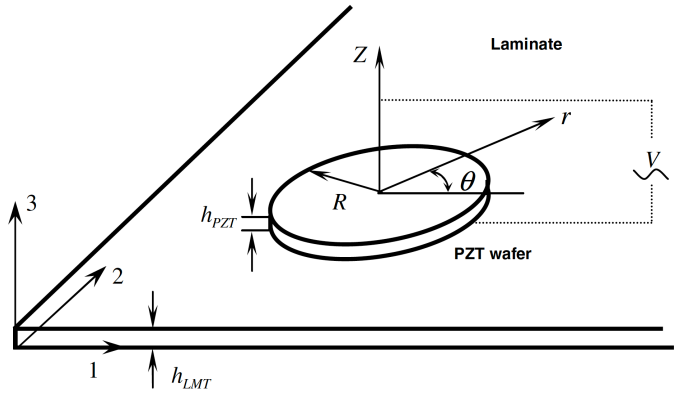

Figure 2.6. Schematic of a PZT actuator in a polar coordinate system [32].

As is shown in Figure 2.6, the PZT actuator is mounted on the surface of the quasi-isotropic or the isotropic laminate. Due to the small size of the PZT actuator, the distribution of the uniform strain can be given by ($\varepsilon_r^i \approx \varepsilon_\theta^i \approx \varepsilon^i$). An equivalent radial deformation d_r along the PZT circumference can be given by integrating the strain ε_r^i at interface [32]:

$$d_r = \int_0^R \varepsilon^i dr = R \cdot \frac{d_{31}}{h_{PZT}} \left[\frac{\tilde{E}(1-v_{PZT})}{E_{PZT}} + 1\right] \cdot V_{inp} \tag{2.43}$$

where R, ε^i and d_{31} are the PZT radius, the interface strain, and the piezoelectric strain constant respectively. E_{PZT}, v_{PZT}, h_{PZT} are the elastic modulus, the Poisson's ratios and the thickness of the PZT actuator. $\tilde{E}$ is a constant related to E_{PZT}, h_{PZT}, E_{LMT}, h_{LMT}.

2.4.4. Modelling Coupled PZT Sensor – Explicit Method

For a thin disk PZT sensor with a radius of R and the thickness of h_{PZT}, given the planar deformation in the absence of the electric field, the electrical displacement is

$$Q = d_{31}(\sigma_r + \sigma_\theta) = d_{31}\frac{E_{PZT}}{1-\nu_{PZT}}(\varepsilon_r + \varepsilon_\theta) \tag{2.44}$$

where σ_r, ε_r, σ_θ and ε_θ are the radial stress and strain, the tangential stress and strain respectively. The output voltage V_{otp} of the PZT sensor under the deformation can then be expressed as:

$$V_{otp} = d_{31}\frac{E_{PZT}h_{PZT}}{4\pi\xi_3 p_0(1-\nu_{PZT})}\cdot\varepsilon_{cen} \tag{2.45}$$

where ξ_3 and p_0 are the relative dielectric constant and the dielectric permittivity of the free space. ε_{cen} is the strain measured at the centre of the PZT sensor.

2.5. Signal Actuation and Postprocessing

2.5.1. Signal Actuation

Researchers have shown that a broadband linear chirp signal covering the entire ranges of interesting input frequencies is one of the most effective excitation signals [106-108]. The equation of the broadband chirp signal in the time domain $s_c(t)$ is

$$s_c(t) = w(t)\sin\left(2\pi f_0 t + \frac{f_1 - f_0}{T}t^2\right), \text{where } w(t) = \begin{cases} 1, & \text{for } 0 \le t \le T \\ 0, & \text{for } t \ge T \end{cases} \tag{2.46}$$

where f_0 and f_1, the lower and the upper frequencies, were given as 25 kHz and 500 kHz respectively. T is the duration of the chirp window which was set as 200 μs in following chapters.

The signal was then converted from the time domain to the frequency domain based on a Fourier transform reconstruction algorithm to obtain the whole ranges of the narrowband Hanning-windowed toneburst signal. The equation for the reconstruction algorithm is

$$R_b(\omega) = R_c(\omega)\frac{S_b(\omega)}{S_C(\omega)} \tag{2.47}$$

where $R_b(\omega)$ and $R_c(\omega)$ are the Fourier transforms of the recorded toneburst response and chirp response, and $S_b(\omega)$ and $S_c(\omega)$ are the Fourier transforms of the narrowband input toneburst excitation signal and the broadband input chirp excitation signal respectively. The narrowband Hanning-windowed toneburst signal in the frequency domain $s_b(t)$ can be expressed

$$s_b(t) = w(t)\sin(2\pi f_c t), \text{where } w(t) = 0.5\left[1 - \cos(\frac{2\pi f_c t}{n_c})\right] \tag{2.48}$$

where f_c is a centre frequency and n_c is the number of the cycle.

2.5.2. Signal Averaging

Lamb wave acquisition needs to have stable signals for minimizing uncertain noises. After averaging 10 magnitudes of signals at each sampling point, random noises can be avoided. There are two basic methods to average Lamb wave signals: synchronous averaging and asynchronous averaging. The synchronous averaging method is often used for the reference/benchmark signal, whilst the asynchronous averaging method is used for the non-reference/benchmark signal [32, 90].

2.5.3. De-noising

There are four commonly ideal-filter frequency responses which can be formulated by [91]:

$$\begin{aligned}
&\text{Lowpass} && H(\omega) = \begin{cases} 1, \omega < \omega_c \\ 0, \ \omega \geq \omega_c \end{cases} \\
&\text{Highpass} && H(\omega) = \begin{cases} 0, \omega < \omega_c \\ 1, \ \omega \geq \omega_c \end{cases} \\
&\text{Bandpass} && H(\omega) = \begin{cases} 1, \omega_L < \omega < \omega_H \\ 0, \ \text{Otherwise} \end{cases} \\
&\text{Bandstop} && H(\omega) = \begin{cases} 1, \omega < \omega_L \ or \ \ \omega \geq \omega_H \\ 0, \ \text{Otherwise} \end{cases}
\end{aligned} \tag{2.49}$$

Figure 2.7 shows commonly ideal digital-filter frequency responses.

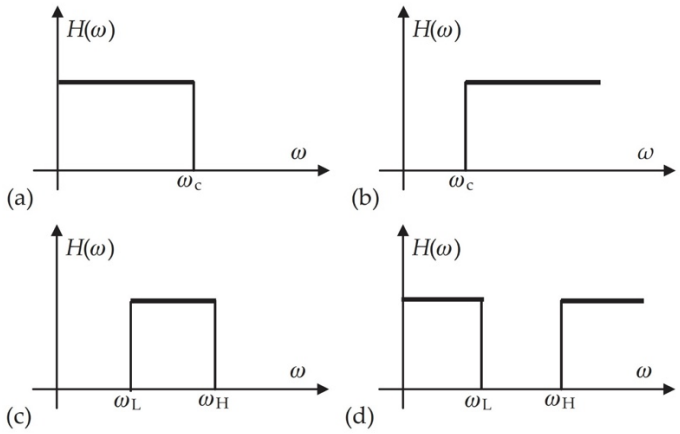

Figure 2.7. Common ideal-filter types: **(a)** the lowpass filter; **(b)** the highpass filter; **(c)** the bandpass filter and **(d)** the bandstop [91].

2.5.4. Time Domain Analysis – Hilbert Transform

Hilbert transform normally shows the energy distribution in the time domain. It is used to obtain the envelope of the signal curve that extracts the signal's amplitude. The purpose of extracting the signal's envelope by applying the Hilbert transform is to obtain the time-of-arrival of wave packets. Mathematically, the definition of the Hilbert transform is [32, 88, 90, 91]

$$H(t) = \frac{1}{\pi}\int_{-\infty}^{+\infty}\frac{f(\tau)}{t-\tau}d\tau \tag{2.50}$$

where $f(\tau)$ is the original signal. The integral is the Cauchy's principal value around the singularity $\tau = t$. In addition, the Hilbert transform is also used to construct the complex analytic signal $F_A(t)$ after 90° phase-shift:

$$F_A(t) = f(t) + iH(t) = e(t)e^{i\emptyset(t)}$$
$$e(t) = \sqrt{f^2(t) + H^2(t)}, \text{and } \emptyset(t) = \frac{1}{2\pi}\cdot\frac{d}{dt}\arctan\frac{H(t)}{f(t)} \tag{2.51}$$

where the real part $f(t)$ is the original signal and the imaginary part $H(t)$ is its Hilbert transform. The envelope $e(t)$ is the module and $\emptyset(t)$ is the instantaneous frequency of the $F_A(t)$.

2.5.5. Frequency Domain Analysis – Fourier Transform

A periodic signal can be defined as [32, 88],

$$f(t) = a \cdot \sin(\omega t) \tag{2.52}$$

where $T = 2\pi/\omega$. The Fourier expansion is

$$f(t) = \sum_{k=-\infty}^{+\infty} C_k e^{ik\omega t}, \quad \infty < t < + \pm, \quad i = \sqrt{-1} \tag{2.53}$$

where

$$\begin{cases} C_0 = \dfrac{1}{T}\displaystyle\int_T f(t)dt \\ C_k = \dfrac{1}{T}\displaystyle\int_T f(t)e^{-ik\omega t}\,dt \end{cases} \tag{2.54}$$

The Fourier transform of a periodic signal $f(t)$ can be expressed by

$$F(\omega) = \int_{-\infty}^{+\infty} f(t) \cdot e^{i\omega t} dt, \qquad -\infty < \omega < +\infty \tag{2.55}$$

The function of the Fourier transform (FT) is to convert the signal from the time domain to the frequency domain.

2.6. Damage Detection and Localization

2.6.1. Damage Detection – Damage Index

The damage index (DI) is generally used to detect the damage by comparing the difference between the baseline and the current signals. The DI of the correlation coefficient is a direct way to access the change in the time domain when damage presents. The equation of the correlation coefficient can be expressed as [109]:

$$DI = 1 - \rho = 1 - \frac{\int_0^T [x(t) - \mu_x][y(t) - \sigma_y]dt}{\sigma_x \sigma_y} \tag{2.56}$$

where ρ is the correlation coefficient, $x(t)$ and $y(t)$ are the baseline and the current signals, and T and σ are the time domain of measurements and the standard deviation, respectively.

2.6.2. Damage Localization – Delay-and-sum Algorithm

The theory of the delay-and-sum (DAS) algorithm is based on the sum of differences of residual signals between the scattered and the pristine signals for each paired path at the corresponding scattered time to predict the probably damaged positions. Calculating the group velocity accurately is the key step in the DAS algorithm [110-112].

The first step is to divide the structure panel into imaging pixel points, the imaging point in the panel for the $i-j$ transducer pair of the actuator is (x_i, y_i) and that of the sensor is (x_j, y_j), which can measure the panel manually.

The second step is to average and filter the pristine and the damaged signals to remove noises.

The third step is to calibrate the group velocity by extracting the time-of-arrival (ToA) from the envelopes of the pristine signals using the Hilbert transform. The reason for using the Hilbert transform of the pristine signal instead of using the original pristine signal directly is that the phenomena of the crosstalk in some pairs can interfere with the measuring results of the ToA. For calculating the group velocity, the distances between each actuator and sensor for each pair can be measured on the panel, and then the relationship between the group velocity (c_g), the ToA (t_{arr}) and the time offset (t_{off}) can be formulated by

$$t_{arr} = \frac{\sqrt{\left(x_i - x_j\right)^2 + \left(y_i - y_j\right)^2}}{c_g} + t_{off} \tag{2.57}$$

After extracting the ToA for each pair path, using the ployfit function in MATLAB to plot the group velocity. Figure 2.8 is the schematic of the ployfit function for calculating the group velocity at 50 kHz. The slope of the below curve is the group velocity c_g, and the intercept of the time axis is the time offset t_{off}.

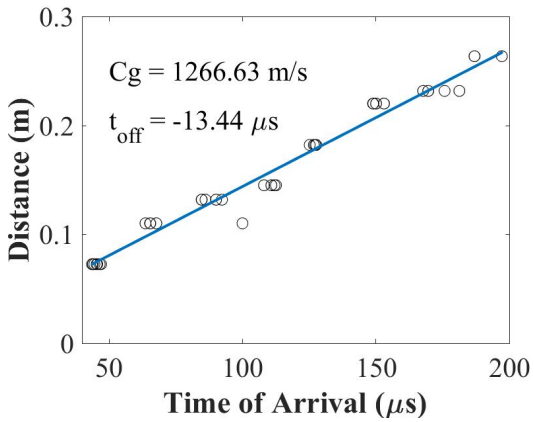

Figure 2.8. Schematic of calculating the group velocity at 50 kHz.

The fourth step is to calculate the residual signals of the differences between the pristine and the damaged signals for each transducer pair. The residual signal can be measured as the magnitude of the complex analytical signal:

$$r_{ij}(t) = \sqrt{u_{ij}(t)^2 + v_{ij}(t)^2} \tag{2.58}$$

where $u_{ij}(t)$ is the difference between the pristine and the damaged signals for the $i-j$ transducer pair, $v_{ij}(t)$ is the Hilbert transform of the $u_{ij}(t)$.

The final step is to the delay-and-sum algorithm to obtain the image value for each spatial location point. The image value $E(x,y)$ can be expressed by

$$E(x,y) = \frac{1}{N}\sum_{i=1}^{N-1}\sum_{j=i+1}^{N} r_{ij}\left(t_{ij}(x,y)\right) \tag{2.59}$$

According to the above equation, the damage position is located at the maximum value $E(x,y)$ with the corresponding scattering time $t_{ij}(x,y)$.

2.7. Scanning Laser Vibrometry for SHM using UGW

Laser Doppler vibrometer (LDV) is an excellent tool to study the guided wave propagation and damage interaction, which provides precise displacement and velocity solutions and is widely used in the aeronautic industry for SHM purposes [113]. In addition, it allows the contactless and interference-free measurement of 3D vibrations in mechanical structures. This laser vibrometry is based on the optical Doppler effect, which leads to UGW scattered on the surface with a movement change in the frequency [114]. The change in frequency is proportional to the value of the vibration velocity determined by the interferometric method accurately although the value is significantly small (less than 10^{-8}) [114]. Figure 2.9 shows the schematic of the PSV-500-3D Polytec 3D Scanning Vibrometer.

Figure 2.9. Schematic of the PSV-500-3D Polytec 3D Scanning Vibrometer [114].

2.7.1. The Doppler Effect

When a wave is reflected by a moving target and scanned by LDV, the measured frequency shift of the wave can be defined as [113]:

$$f_D = \frac{2v}{\lambda} \tag{2.60}$$

where v is the target's velocity and λ is the wavelength of the wave. In turn, to determine the target's velocity, the frequency shift needs to be measured at a known wavelength, which is done by the laser interferometer in LDV.

2.7.2. Interferometry

LDV is based on optical interference, that is, essentially requires the overlap of two coherent light beams with their respective intensities I_1 and I_2. The total intensity of the two beams is not a simple sum of individual intensities but is derived from the following formula [113]:

$$I_{tot} = I_1 + I_2 + 2\sqrt{(I_1 I_2)\cos[\frac{2\pi(r_1 - r_2)}{\lambda}]} \tag{2.61}$$

where r is the optical path. The interference relates to the difference in path length between both beams.

2.7.3. Optical Setup of Laser Doppler Vibrometry

Figure 2.10 shows the schematic of the physical law of the optical design for LDV. As is shown in Figure 2.10, the laser beam is split by the beam splitter I (BS 1) into a reference beam and a measurement beam. After passing through the beam splitter II (BS 2), the measurement beam focuses on the sample and reflects it. This reflected beam then deflects downwards by the BS 2 and will merge with the reference beam to the detector in the end [113]. Due to the constant of the optical path of the references beam ($r_2 = \text{const.}$) (except for the negligible thermal effects on the interferometer), the sample movement ($r_1 = r(t)$) generates a light/dark pattern on the detector, which is a typical interference method. A complete light/dark cycle on the detector corresponds exactly to the amount of displacement of half a wavelength of the light used.

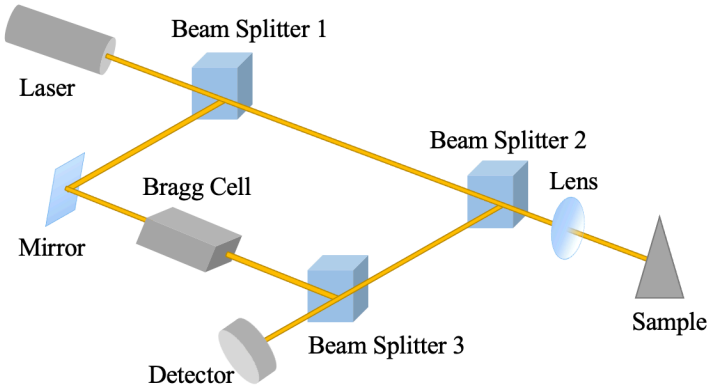

Figure 2.10. Schematic of the physical law of the optical design for LDV [114].

The change of optical path per unit time represents the Doppler frequency shift of the measured beam. In terms of metrology, the modulation frequency of the interferometer is directly proportional to the sample vibration velocity. Since the light/dark pattern (and modulation frequency) generated by an object moving away from the interferometer are the same as those generated by an object moving toward the interferometer, this setup alone cannot determine the direction of the object moving. Therefore, an acousto-optic modulator (Bragg cell) with a typical optical frequency shift of 40 MHz is placed in the reference beam (laser frequency is $4.74 \cdot 10^{14}$ Hz for comparison purposes). When the sample is static, a typical interference modulation frequency of 40 MHz will be generated. Hence, if the sample moves towards the interferometer, the modulation frequency increases; if the sample moves away from the interferometer, the frequency received by the detector is less than 40 MHz. This means it is now possible to detect not only the length of the optical path but also the direction of the movement.

2.7.4. Displacement or Velocity of Vibrations

In principle, LDV can directly measure the displacements and the velocities. Instead of integrating the velocity, the displacement is calculated by counting the light/dark fringes on the LDV detector. By using suitable interpolation techniques, LDV achieves displacement resolution of up to 2 nm and pm level with digital demodulation technology. The maximum amplitudes of the harmonic vibrations can be defined as [113]:

$$v = 2\pi \cdot f \cdot s \tag{2.62}$$

where v, f and s are the vibration velocity, the vibration frequency and the vibration displacement respectively.

2.8. Summary

This chapter introduced the fundamentals of UGW in different types of plates and dispersive properties. After that, the polarization, the piezoelectricity and the EMI properties of the PZT transducer have been reviewed, and the theories of the finite element modelling including explicit and implicit time integration methods and modelling coupled PZT actuator/sensor using the explicit dynamic analysis have also been presented. Furthermore, the signal actuation and the postprocessing were introduced, followed by the theories of the damage index (DI) – the correlation coefficient for damage detection, the delay-and-sum algorithm for damage localization, and laser Doppler vibrometry for damage identification.

Chapter 3

3. Manufacturing

3.1. Introduction

PZT transducers are widely used in SHM systems as they are lightweight and relatively inexpensive [33, 34, 115]. In addition, they can simultaneously exhibit actuator/sensor behaviours, which allows for both passive and active detections [33-35]. They are usually embedded inside or surface-mounted on the composites. For embedding techniques, Mall and Yocum *et al.* [116-118] proposed two traditional methods: the insertion and the cut-out methods. However, the traditional wire connecting methods to embed and surface mount PZT transducers can significantly increase the weight of the host structure. Therefore, an alternative approach that PZT transducers were connected on SMART (Stanford Multi-Actuator Receiver Transduction) Layer^{TM} as an extra ply during lay-up was reported in [2, 119-121]. This layer based on the circuit-printed technique acted as an extra ply during the lay-up instead of simply embedding PZT transducers into composite laminates.

Earlier, Salmanpour M. S. et al. [122] reported that the SMART layer did not meet the operational and environmental conditions of the regional aircraft as related to low/high temperature changes under cyclic loadings. In addition, the SMART layer was the most fragile before and during the bonding procedures. Recently, Bekas D. G. et al. developed diagnostic layer [123] utilizing inkjet-printed technology. This layer had been shown to reduce the thickness of integrated layers (25.4 μm) [124] by 50% compared to that of the SMART layer (50.8 μm) [125]. They found this diagnostic film was effective for thin composites and can be performed well in the tests for low/high temperatures changes under the cyclic loadings [126].

However, as will be demonstrated in this thesis, surface-mounted PZT transducers cannot effectively detect damage in thick composites since there are designed to generate surface waves (Lamb waves). In addition, surface-mounted PZT transducers can be easily damaged during routine maintenance if not protected by additional protective layers which in turn add weight to the overall structure. Furthermore, for thick composite parts, PZT transducers become less sensitive to internal damage such as delamination [124]. Hence, embedding PZT transducers into thick composites is a challenge which needs to be overcome for the thick composites.

On the other hand, any inclusion during composite manufacturing may cause material degradation and affect the strength [127]. Hence, it is important to evaluate the effect of embedded PZT transducers on the mechanical properties of the host composite structures. Lin *et al.* [120] tested the mechanical properties of embedding “SMART Layers” into composites

for SHM purposes, the results showed that the embedding of "SMART Layers" in an isolated section and small parts related to the overall structure did not degrade the structural integrity of the host composite structure. Masmoudi *et al.* [127, 128] embedded PZT transducers into thick glass fibre reinforced plastic (GFRP) composites and mechanical tests showed there were no differences for GFRP composites with and without embedded PZT transducers. Tuloup *et al.* [129] embedded PZT transducers into polymer-matrix composites (PMC) and found reductions of elastic modulus and Poisson's ratios were 5% and 26% respectively. Recently, Andreads *et al.* [130, 131] proposed a novel embedding technique that uses E-glass fibres to cover the tops of PZT transducers during the lay-up to improve the mechanical properties of carbon fibre reinforced plastic (CFRP) composites. These mechanical results showed that their embedding technique had no effects on the integrity of CFRP composites.

In this chapter, the state-of-the-art of the embedding techniques into composites will be reviewed first. Then a novel edge cut-out embedding technique based on circuit printing will be proposed. The use of thin diagnostic films with printed circuits instead of traditional cables was shown to significantly reduce the weight of the composite structure. In addition, the novel edge cut-out method allows edge trimming possible which can be used in industrial mass manufacturing for the next higher assembly. After the fabrication, sensor integrities and bonding properties for surface-mounted and embedded PZT transducers will be investigated. Then the crosstalk issue will be discussed and a method to reduce the amplitude of the crosstalk will be proposed.

After that, the structural integrity of composites with the embedded diagnostic film and PZT transducers will be assessed. Initially, the effect of fatigue tests on the electro-mechanical impedance (EMI) properties of PZT transducers under different loading cycles (up to 1 million) was studied. In addition, the effect of fatigue tests on active sensing behaviours based on UGW under different loading cycles was investigated. Finally, the tensile and the compressive tests were conducted to assess the effect of the novel embedding technique on elastic moduli of composite coupons.

3.2. Literature Review of Embedding Techniques

3.2.1. Insertion Method

The insertion method [86, 117, 132, 133] is the easiest way to embed PZT transducers, which simply inserts PZT transducers connecting to wires into middle plies. However, this method would increase the partial thickness of the laminate and change laminate surface properties. In addition, it has been concluded from other studies that this approach can result in embedded PZT transducers being damaged by residual stresses due to edge pinching during the curing procedure. The previous researcher used unidirectional prepregs with quasi-isotropic stacking sequences $(0°/+45°/-45°/+90°)_s$ to lay up a specimen and inserted PZT transducers between the

middle of two +90°, which would have the minimum effect on the integral strength of the specimen under uniaxial loading condition.

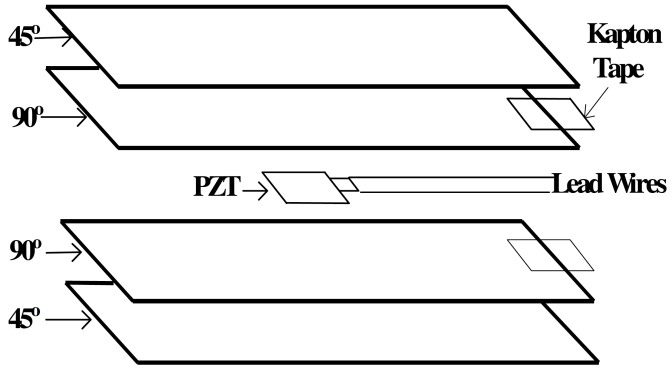

Figure 3.1. Schematic of the insertion method to embed a PZT transducer [134].

The schematic of the insertion method to embed a PZT transducer is shown in Figure 3.1. The PZT transducer bonded with two fine silver wires was first pre-packaged in insulating graphite/PEEK composite or polyimide covering or epoxy film before insertion. The bonding agent is a high-temperature conductive adhesive compound, which concentrates on high temperature during manufacturing and remains firmly in electrical and physical contact on the transducer through the whole laminate consolidation process. The lead wires are formed into a stress-relieving pattern before bonding the PZT transducer. Figure 3.2 shows the schematic of the insulation of a PZT transducer.

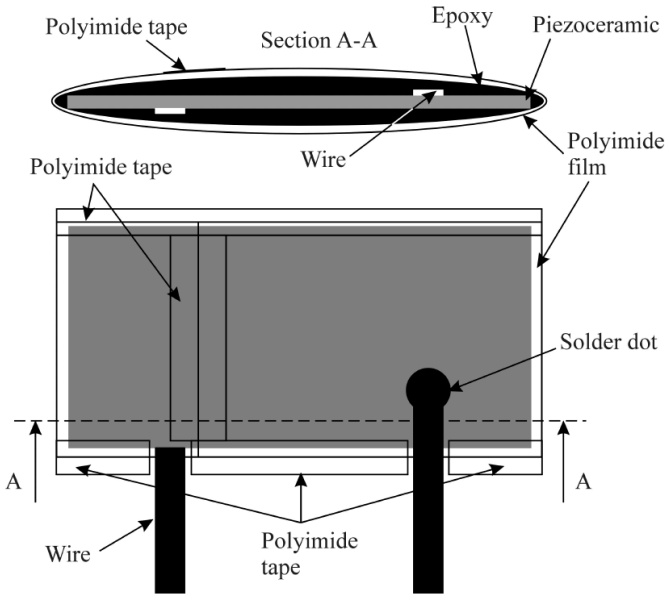

Figure 3.2. Schematic of insulation of a PZT transducer [86].

Two small pieces of square KAPTON® tape were placed at the edge area of the composite laminate to prevent the lead wires damaged and to track the central location at the edge. It is

important to make sure that the maximum curing temperature in the autoclave is lower than the Curie transition temperature of the PZT transducer, which could cause depoling or loss of the piezoelectric property entirely.

3.2.2. Cut-out Method

The main difference between the cut-out [116-118] and the insertion methods is that the cut-out method removes a similar area to the PZT transducer from the middle plies, which in turn would require very precise lay-up during the manufacturing. As shown in Figure 3.3:

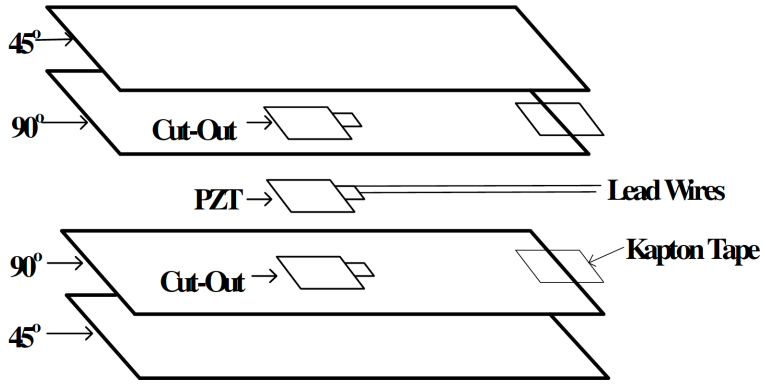

Figure 3.3. Schematic of the cut-out method for embedding a PZT transducer [134].

3.2.3. SMART Layer™

The SMART (stands for "Stanford Multi-Actuator Receiver Transduction) Layer™ with the phased array PZT transducers has been developed in recent decades. It bases on a circuit-printed technique and is considered as an extra ply during the lay-up instead of simply embedding PZT transducers into the composite laminates [2, 120, 121, 135]. Figure 3.4 shows the schematic of the embedded SMART Layer™.

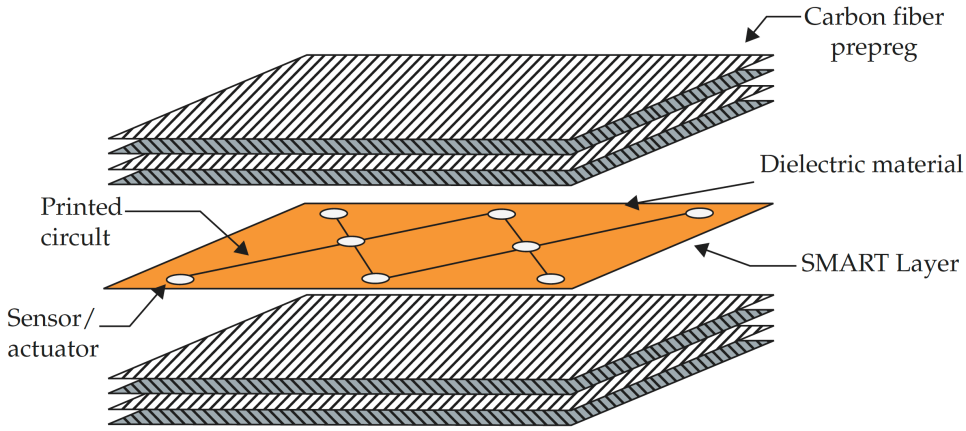

Figure 3.4. Schematic of the embedded SMART Layer™ [37].

3.3. Experimental Setup

3.3.1. Diagnostic Layer

The diagnostic layer was prepared following the process reported in [123]. For printing conductive circuits, a silver-based ink with nanoparticle concertation of 30–35 wt. % was used. The Dimatix Materials Printer (DMP-2580) was used to print circuits onto a transparent KAPTON® polyimide film (DuPont™ HN) with a thickness of 25.4 µm. For the inkjet-printed process, the piezo voltage was set at 20 V and an optimized waveform with a jetting frequency of 5 kHz enabled a satisfactory drop formation. The substrate's temperature during printing was 55 °C and the drop spacing was 35 µm, resulting in a uniform line formation. To decrease the electrical resistivity of the printed circuits, 3 layers of inks were printed on top of each other while the width of the printed lines was selected at 1.4 mm. Sintering of ink took place in the laboratory oven (OF-01E/11E/21E) for 1 hour at 135 °C to fuse the conductive particles into a cohesive conductive trace. Figure 3.5 shows the schematics of the Dimatix Materials Printer and the diagnostic (KAPTON®) film with printed circuits.

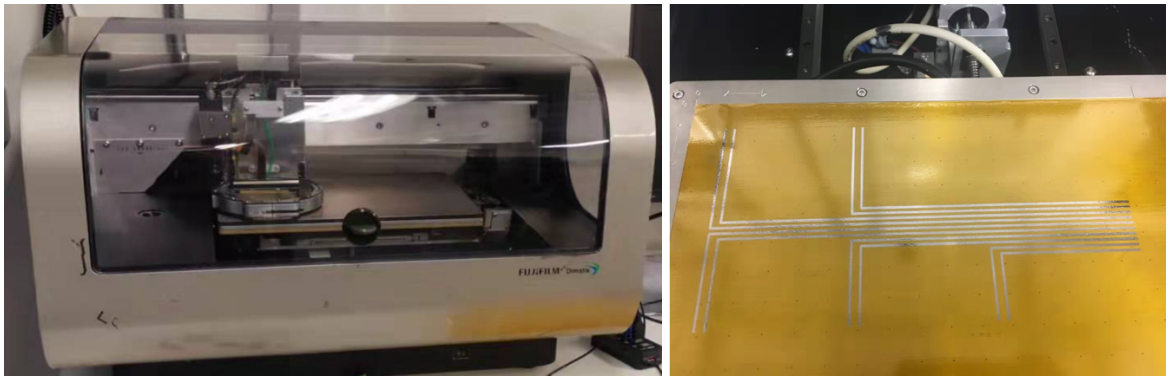

(a) **(b)**

Figure 3.5. Schematics of **(a)** the Dimatix Materials Printer and **(b)** a diagnostic (KAPTON®) film with printed circuits.

3.3.2. Sensor Installation

DuraAct PZT transducers (P-876K025) and high temperature connecting terminals (TML Co. TPF-2M) were used in this experiment. Two-part silver conductive epoxy adhesive resin/hardener (RS 186-3616) were used as conductive agents to connect PZT transducers and connecting terminals to circuits. For embedding, two PZT transducers were pre-bonded with the KAPTON® by adhesive films (TPU-Pontocal AG) to prevent delamination between the PZT transducers and the KAPTON® film. Then four connecting terminals were connected to the other side of printed circuits by applying the above conductive agents for convenient soldering and connecting exposed wires without damaging printed circuits after curing.

Figure 3.6 shows the schematic of the pre-bonding procedure. Two small pieces of adhesive film layers were placed over the KAPTON® film in the designated position, followed by a PZT transducer. The transducer was then fixed with blue tape. The KAPTON® film was placed into an oven for 20 minutes at 80 °C to cure conductive agents first to prevent them from flowing and causing short-circuited during the pre-bonding procedure. Then the KAPTON® film was put into a heated vacuum table (G-Sub-1310) to cure for one hour at 150 °C and cooled down to room temperature with the vacuum to make sure the melted adhesive liquids would not flow out. For surface-mounting, two PZT transducers and four connecting terminals were connected to the circuits by applying epoxy adhesives and cured at 80 °C for 20 minutes. After pre-bonding, the blue tape was removed carefully.

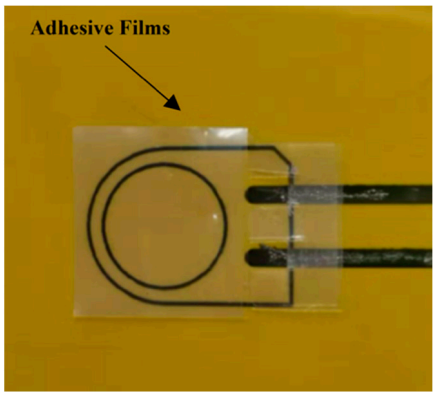

Figure 3.6. Schematic of the pre-bonding procedure.

3.3.3. Manufacturing of Carbon Fibre Reinforced Composites

The composite specimen was manufactured using unidirectional carbon fibre prepregs Hexply® IM7/8552 with a quasi-isotropic stacking sequence of $[(0°/+45°/-45°/+90°)_9]_s$. The

size of the specimen was 260 mm × 45 mm, and the average thickness was 9 mm. The distance between two PZT transducers was 180 mm. Distances from the centres of two embedded PZT transducers to each edge were 40 mm in the x-direction and 22.5 mm in the y-direction. The embedding position was in the middle of the panel between two +90° plies to have the minimum effect on integral strength under uniaxial loading conditions.

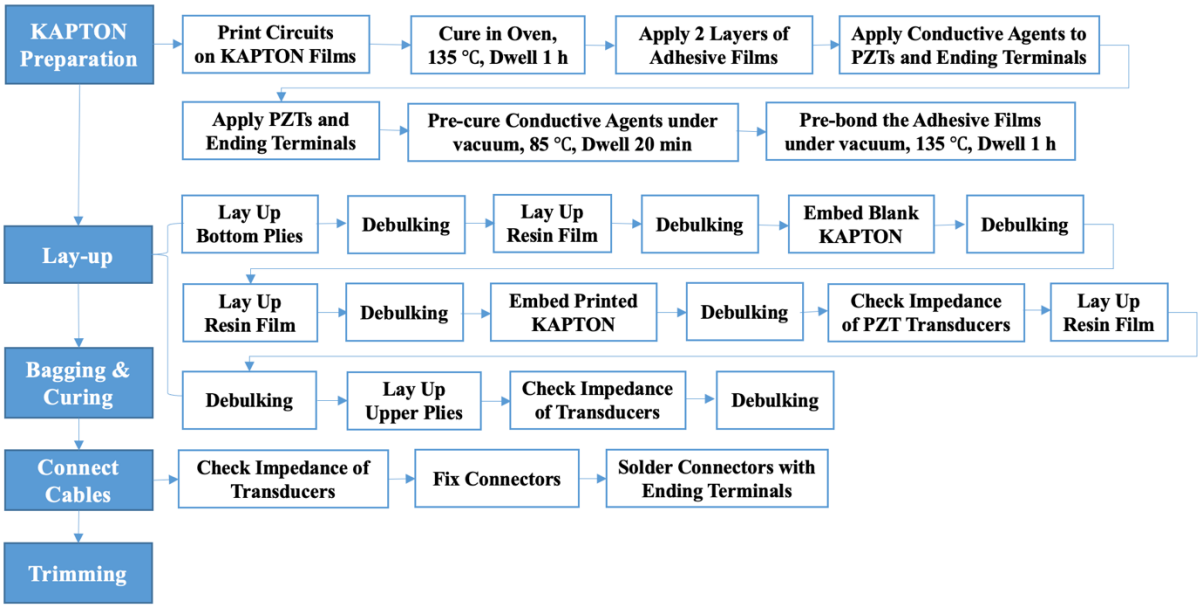

Figure 3.7. Flow chart of the manufacturing procedure.

In this section, a novel cut-out embedding method is proposed. Figure 3.7 shows the flow chart of the embedding technique for composite manufacturing. A key difficulty with the previous PZT embedding method is the leading wires coming out of the edge of the composites. This will prevent the edge trimming of composites, which is a requirement for industrial manufacturing and next higher assembly. There is also a potential risk that leading wires suspended in the air may be broken during transferring and testing. In this method, a small edge area is cut out from the upper prepregs of the specimen to trim the edge of the specimen and keep the embedded leading wires after curing. The prepregs' ply-cutting plan is divided into three parts, the bottom prepregs, the main upper prepregs and the cut-out prepregs, as is shown in Figure 3.8a, and the schematic of the assembly model is shown in Figure 3.8b.

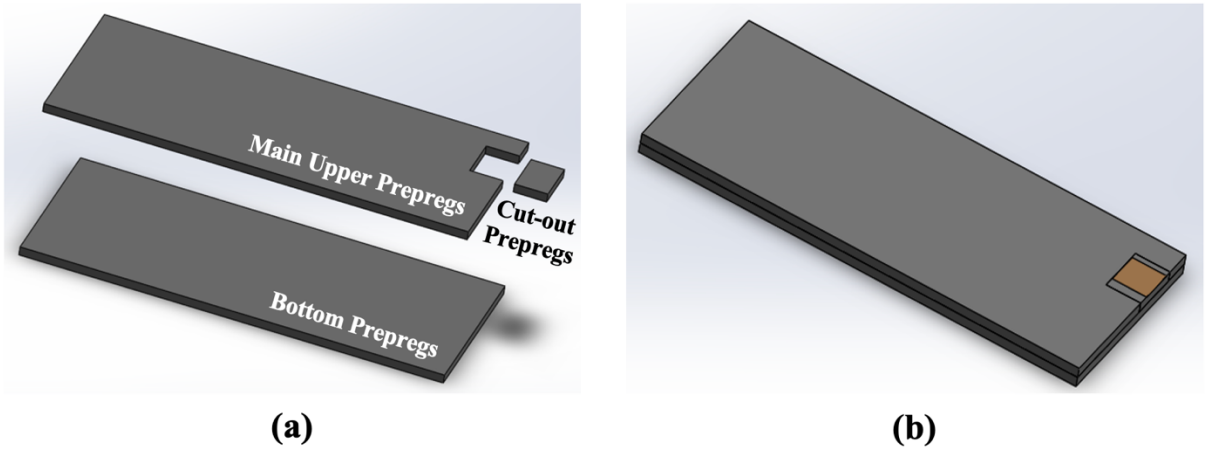

Figure 3.8. Schematics of **(a)** the ply-cutting plan and **(b)** the prepregs assembly model.

Figure 3.9 illustrates the schematic of the cross-sectional area of the cut-out part of the composite specimen. During the initial stage of the embedding process, a small area of a release film was placed over the upper cut-out area to separate the embedded KAPTON® film from the bottom prepregs at that area easily. A layer of resin film (Hexply® M56) was then placed over the bottom prepregs to increase the bonding property between the bottom prepregs and the KAPTON® film. A blank KAPTON® film was then laid in the designated position of the middle layer of the panel to prevent circuits from short-circuiting during the curing procedure. A layer of resin film was placed over the embedded film to prevent delamination, followed by the printed KAPTON® film. Another layer of the resin film was then placed over the printed KAPTON® film to increase the bonding property between the main upper prepregs and the KAPTON® film.

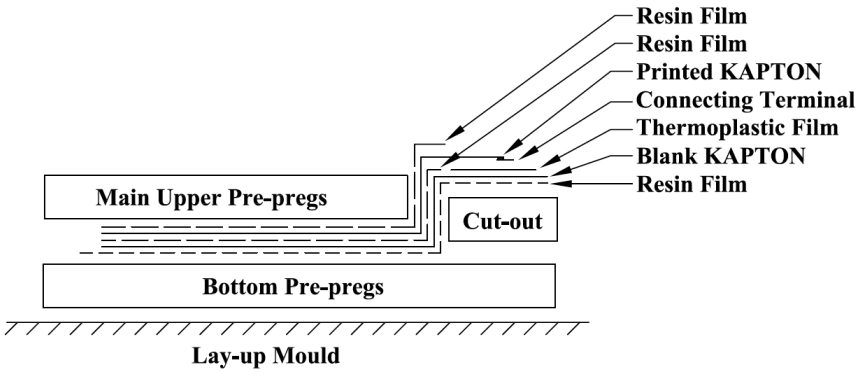

Figure 3.9. Schematic of the embedding procedure.

For the remainder of the embedding process, the main upper prepregs were then placed on top of the resin film, and the exposed KAPTON® film at the cut-out area was attached tightly to the vertical side of the main upper prepregs. Subsequently, the release film at the cut-out area was removed and the upper cut-out prepregs were then inserted into the cut-out area. Once it had been inserted, the exposed part of the KAPTON® film was placed over the upper cut-out

area of the specimen. When the lay-up was finished, two layers of adhesive films were placed under connecting terminals to prevent these surfaces from being covered by melt resin films during the curing procedure due to their stable properties at high temperatures. Figure 3.10 shows the embedded diagnostic film with PZT transducers during the lay-up. During the bagging procedure, a caul plate (thick aluminium panel) was applied on the top of the composite specimen to have a flat finishing quality for the bag side same as the mould side of the specimen. After the bagging procedure, the composite specimen was cured at 180 °C in an autoclave, the curing cycle followed the specification of curing conditions from its datasheet.

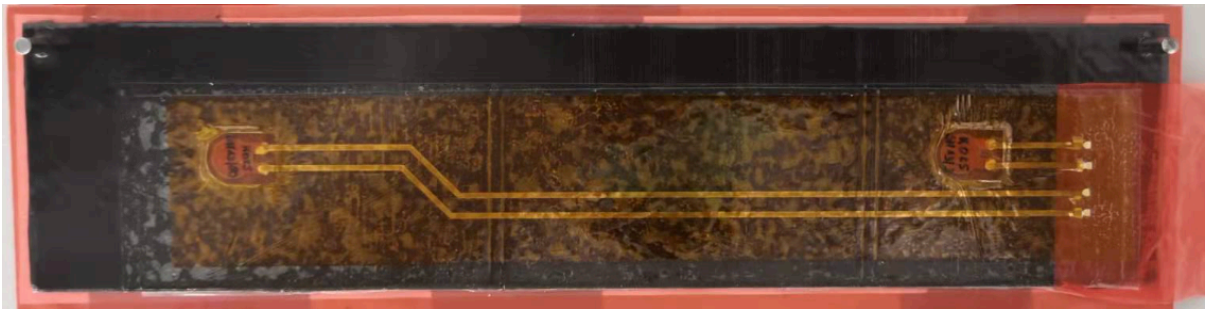

Figure 3.10. Examples of an embedded diagnostic film with PZT transducers.

At the end of the manufacturing process, the composite specimen was inspected via C-Scan (DolphiCam CF08), and the non-destructive test (NDT) results are shown in Figure 3.11. As can be seen in Figure 3.11a, the position of the embedded PZT transducer can be detected which is in the middle of the panel according to the vertical/horizontal B-Scan. In Figure 3.11b, the non-embedding areas show the bonding quality of the specimen is good and there is no defect in the specimen.

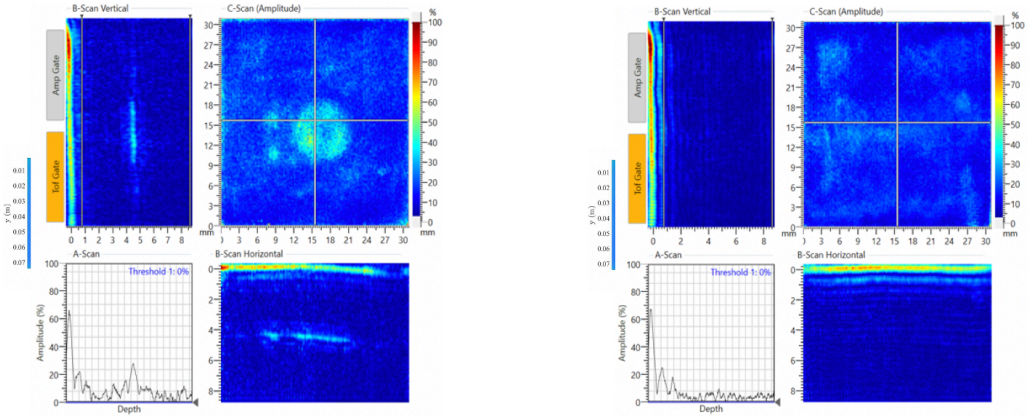

(a) **(b)**

Figure 3.11. The C-Scan results of **(a)** the embedded areas and **(b)** the non-embedded areas.

For the surface-mounting procedure, two small layers of adhesive film were placed over the mould side of the specimen to bond the KAPTON® film and the specimen. The surface-mounted KAPTON® film was placed over the adhesive films at the designated position where

two PZT transducers were placed in the same positions as embedded PZT transducers. Then these extra adhesive films were removed slightly using a knife, and the edge of the surface-mounted KAPTON® film was sealed by the blue tape. The panel was then placed on the heated vacuum table to cure for one hour at 150 °C and allowed to cool down to room temperature to make sure the melting adhesive liquids would not flow out. After bonding, the specimen was trimmed, and two connectors (RS 514-4408, operating temperature range: -40°C to +85°C) were placed in the designated areas to connect the embedded and the surface-mounted connecting terminals and bonded by the superglue (RS 473-445, operating temperature range: -50°C to +80°C). The finished specimen with the surface-mounted diagnostic film is shown in Figure 3.12.

Figure 3.12. A surface-mounted diagnostic film with PZT transducers.

3.4. Sensor Integrity Assessment

In this experiment, SinePhase Impedance Analyser (Model 16777K) was used to measure the imaginary and the real parts of the admittance of the PZT transducer to compare with that of the free-free transducer. The frequency range was from 0~1000 kHz. Figure 3.13 depicts the imaginary and the real parts of the admittance for the free-free, the embedded and surface-mounted PZT transducers with a range of excitation frequencies respectively. In Figure 3.13a, the first resonance vibration features for the free-free, the embedded and surface-mounted PZT transducers appear at 192 kHz, 347 kHz and 254 kHz respectively. In addition, both the slopes of the imaginary part of the admittance for the embedded and surface-mounted PZT transducers are higher than that of the free-free transducer from 0~20 kHz. Furthermore, that of embedded PZT transducers is much higher than that of surface-mounted PZT transducers, this is because boundary conditions between the embedded and surface-mounted PZT transducers are different. The embedded transducers are bonded from both sides, while surface-mounted PZT transducers are only bonded from one side. In Figure 3.13b, the first resonance vibration features for the free-free, the embedded and surface-mounted PZT transducers appear at 195 kHz, 328 kHz and 265 kHz respectively. According to the EMI technique, there is no obvious slope shifting of the imaginary part of the admittance between the embedded and surface-mounted PZT transducers at the low-frequency range of 0~20 kHz [124]. Therefore, both the

embedded and surface-mounted PZT transducers have ideal bonding properties with the host structure.

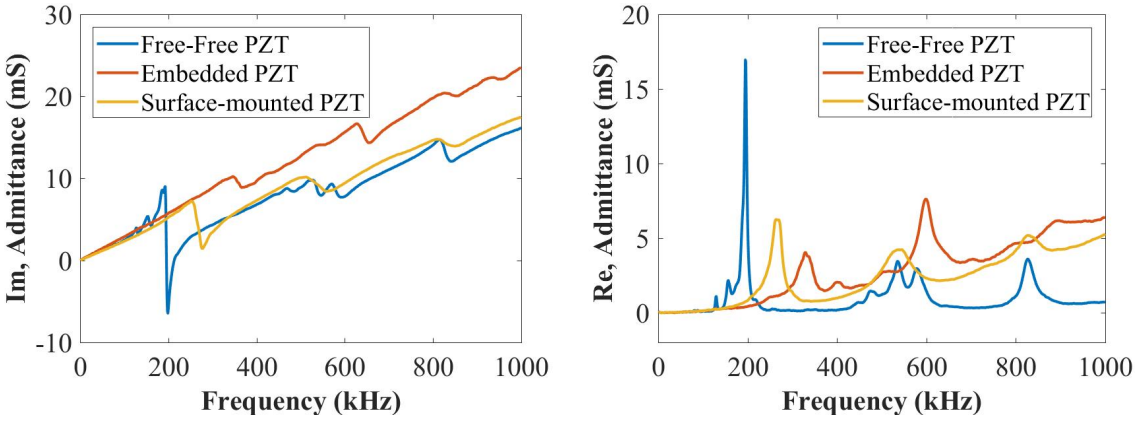

Figure 3.13. The EMI results of **(a)** the imaginary and **(b)** the real parts of the admittance for the free-free, the embedded and surface-mounted PZT transducers.

3.5. Crosstalk Issue

The crosstalk occurs when printed circuits are not isolated and affected by a magnetic field. The troubleshooting to eliminate the crosstalk has been done by increasing the distance between the circuits of each PZT transducer. It was found the crosstalk can be eliminated by connecting two more connectors or adjusting the angles of connecting wires during the setup for chamber measurements, as is shown in Figure 3.14, However, it still cannot be controlled in the current situation.

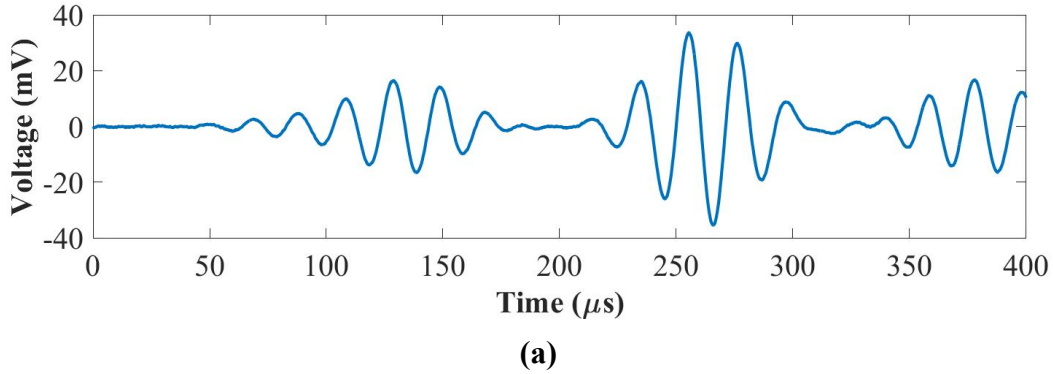

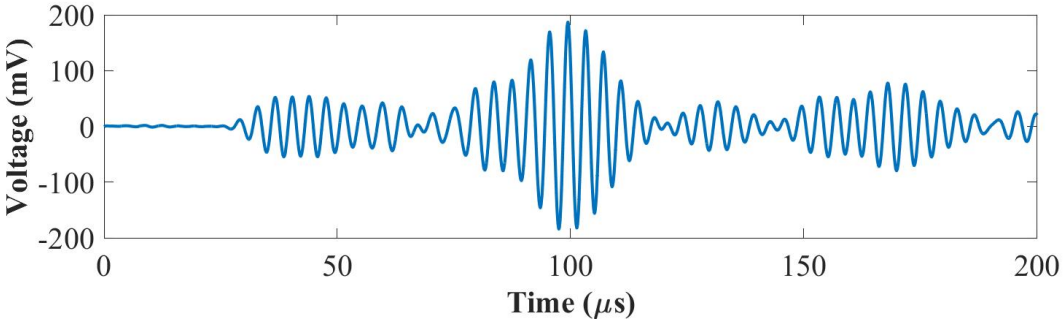

(b)

Figure 3.14. UGW signals at **(a)** 50 kHz and **(b)** 250 kHz.

However, when printed circuits were embedded in the middle and mounted on the surface of the composite panel at the same time or the density of printed circuits increased for connecting more PZT transducers, the crosstalk happens again and cannot be eliminated (shown in Figure 3.15).

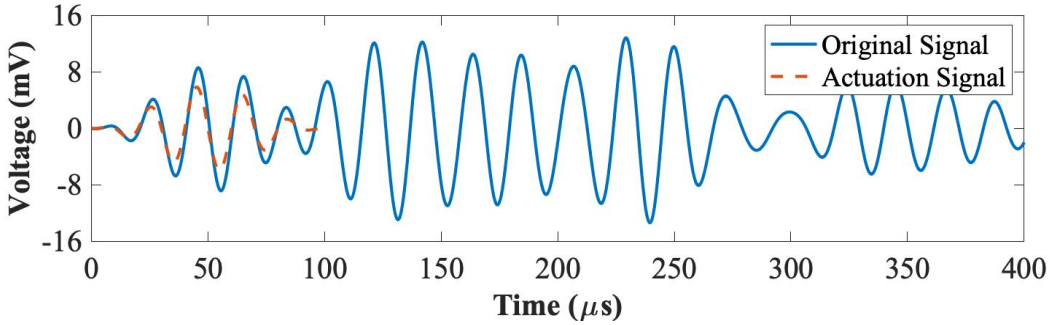

Figure 3.15. UGW with the crosstalk at 50 kHz.

Figure 3.16 shows an approach to reduce the amplitude of the crosstalk during the postprocessing. As is shown in Figure 3.16a, the actuation signal is scaled up to match the crosstalk of the original signal first, then the postprocessing signal is the difference between the original signal and the scaled actuation signal (shown in Figure 3.16b).

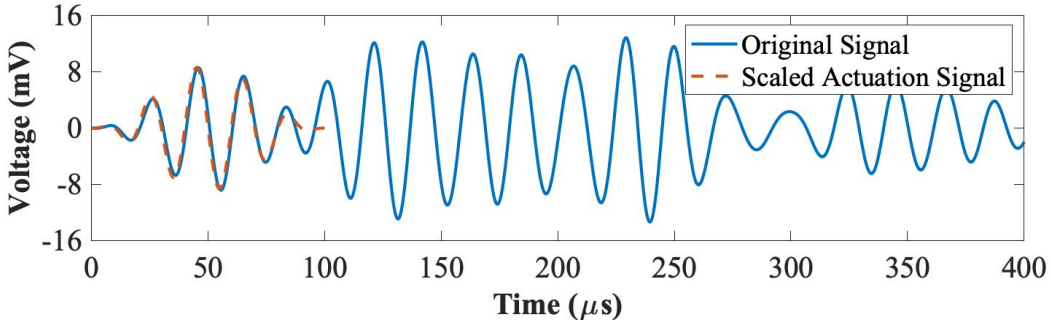

(a)

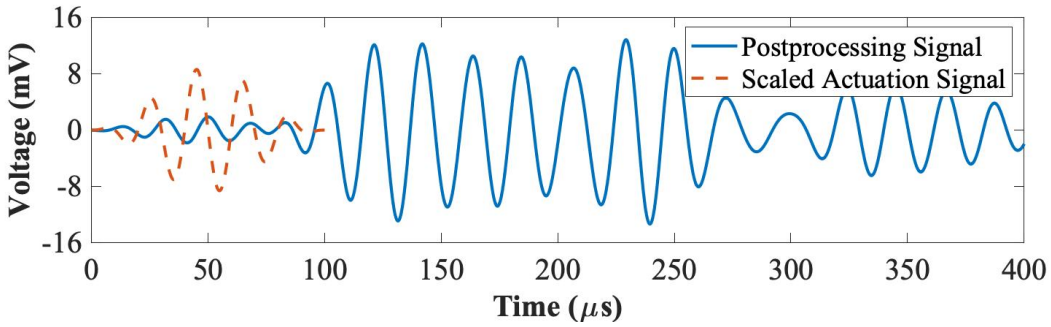

(b)

Figure 3.16. Schematics of **(a)** the original signal with the scaled actuation signal and **(b)** the postprocessing signal with the scaled actuation signal.

3.6. Structural Integrity Assessment

In this section, the effect of fatigue tests on the integrity of embedded PZT transducers is investigated. Furthermore, the reduction in mechanical properties of the host composite structure is investigated through consideration of the *worst-case scenario of the embedded film being embedded along with the entire coupon*. This is unlike previous studies cited above, where the embedding only covered a small area of the host structure.

3.6.1. Experimental Setup

Unidirectional carbon fibre prepregs Hexply® IM7/8552 were used and the quasi-isotropic stacking sequence for the lay-up was $[(0°/+45°/-45°/+90°)_9]_s$. The manufactured size of these coupons for machinal tests was according to the ASTM D695 standard. Figure 3.17 shows the general drawings for the standard coupon and the coupon with embedded PZT transducers, respectively. The fabrication of composite coupons with the embedded diagnostic film and PZT transducers follows the same procedure in section 3.3. After trimming, the wires were soldered to connecting terminals to connect the embedded printed circuits and PZT transducers. Figure 3.18 shows the pictures of manufactured coupons with and without embedded PZT transducers, respectively.

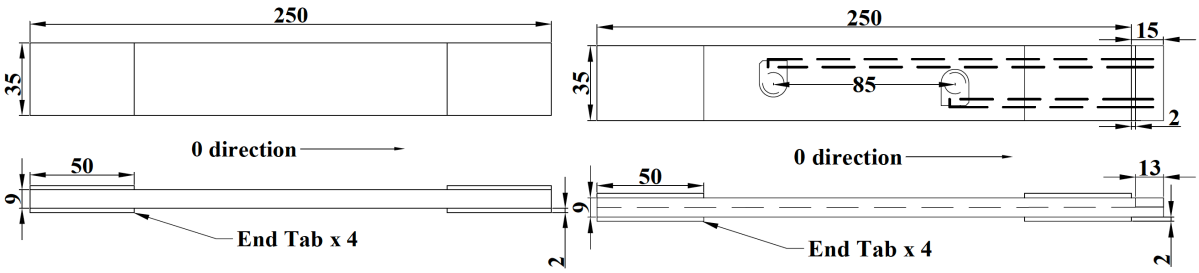

(a) **(b)**

Figure 3.17. General drawings for **(a)** the normal coupon and **(b)** the coupon with embedded PZT transducers (unit: mm).

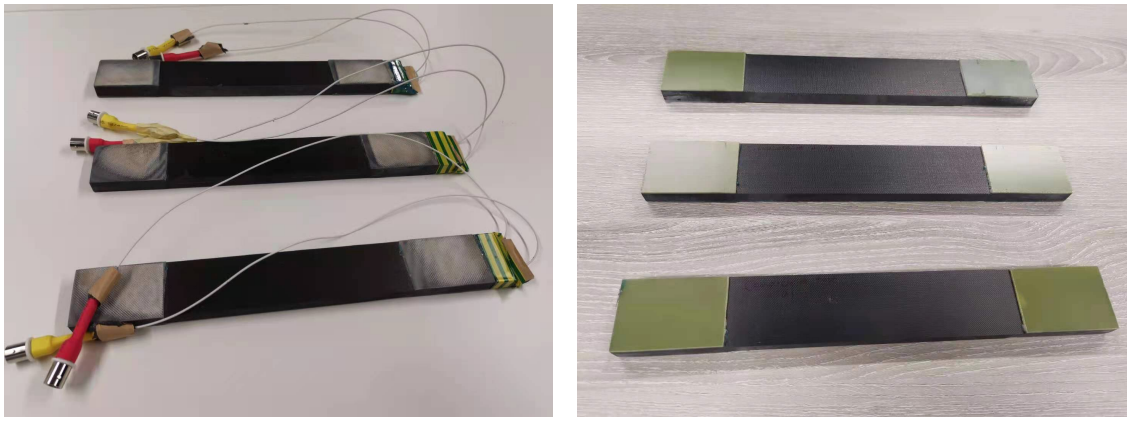

(a) **(b)**

Figure 3.18. Examples of **(a)** coupons with embedded PZT transducers and **(b)** the standard coupons.

3.6.2. Fatigue Tests

To study the effect of fatigue loading on the integrity of the bonding properties and the sensing performance of the embedded sensors, tension-tension fatigue tests for composite coupons with embedded PZT transducers were conducted. The EMI properties of embedded PZT transducers and signal stabilities under different loading cycles (up to 1 million cycles) are presented in this section. An Instron Hydraulic 250 kN test machine was used for fatigue tests, as shown in Figure 3.19. There were two scenarios for the force range in fatigue tests: a) 0.5~5 kN and b) 1~10 kN (stress ratio 0.1 for aeronautic research). The reason for choosing these two force ranges was to verify if the composite coupons with the embedded diagnostic film and PZT transducers can perform well starting from lower force ranges. Table 3.1 shows the test plan, the machine was stopped after each cycle step, to allow for the EMI and the UGW data to be measured for each load range.

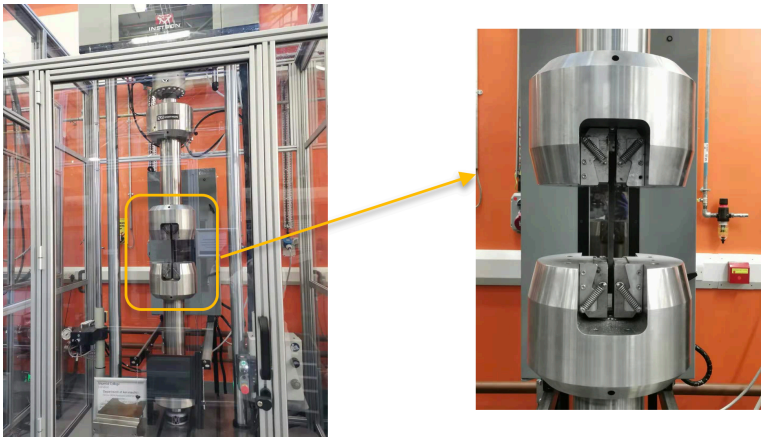

Figure 3.19. Schematic of an Instron Hydraulic 250 kN test machine.

Table 3.1. Fatigue test plan.

No.	Loading Cycles
1	0
2	50
3	1,000
4	5,000
5	20,000
6	50,000
7	100,000
8	500,000
9	1,000,000

3.6.3. Electro-Mechanical Impedance (EMI) Properties

In this section, the EMI method was used to investigate the integrity of the bonding properties by comparing the slope difference of the imaginary part of admittance of PZT transducers at a low-frequency range under different loading cycles. The aim is to investigate the effect of fatigue tests on the integrity of the bonding properties of embedded PZT transducers after up to 1 million loading cycles. A KEYSIGHT Impedance Analyzer E4990A was used to measure the impedance value. A SinePhase Impedance Analyser (Model 16777K) was used to measure the imaginary part of the admittance of a PZT transducer to compare differences between the embedded transducer under different loading cycles and its free-free situation. Figure 3.20 to Figure 3.21 show the EMI results of the impedance and the imaginary part of the admittance at low frequency ranges for the PZT transducer under force ranges of 0.5~5 kN and 1~10 kN after 1 million cycles. As can be seen in these figures, there is no obvious difference between the impedance and the slope of the imaginary part of the admittance at low-frequency ranges after 1 million loading cycles. Therefore, the effect of fatigue tests on embedded PZT

transducers can be ignored, and the stability and durability of these PZT transducers can be considered stable for up to 1 million cycles.

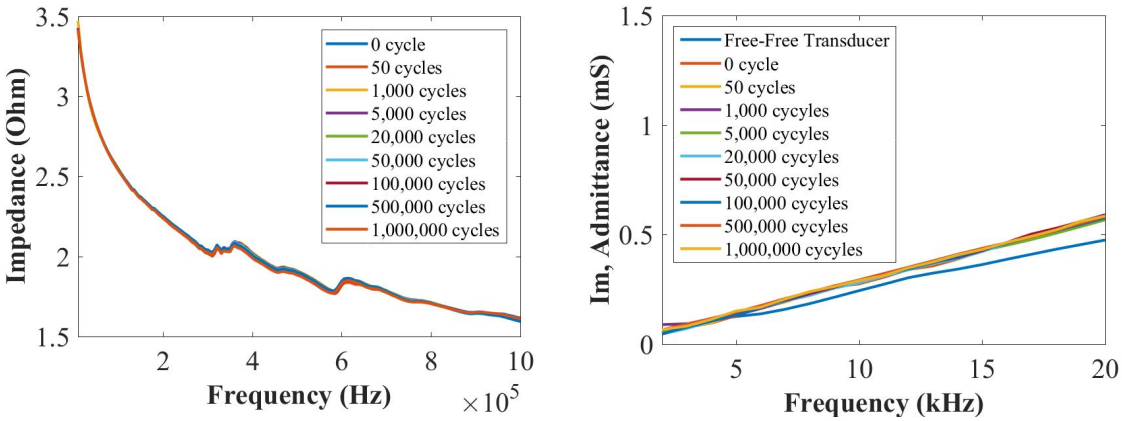

Figure 3.20. The EMI results of **(a)** the impedance and **(b)** the imaginary part of the admittance for the embedded PZT transducer under the force range of 0.5~5 kN.

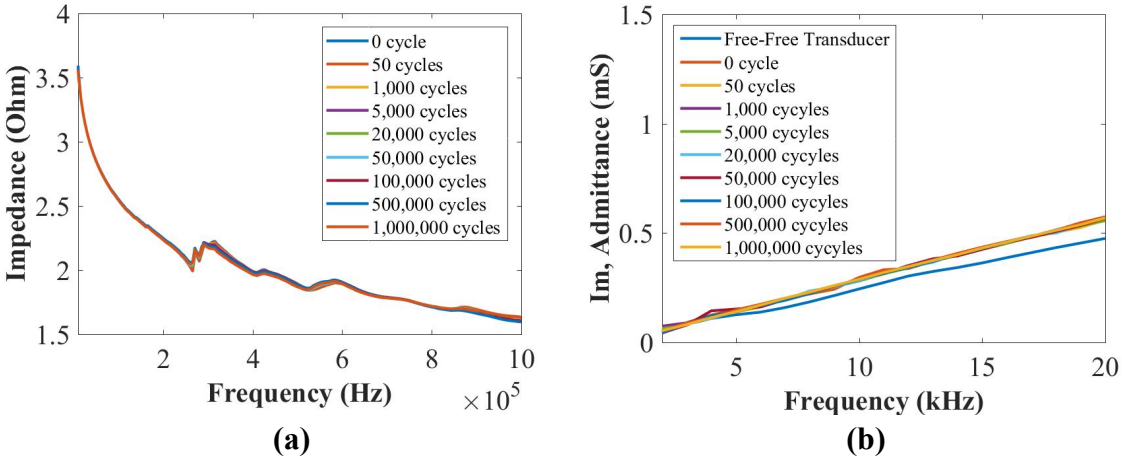

Figure 3.21. The EMI results of **(a)** the impedance and **(b)** the imaginary part of the admittance for the embedded PZT transducer under the force range of 1~10 kN.

3.6.4. Sensing Performance of PZT Transducers

To investigate the effect of fatigue tests on the sensing performance after 1 million loading cycles by measuring UGW signals, a National Instrument (NI) PXIe-1073 with a NI PXI-5412 arbitrary signal generator was used for signal generation, and a NI PXI-5105 digitizer was used to record UGW signals. Five-cycle Hanning-windowed toneburst signals at central frequencies of 50 kHz and 250 kHz were used as actuation signals respectively, and the actuation amplitude and the sampling frequency were 6 V and 100 MHz respectively. The stability of UGW following tests with different loading cycles according to Table 3.1 was assessed.

Figure 3.22a and Figure 3.23a plot guided wave signals after each fatigue cycle at 50 kHz and 250 kHz, respectively. Figure 3.22b and Figure 3.23b plot residual signals (difference between the current and baseline signals) from 20,000 cycles to 1 million cycles at 50 kHz and 250 kHz, respectively. In Figure 3.22a, the signal up to 1 million cycles maintains the same phase with amplitude reduction. The amplitude reduction can be related to the damage index mentioned in section 2.6.1. Since the insertion of the diagnostic film and PZT transducers into the composite coupon would cause the degradation of mechanical properties. Therefore, the internal delamination generated in the composite coupon may happen during fatigue tests. As can be seen in Figure 3.22b, amplitudes of residual signals maintain at noise levels from 20,000 cycles up to 1 million cycles. Therefore, the sensing performance remains good after 1 million loading cycles at 50 kHz.

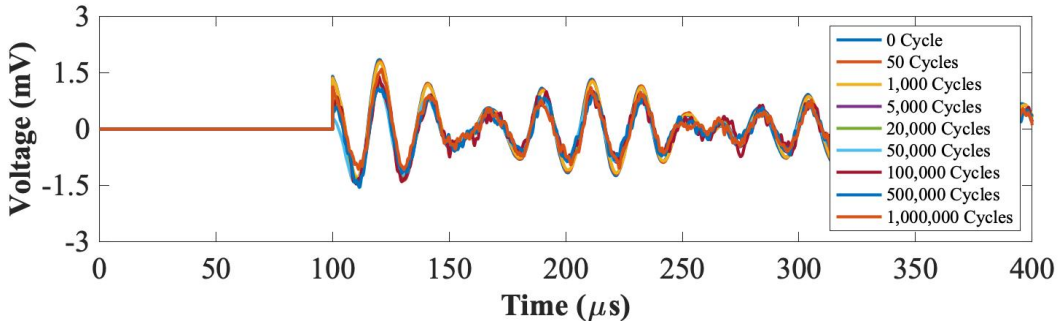

(a)

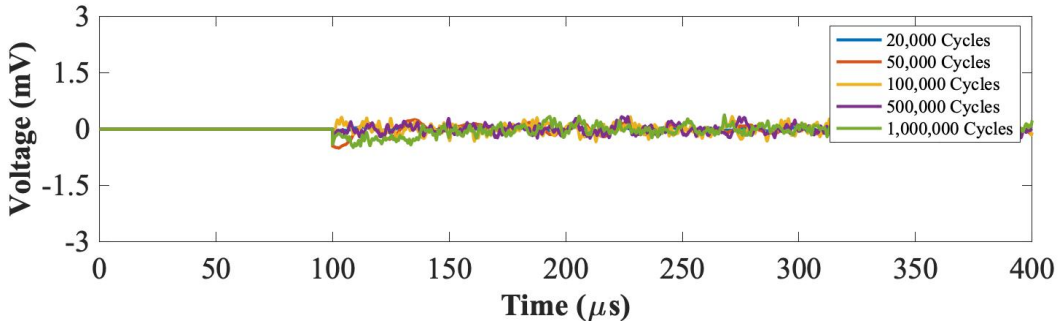

(b)

Figure 3.22. UGW comparisons within 1 million cycles for **(a)** the original signals and **(b)** the residual signals under the force range of 0.5~5 kN at 50 kHz.

As can be seen in Figure 3.23a, the amplitude of the first wave packet reduces after 1 million cycles due to the internal delamination generated in the composite coupon during the fatigue test. Figure 3.23b shows that the first wave packets of residual signals were almost the same from 20,000 cycles to 1 million cycles at 250 kHz. Therefore, the sensing performance for the fatigue tests under the force range of 0.5~5 kN is stable at 50 kHz and 250 kHz.

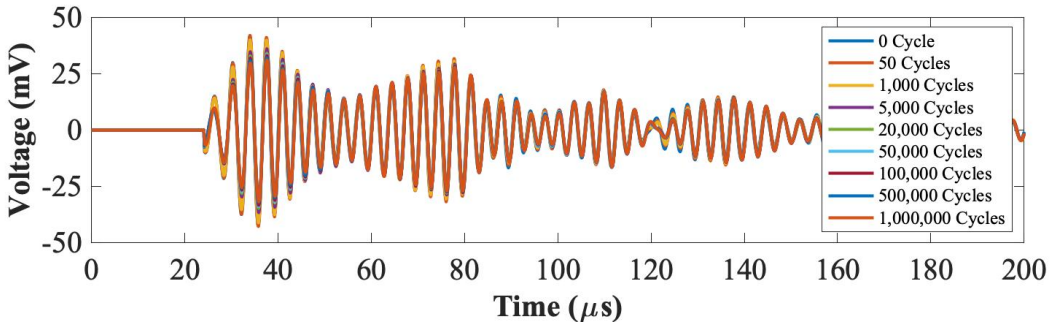

(a)

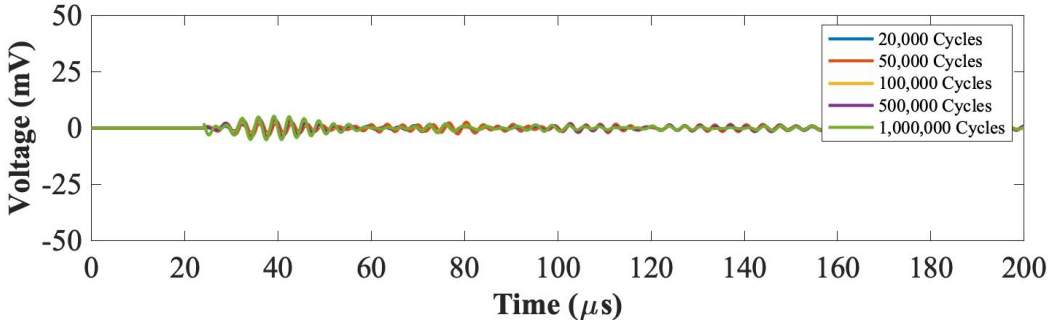

(b)

Figure 3.23. UGW comparisons within 1 million cycles for **(a)** original signals and **(b)** residual signals under the force range of 0.5~5 kN at 250 kHz.

Figure 3.24a and Figure 3.25a plot the original guided wave signals after each fatigue cycle at 50 kHz and 250 kHz, respectively. Figure 3.24b and Figure 3.25b plot the residual signals from 20,000 cycles to 1 million cycles at 50 kHz and 250 kHz, respectively. As can be seen in Figure 3.24, there are no obvious differences between the original guided wave signals and the residual signals maintained at noise levels from 20,000 cycles to 1 million cycles at 50 kHz. In Figure 3.25, the amplitude of the first wave packets of the original guided wave signals reduces slightly due to the internal delamination generated in the composite coupon during fatigue tests. In addition, residual signals are almost the same from 20,000 cycles to 1 million cycles at 250 kHz. Hence, guided wave signals under the fatigue tests with a load range of 1~10 kN are stable at 50 kHz and 250 kHz.

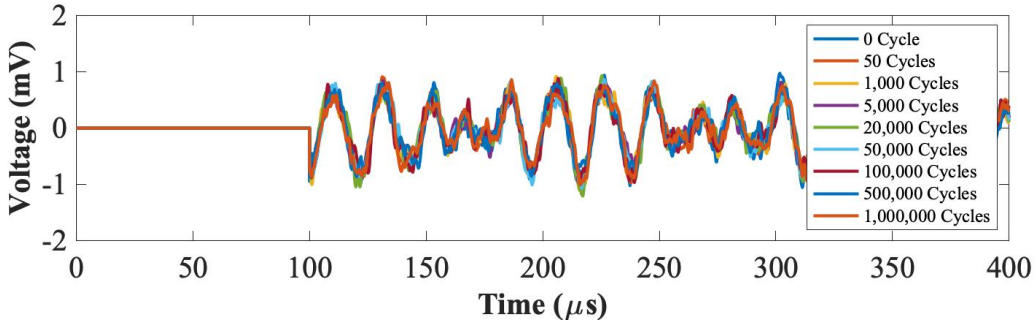

(a)

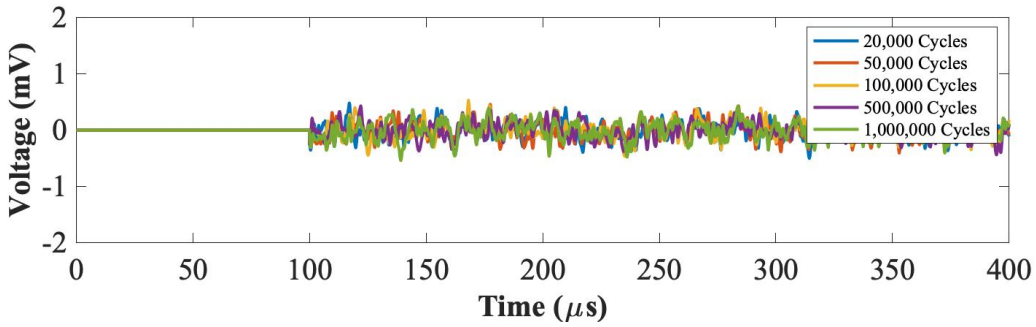

(b)

Figure 3.24. UGW comparisons within 1 million cycles for **(a)** the original signals and **(b)** the residual signals under the force range of 1~10 kN at 50 kHz.

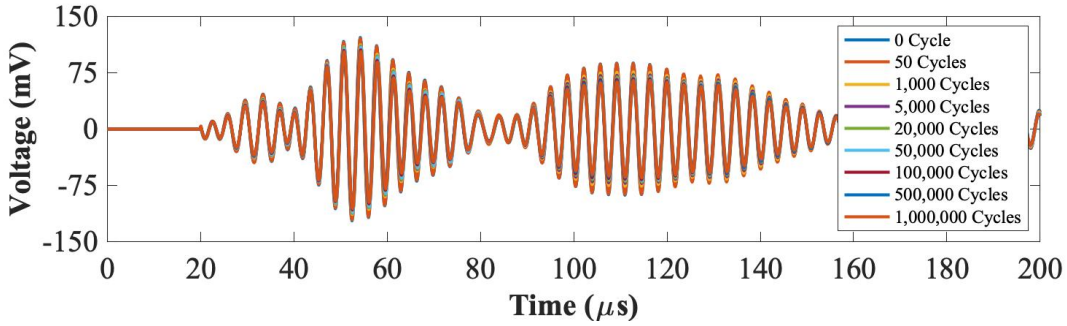

(a)

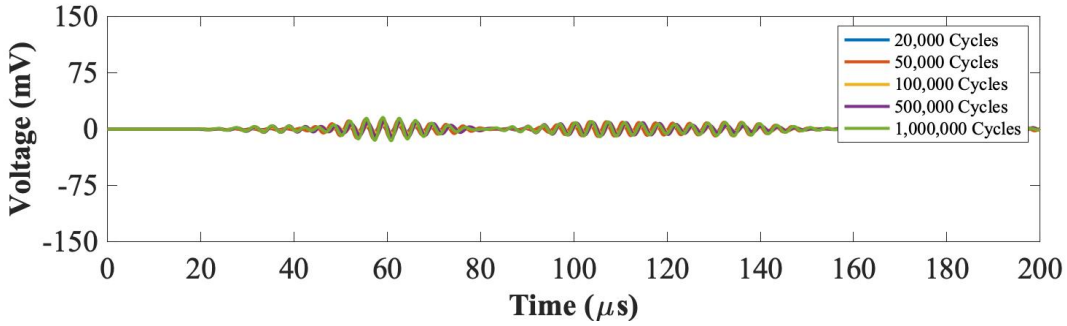

(b)

Figure 3.25. UGW comparisons within 1 million cycles for **(a)** the original signals and **(b)** the residual signals under the force range of 1~10 kN at 250 kHz.

3.6.5. Tensile and Compressive Tests

To investigate the effect of the embedding technique on the elastic modulus of composites, the tensile and the compressive tests were conducted by comparing the difference between the coupon with and without embedded PZT transducers. An Instron Hydraulic 250 kN test machine was used for the tensile and compressive tests, as is shown in Figure 3.19. For setting up parameters of the tensile and the compressive tests, the duration of the ramp for the

waveform was 1.5 minutes, and the ending point was 150 kN (200 kN for the failure load) for tensile tests and -80 kN (-120 kN for the failure load) for compressive tests. Figure 3.26a and Figure 3.26b plot the stress-strain curve before the failure between the coupon with and without embedded PZT transducers for the tensile and the compressive tests, respectively. As can be seen in these figures, stress-strain curves are not linear. This may be the whole procedure combined with the elastic and the plastic deformations during the tests. Therefore, the elastic modulus can be calculated by fitting the curve to get the slope of the curve using the polyfit function in MATLAB during the postprocessing procedure.

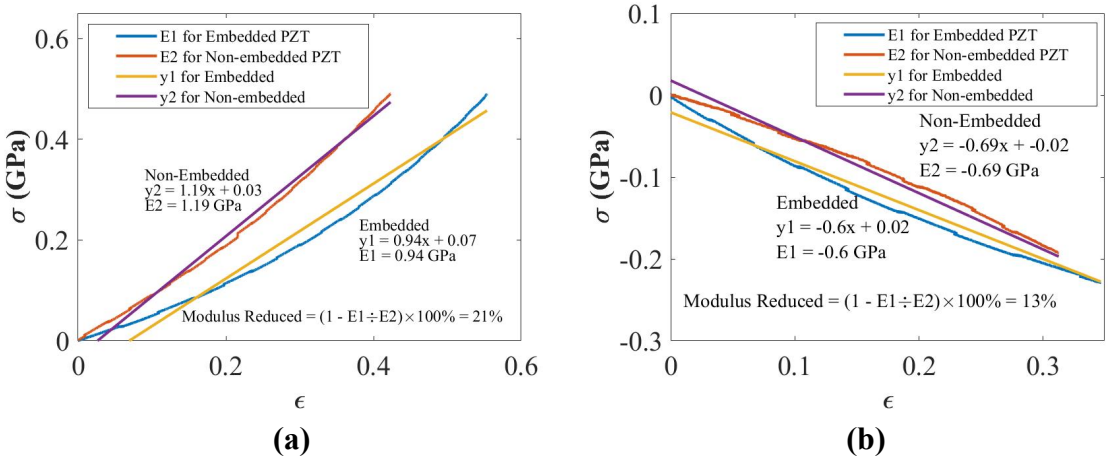

(a) **(b)**

Figure 3.26. Mechanical properties studies for **(a)** the tensile and **(b)** the compressive moduli reductions compared to composite coupons without embedded PZT transducers.

As can be seen in Figure 3.26, elastic moduli reduce about 21% for tensile tests and 13% for compressive tests. Although the elastic moduli for the tensile/compressive tests were reduced more than in other authors' works, this case presented for these coupons was the worst possible case, which was impractical for manufacturing real composite components with embedded diagnostic films and PZT transducers for SHM purposes. Considering other authors' work [127, 128, 130, 131], they only embedded a small part/area of types of the sensors, while in this case, a whole entire layer completely across the entire coupon due to its limited size. Furthermore, the thickness of the coupon may also affect the results. Aoki R. et al. [136] numerically and experimentally studied the effect of the ply thickness on the strength. Their results show that lower ply thickness results in higher strength. For the above authors' work, the thinner thickness compared to this case (9 mm) would also improve their work. Therefore, the level of reduction is considered reasonable given the fact that the diagnostic film embedded covers the entire surface of the test specimen.

3.7. Summary

In this chapter, the state-of-the-art of embedding techniques has been reviewed. A novel strategy for SHM of thick composites was investigated by embedding diagnostic layers in the structure. The developed embedding technique alleviates difficulties of the wires coming out of the edge of the composites which has proved so far to be a key impediment to embed sensors into composites. The EMI technique was used to access the integrity of the bonding properties between PZT transducers and their host structure. It was found the slope of the imaginary part of the admittance of the embedded PZT transducer is higher than that of the surface-mounted and the free-free PZT transducers at 0~20 kHz. In addition, the first resonance vibrations to the free-free, the embedded and the surface-mounted PZT transcoders are 192 kHz, 347 kHz and 254 kHz for the imaginary part of the admittance, and are 195 kHz, 328 kHz and 265 kHz for the real part of the admittance. Furthermore, the bonding integrity of embedded PZT transducers meets the double-side bonded requirement. The crosstalk issue for the printed circuits has been discussed. The crosstalk can be only eliminated by reducing the density of the printed circuits or adjusting the angles of the connecting wires.

Furthermore, the mechanical tests for composite coupons embedded with PZT transducers were investigated. First, the fatigue tests for the force range of 0.5~5 kN and 1~10 kN with 1 million cycles were studied. The stability of the EMI properties and active sensing behaviours of UGW remained good up to 1 million cycles at 50 kHz and 250 kHz. It has been demonstrated that the novel embedded circuits printed on the diagnostic film remain conductive and embedded PZT transducers remain active and intact after 1 million loading cycles, which indicates the embedded diagnostic film with the networks of PZT transducers can withstand the mechanical loads applied to them.

In addition, for the tensile and the compressive tests, the reduction of elastic moduli between standard coupons and coupons embedded with the diagnostic film and PZT transducers was compared. It was found that the embedded diagnostic film with PZT transducers made tensile modulus reduce by around 21% and made compressive modulus reduce by around 13%. Although the strength reduction was not ideal for this situation, the anticipated results would be significantly less when reducing the unprinted area of the diagnostic film during the lay-up. However, considering the benefits of this novel embedding technique, the embedded diagnostic film with networks of PZT transducers can be applied as a layer (prepreg) during the lay-up. Moreover, this technique allows for embedding larger sensor networks with optimizing the design of connections. Therefore, this embedding technique would be a promising technique for SHM applications.

Chapter 4

4. Finite Element Modelling of Ultrasonic Guided Waves

4.1. Introduction

In this chapter, finite element modelling (FEM) will be used to simulate UGW in composite laminates using commercial software ABAQUS. First, UGW actuated by surface-mounted PZT transducers using explicit and implicit dynamic analyses will be compared. In addition, three embedded strategies will be proposed and those guided wave results will be compared to the experimental results to find the optimum method to simulate UGW actuated by embedded PZT transducers. Then the composite damping will be investigated to study these damping effects on UGW. In the end, guided wave interaction with the surface-mounted artificial damage and the impact damage will be simulated.

4.2. Explicit and Implicit Dynamic Analyses for Surface-mounted PZT Transducers

In this section, comparisons between explicit and implicit dynamic analyses for surface-mounted PZT transducers were conducted to verify the parameters of the piezoelectric coefficients matrix and the dielectric permittivity for the PZT transducer in the ABAQUS simulation. Those verified parameters of the piezoelectric matrix and the dielectric permittivity for the PZT transducer will be used for simulating UGW propagation in composite laminate with embedded PZT transducers later. Since the explicit time integration reported in sections 2.4.3 and 2.4.4 can only be used for surface-mounted PZT transducers, there is no analytical solution for the embedded PZT transduces based on the explicit algorithm for the Abaqus/Explicit dynamic analysis. However, there is no piezoelectric element in the Abaqus/Explicit dynamic analysis. Therefore, the implicit dynamic analysis (Abaqus/Standard) is the only way to simulate UGW propagation in composite laminate with embedded PZT transducers and the piezoelectric matrix and the dielectric parameters permittivity for the PZT transducer have to be verified in advance.

To compare the thickness of 2 mm, 4 mm and 9 mm panels, the size of the model part was created by 0.19 m × 0.08 m and the depths of each model were 0.002 m, 0.004 m and 0.009 m, respectively. The distance between two PZT transducers was 0.11 m, and distances between the centre of the PZT transducer to the edge in the x- and the y- directions were 0.04 m. For the definition of the composite lay-up, the element type was set to continuum shell, and the

stacking sequences and the single thickness of each ply were $[(0°/+45°/-45°/+90°)_n]_s$, (n=2, 4, 9) and 0.000125 m.

Material properties for unidirectional carbon fibre prepregs and the PZT actuator are listed in Table 4.1. Calculations of the piezoelectric and the dielectric parameters used for the implicit dynamic analysis can be referred to in section 2.3.2 based the Table 4.1. For meshing the composite part, the element size was 0.001 m in the x-y plane and only one element in the z-direction. The family type was continuum shell and the element type was chosen as SC8R in the mesh control. The diameter of the PZT transducer was 0.01 m and the thickness was 0.0002 m. For meshing the PZT actuator, the element size was 0.0005 m in all directions. The family type was piezoelectric with the element type of an 8-node linear piezoelectric brick C3D8E.

Table 4.1. Material Properties for ABAQUS simulation.

Unidirectional Carbon Fibre Prepregs IM7/8552

E_{11} (Mpa)	E_{22} (Mpa)	ν_{12}	G_{12} (Mpa)	G_{13} (Mpa)	G_{23} (Mpa)	ρ (kg/m^3)
161,000	11,380	0.32	5170	5170	3980	1570

DuraAct PZT (PIC255)

ρ (kg/m^3)	d_{31} (C/N)	d_{33} (C/N)	d_{15} (C/N)	$\varepsilon_{33}^T/\varepsilon_0$	$\varepsilon_{11}^T/\varepsilon_0$	S_{11}^E (m^2/N)	S_{33}^E (m^2/N)
7800	-180×10^{-12}	400×10^{-12}	550×10^{-12}	1750	1650	16.1×10^{-12}	20.7×10^{-12}

To verify the time step of the signal, the increment size of the time period was set to $2e^{-8}$ by choosing the type of fixed and unlimited by choosing the type of automatic under the incrementation window in the STEP procedure. The results showed that there were no differences between these two different settings. The frequency was set as every time increment for the explicit dynamic procedure and every n increments (n=10) for the implicit dynamic procedure. The input amplitude of the electrical potential used for the implicit dynamic analysis (Abaqus/Standard) was the chirp signal, the frequency range was from 25 kHz to 500 kHz with a time duration of 200 μs. The input signal of the equivalent radial displacement based on the above chirp signal and output converted signal of electrical potential used for the explicit dynamic analysis (Abaqus/Explicit) can be referred to in section 2.4.3. Figure 4.1 shows input signals with the voltage and the equivalent radial displacement for implicit and explicit dynamic analyses, respectively. Generally, the explicit dynamic analysis costs less than 1 hour to run the result using high-performance computing (HPC) resources for the size with this kind of model, while the implicit dynamic analysis costs more than 24 hours (less than 48 hours for the 9 mm panel).

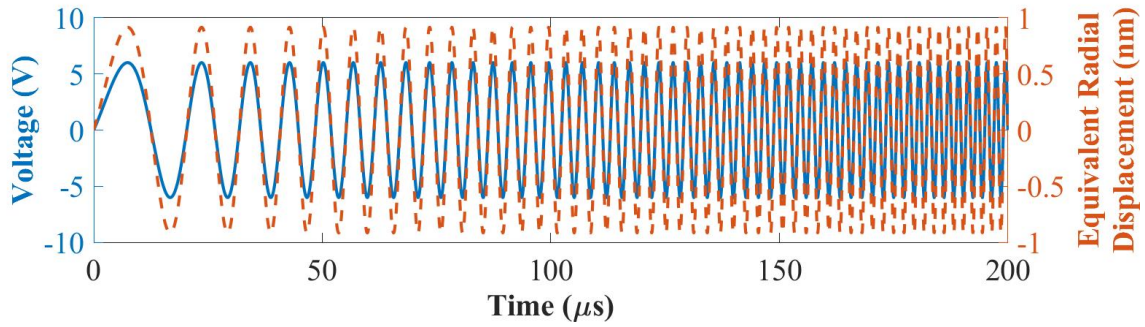

Figure 4.1. Input chirp signals for implicit and explicit dynamic analyses.

After submitting and running these jobs, these chirp results were reconstructed to five-cycle Hanning-windowed toneburst signals at 50 kHz and 250 kHz, respectively. Figure 4.2 verifies the convergence using the implicit dynamic analysis between the mesh size of 0.001 m and 0.0005 m in the x-y plane at 50 kHz and 250 kHz, respectively. As can be seen in Figure 4.2, there is no obvious difference between the first wave packets of these signals at 50 kHz and 250 kHz, so the convergence is assumed for the mesh size of 0.001 m.

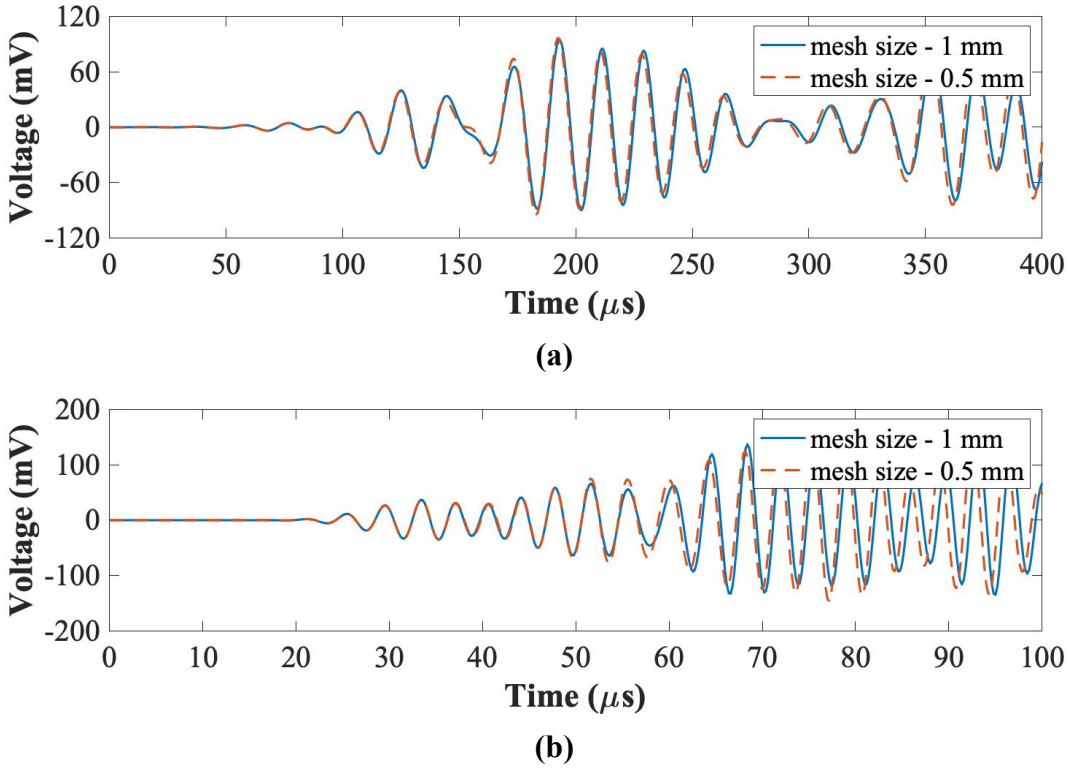

Figure 4.2. Convergence verification between mesh sizes of 0.001 m and 0.0005 m at **(a)** 50 kHz and **(b)** 250 kHz.

4.2.1. Comparisons of Explicit and Implicit Dynamic Analyses

Figure 4.3 and Figure 4.4 compare FEM results between the normalized explicit and implicit results for the thickness of 2 mm, 4 mm and 9 mm panels at 50 kHz and 250 kHz, respectively. As can be seen in these figures, these signals for the first wave packets between the normalized explicit and implicit results match, so the piezoelectric and the dielectric properties of the PZT transducer can be used for further simulation of embedded PZT transducers.

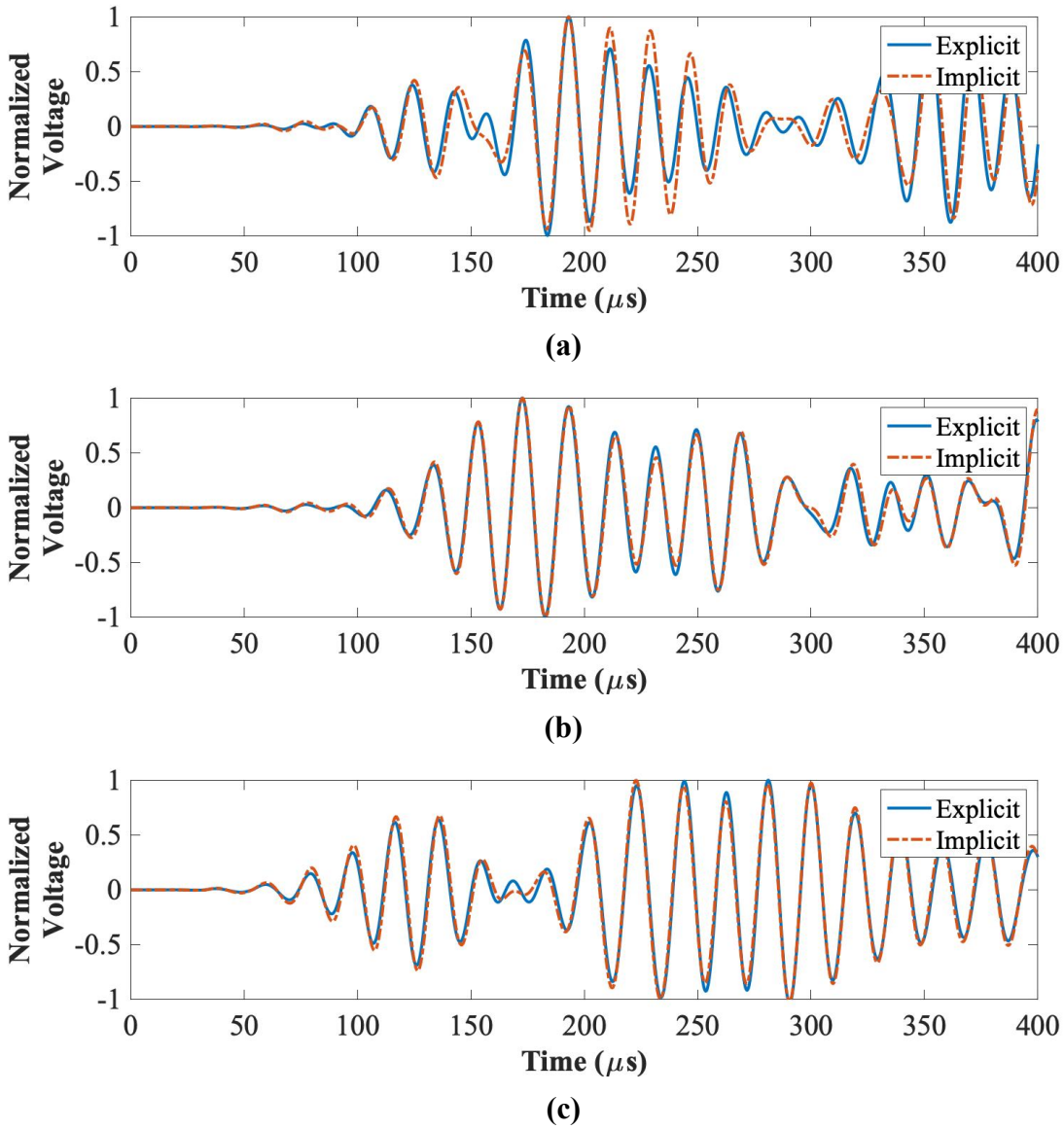

Figure 4.3. FEM comparisons between explicit and implicit dynamic analyses for the thickness of **(a)** 2 mm, **(b)** 4 mm and **(c)** 9 mm panels at 50 kHz.

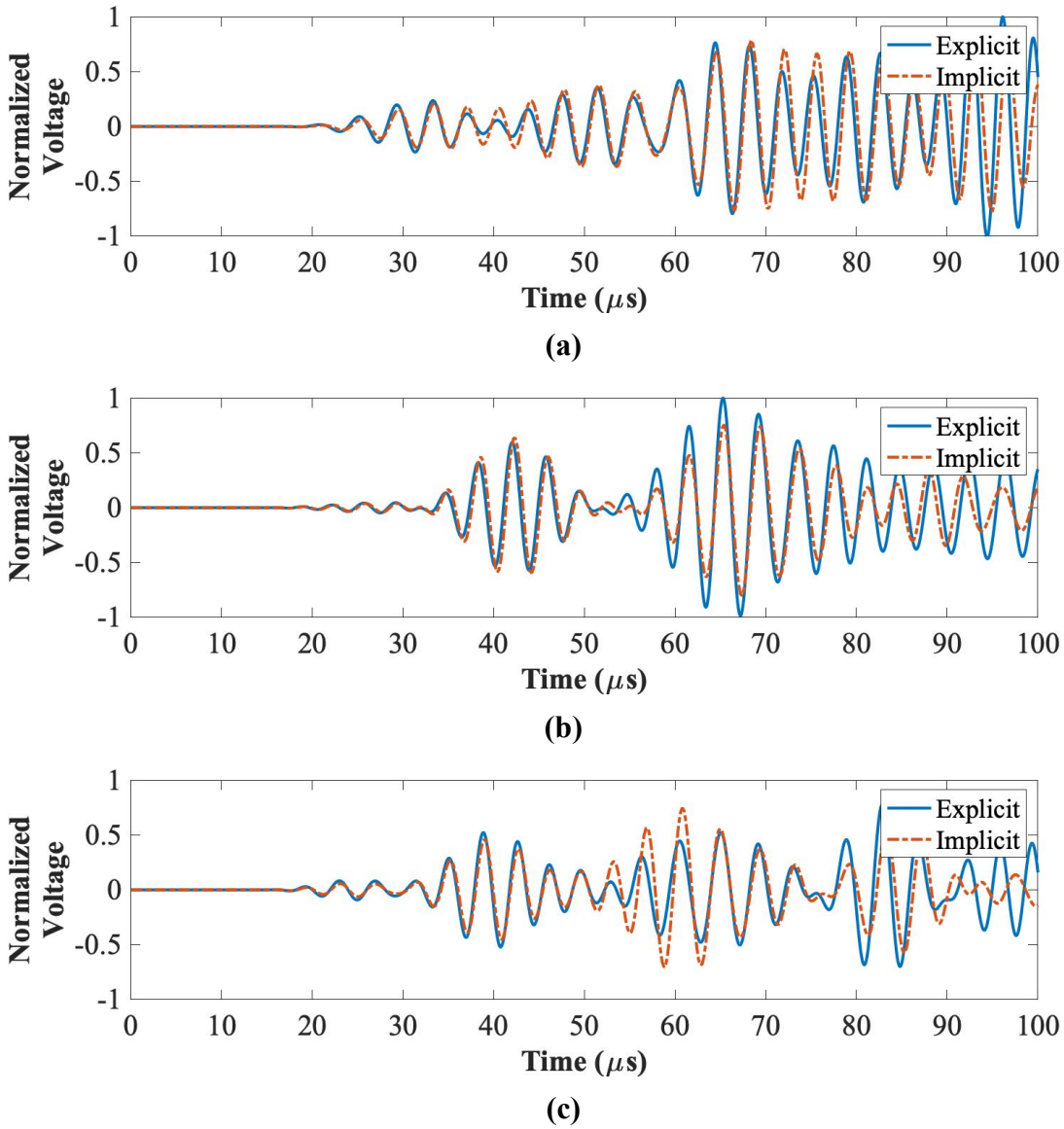

Figure 4.4. FEM comparisons between explicit and implicit dynamic analyses for the thickness of **(a)** 2 mm, **(b)** 4 mm and **(c)** 9 mm panels at 250 kHz.

4.2.2. Comparisons of Explicit Results and Experimental Results

The ABAQUS explicit results for the thickness of 2 mm, 4 mm and 9 mm panels at 50 kHz were compared to the experimental results (300 mm × 225 mm). As is shown in Figure 4.5, the shapes of the first wave packets of the explicit results for the thickness of 2 mm, 4 mm and 9 mm panels match closely to those of experimental results at 50 kHz. Therefore, the FEM modelling at 50 kHz can be used for further numerical simulation.

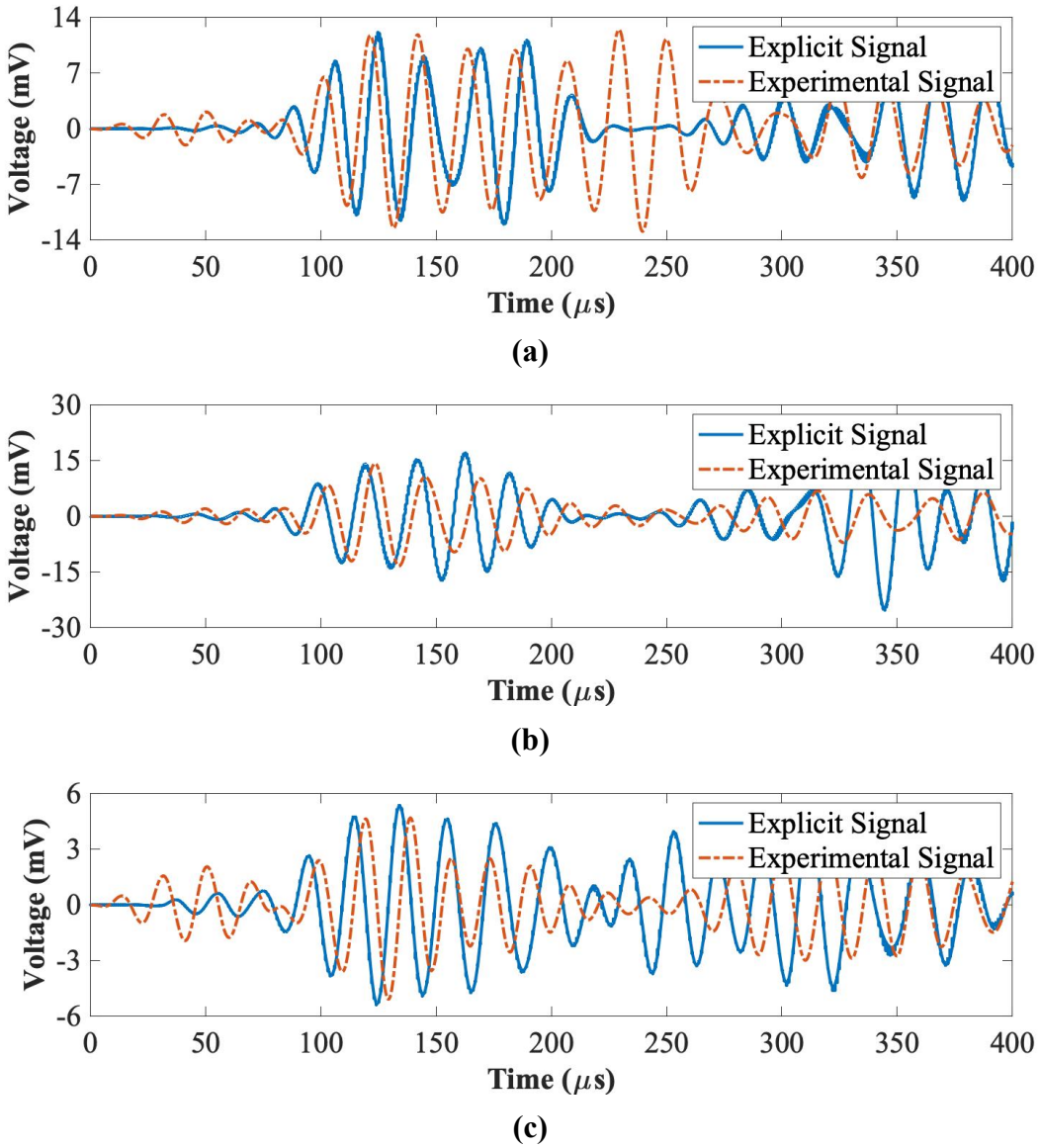

Figure 4.5. Signal verification between explicit results and experimental results for the thickness of **(a)** 2 mm, **(b)** 4 mm and **(c)** 9 mm panels at 50 kHz.

4.3. Implicit Dynamic Analysis for Embedding PZT Transducers

4.3.1. Modelling Strategies for Embedding

For modelling embedded PZT transducers into composite laminates, the implicit dynamic analysis (Abaqus/Standard) is used since there is no relative theory which can convert the input signal with the voltage to the embedded equivalent radial displacement using the explicit dynamic analysis (Abaqus/Explicit). In this section, three modelling strategies are proposed for the embedding procedure. Figure 4.6 shows the schematics of the assembly strategies for embedding PZT transducers into the composite laminate.

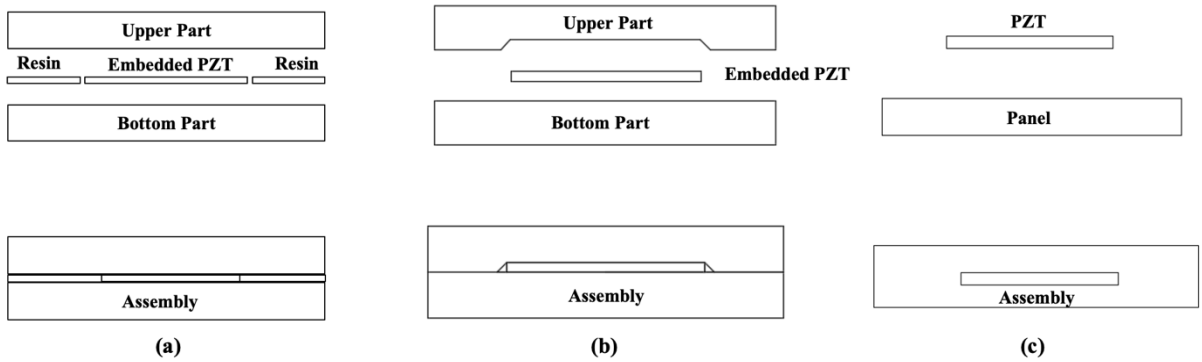

Figure 4.6. Modelling of the **(a)** strategy I, **(b)** strategy II and **(c)** strategy III for the embedding.

Figure 4.7 and Figure 4.8 compare the numerical results between these three modelling strategies at 50 kHz and 250 kHz, respectively. As can be seen in Figure 4.7, the only difference for these three embedded signals at 50 kHz is the different amplitude of the first wave packet for the thickness of 2 mm, 4 mm and 9 mm panels. The amplitudes of the first wave packets for these modelling strategies I and II are similar while that of strategy III is much higher for the thickness of 2 mm, 4 mm and 9 mm panels.

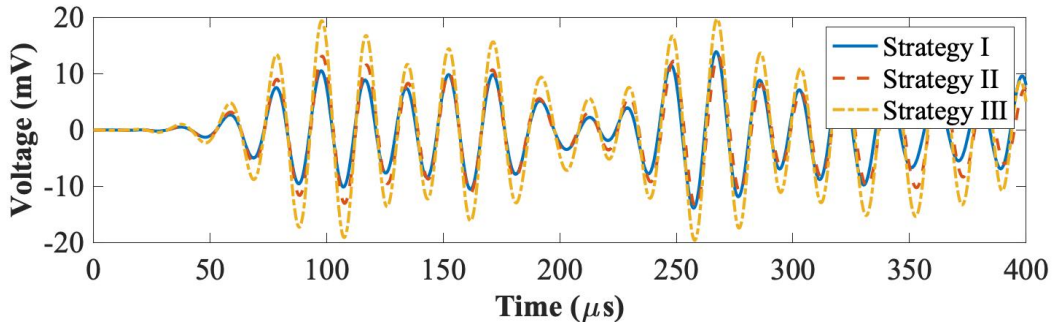

(a)

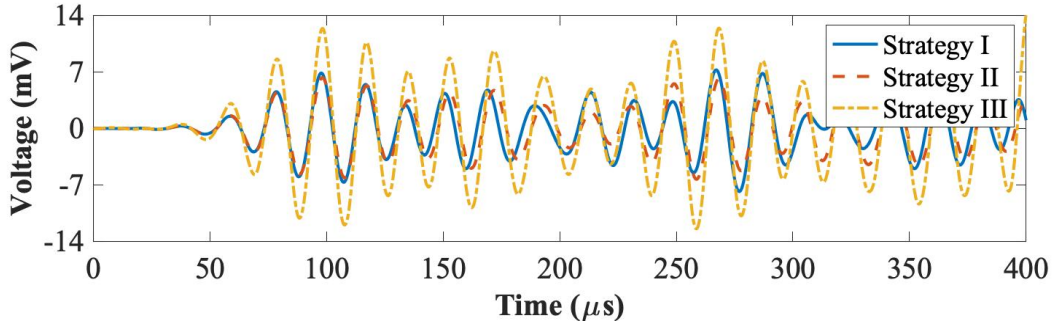

(b)

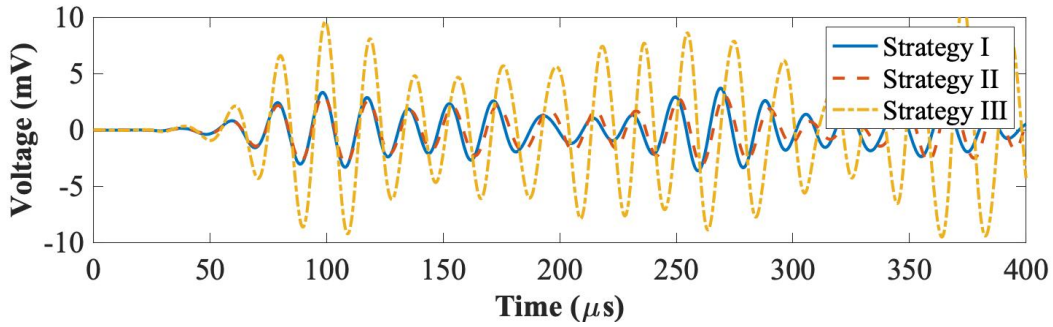

(c)

Figure 4.7. Strategy comparisons for the **(a)** 2 mm, **(b)** 4 mm and **(c)** 9 mm panels at 50 kHz.

In Figure 4.8a, the amplitudes of the first wave packets for these three strategies are similar to the 2 mm panel at 250 kHz. In Figure 4.8b, the amplitude of the first wave packet for strategy II is very small compared to strategies I and III for the 4 mm panel at 250 kHz. Furthermore, in Figure 4.8c, amplitudes of first wave packets for strategies I and II are similar but that of strategy III is close to zero for the 9 mm panel at 250 kHz. Hence, the embedded strategy I can have reasonable results for the thickness of 2 mm, 4 mm and 9 mm panels at 50 kHz and 250 kHz frequencies.

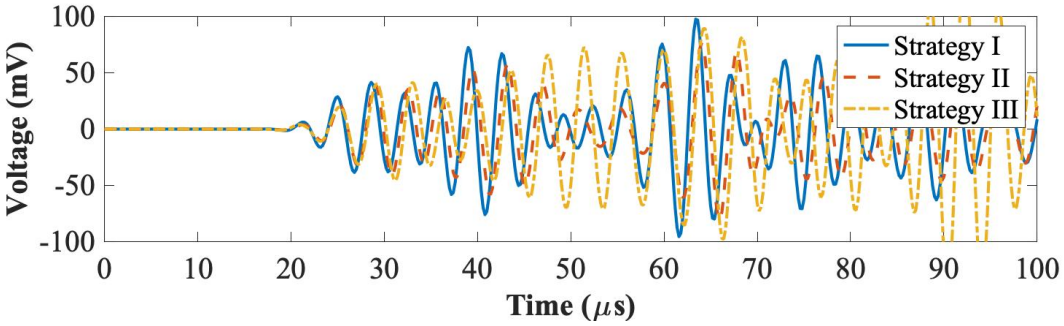

(a)

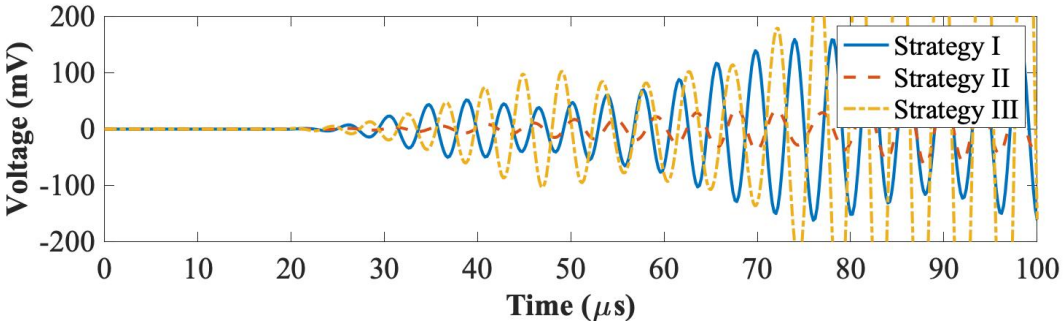

(b)

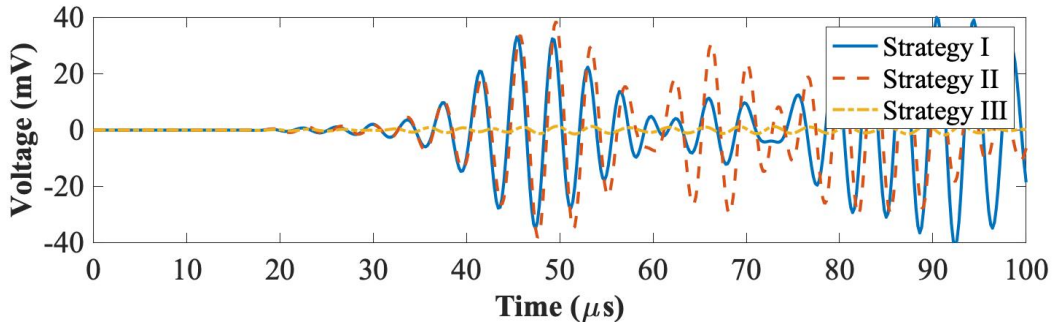

(c)

Figure 4.8. Strategy comparisons for the thickness of **(a)** 2 mm, **(b)** 4 mm and **(c)** 9 mm panels at 250 kHz.

4.3.2. Modelling Verification with Experimental Result

To verify if the embedding modelling strategy I is yielding an acceptable result, the implicit result for the 4 mm panel at 250 kHz (see Figure 4.8b and Figure 4.8c) is compared to the experimental result. As is shown in Figure 4.9, the shape and the amplitude of the first wave packet are found to be similar to the experimental result. Therefore, the embedded strategy I will be used from here onwards for the modelling purpose of SHM.

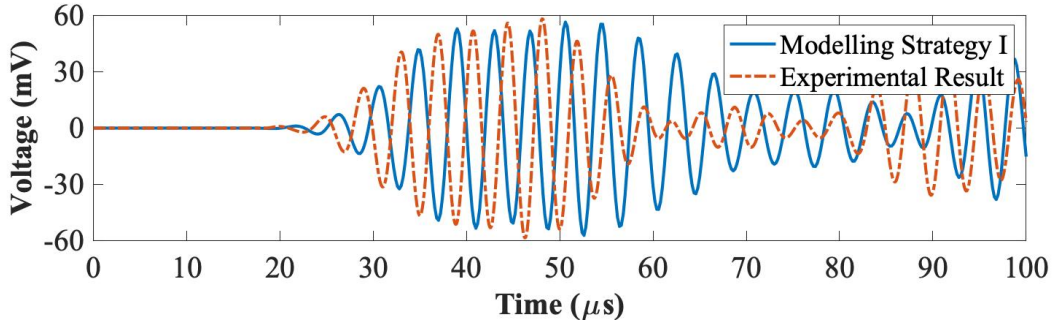

Figure 4.9. Comparison between the modelling strategy I and the experimental result for the 4 mm panel at 250 kHz.

4.4. Structural Damping

As the group velocities of the first wave packet of the experimental results are faster than that of the numerical results shown in Figure 4.5 and Figure 4.9, the damping effects on UGW were investigated to compensate for the group velocity for the numerical results. As introduced in section 2.4, the mass matrix has little effect on high-frequency problems in UGW for the Rayleigh damping, and the stiffness matrix is associated with the strain rate [105], so frequency-based structural damping was investigated to compensate for the group velocity of

numerical signals. According to the ABAQUS Manual, the structural damping can be only used when the displacement is perpendicular to the velocity [105], so the structural damping for the 2 mm panel at 50 kHz (out-of-plane motion) is shown in Figure 4.10. As can be seen in Figure 4.10, different structural damping values do not accelerate the group velocity of the first wave packet of numerical results too much. Therefore, structural damping was not used for numerical modelling in this research.

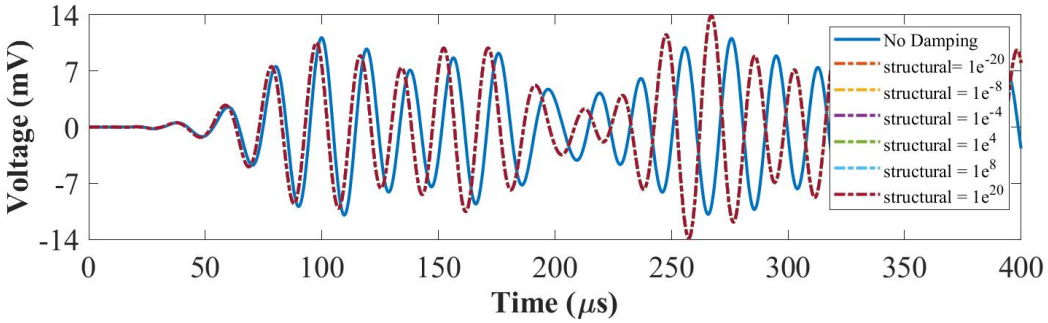

Figure 4.10. Structural damping for the 2 mm panel at 50 kHz.

4.5. Modelling of UGW Interaction with Damage

In this section, the interactions of UGW with the surface-mounted artificial damage (blue-tack) and the impact damage are studied using the ABAQUS models described earlier. The size of the part model was 0.17 m × 0.17 m, with a thickness of 0.009 m. Continuum shell was used with the stacking sequences $[(0°/+45°/-45°/+90°)_9]_s$ and the ply thickness was 0.000125 m. To obtain the displacements generated due to the guided wave propagation on the surface of the composite with embedded PZT transducers, the modelling strategy I using the implicit dynamic analysis (Abaqus/Standard) was employed. A resin part between the top and the bottom composite parts was modelled to fill the gap caused by embedded PZT transducers, as is shown in Figure 4.11.

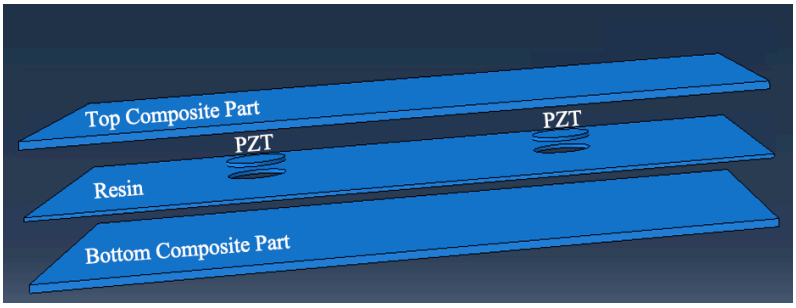

Figure 4.11. Schematic of the embedding strategy I.

4.5.1. Surface-mounted Artificial Damage

Material properties for unidirectional carbon fibre prepregs, the PZT actuator, the resin and the surface-mounted artificial damage (blue-tack) are listed in Table 4.1 and Table 4.2, respectively. For meshing the composite part, the element size was 0.0005 m in the x-y plane to have a better in-plane resolution and only one element in the z-direction. Continuum shell elements with reduced integration (SC8R) were used for the problem discretization. For meshing the PZT actuator, the element size was 0.0005 m in all directions. The family type was piezoelectric with the element type of an 8-node linear piezoelectric brick C3D8E. For meshing the blue-tack (aluminium), the element size was 0.0005 m, and the element family was 3D stress with the type of an 8-node linear brick C3D8R. Figure 4.12 shows the schematic of the assembly position of the model for the surface-mounted artificial damage (blue-tack) and the PZT actuator.

Table 4.2. Material Properties for Damage Identification

Hexply 8552 (Resin)		
ρ (kg/m^3)	E (MPa)	ν
1300	4,130	0.27
Blue-tack (Al)		
ρ (kg/m^3)	E (MPa)	ν
2700	70,000	0.3

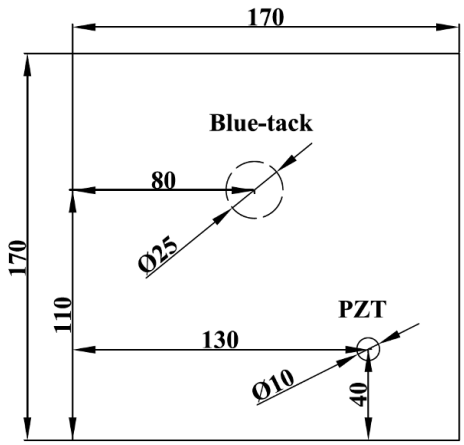

Figure 4.12. Schematic of the assembly position of the model.

Figure 4.13 plots interactions of UGW with the surface-mounted artificial damage actuated by the embedded PZT actuator in the z-direction for the 9 mm panel at 50 kHz and 250 kHz, respectively. As can be seen in Figure 4.13, the surface-mounted artificial damage can interact with propagating UGW at both 50 kHz and 250 kHz in the z-direction.

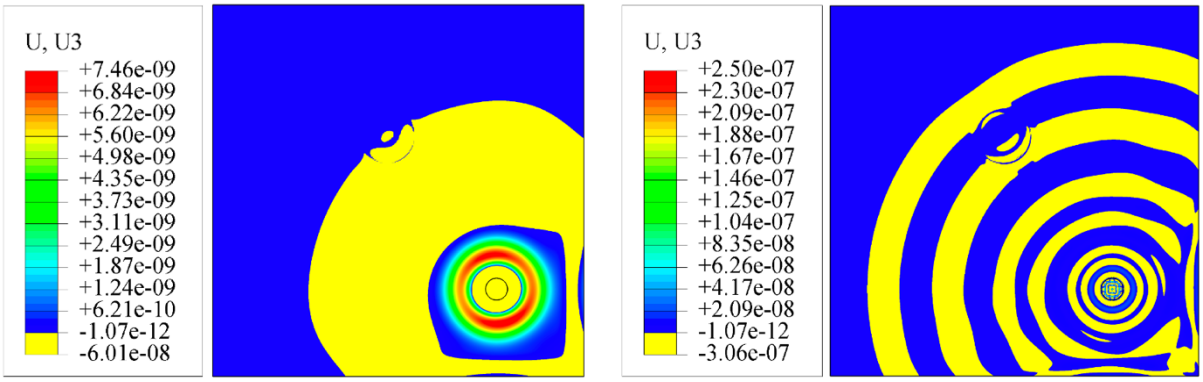

(a) **(b)**

Figure 4.13. Interactions of UGW with the surface-mounted artificial damage in the z-direction for the 9 mm panel at **(a)** 50 kHz and **(b)** 250 kHz.

4.5.2. Impact Damage

In this section, guided wave interaction with the impact damage will be numerically studied. The impact position was the same as the mirror image in Figure 4.12, and the modelling was the same as the one for the surface-mounted artificial damage in section 4.5.1. The diameter of the impact damage was Ø25 mm. The elastic modulus for the damaged prepregs was reduced to 40% compared to the original one, and the definition of the composite lay-up for the damaged area was the same as the undamaged area.

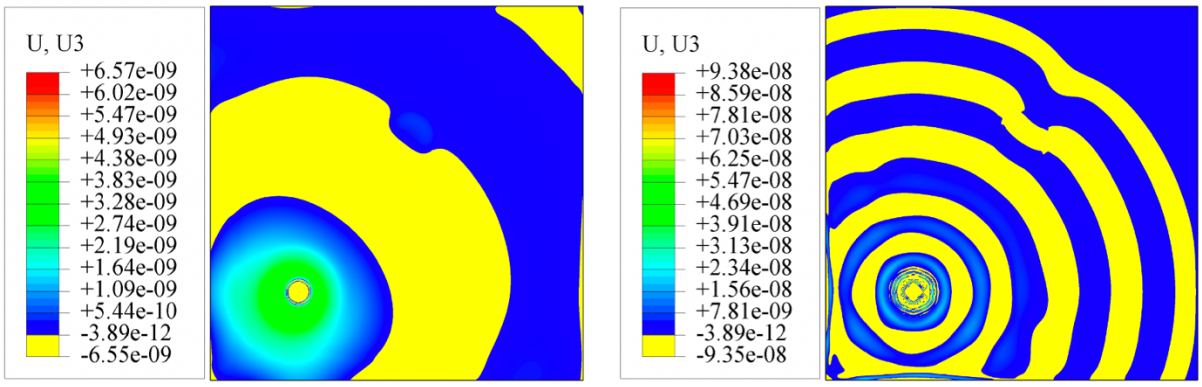

(a) **(b)**

Figure 4.14. Interactions of UGW with the impact damage in the z-direction for the 9 mm panel at **(a)** 50 kHz and **(b)** 250 kHz.

Figure 4.14 plots interactions of UGW with the impact damage in the z-direction for the 9 mm panel at 50 kHz and 250 kHz, respectively. As can be seen in Figure 4.14, the impact damage can interact with propagating UGW at both 50 kHz and 250 kHz in the z-direction.

4.6. Summary

In this chapter, FEM explicit and implicit dynamic analyses were investigated for simulating UGW actuated by surface-mounted and embedded PZT transducers. Three strategies were proposed to model embedded PZT transducers into the composite laminate for the implicit dynamic analysis. It was found that the result of the embedded strategy I was in good agreement with the experimental result. The influence of the structural damping on the group velocity of UGW was also investigated. It was found that values of the structural damping for composite damping cannot compensate for the group velocity of UGW very much. Finally, interactions of UGW with the surface-mounted artificial damage and the impact damage have been investigated. It was found that UGW can successfully interact with both the surface-mounted artificial damage and the impact damage at 50 kHz and 250 kHz.

Chapter 5

5. Thickness Effects on Ultrasonic Guided Waves

5.1. Introduction

The aim of this chapter is to carry out an in-depth investigation into the influence of composite thickness on the effectiveness of ultrasonic guided waves (UGW) for damage detection under different temperatures. Guided wave propagation in a thick composite plate (9 mm) will be compared to thin composite plates (2 mm and 4 mm) to highlight different propagation properties that are thickness dependant and can influence the reliability of a detection methodology. Moreover, the diagnostic film with integrated PZT transducers based on the circuit-printing technique has been developed [124, 137] to replace the traditional coaxial cables and reduce the weight of the host structure [60].

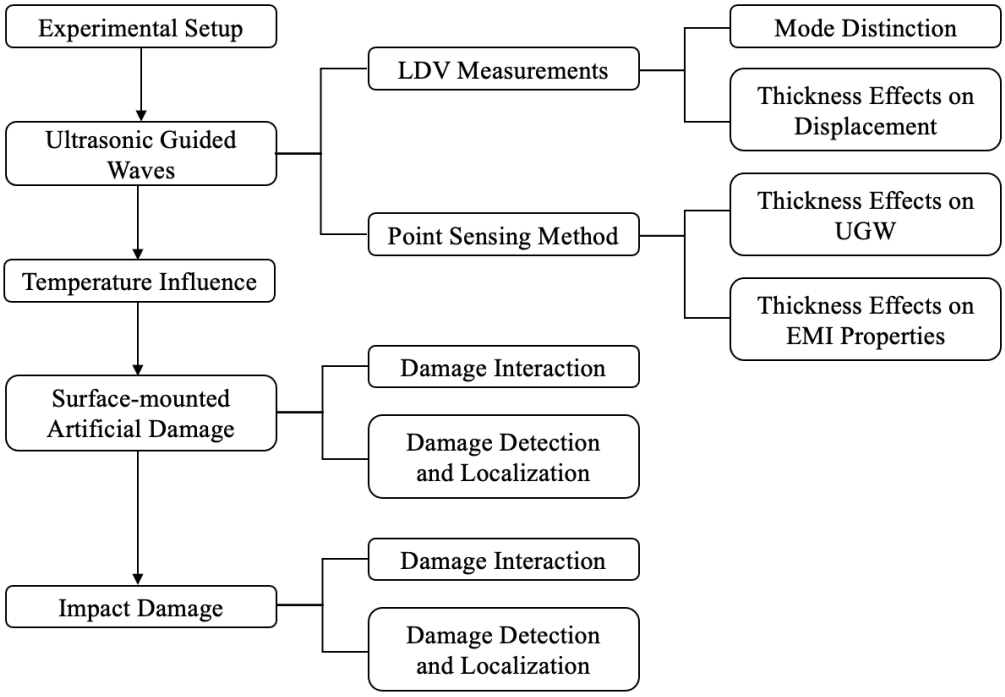

Figure 5.1. Schematic of the flow chart for all investigations of chapter 5.

Figure 5.1 shows the flow chart to illustrate all investigations of chapter 5. First, a laser Doppler vibrometer (LDV) was used to measure guided wave propagation through the thickness of 2 mm, 4 mm and 9 mm composite laminates, respectively. The S_0 and the A_0 modes will be distinguished and the group velocity of each mode for each thickness laminate

will be computed. Next, the electro-mechanical impedance (EMI) method is used to evacuate the dynamic of the frequency of different thickness plates. The behaviour of UGW under varying temperatures in different thickness plates is also investigated. The surface-mounted artificial damage and the impact damage interacted with UGW will be studied using LDV measurements, followed by using the damage index correlation coefficient and the delay-and-sum (DAS) algorithm to detect and locate those damages.

5.2. Experimental Setup

To compare the thickness effect on Lamb waves, three different composite panels with thicknesses of 2 mm, 4 mm and 9 mm, respectively were fabricated. Unidirectional carbon fibre prepregs Hexply® IM7/8552 were chosen and the average thickness of each cured ply was 0.125 mm. The quasi-isotropic stacking sequence for the lay-up was $[(0/45/-45/90)_n]_s$, where n was 2, 4 and 9 for each panel, respectively. The general drawing of these panels and locations for each PZT transducer is shown in Figure 5.2a. The fabrication details of the composite specimen can be referred to in section 3.3. Figure 5.2b shows one of the fabricated composite panels with diagnostic films and PZT transducers.

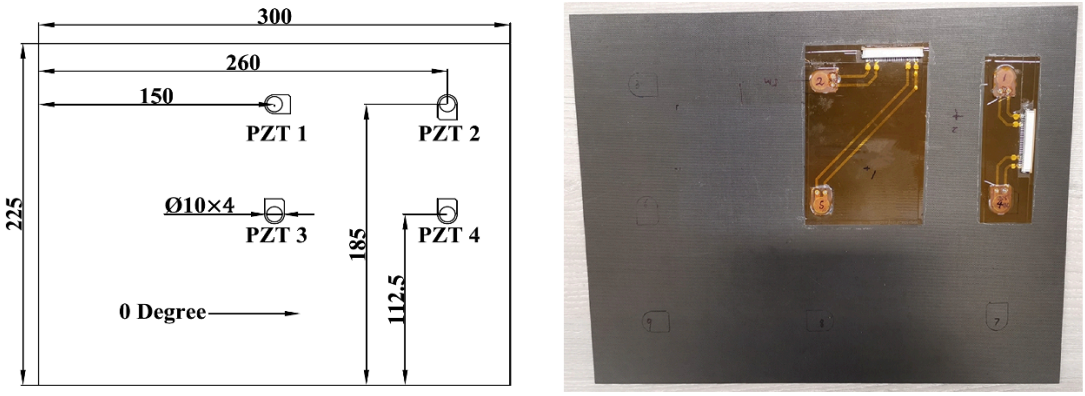

Figure 5.2. **(a)** General drawing of the specimen; **(b)** Example of the composite panel with PZT transducers.

5.3. Ultrasonic Guided Waves

In this section, propagations of guided wave signals in the thicknesses of 2 mm, 4 mm and 9 mm panels are studied. First, mode distinction and the effect of displacement on thickness are studied using a laser Doppler vibrometer (LDV). Second, comparisons of UGW for all these panels are investigated and amplitudes of the first wave packets will be compared to investigate

the thickness influence to develop optimum excitation parameters for damage detection purposes for various plate thicknesses.

5.3.1. LDV Measurements

To experimentally distinguish guided wave modes and compute the group velocity, LDV measurements were conducted using PSV-500-3D-M. For the LDV setup, a chirp signal was used as the input signal with a frequency range of 50~500 kHz and the duration was 0.5 ms. The amplitude of the input signal was 2 V and the period of the burst was 15 ms. To filter noise, a bandpass filter from 25 kHz to 550 kHz was applied, and the scanning grid was measured 200 times and averaged. The sampling frequency was set to 2.56 MHz and a total of 2048 points were recorded. A total of 80 scanning grids (1×80) with a length of 100 mm were generated. Figure 5.3 shows the schematics of the LDV setup and measurements. After postprocessing, these chirp signals were reconstructed to five-cycle Hanning-windowed toneburst signals at 50 kHz and 250 kHz.

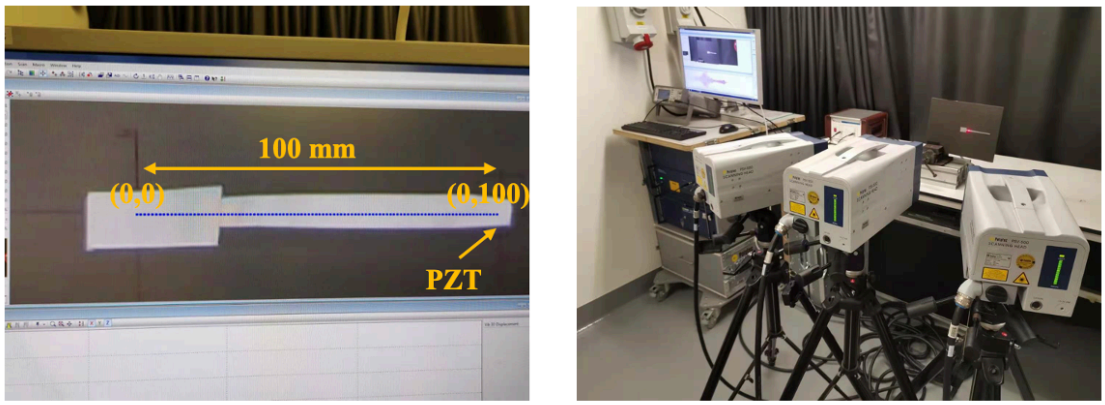

(a) **(b)**

Figure 5.3. Schematics of **(a)** LDV set up and **(b)** measurements to compute the group velocity.

5.3.1.1. Mode Distinction

To distinguish wave modes (S_0 and A_0 modes) for the thickness of 2 mm, 4 mm and 9 mm panels at 50 kHz and 250 kHz, 2-D wave propagations in the x-y and the z-direction were investigated. Figure 5.4 shows the example of the 2-D wave propagation in the z-direction for the 9 mm panel. As can be seen in Figure 5.4, it is evident that at 50 kHz the A_0 mode is dominant while at 250 kHz the S_0 mode is dominant for the thickness of 2 mm, 4mm and 9 mm panels by comparing the slope of the group velocity of the first wave packet of these signals.

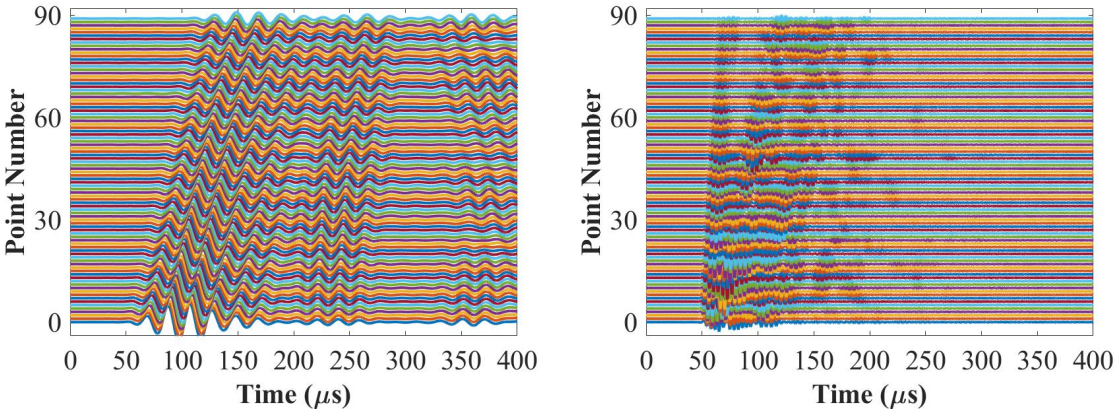

Figure 5.4. 2-D wave propagation in the z-direction at **(a)** 50 kHz and **(b)** 250 kHz for the 9 mm panel.

5.3.1.2. Propagation Modes

In this section, the effects of thickness on the fundamental propagation modes of displacement in the x-y direction (in-plane motion) and the z-direction (out-of-plane motion) will be investigated separately. The in-plane displacement in the x-y direction was computed by averaging these data of the x- and the y- directions. Figure 5.5 and Figure 5.6 plot displacements from the position at 100 mm away from the centre of the PZT actuators (shown in Figure 5.3a) in the x-y and the z- directions for the thickness of 2 mm, 4 mm and 9 mm panels at 50 kHz and 250 kHz, respectively. In Figure 5.5, the amplitude of the first wave packet at 50 kHz (A_0 mode dominates) decreases from the 2 mm panel to the 4 mm panel and then to the 9 mm panel in the x-y and the z- directions. In addition, amplitudes of the out-of-plane motion for the A_0 mode are much higher than those of the in-plane motion.

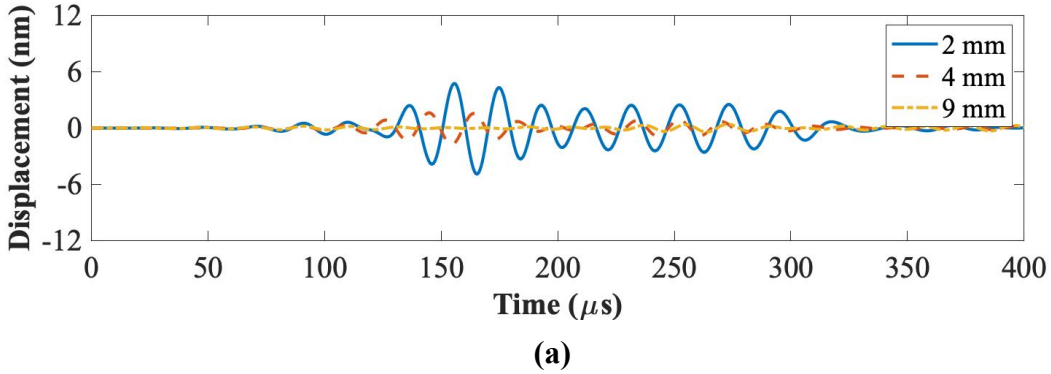

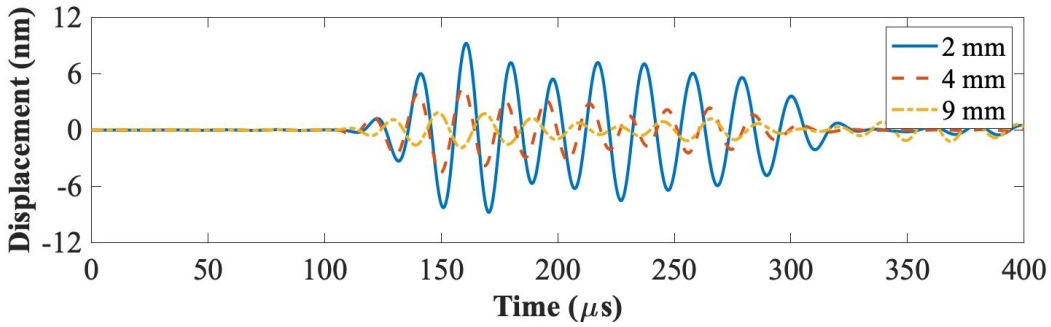

(b)

Figure 5.5. Displacement in **a)** the x-y and **b)** the z- directions for the 2 mm, 4 mm and 9 mm panels at 50 kHz.

In Figure 5.6, the amplitude of the first wave packet at 250 kHz (S_0 mode dominates) for the 2 mm panel is smaller than that of the 4 mm panel but higher than that of the 9 mm panel in the in-plane motion, while the amplitudes of the S_0 mode for the out-of-plane motion are consistent and do not change too much for these panels. In addition, the amplitudes of the in-plane motion for the S_0 mode are much higher than that of the out-of-plane motion, in contrast to the A_0 mode.

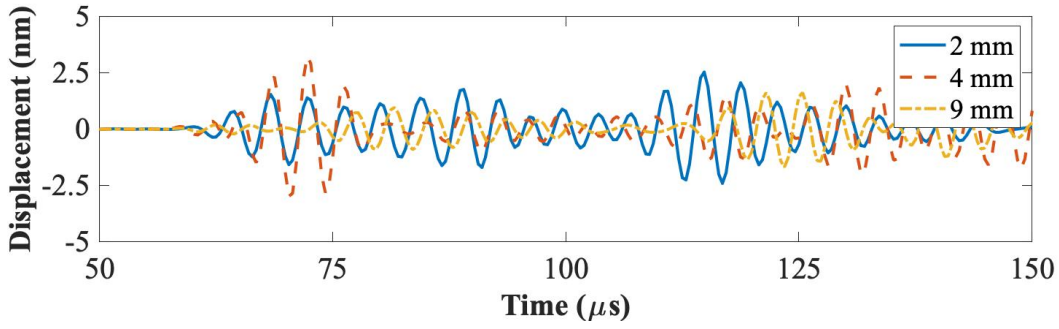

(a)

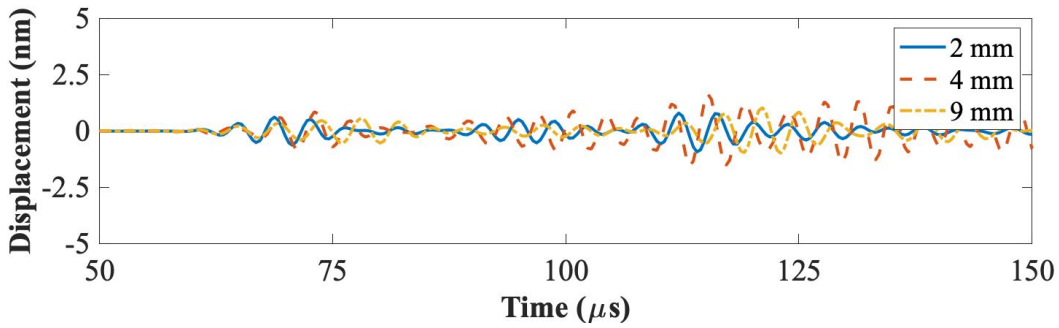

(b)

Figure 5.6. Displacement in **a)** the x-y and **b)** the z- directions for the thickness of 2 mm, 4 mm and 9 mm panels at 250 kHz.

Figure 5.7 summarizes the peak amplitudes of the first wave packets for the A_0 mode and the S_0 mode from the above results for the in-plane motion (x-y direction) and the out-of-plane motion (z-direction) at 50 kHz and 250 kHz, respectively. The peak amplitude was computed by choosing the peak amplitude of the first wave pack of each measured displacement signal. As can be seen in Figure 5.7, the amplitude of the A_0 mode (50 kHz) is thickness dependent and reduces with the increase of the thickness. Therefore, the A_0 dominant mode should be avoided use for large area detections of thick composites since the amplitude of the A_0 dominant mode will drop significantly. In addition, the amplitude of the A_0 mode for the out-of-plane motion is higher than that for the in-plane motion and the amplitude of the S_0 mode (250 kHz) for the in-plane motion is higher than that for the out-of-plane motion, so the A_0 dominant mode is more sensitive to surface damage and the S_0 dominant mode is more sensitive to in-plane damage. Furthermore, the amplitude of the S_0 mode is not changed significantly for the out-of-plane motion.

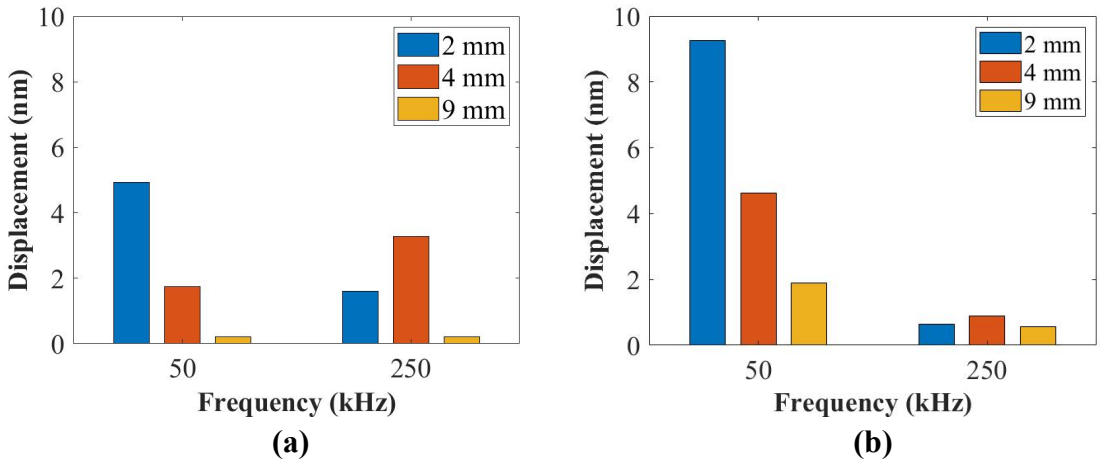

Figure 5.7. The summary of the peak amplitude of the first wave packet in **(a)** the x-y and **(b)** the z- directions at 50 kHz and 250 kHz.

Figure 5.8 shows the comparison of the group velocities of the A_0 mode and the S_0 mode for the in-plane motion (x-y direction) and the out-of-plane motion (z-direction) at 50 kHz and 250 kHz, respectively, for different thickness plates. In Figure 5.8, the group velocity of the A_0 mode in the in-plane and the out-of-plane motions is affected by the thickness, while that of the S_0 mode in the in-plane motion and the out-of-plane motion is not.

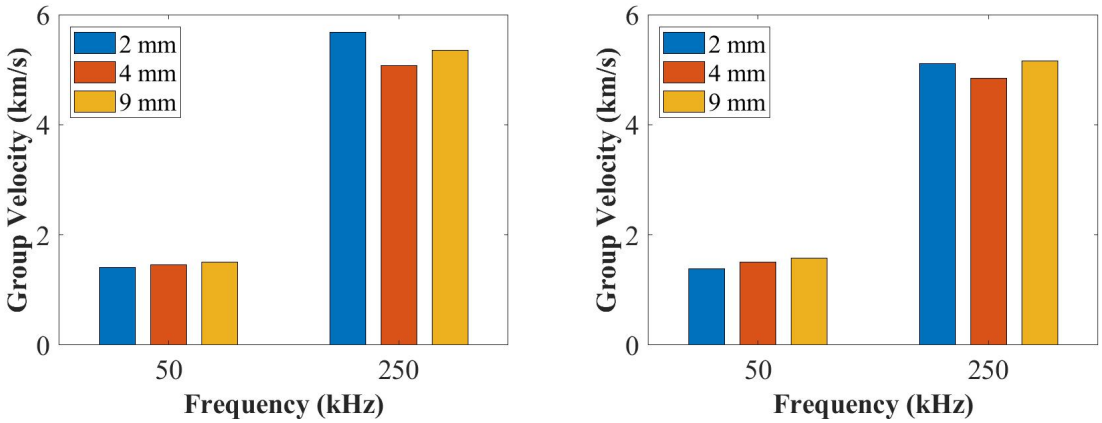

Figure 5.8. The summary of the group velocity in **(a)** the x-y and **(b)** the z- directions at 50 kHz and 250 kHz.

5.3.2. UGW Comparisons

The previous section investigated the full wave field response (x, y, z directions) of the plates' measures with LDV measurements to get detailed propagation properties of waves in different thickness composite panels. However, SHM systems utilise point sensors such as the PZT actuators, and therefore the response (in-plane) of the guided wave propagation recorded by the PZT sensors is investigated in detail next, as these results are used for damage detection and characterization and can defer from the recorded full field response. The experimental results are from the plate configuration shown in Figure 5.2.

5.3.2.1. Active Sensing Results

To compare the amplitude differences of guided wave signals of each panel, two PZT transducers with path 3-4 is shown in Figure 5.2a, together with five-cycle Hanning-windowed toneburst signals (the setup of the input signal can be referred to in section 3.6.4) at 50 kHz and 250 kHz shown in Figure 5.9.

As is shown in Figure 5.9a, the amplitude of the first wave packet (A_0 mode) for the 2 mm panel is higher than that of the 4 mm and the 9 mm panels at 50 kHz. In Figure 5.9b, the amplitude of the first wave packet for the 2 mm panel is lower than that of the 4 mm panel and higher than that of the 9 mm panel at 250 kHz. In conclusion, the amplitude of the first wave packet for the A_0 mode reduces with increased thickness. The group velocity of the A_0 mode increases from the 2 mm panel to the 4 mm panel and then to the 9 mm panel. In addition, the amplitude of the first wave packet for the S_0 mode increases first and then reduces. The group

velocity of the S_0 mode becomes slower from the 2 mm panel to the 4 mm first and then becomes faster with the increased thickness from the 4 mm panel to the 9 mm panel.

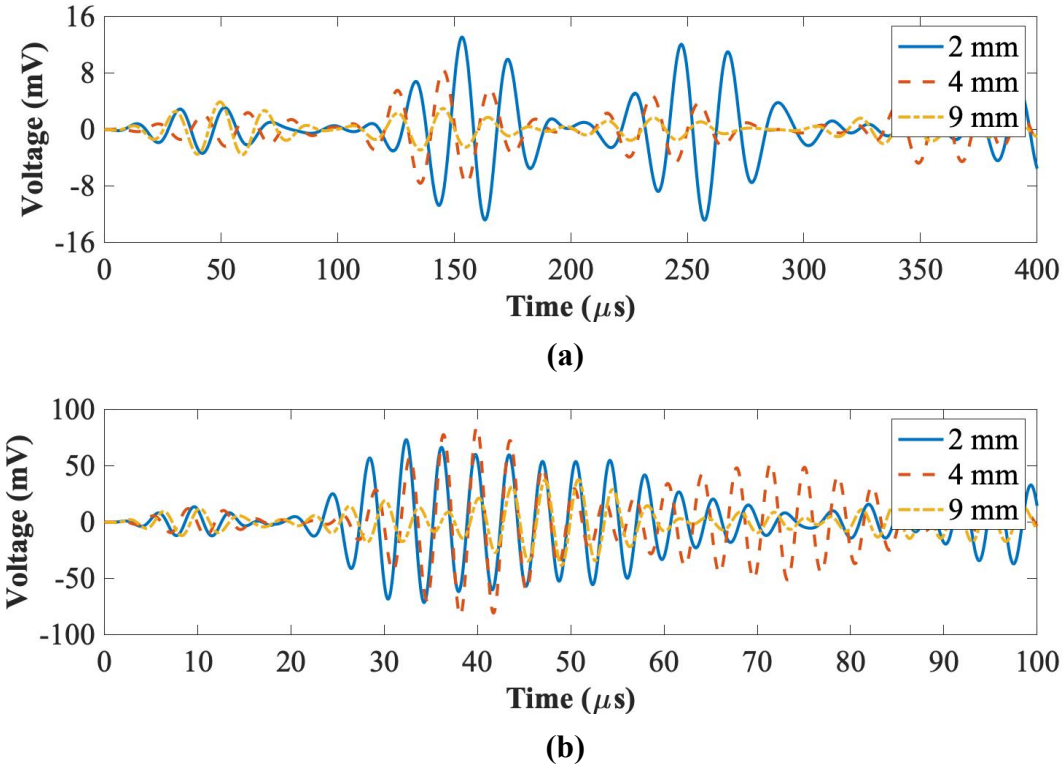

Figure 5.9. UGW comparisons for the thickness of 2 mm, 4 mm and 9 mm panels at **(a)** 50 kHz and **(b)** 250 kHz.

Figure 5.10 summarizes the amplitude and the group velocity for the thickness of 2 mm, 4 mm and 9 mm panels at 50 kHz (A_0 mode) and 250 kHz (S_0 mode), respectively. The peak amplitude was computed by choosing the peak amplitude of the first wave packet of the measured sensing signals. The group velocity was computed by the distance between the actuator and the sensor divided by the time-of-arrival of their signals. As can be seen in Figure 5.10a, the amplitude of the A_0 mode is influenced more than that of the S_0 mode by the thickness. This is because the A_0 mode is the out-of-plane motion and the S_0 mode is the in-plane motion. In Figure 5.10b, the group velocity of the A_0 mode increases with the increased thickness at 50 kHz, which is affected by the thickness. Furthermore, the group velocity of the S_0 mode for the 9 mm panel is faster than that of the 4 mm panel and slower than that of the 2 mm panel, which are not affected by the thickness.

For active sensing, the group velocity needs to be considered during the design of the network of PZT transducers since the time-of-arrival (ToA) can be calculated by the distance between each PZT transducer and the group velocity. Due to the printed diagnostic film having the crosstalk issue as mentioned in section 3.5, the distance between each PZT transducer shall increase for the thicker composite panel when using the A_0 mode at 50 kHz, because the thicker composite panel will cause an earlier ToA and the crosstalk will overlap with the first wave

packets of the guided wave signals if it does not design properly. In addition, by comparing those trends of the sensing results (in-plane wave) in Figure 5.10 to the trends of the LDV results in Figure 5.7a and Figure 5.8a (in-plane displacement), both the peak amplitude and the group velocity have similar trends for the A_0 and the S_0 modes through the thickness.

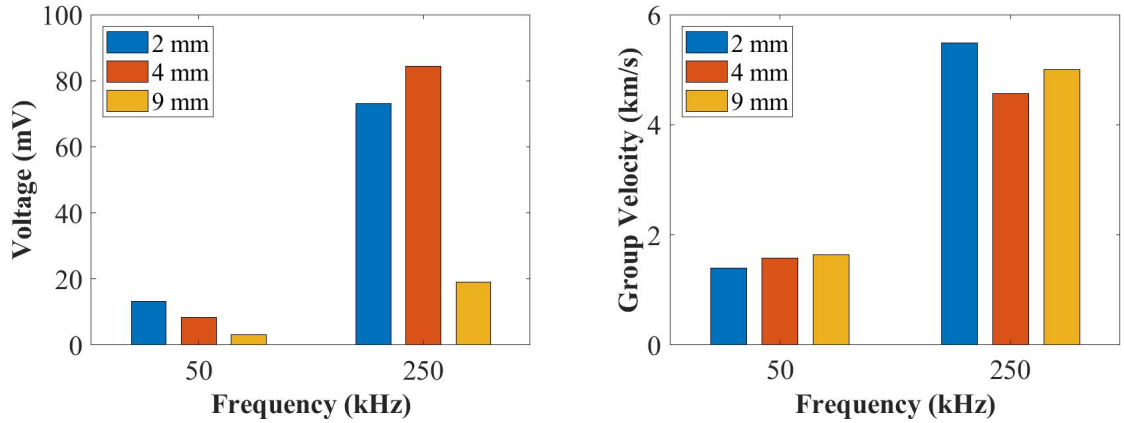

Figure 5.10. The summary of **(a)** the amplitude and **(b)** the group velocity of UGW for the thickness of 2 mm, 4 mm and 9 mm panels at 50 kHz and 250 kHz.

Comparing the results of LDV measurements (in-plane motion only) and the PZT responses (Figure 5.7a, Figure 5.8a and Figure 5.10), it emphasises the influence of the surface-mounted sensors on the A_0 and the S_0 mode amplitudes. It also shows the differences in the ease of excitability of the different modes, which is a function of the local dynamics of the plate plus sensor. Therefore, in the next section, the electro-mechanical response of the system is investigated to understand the frequency response of different thickness plates.

5.3.2.2. Electro-mechanical Impedance Response

To further investigate the effect of the plate thickness on the ease of excitation of each mode, attenuation and dispersion, the modal response of the transducer bonded to the plate is measured through the electro-mechanical impedance (EMI) measurement. The EMI shows the frequency response of the dynamic system which is the sensor plus the host structure (i.e., different thickness plates). Since the sensors for each thickness plate are the same, any modal changes in the response will be attributed to the thickness effect of the plate.

In this section, The EMI results for the thicknesses of 2 mm, 4 mm and 9 mm panels are compared. Figure 5.11 shows the imaginary and the real parts of admittances for the PZT 3. As can be seen in Figure 5.11a, the slope of lines is similar to all panels, with a slight increase in the 4 mm panel in the range 0~250 kHz. Similarly, in Figure 5.11b, the peak amplitude response of the real part of the admittance for the 2 mm panel is higher than that of the 4 mm

and the 9 mm panels. As is shown in Figure 5.11a, there is no obvious difference in the imaginary part of the admittance at the range of low frequencies (below 20 kHz), so the thickness has no influence on the EMI properties. This can explain the linear trend of the amplitude reduction with the increased thickness for 50 kHz, shown in Figure 5.10a.

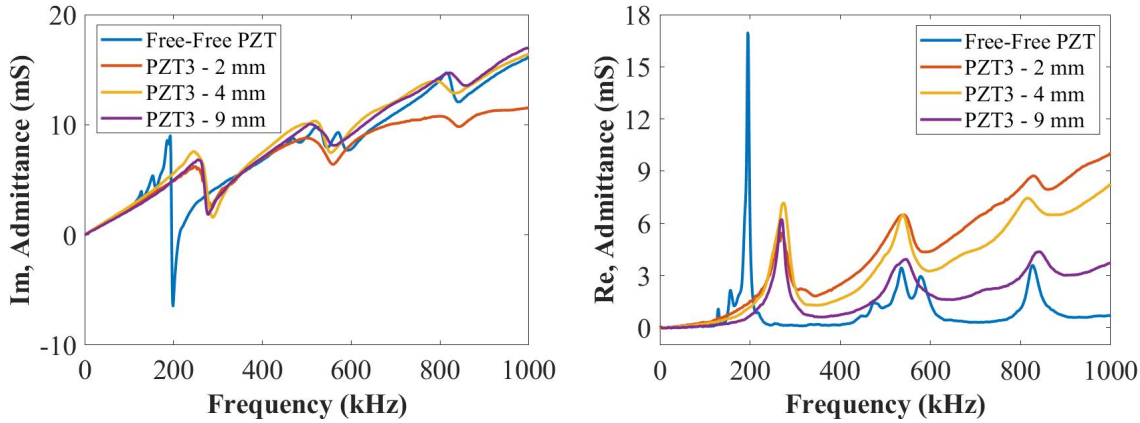

Figure 5.11. EMI results of **(a)** the imaginary and **(b)** the real parts of the admittance for the 2 mm, 4 mm and 9 mm panels.

By comparing the sensor response results in Figure 5.10a to the LDV results in Figure 5.7a, the sensor response results show the S_0 mode is much higher than the A_0 mode, while the LDV results show the A_0 mode is much higher than the S_0 mode. This is because LDV only measures the displacement in the plate, it does not account for the dynamic of the sensor being attached to it. When considering the attached sensors, the response of the sensor for the frequency with the plate is around 250 kHz (shown in Figure 5.11), this amplifies the results significantly. Therefore, although the LDV results can explain the response of the wave propagation well in the plate, the dynamic of the whole system shall also be considered for designing the network of the sensors. In conclusion, the EMI results show one can get a much higher amplitude at 250 kHz with the sensor because of the dynamic of the frequency.

The dynamic index mainly inspects the performance of the sensor under fast conditions, which includes the frequency response and the step response [138]. The frequency response characteristics of the sensor determine the frequency range to be measured. The higher the frequency response of the sensor, the wider the measurable signal frequency range. The step response characteristics of the sensor relate to maximum deviation, delay time, rise time, peak time, and response time. In practice, the dynamic characteristics of the sensor are often expressed by the response to some standard input signals. This is because the sensor response to the standard input signal is easy to be obtained by the experimental methods, and there is a certain relationship between the response to the standard input signal and its response to any input signal, often knowing the former can infer the latter [138].

The results presented so far were obtained under room temperature with little variations. Next, the effect of guided wave propagation under varying temperatures in different thickness

plates is investigated, which is of high interest for real structures under operational conditions and can affect the reliability of damage detection.

5.4. Temperature Effect on Guided Waves

In this section, the temperature effect on the peak amplitude and the group velocity of guided wave signals is evaluated. The three panels were placed into an environmental chamber and the temperature varied from -40 °C to 80 °C with a step of 10 °C. The PZT transducer path 3-4 shown in Figure 5.2a was measured by five-cycle Hanning-windowed toneburst signals at 50 kHz and 250 kHz, respectively. Figure 5.12 plots an example of UGW for the 2 mm panel at 50 kHz and 250 kHz. The peak amplitudes of the first wave packets under each temperature were computed automatically to measure the amplitude reduction and the phase shift.

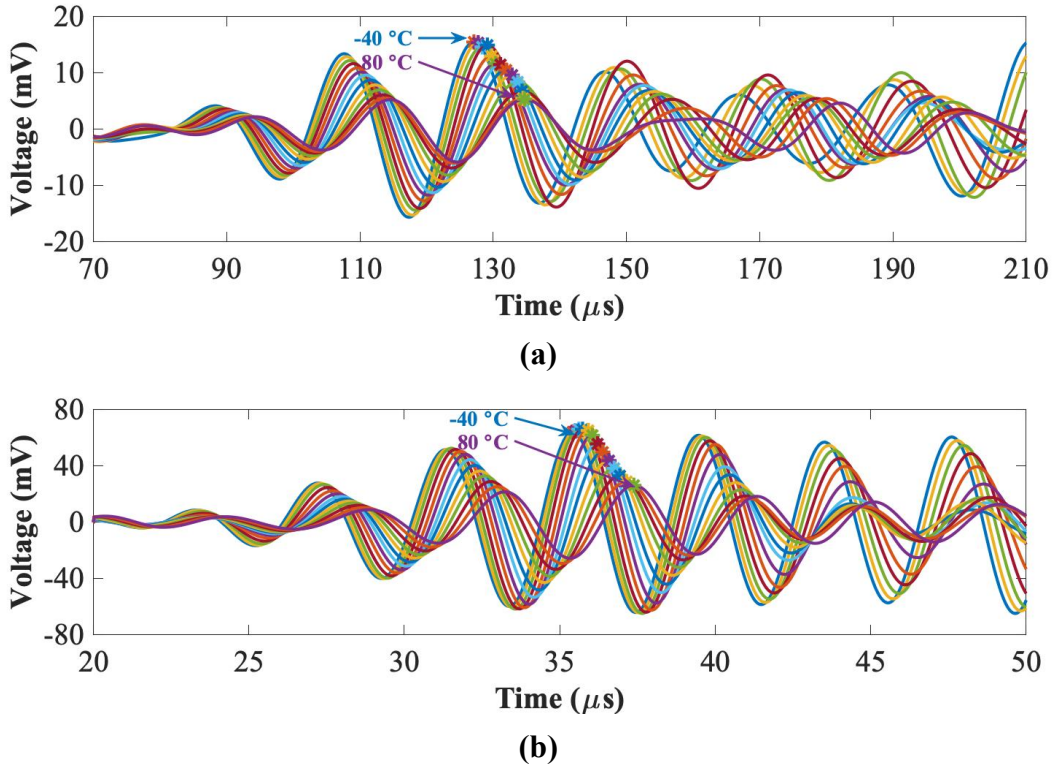

Figure 5.12. UGW with peak amplitudes under varying temperatures at **(a)** 50 kHz and **(b)** 250 kHz for the 2 mm panel.

Figure 5.13 summarizes the relationships of the temperature with the amplitude and the time-of-flight (ToF) at 50 kHz (A_0 mode) and 250 kHz (S_0 mode) for the thickness of 2 mm, 4 mm and 9 mm panels. The amplitude value was chosen from the peak amplitude of the first wave packet of each signal, and the ToF value was the difference between the time at the peak amplitude of the first wave packet and the half of the actuation signal. In Figure 5.13a, the amplitude of the A_0 mode for the thickness of 2 mm, 4 mm and 9 mm panels decrease at 50

kHz. In Figure 5.13b, the amplitude of the S_0 mode for the 2 mm decreases, and that for the 4 mm panel increases slightly first and decreases, while that for the 9 mm panel increases from -40 °C to 40 °C then decreases from 40 °C to 80 °C at 250 kHz with the increased temperature. In Figure 5.13c and Figure 5.13d, the ToF of the A_0 mode and the S_0 mode increases for the thickness of 2 mm 4 mm and 9 mm panels with the increased temperature at 50 kHz and 250 kHz, respectively.

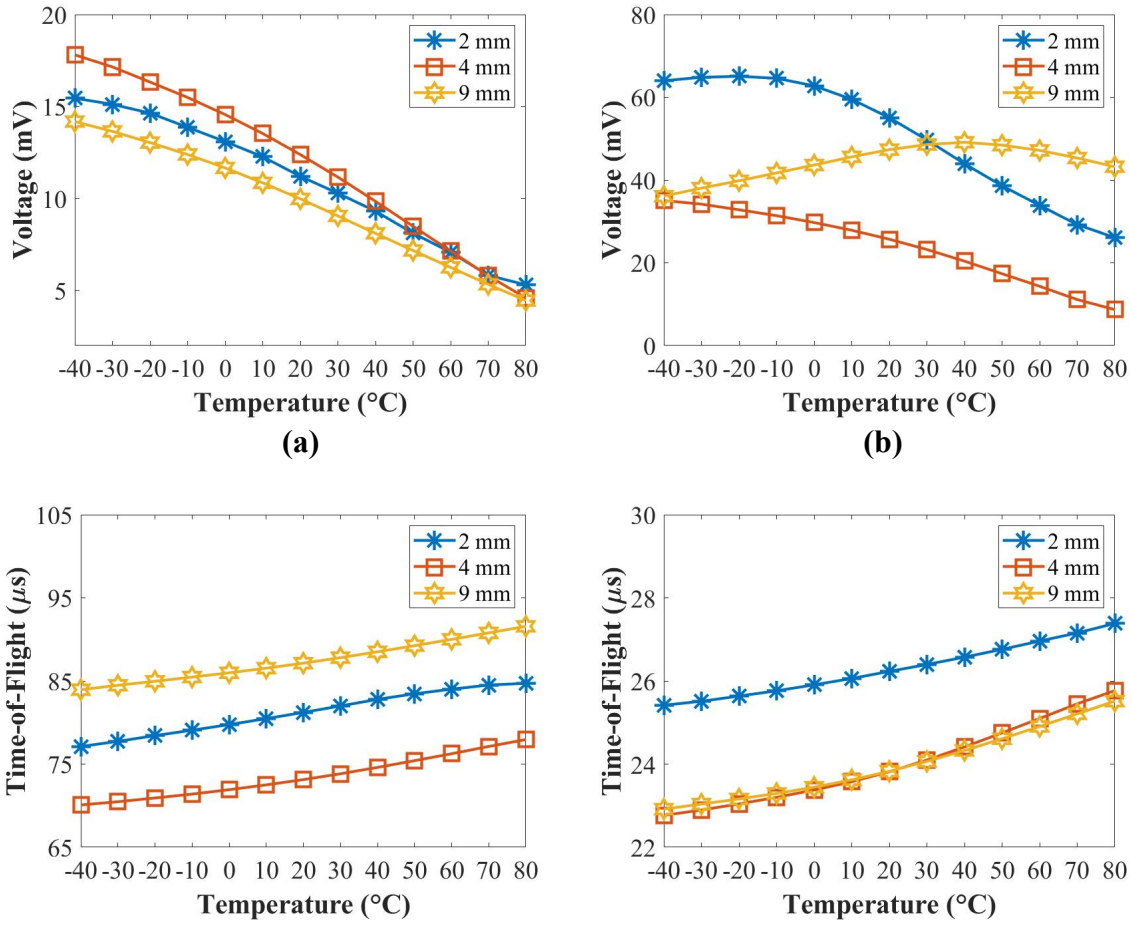

Figure 5.13. Relationships of the temperature with the peak amplitude at **(a)** 50 kHz, **(b)** 250 kHz and the time-of-flight at **(c)** 50 kHz and **(d)** 250 kHz.

Overall, the amplitude of the A_0 mode reduces with the increased temperature for all panels, which is not dependent on thickness, while that of the S_0 mode has different trends for panels of different thicknesses. In addition, the group velocities become slow for both the A_0 and the S_0 modes for all those panels with the increase in temperature, which are not dependent on thickness.

The changes in temperature can be attributed to the below factors: First, the piezoelectric constants d_{31} and g_{31} vary with the temperature [124, 139-141]. These piezoelectric constants are associated with the shear strain and the piezo sensitivity respectively, which affects the

output amplitude of the signals. In addition, the thermal expansion also affects the changes in the thickness of the panel, wave propagation and material density, which are key parameters to computing dispersion curves under different temperatures [124].

Next, the temperature has a big effect on the resin properties, the resin is more brittle under a very low temperature while the resin is softer under a higher temperature. The change of the resin will change the engineering properties of the composite laminate, which will cause a change in the shear modulus. The resin interfaces with the carbon, which is sensitive to the temperature and glass transition temperature.

Furthermore, higher residual strains remain existing from the curing process inside the laminate when manufacturing composite laminate. Temperature can affect the residual strains. The efficiencies of the engineering properties could be the residual strains built in the laminate. All of this could be affecting the temperature. Therefore, it is very important to define the relationship between the phase and the velocity change for composite panels, depending on their thickness, so that the compensation algorithm can be applied and damage detection can be carried out under different temperatures reliably.

5.5. Surface-mounted Artificial Damage

To demonstrate the difference between the guided wave interaction with a through thickness damage (i.e. interlaminar delamination due to an impact event) and surface damage (i.e. debonding between two structures), the impact damage and the artificial damage is introduced to the plates of different thickness. The surface-mounted artificial damage (weighted blue-tack) is used in the first instance to simulate the surface damage (in this case it is increased mass) which is also reversible before the plates are impacted to cause the barely visible impact damage. For both cases, the full field response of the two main guided wave modes interacting with the damage is also recorded with LDV, prior to PZTs.

5.5.1. LDV Measurements

To study the thickness effects on damage identification for the surface-mounted artificial damage, LDV measurements were conducted. The relative position between the PZT actuator and the blue-tack is shown in Figure 5.14. The LDV setup was the same as the one for computing the group velocity in section 5.3.1. For the 2 mm panel, 7569 scanning grids (87× 87) were created with a scanning area of 66 mm × 66 mm, the grid spacing was about 0.76 mm. For the 4 mm panel, a total of 7569 grids (87× 87) were scanned, the scanning area was about 65 mm × 65 mm and the grid spacing was about 0.75 mm. For the 9 mm panel, 6889 scanning grids (83× 83) were scanned, the scanning area was about 62 mm × 62 mm and the grid spacing was about 0.75 mm.

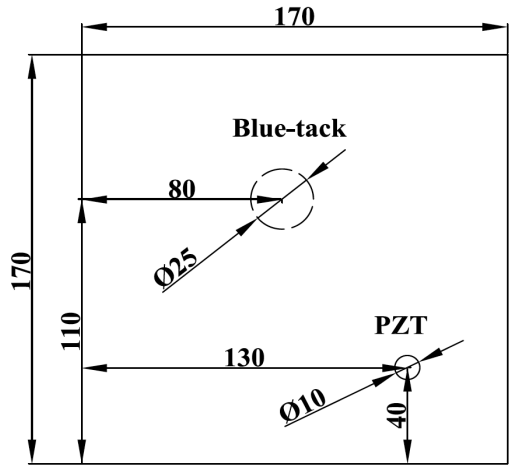

Figure 5.14. The relative position between the PZT actuator and the blue-tack.

After postprocessing, these chirp signals were reconstructed to five-cycle Hanning-windowed toneburst signals at 50 kHz and 250 kHz. The experimental LDV measurement results (z-direction) are shown in Figure 5.15. As can be seen in Figure 5.15, only the A_0 mode (50 kHz) interacted with the surface-mounted artificial damage for the thickness of 2 mm, 4 mm and 9 mm panels and it is concluded as the more appropriate mode for the surface damage interaction. To validate this conclusion, the UGW response with PZT transducers is used for damage detection next.

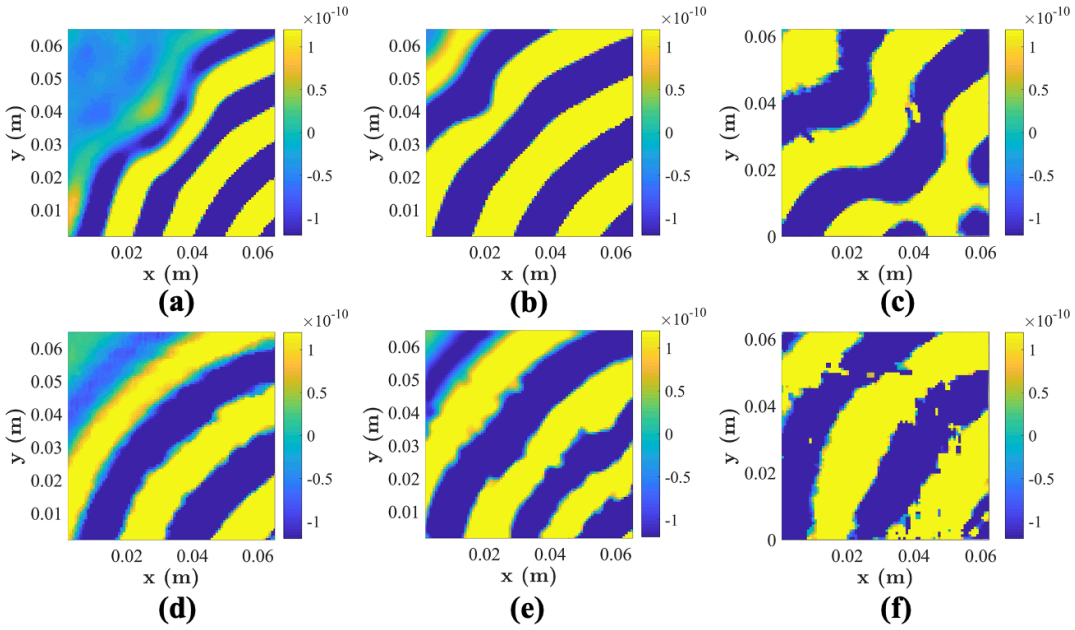

Figure 5.15. UGW interaction with the surface-mounted artificial damage at 50 kHz for the thickness of **(a)** 2 mm, **(b)** 4 mm and **(c)** 9 mm panels and at 250 kHz for the thickness of **(d)** 2 mm, **(e)** 4 mm and **(f)** 9 mm panels.

5.5.2. Damage Detection and Localization

In this section, the damage index (DI) correlation coefficient was used to evaluate damage severities of the structure by comparing the difference between the baseline signals and the current signals. The delay-and-sum (DAS) algorithm was used to locate the damage position.

In these experiments, a weighted blue-tack was closely attached on the surface of the composite panel to simulate the type of surface-attached damage. To verify the thickness effects on damage detection and localization for PZT transducers, the blue-tack was attached on the composite surface on the opposite side (off-centre) of PZT transducers for each panel respectively, and the schematic of the surface-mounted artificial damage (a weighted blue-tack) can be seen in Figure 5.16.

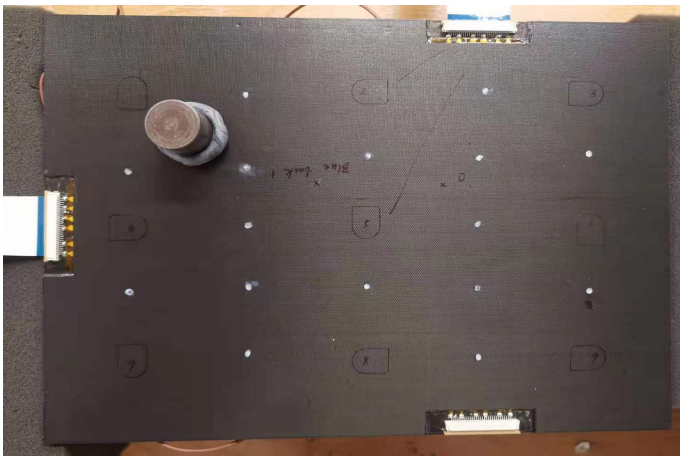

Figure 5.16. Schematic of the surface-mounted artificial damage attached on the surface of the 2 mm panel.

Figure 5.17 to Figure 5.22 plot results of damage detections and localizations at 50 kHz and 250 kHz when the damage was closely attached on the opposite side of PZT transducers. As can be seen in these figures, the surface-mounted artificial damage (added mass) can be detected by the DI for the thickness of 2 mm 4 mm and 9 mm panels. Meanwhile, the DI results show that the A_0 mode has better detection of the surface type of damage (blue-tack) for the 2 mm and 4 mm panels. Therefore, the accuracy of the DI results may be affected when increasing the thickness to 9 mm.

In addition, the DAS algorithm shows this type of damage can be located accurately except for the S_0 mode in the 9 mm panel at 250 kHz. These can be related to the analytical results of the dispersion curve shown in Figure 9.1 to Figure 9.3. The group velocities of the A_0 and the S_0 modes are getting closer which may affect the results of damage localization.

However, when the surface-mounted artificial damage was attached on the same side of PZT transducers, the damage can be located accurately at 250 kHz for the 9 mm panel (shown in Figure 9.9b in the appendix in section 9.2). This may be because the S_0 mode is less sensitive for the thick composites that the accuracy of the DAS algorithm is affected.

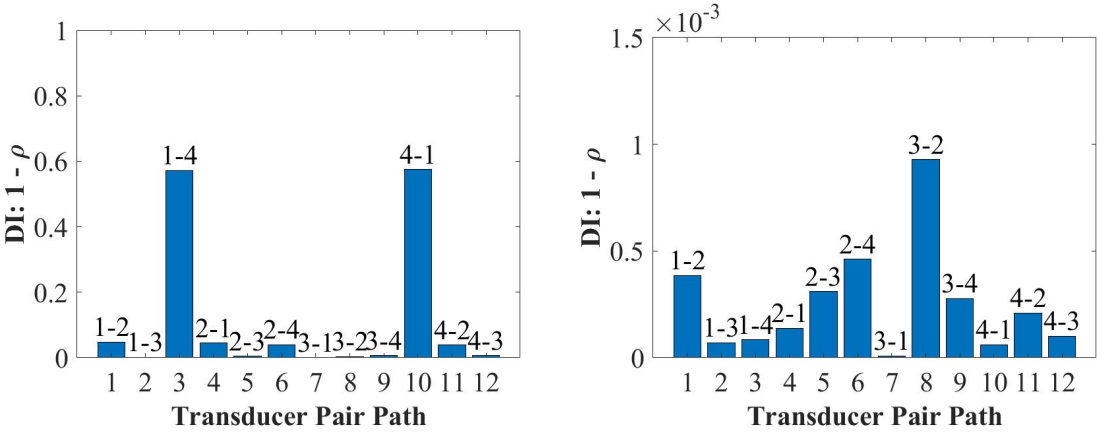

(a) **(b)**

Figure 5.17. Damage detection for the 2 mm panel at **(a)** 50 kHz and **(b)** 250 kHz.

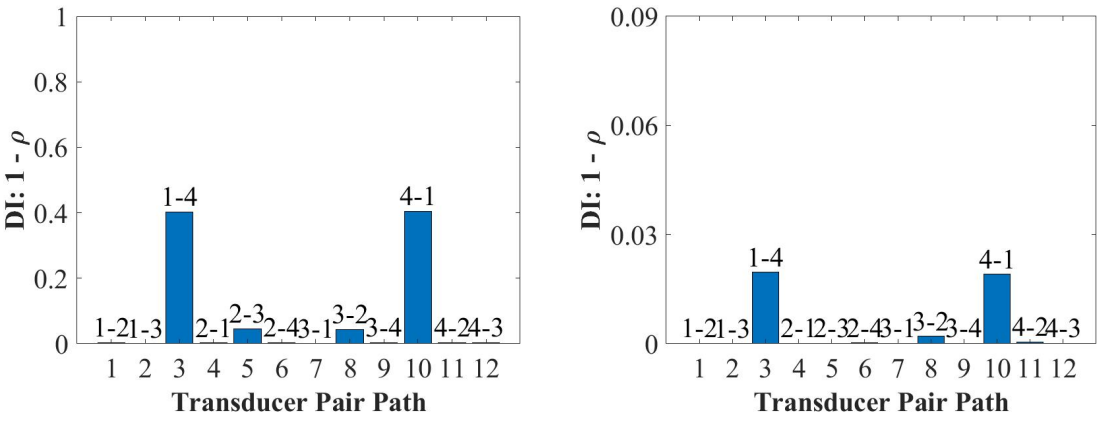

(a) **(b)**

Figure 5.18. Damage detection for the 4 mm panel at **(a)** 50 kHz and **(b**) 250 kHz.

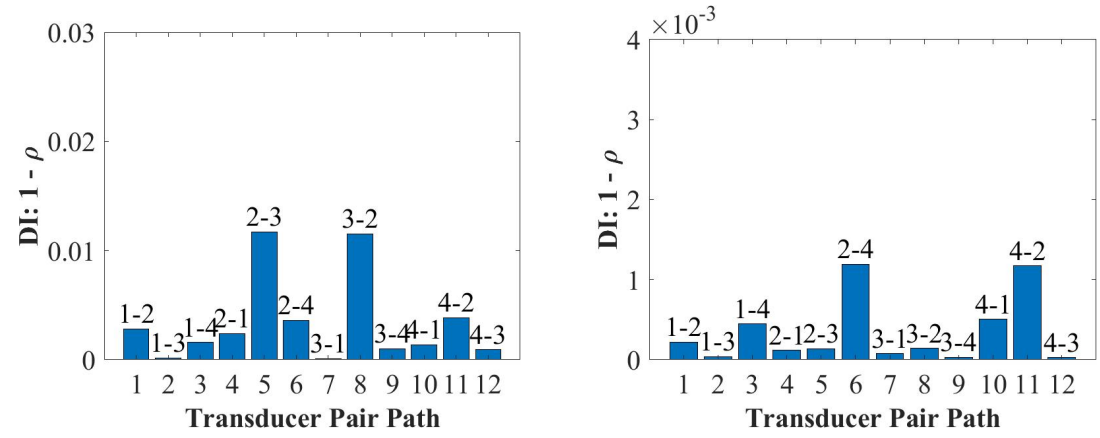

(a) **(b)**

Figure 5.19. Damage detection for the 9 mm panel at **(a)** 50 kHz and **(b)** 250 kHz.

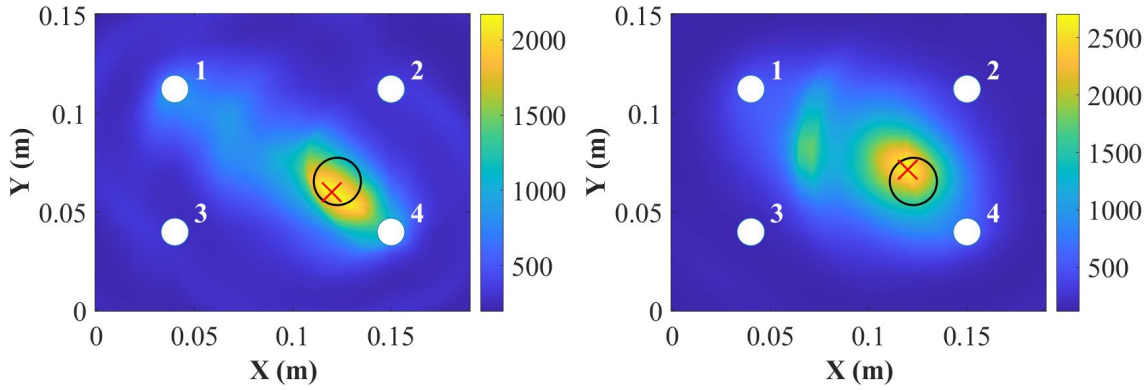

(a) **(b)**

Figure 5.20. Damage localization for the 2 mm panel at **(a)** 50 kHz and **(b)** 250 kHz (where the "○" is the position for real damage and the "×" is the position for predicted damage).

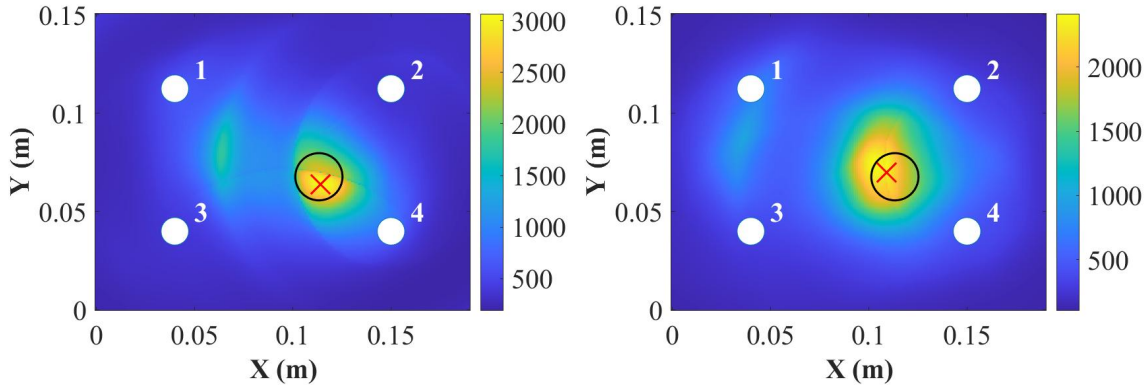

(a) **(b)**

Figure 5.21. Damage localization for the 4 mm panel at **(a)** 50 kHz and **(b)** 250 kHz (where the "○" is the position for real damage and the "×" is the position for predicted damage).

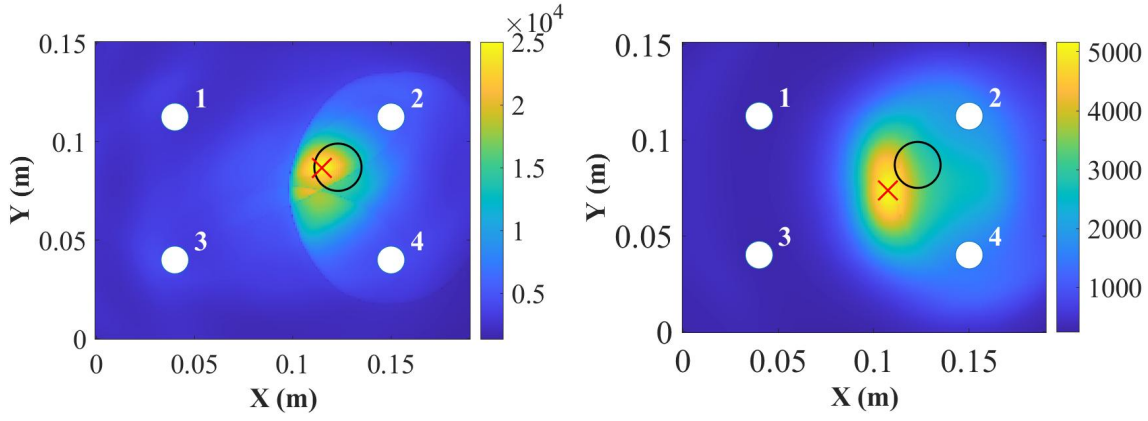

(a) **(b)**

Figure 5.22. Damage localization for the 9 mm panel at **(a)** 50 kHz and **(b)** 250 kHz (where the "○" is the position for real damage and the "×" is the position for predicted damage).

Although LDV results demonstrated the superiority of the A_0 mode can interact with the surface damages, the results of the damage localization with PZT recorded sensors shows that both 50 kHz and 250 kHz results are of good accuracy. This is due to the high signal to noise ratio of the dynamical structure (plate + sensor) at 250 kHz as demonstrated in Figure 5.11. Next, the panels were impacted to cause damage and investigate the appropriateness of the different modes for detection.

5.6. Impact Damage

5.6.1. Impact Test

To study the real impact damage, impact tests were conducted on the above 2 mm, 4 mm and 9 mm panels. The barely visible impact damage (BVID) was considered in these tests. A drop tower INSTRON CEAST 9350 was used for these impact tests, as is shown in Figure 5.23. The impact position for each panel was on the opposite side of PZT transducers and was the same as one of the positions for the surface-mounted artificial damage in section 5.5.2. The impact energy started from a low level and then increased step by step until a suitable damage area can be detected by a DolphiCam C-scan (CF08). For the 2 mm panel, the hemisphere diameter of the impactor was 20 mm, and the 22 kN load cell with 3 kg additional mass was used. The impact energy was 15 J and the impact velocity was 3.53 m/s. For the 4 mm and 9 mm panels, the hemisphere diameter of the impactor was 20 mm, and the 90 kN load cell with 3 kg additional mass was used. The impact energy was 20 J with an impact velocity of 2.72 m/s for the 4 mm panel, and 57 J with an impact velocity of 4.59 m/s for the 9 mm panel. After the impact, the surface cracks can be visible on these panels.

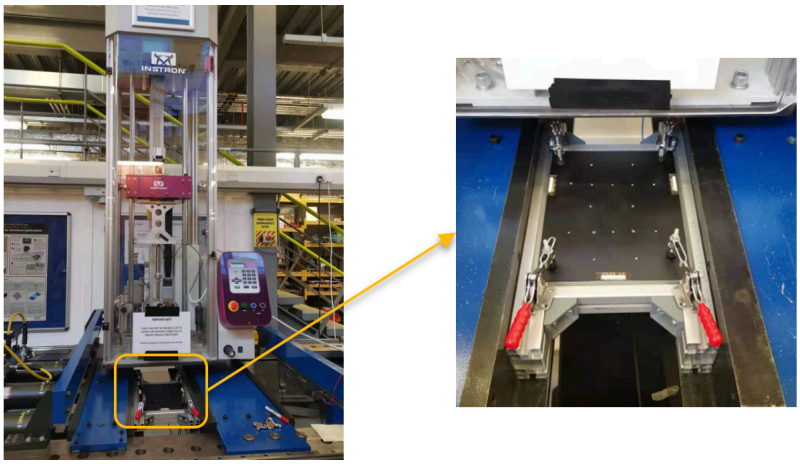

Figure 5.23. INSTRON CEAST 9350 drop tower for the impact test.

Figure 5.24 shows C-scan results for the impact damage of each panel. In Figure 5.24a, the detected damage area is about 176 m^2, and the delamination happens from the 9th ply to the top surface according to the B-scan horizontal and vertical for the 2 mm panel. In Figure 5.24b, the detected damage area is about 452 mm^2 for the 4 mm panel, and the damage is from the 24th layer to the top surface according to the B-scan horizontal and vertical. As is shown in Figure 5.24c, the detected damage area is about 254 mm^2 for the 9 mm panel, and the delamination happens from the 8th layer to the top surface according to the B-scan horizontal and vertical.

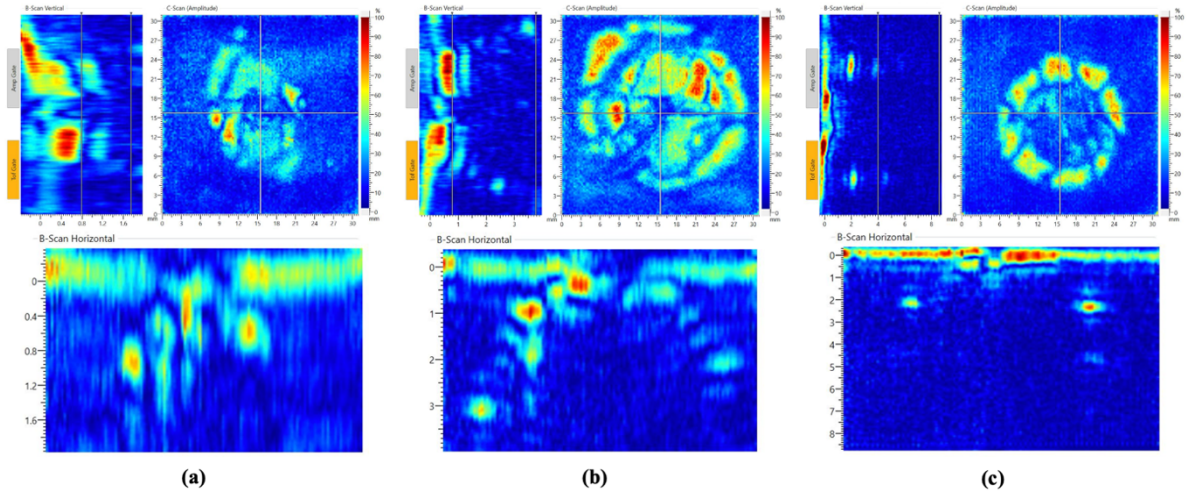

Figure 5.24. The C-scan results of the impact damage at **(a)** 15 J for the 2 mm panel, **(b)** 20 J for the 4 mm panel, and **(c)** 57 J for the 9 mm panel

5.6.2. LDV Measurements

LDV measurements were also conducted to compare with the surface-mounted artificial damage. For the 2 mm panel, 8649 scanning grids (93×93) were created and the scanning area was about 67.5 mm × 67.5 mm with a grid spacing of 0.73 mm. For the 4 mm panel, 8649 scanning grids (93×93) were created and the scanning area was about 64.3 mm × 64.3 mm, and the grid spacing was about 0.69 mm. For the 9 mm panel, 8649 scanning grids (93×93) were created and the scanning area was about 64 mm × 64 mm, and the grid spacing was about 0.69 mm.

Figure 5.25 shows the experimental results in the z-direction at 50 kHz and 250 kHz respectively. Both the A_0 mode (50 kHz) and the S_0 mode (250 kHz) show significant disturbance (reflection and refraction) with the impact damage (surface cracks and internal delamination) for the thickness of 2 mm, 4 mm and 9 mm panels.

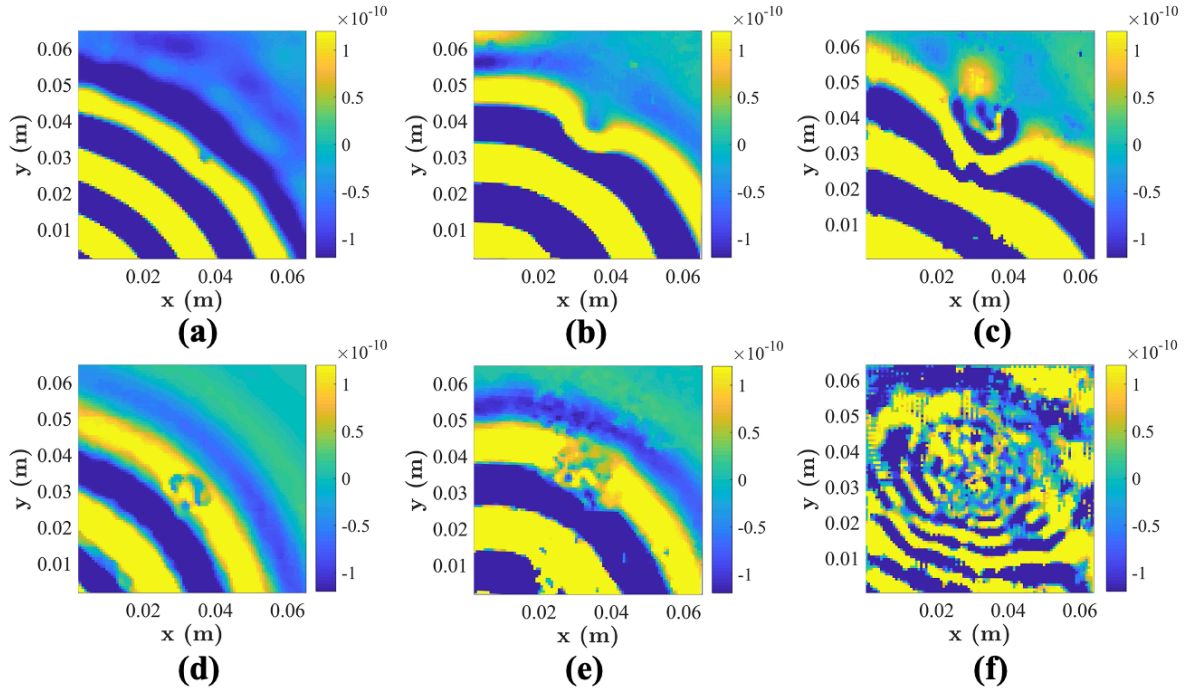

Figure 5.25. UGW interaction with the impact damage at 50 kHz for the thickness of **(a)** 2 mm, **(b)** 4 mm and **(c)** 9 mm panels and at 250 kHz for the thickness of **(d)** 2 mm, **(e)** 4 mm and **(f)** 9 mm panels.

5.6.3. Damage Detection and Localization

In this section, the impact damage on the thickness of 2 mm, 4 mm and 9 mm panels was detected by the correlation coefficient and located by the DAS algorithm. Figure 5.26 to Figure 5.31 plot results for damage detection and localization at 50 kHz and 250 kHz. The damage index can detect the impact damage, but the DAS algorithm cannot locate the impact damage accurately.

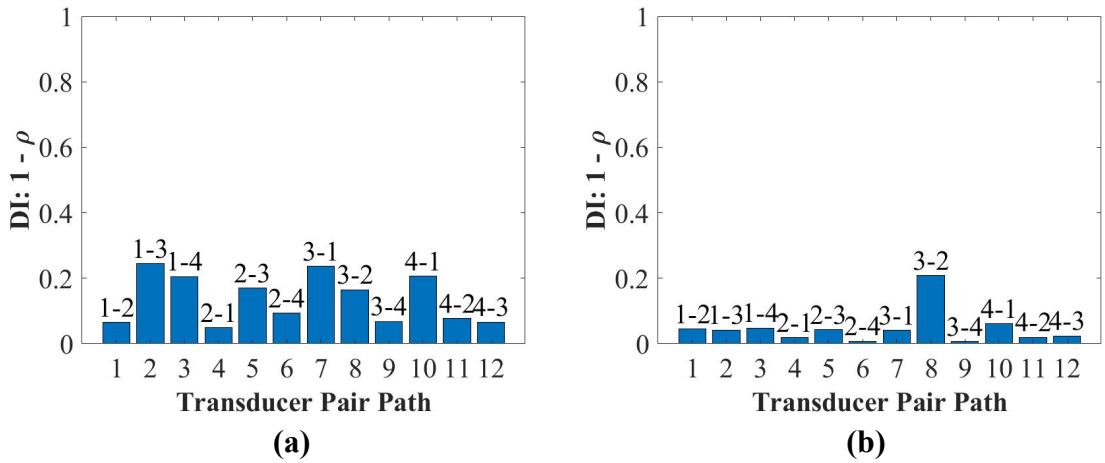

Figure 5.26. Damage detection for the 2 mm panel at **(a)** 50 kHz and **(b)** 250 kHz.

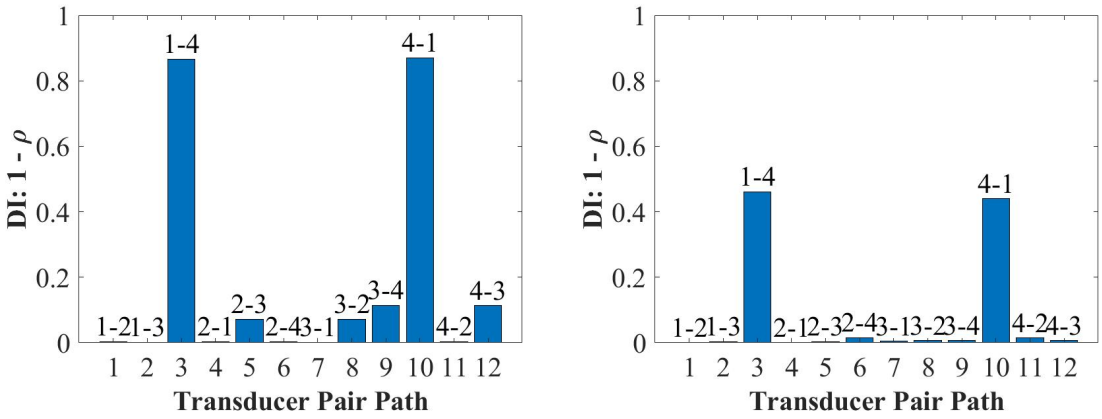

(a) **(b)**

Figure 5.27. Damage detection for the 4 mm panel at **(a)** 50 kHz and **(b)** 250 kHz.

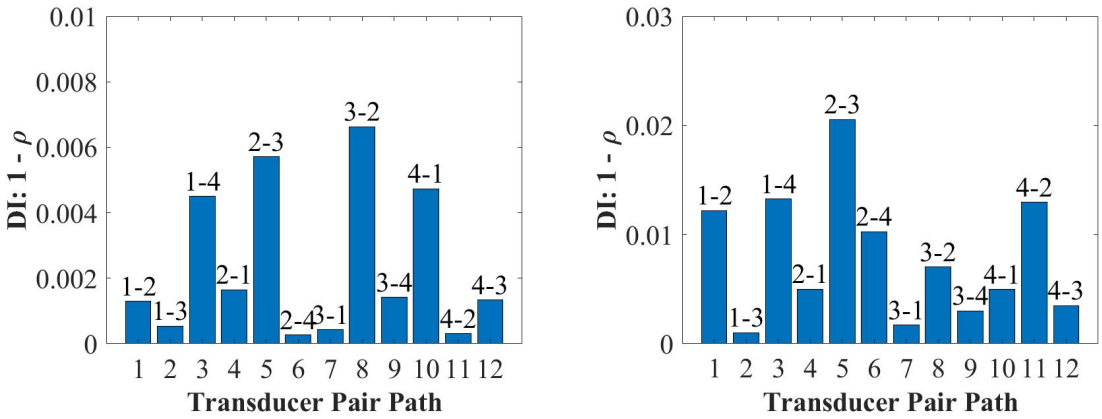

(a) **(b)**

Figure 5.28. Damage detection for the 9 mm panel at **(a)** 50 kHz and **(b)** 250 kHz.

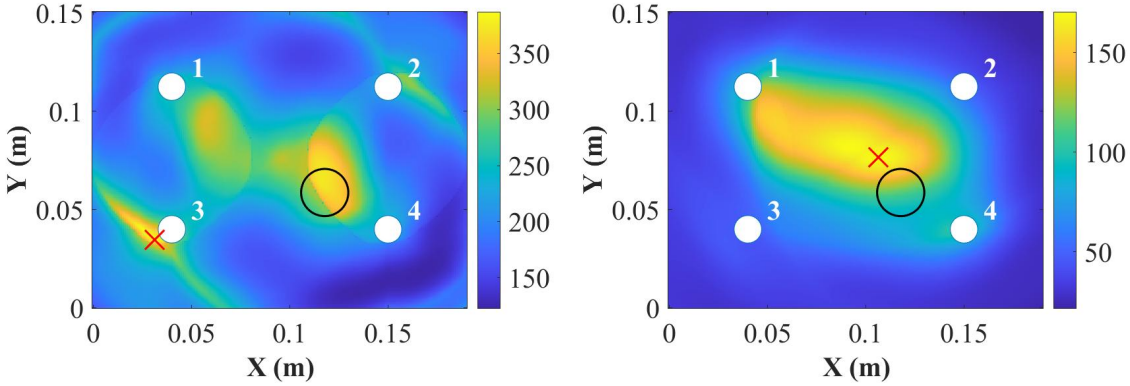

(a) **(b)**

Figure 5.29. Damage localization for the 2 mm panel at **(a)** 50 kHz and **(b)** 250 kHz (where the "○" is the position for real damage and the "×" is the position for predicted damage).

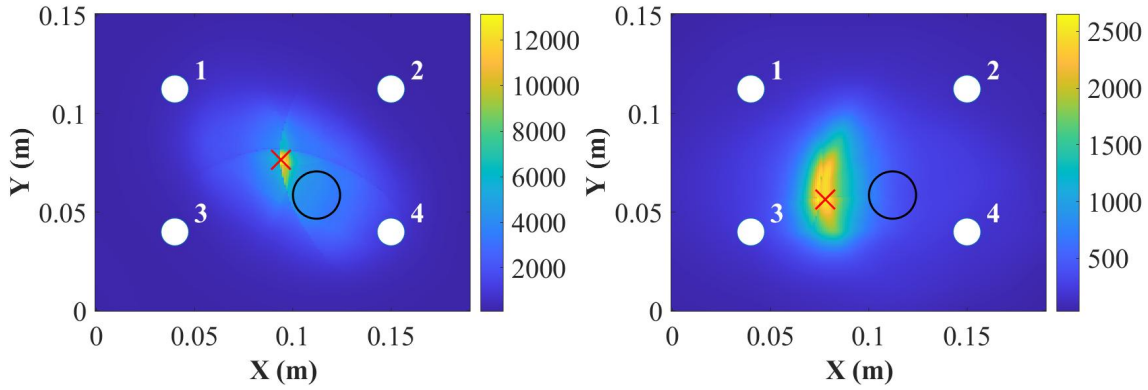

Figure 5.30. Damage localization for the 4 mm panel at **(a)** 50 kHz and **(b)** 250 kHz (where the "○" is the position for real damage and the "×" is the position for predicted damage).

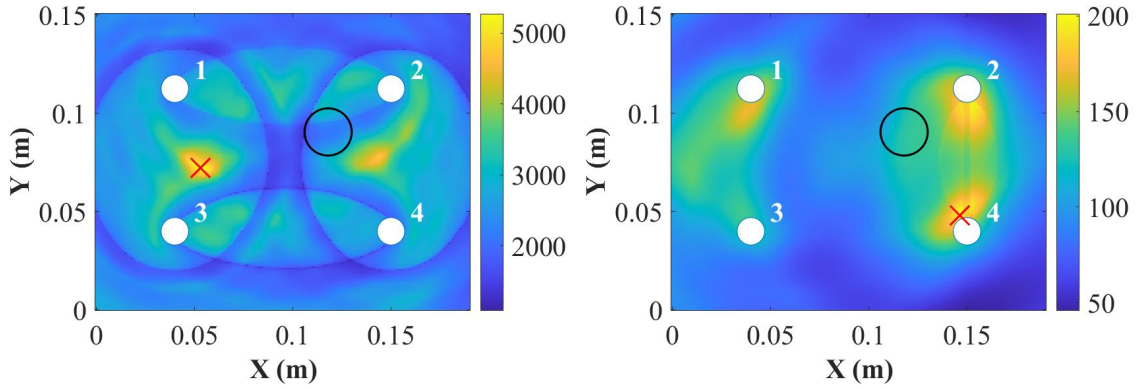

Figure 5.31. Damage localization for the 9 mm panel at **(a)** 50 kHz and **(b)** 250 kHz (where the "○" is the position for real damage and the "×" is the position for predicted damage).

The results demonstrate that the 250 kHz better results for detection and localization for the 2 mm and the 4 mm panels which also matches the observation previously reported for the higher amplitude of the S_0 mode and hence higher reliability in damage detection. For the 9 mm panel, neither of the frequencies shows robust and reliable results in detection and localization which is attributed to the small severity of the damage as shown in Figure 5.24c. The extent of damage can be hardly noticed in the C-scan through the thickness, therefore the damage reflected waves are of small amplitude and fall mainly within the noise level (very small DI values).

The difference between LDV measurements and the DAS algorithm based on point sensing is that LDV shows a full field analysis with complete wave interaction with the damage, whereas the points sensing method only records the response of one point (PZT location). Therefore, capturing the damage reflection in that path based on point sensing is a lot more challenging than a full field analysis (LDV). Furthermore, the direction and the intensity of the

reflection are not uniform in the LDV results, so the minute changes picked up by the sensors have to be relied on. In addition, LDV records the strain in the plate and not at the sensor. The effect of the sensor and the bonding is not considered which can reduce the amplitude.

Therefore, the damage should be extended for reliable detection. Another important factor is that for the delay-and-sum results usually guided waves are chosen in their non-dispersive zone. As can be seen from Figure 9.1b to Figure 9.3b, the thickness affects the group velocity of the S_0 mode at 250 kHz a lot. In addition, 250 kHz for the 9 mm plate is dispersive, which will cause the S_0 and the A_0 modes to interact with each other. Therefore, the localization results will not be accurate as is also noticed here.

5.7. Summary

In this chapter, the influence of composite thickness on guided wave propagation under varying temperatures and resulting damage detection were studied. It has been found that the amplitude of the A_0 mode is influenced more than that of the S_0 mode by the thickness variation because the A_0 mode (out-of-plane motion) needs more energy for the particles to move in the thicker composite laminates than the S_0 mode (in-plane motion). In addition, the group velocity of the A_0 mode increases with the increased thickness, while the group velocity of the S_0 mode for the 9 mm panel is faster than that of the 4 mm panel and slower than that of the 2 mm panel. This was later attributed to the dispersive nature of the S_0 mode at the frequency thickness product of 250 kHz and the 9 mm plate.

Overall, the amplitude of the A_0 mode is not dependent on the thickness that it reduces with the increase of the temperature for all panels, while that of the S_0 mode has different trends for panels of different thicknesses. In addition, the group velocities become slow for both the A_0 and the S_0 modes for all those panels with the increase of the temperature, which are not dependent on thickness. Therefore, it is very important to define the relationship between the phase and the velocity change for composite panels, depending on their thickness, so that the compensation algorithm can be applied and damage detection can be carried out under different temperatures reliably.

The LDV measurement results showed only the A_0 mode (50 kHz) interacted with the simulated damage for the thickness of 2 mm, 4 mm and 9 mm panels and it was concluded as the more appropriate mode for the surface damage detection. The DI results showed that the A_0 mode has better detection of the surface simulated damage (added mass) for the 2 mm and 4 mm panels and the DAS algorithm showed this type of damage could be located accurately excepted for the S_0 mode in 9 mm panel at 250 kHz. As it had been demonstrated in the appendix in section 9.2 the damage could be located accurately at 250 kHz for the 9 mm panel when the surface-mounted artificial damage was attached on the same side of PZT transducers. Hence, the S_0 mode became less sensitive when the thickness of the composite panel increased. Although the LDV results demonstrated the superiority of the A_0 mode for detecting surface damages, the results of the damage localization with the PZT recorded sensors showed that

both 50 kHz and 250 kHz results were of good accuracy. This was due to the high signal to noise ratio at 250 kHz due to the dynamical structure (plate + sensor).

Then the guided wave propagation and response with PZTs for the detection of impact damage were studied. The LDV results showed that both the A_0 (50 kHz) and the S_0 (250 kHz) modes had significant disturbance (reflection and refraction) with the impact damage (surface cracks and internal delamination) for the thickness of 2 mm, 4 mm and 9 mm panels. The damage index results showed the S_0 mode had better results for detection and localization for the 2 mm and the 4 mm panels which matched with the conclusion from the EMI results and hence higher reliability in damage detection. For the 9 mm panel, neither of the frequencies showed robust and reliable results in detection and localization which was attributed to the small severity of the damage in the C-scan result (hardly noticed through thickness). Therefore, the damage reflected waves were of small amplitude and falls mainly within the noise level and the damage should be extended for reliable detection. Another important factor was that for the delay-and-sum results usually guided waves are chosen in their non-dispersive zone, but the dispersion curve results for the 9 mm panel at 250 kHz showed that the group velocities for the A_0 and the S_0 modes were too close to be distinguished from each other and the localization results would not be accurate.

Chapter 6

6. Thickness Effects on UGW using Embedded Layers

6.1. Introduction

Embedded PZT transducers are highly desired for SHM when considering the composite repair patch [10]. In addition, they can also increase the capabilities of damage detection, and possess excellent stability, durability and repeatability since embedded PZT transducers are isolated from the exposed environmental conditions which extend their ageing [10, 32]. This chapter presents an investigation into the effect of composite thickness on the effectiveness of UGW damage detection under varying temperatures by embedded PZT transducers.

There are many applications to embed PZT transducers into composite laminates for SHM purposes. Dziendzikowski M. *et al*. [10] compared the A_0 mode of UGW at 100 kHz actuated by surface-mounted and embedded PZT transducers for glass fibre reinforced plastic (GFRP) composites. The electro-mechanical impedance (EMI) properties were also compared. The EMI results showed that the embedded EMI coupling factor was 50% higher than the surface-mounted coupling factor in GFRP composites. It was found that embedded PZT transducers can have a better signal to noise ratio (SNR), which manifests a better detection capability of the barely visible impact damage (BVID). Furthermore, the damage localization algorithm RAPID was also used to locate the BVID for different impact energies.

Andreades C. *et al*. [142] proposed a novel embedding technique that uses woven E-glass fibre fabric to cover the top of embedded PZT transducers for electrical insulation. They found that the artificial delamination and the BVID can be detected by both second harmonic generation and nonlinear modulation of ultrasonic spectrum using laser Doppler vibrometer (LDV). Their results revealed that the novel embedding technique can be used for real-time ultrasonic inspection of carbon fibre reinforced plastic (CFRP) composites. Dziendzikowski M. *et al*. [143] also investigated the detection and the classification of the surface-mounted artificial damage and the BVID for GFRP composites with embedded PZT transducers. The results showed the detection rate was above 90% and the acceptable ratio of false-positive indications was below 3% which was acceptable for the SHM system in early-stage development. In addition, they also proposed a novel Bayesian approach for damage classification. According to the results, the damage detection rate for the Bayesian approach was above 93% and the false rate was below 3%.

Cenek S. *et al*. [144] used the WEMAT approach to detect low energy impact damage measured by PZT transducers mounted on the surface or embedded into different positions of CFRP composites. Although all PZT transducers can detect the impact damage, the sensitivity

was getting better when the transducers were closer to the surface. Her S. *et al*. [145] analytically proposed an approach to investigate the deformation of the composite laminated actuated by surface-mounted and embedded PZT transducers and the influence of the embedded depth on PZT transducers. They demonstrated that the deflection of composites reduced with the increase of the embedded depth of PZT transducers. Furthermore, the deformation actuated by surface-mounted PZT transducers was bigger than that of embedded PZT transducers. A close match between those analytical and numerical results, so this analytical approach can be used to predict the composite deformation actuated by PZT transducers.

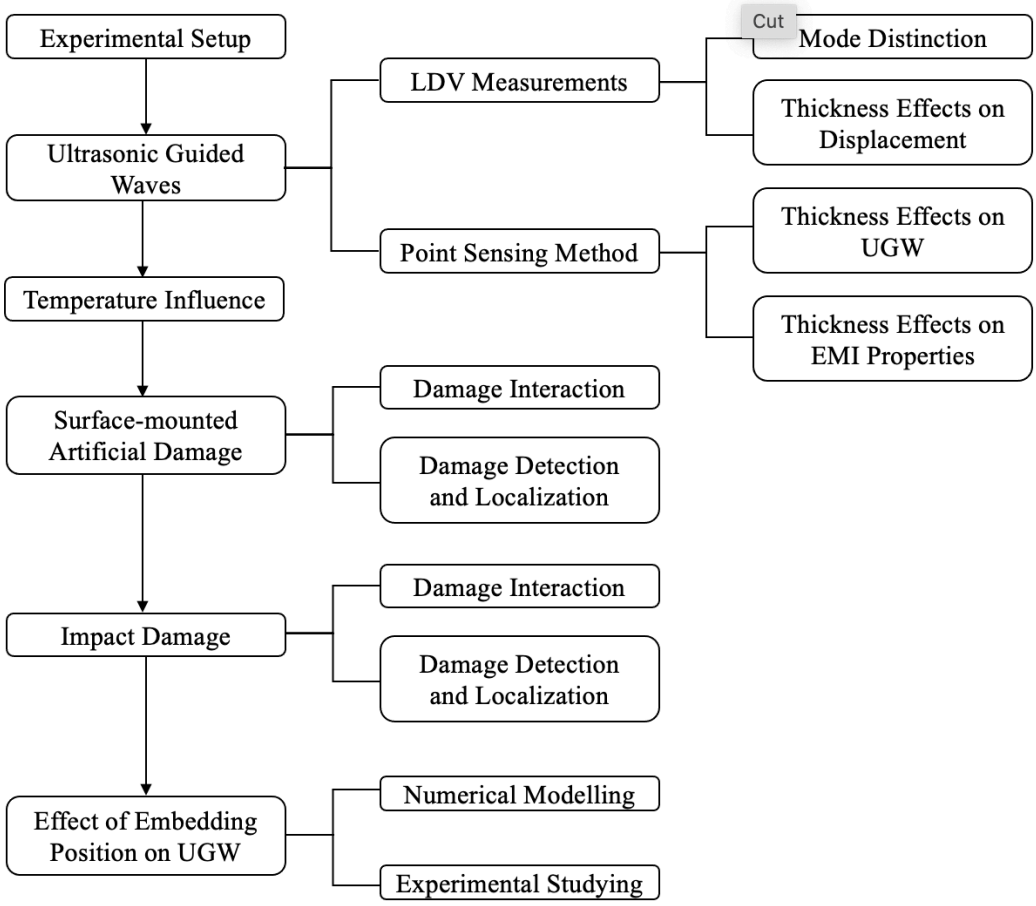

Figure 6.1. Schematic of the flow chart for all investigations of chapter 6.

In this chapter, wave propagation in thick composite laminates (9 mm) will be compared to thin laminates (2 mm and 4 mm) to investigate how the thickness can affect the propagation properties and hence affect the reliability of the damage identification by embedded PZT transducers. Figure 6.1 shows the flow chart to illustrate all investigations of chapter 6. First, laser Doppler vibrometer (LDV) measurements and the active sensing method were used to study guided wave propagation through the thickness of 2 mm, 4 mm and 9 mm panels to compare the amplitude and the group velocities of the S_0 and the A_0 modes. Next, temperature

influence on embedded wave propagation for changes in amplitudes and phase shifts through different thicknesses of composite laminates will be evaluated. Furthermore, embedded wave propagation for damage identification will be experimentally studied to identify the surface-mounted artificial damage and the impact damage for different composite laminates by LDV measurements. Then the damage index (DI) correlation coefficient and the delay-and-sum (DAS) algorithm will be used to detect and locate these types of damages respectively. Finally, the influence of different embedded positions of PZT transducers on UGW is also numerically and experimentally studied. The reversibility of the peak amplitude of the first wave packet of UGW actuated/received by PZT transducers in different positions is compared.

6.2. Experimental Setup

Three composite specimens were fabricated in the experiment to compare thickness effects on guided wave propagation in composites actuated by embedded PZT transducers. The prepregs, stacking sequences, specimens' sizes and thicknesses for the fabrication are the same as reported in section 5.2. The general drawing of the specimen with positions of embedded PZT transducers is shown in Figure 6.2a, and the schematic of diagnostic layers with PZT transducers during the embedding is shown in Figure 6.2b.

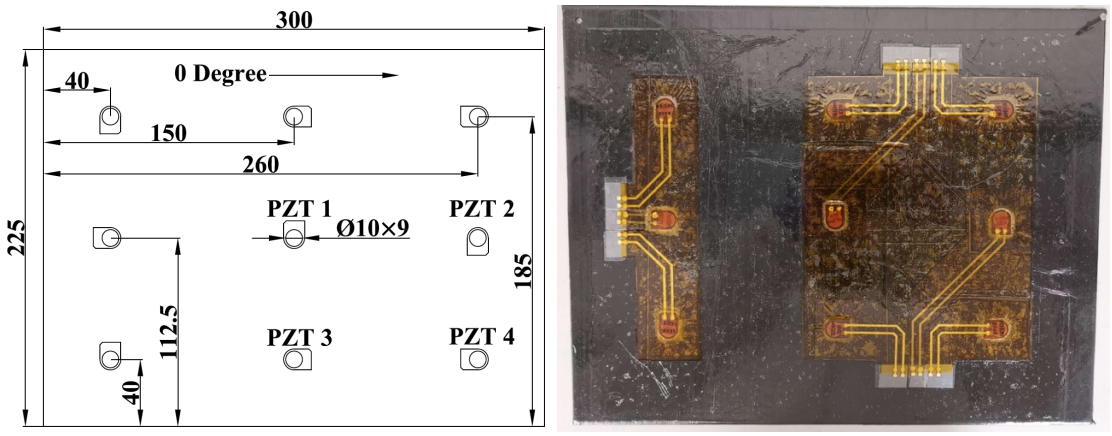

Figure 6.2. **(a)** General drawing of specimens; **(b)** Schematic of embedded PZT transducers during the lay-up.

The diagnostic layers with printed circuits shown in Figure 6.2b were prepared in advance of the embedding. The manufacturing details including the preparation of the printed diagnostic layer, sensor installation and composite fabrication are as reported in section 3.3. Figure 6.3 shows one of the examples of the composite panel with embedded PZT transducers after trimming for the 2 mm panel.

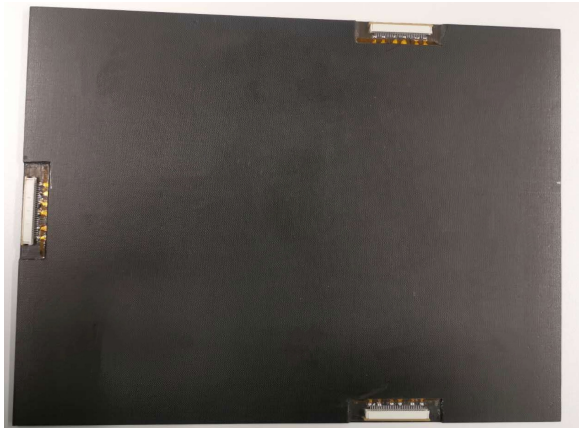

Figure 6.3. Schematic of the panel with embedded PZT transducers after trimming

6.3. Ultrasonic Guided Waves (UGW)

In this section, guided wave propagation actuated by embedded PZT transducers in thicknesses of 2 mm, 4 mm and 9 mm panels are studied using LDV. The LDV setup can be referred to in section 5.3.1. For postprocessing, five-cycle Hanning-windowed toneburst signals at 50 kHz and 250 kHz reconstructed by the chirp signal were used for analysis.

6.3.1. Mode Distinction

To distinguish guided wave modes (the S_0 and the A_0 modes) of the first wave packets of measured signals actuated by embedded PZT transducers for the thickness of 2 mm, 4 mm and 9 mm panels at 50 kHz and 250 kHz, 2-D wave propagations in the x-y direction (averaging the x- and the y- directions) and the z-direction were plotted. Figure 6.4 and Figure 6.5 show examples of the wave propagation in the x-y and the z- directions for the 2 mm panel at 50 kHz and 250 kHz, respectively. It is evident that the S_0 mode is the dominant mode at both 50 kHz and 250 kHz in the x-y direction, while the A_0 mode is the dominant mode at 50 kHz and the S_0 mode is the dominant mode at 250 kHz in the z-direction.

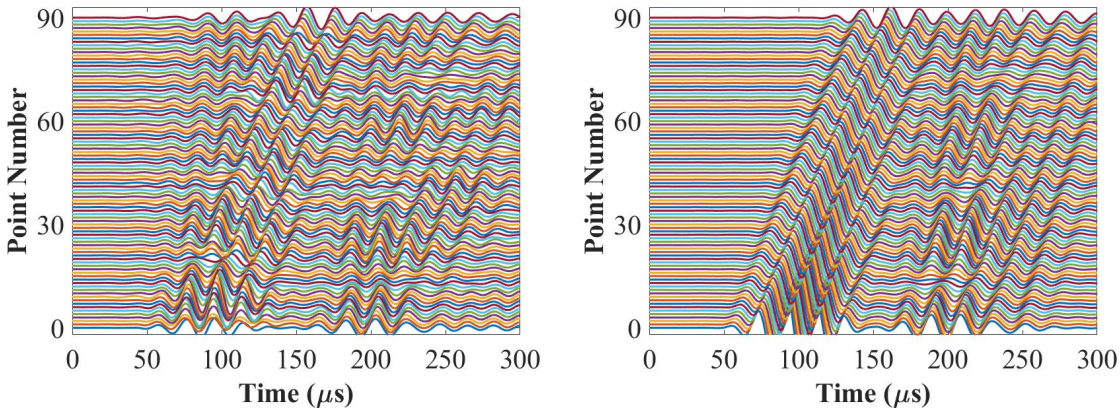

Figure 6.4. Wave propagation in **(a)** the x-y and **(b)** the z-directions for the 2 mm panel at 50 kHz.

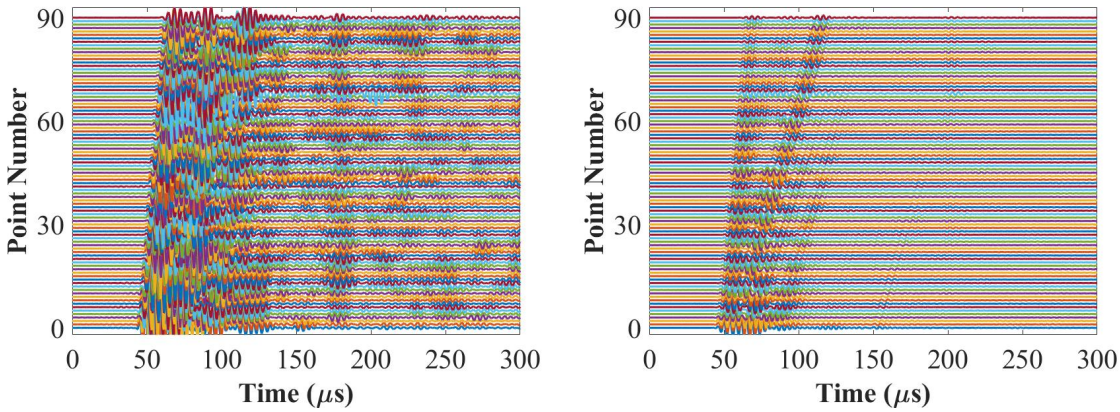

Figure 6.5. Wave propagation in **(a)** the x-y and **(b)** the z-directions for the 2 mm panel at 250 kHz.

6.3.2. Thickness Effects on Displacement

In this section, the effects of thickness on the fundamental propagation modes of displacement in the x-y direction (in-plane motion) and the z-direction (out-of-plane motion) actuated by embedded PZT transducers will be investigated separately. Figure 6.6 and Figure 6.7 plot displacement signals from the end point at 100 mm away from the centre of the PZT actuators (shown in Figure 5.3) for the in-plane and the out-of-plane motions for the thickness of 2 mm, 4 mm and 9 mm panels at 50 kHz and 250 kHz, respectively. In Figure 6.6, the amplitude of the first wave packet at 50 kHz decreases from the 2 mm panel to the 9 mm panel in the x-y (S_0 mode dominates) and the z-directions (A_0 mode dominates). In addition, the amplitudes of the A_0 mode for the out-of-plane motion are much higher than that of the S_0 mode for the in-plane motion.

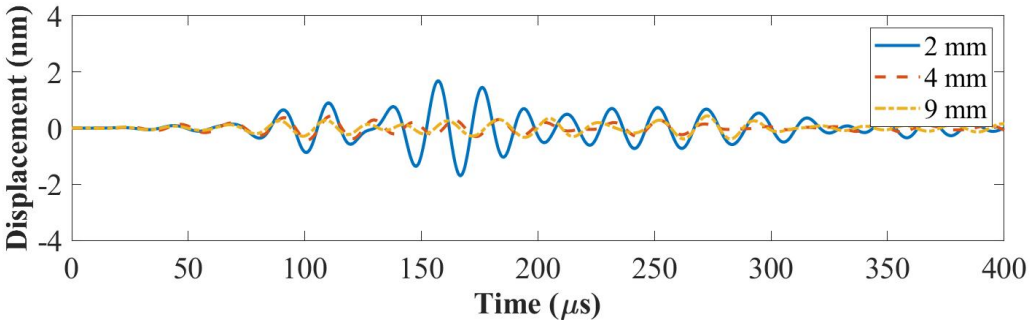

(a)

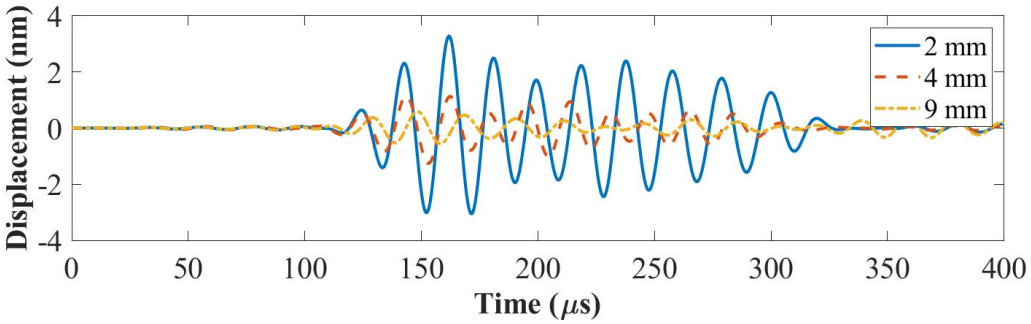

(b)

Figure 6.6. Displacement in **(a)** the x-y and **(b)** the z- directions for the thickness of 2 mm, 4 mm and 9 mm panels at 50 kHz.

In Figure 6.7, the amplitude of the first wave packet at 250 kHz for the 9 mm panel is smaller than that of the 2 mm panel but higher than that of the 4 mm panel for the in-plane motion (S_0 mode dominates), while that of the out-of-plane motion for the 2 mm panel is smaller than that of the 4 mm panel but higher than that of the 9 mm panel.

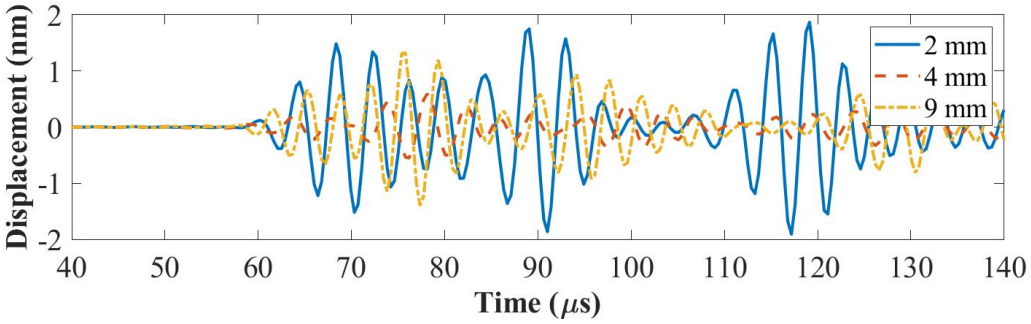

(a)

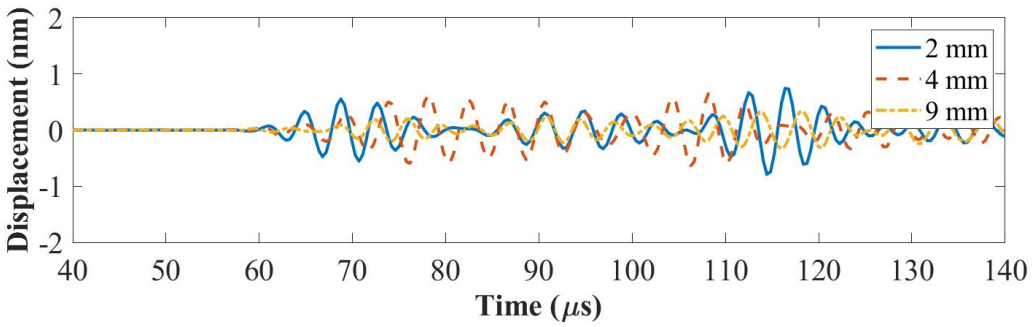

(b)

Figure 6.7. Displacement in **(a)** the x-y and **(b)** the z- directions for the thickness of 2 mm, 4 mm and 9 mm panels at 250 kHz.

Figure 6.8 plots peak amplitudes of the A_0 and the S_0 modes in the x-y and the z- directions at 50 kHz and 250 kHz, respectively. The peak amplitude of each wave mode was computed by finding the peak amplitude of the first wave packet of each measured signal. As can be seen in Figure 6.8, both amplitudes of the S_0 (in-plane motion) and the A_0 (out-of-plane motion) modes at 50 kHz are thickness dependent and the amplitude reduces with the increase of the thickness. In addition, the amplitudes of the A_0 mode (out-of-plane motion) are much higher than that of the S_0 mode (in-plane motion) at 50 kHz, while the S_0 mode for the in-plane motion is higher than of out-of-plane motion at 250 kHz except for the 4 mm panel. Therefore, the A_0 mode (out-of-plane motion) is more sensitive to the surface related damage and the S_0 mode (in-plane motion) is more sensitive to the internal related damage. By comparing the results in Figure 6.8 for the embedded PZT transducer with the results in Figure 5.7 for the surface-mounted PZT transducer, the above conclusion is suitable for both the embedded and surface-mounted PZT transducers for the LDV measurements.

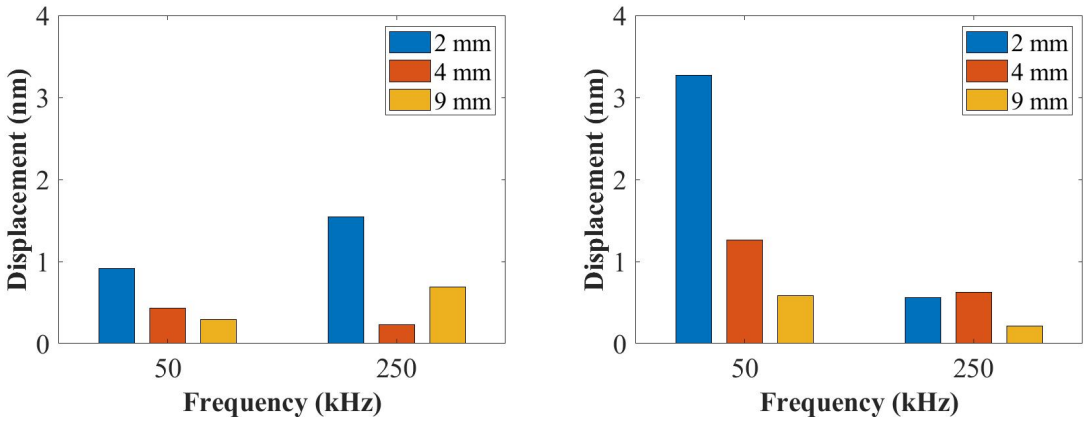

(a) **(b)**

Figure 6.8. The summary of the peak amplitude of the first wave packet in **(a)** the x-y and **(b)** the z- directions at 50 kHz and 250 kHz.

Figure 6.9 summarizes the group velocity of the S_0 mode and the A_0 mode in the x-y and the z- directions for the thickness of 2 mm, 4 mm and 9 mm panels at 50 kHz and 250 kHz, respectively. In Figure 6.9a, the group velocity for the S_0 mode (in-plane motion) increases with the increase of the thickness at 50 kHz and 250 kHz. In Figure 6.9b, the group velocities for the A_0 mode (50 kHz) and the S_0 mode (250 kHz) increase with the increased thickness.

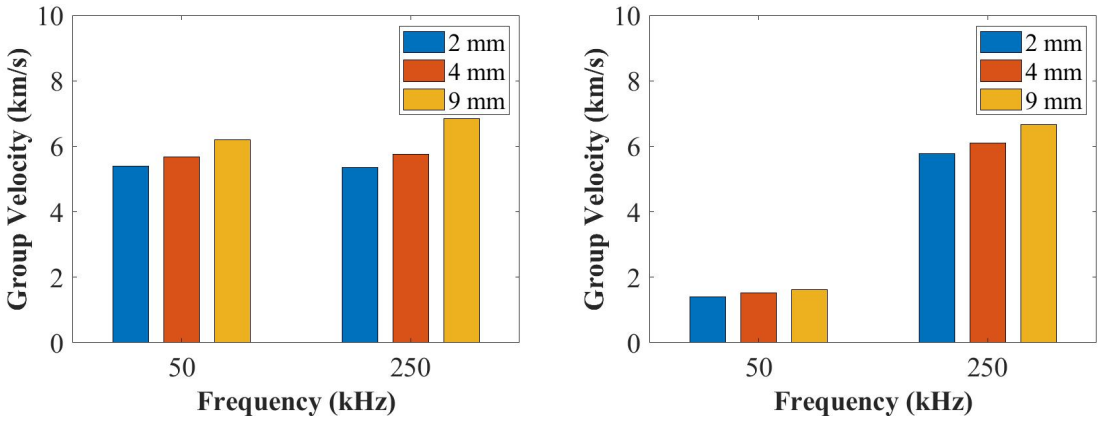

Figure 6.9. The summary of the group velocity in **(a)** the x-y and **(b)** the z- directions at 50 kHz and 250 kHz.

6.3.3. Active Sensing Comparisons

In this section, the active sensing method will be used to investigate the response of UGW (in-plane motion) and the thickness effect on UGW actuated/recorded by embedded PZT transducers. These active sensing results will be used for damage detection and characterization later for SHM application. The actuation signals were five-cycle Hanning-windowed toneburst signals with the input amplitude of 6 V at 50 kHz and 250 kHz, respectively. An embedded transducer pair path 1-2 from the plate configuration shown in Figure 6.2a was chosen for all three panels. Figure 6.10 plots the embedded signals for the thickness of 2 mm, 4 mm and 9 mm panels at 50 kHz and 250 kHz, respectively. In Figure 6.10, the amplitude of the first wave packet of the measured signal for the 2 mm panel is higher than that of the 4 mm and the 9 mm panels at 50 kHz and 250 kHz. In conclusion, the amplitudes of the A_0 (50 kHz) and the S_0 (250 kHz) modes reduce with the increased thickness.

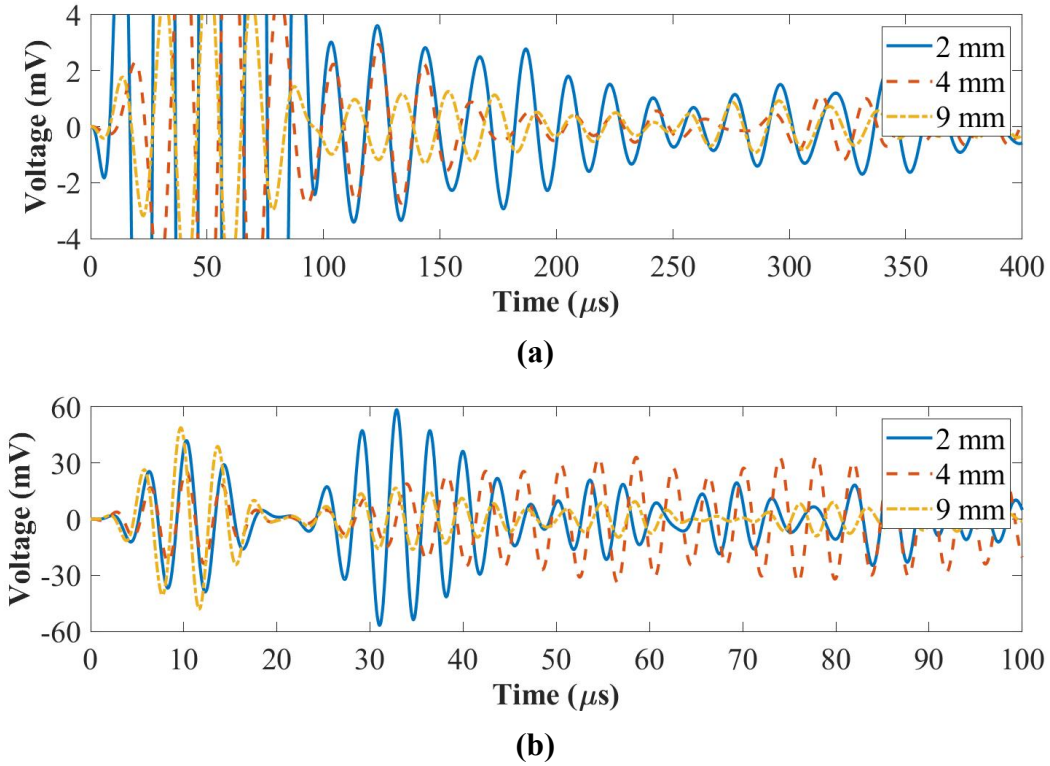

Figure 6.10. Comparisons of the embedded signals at **(a)** 50 kHz and **(b)** 250 kHz.

Figure 6.11 plots the summary of the amplitude and the group velocity for these panels at 50 kHz and 250 kHz, respectively. As can be seen in Figure 6.11a, both the amplitudes of the A_0 and the S_0 modes reduce with the increased thickness. In Figure 6.11b, the group velocity of the A_0 mode reduces with the increased thickness at 50 kHz, while the group velocity of the S_0 mode for the 9 mm panel is faster than that of the 2 mm panel but slower than that of the 4 mm panel.

In addition, by comparing those trends of sensing results (in-plane motion) in Figure 6.11 to the trends of the LDV results in Figure 6.8a and Figure 6.9a (in-plane motion), the peak amplitude reduces with the increase of the thickness although the S_0 mode dominates for the LDV results while the A_0 mode dominates for the active sensing results at 50 kHz. The amplitude trend of the S_0 mode for the LDV results at 250 kHz is also different from that of the active sensing results for the 4 mm panels. Furthermore, the group velocity of the S_0 mode at 50 kHz increases with the increased thickness for the LDV results while that of the A_0 mode for the active sensing results reduces with the increased thickness at 50 kHz. The group velocity of the S_0 mode at 250 kHz increases with the increased thickness for the LDV results while that of the active sensing results for the 4 mm panel is higher than that for the 2 mm and the 9 mm panels.

The reason why the LDV results are different from the active sensing results is that LDV can only capture the surface wave movements actuated by the embedded actuators while the active sensing method is the embedded PZT sensor recorded UGW from the embedded PZT actuator, which is a function of the local dynamics of the host structure plus the embedded

sensor. Here, the next section will investigate the electro-mechanical response of the whole structure to study the frequency response for different thickness plates.

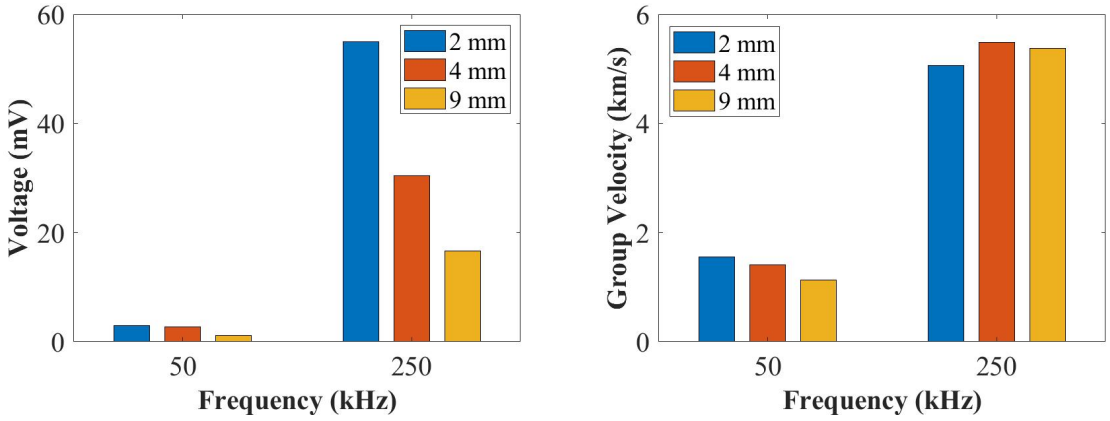

Figure 6.11. The summary of the peak amplitude of the first wave packet at **(a)** 50 kHz and **(b)** 250 kHz.

6.3.4. Electro-Mechanical Impedance Response

In this section, the electro-mechanical impedance (EMI) properties for embedded PZT transducers will be measured to investigate thickness influences on the ease of the wave mode excitation and attenuation.

Figure 6.12 compares the EMI results for the thickness of 2 mm, 4 mm and 9 mm panels. In Figure 6.12a, the slope of the lines slightly increases from the 2 mm panel to the 9 mm panel in the range of 0~250 kHz and there is no obvious difference in the imaginary part of the admittance at the range of low frequencies (below 20 kHz). Hence, the thickness has no influence on the EMI properties. The trend of linear amplitude reduction with the increased thickness at 50 kHz and 250 kHz (shown in Figure 6.11a) can be explained because of this. In Figure 6.12b, the peak amplitude response of the real part of the admittance for the 2 mm panel is slightly higher than that of the 4 mm panel at around 250 kHz, whereas that of the 9 mm panel happens at 347 kHz. This means the most suitable actuation frequency is 350 kHz for the 9 mm panel to obtain the highest amplitude response of UGW actuated by the embedded PZT transducer. However, this actuation frequency (350 kHz) for active sensing will cause more modes existing (A_1 mode) shown in Figure 9.3, which will make the measured signals more complicated that each wave mode will interact with each other due to the similar group velocities and more difficult to analyze the result for damage localization. Therefore, it has to be compromised for choosing a low-frequency range instead of choosing the frequency at resonance value.

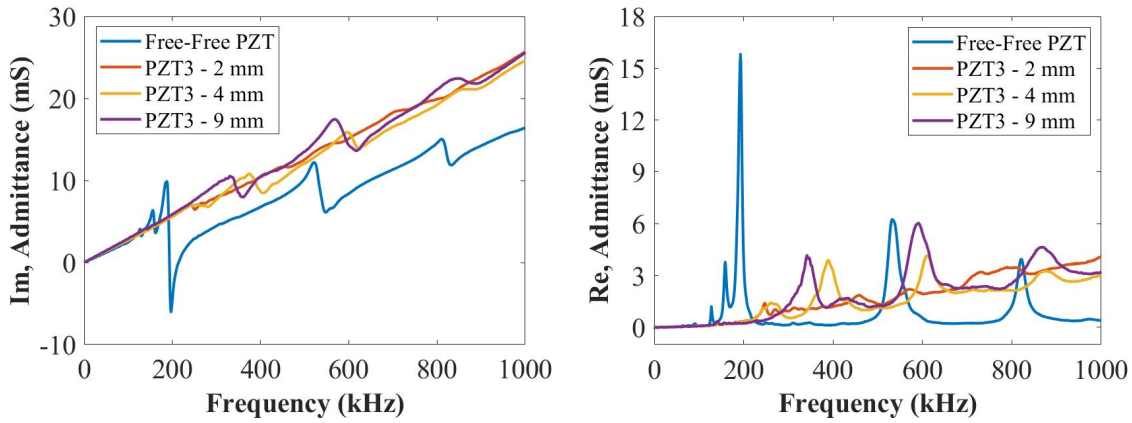

Figure 6.12. The EMI results of **(a)** the imaginary and **(b)** the real parts of the admittance for the embedded PZT transducer.

6.4. Temperature Influence on UGW

In this section, the influence of temperature on the peak amplitude of the first wave packet and the time-of-flight for the embedded signals will be evaluated. These composite panels were placed into an environmental chamber and the temperature range was from -40 °C to 80 °C with the step of 10 °C. A transducer pair path 1-2 shown in Figure 6.2a were measured by five-cycle Hanning-windowed toneburst signals at 50 kHz and 250 kHz. Each composite panel were held for 20~30 minutes during dwell time at each step to make sure the composite panel achieved the target temperature and kept a stable state. Figure 6.13 plots an example of the embedded signals under different temperatures at 50 kHz and 250 kHz for the thickness of the 2 mm panel. As can be seen in Figure 6.13, the peak amplitude of each first wave pack packet of the embedded signals was computed automatically to measure the amplitude reduction and the phase shift.

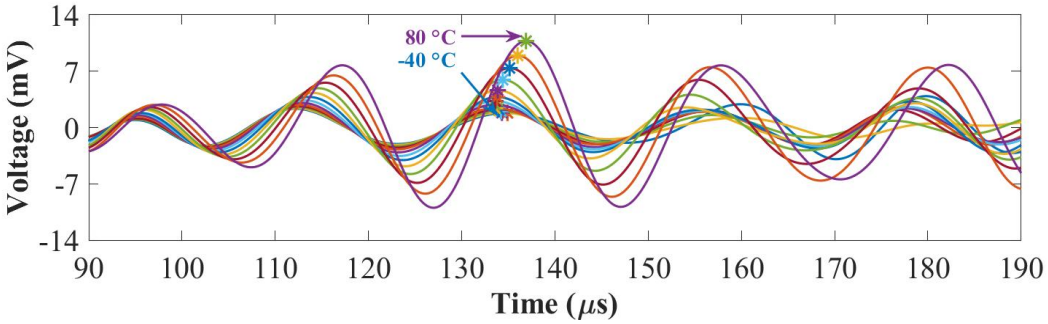

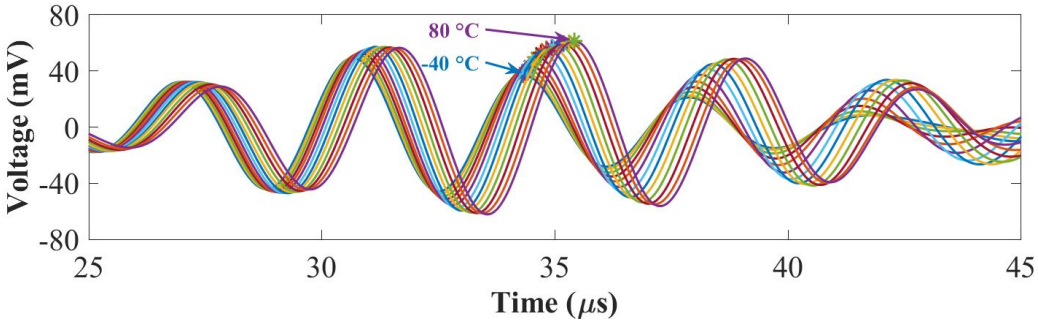

(b)

Figure 6.13. Examples of the embedded UGW under different temperatures at **(a)** 50 kHz and **(b)** 250 kHz.

Figure 6.14 summarises the relationships of the temperature with the peak amplitude of the first wave packet and the time-of-flight (ToF) of the embedded signals at 50 kHz (A_0 mode) and 250 kHz (S_0 mode) for the thickness of 2 mm, 4 mm and 9 mm panels. The peak amplitude was chosen from the peak value of the first wave packet of each signal, and the ToF was the difference in the time between the peak amplitude of the first wave packet and half of the actuation signal. In Figure 6.14a, the amplitude of the A_0 mode increases in different slopes with the increase of the temperature at 50 kHz for the thickness of 2 mm, 4 mm and 9 mm panels. In Figure 6.14b, the amplitude of the S_0 mode increases for the 2 mm and the 9 mm panels while reducing for the 4 mm panel with the increased temperature at 250 kHz. In Figure 6.14c, the ToF of the A_0 mode for the 2 mm panel drops down first from -40 °C to 20 °C and then increases from 20 °C to 80 °C at 50 kHz, while those of the 4 mm and the 9 mm panels increase with the increased temperature. In Figure 6.14d, the ToF of the S_0 mode increases with the increased temperature for the thickness of 2 mm, 4 mm and 9 mm panels at 250 kHz.

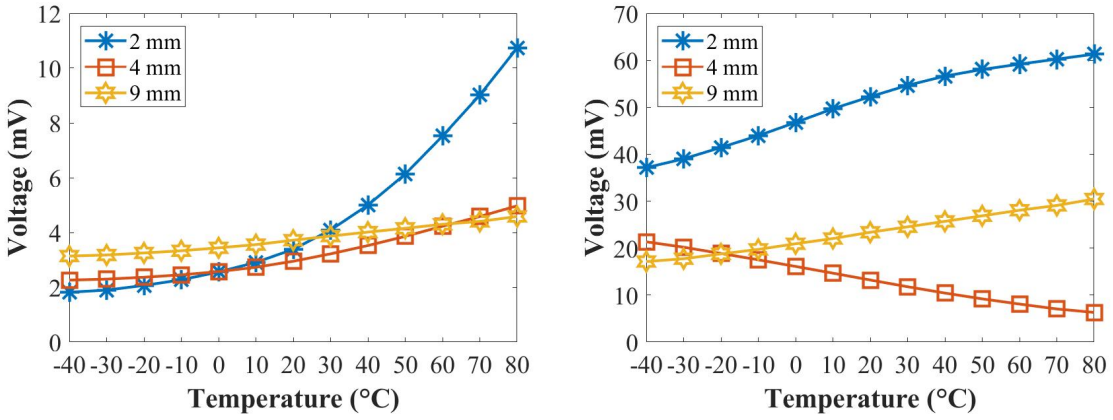

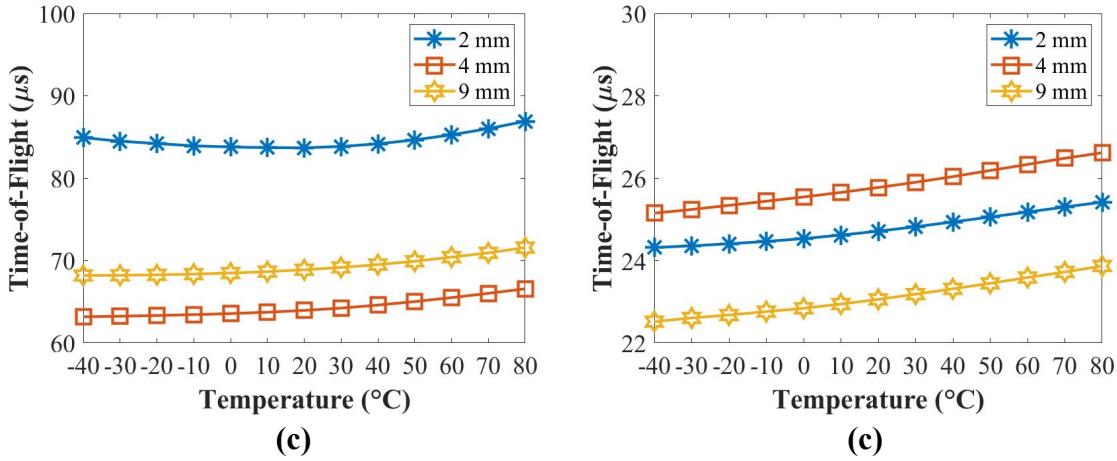

Figure 6.14. Relationships of the temperature with the peak amplitude at **(a)** 50 kHz, **(b)** 250 kHz and the time-of-flight at **(c)** 50 kHz and **(d)** 250 kHz.

In conclusion, the peak amplitude of the first wave packet and the ToF of embedded signals for the thickness of 2 mm, 4 mm and 9 mm panels can be significantly affected by the temperature. The amplitudes of the A_0 and the S_0 modes increase with the increased temperature except for the S_0 mode of the 4 mm panel at 250 kHz, and the ToF increases with the increased temperature except for the 2 mm panel at 50 kHz.

Comparing the above embedded results to the surface-mounted results reported in Figure 5.13, the peak amplitude of the A_0 mode (50 kHz) reduces for the surface-mounted signals but increases for the embedded signals with the increase of the temperature for the thickness of 2 mm, 4 mm and 9 mm panels. In addition, the peak amplitude of the S_0 mode (250 kHz) increases first and then reduces for the surface-mounted signals but increases only for the embedded signals for the 2 mm panel. The ToF of the A_0 mode (50 kHz) for the 2 mm panel increases for the surface-mounted signals but reduces first then increases for the embedded signals.

Four factors may affect the above results. First, the elastic modulus of composites is a key parameter for thermal variations. The elastic modulus is associated with mechanical stiffness. When increasing the temperature, the elastic modulus decreases significantly as a result of decreasing in stiffness, which causes the velocity reduction in guided waves [139-141, 146-148]. Second, the piezoelectric properties of PZT transducers (d_{31} and g_{31}) vary with the temperature significantly. The piezoelectric constants d_{31} and g_{31} are associated with the shear strain and the piezo sensitivity respectively. The dielectric constant also has a linear relationship with the temperature. Both these constraints depend on the output voltage (amplitude) of the signals [139-141].

In addition, thermal expansion causes changes in panel thickness, piezo dimensions, propagation distance of guided waves and material density, and these key factors are used to compute dispersion curves of UGW in different temperatures [139, 146]. Since dispersion properties are associated with the group velocity of UGW, the difference in the ToF at 50 kHz

for the 2 mm panel compared to other panels may be caused by the thickness effectiveness of dispersion properties for composites.

Furthermore, thermal expansion and temperature-induced change also affect PZT transducers and their bonding properties [147]. In this experiment, the resin film was used to bond embedded PZT transducers to meet the specification of carbon fibre prepreg fabrication, while the adhesive film was used to bond surface-mounted PZT transducers. Experimental results and more details related to adhesive films were reported in previous research [149]. Hence, the selection of adhesive film used to bond the PZT transducer is one of the factors affecting experimental results.

6.5. Surface-mounted Artificial Damage

The damage detection section will demonstrate the difference between UGW interaction with the surface artificial damage and the impact damage (i.e. interlaminar delamination and debonding) to the panels with different thicknesses. First, an added mass (blue-tack) is used to simulate the surface-mounted artificial damage, which makes the panel reusable for the impact test. The LDV measurements will be conducted first, followed by active sensing detection for both cases.

6.5.1. LDV Measurements

To experimentally study the thickness influence on the guided wave interaction with the surface-mounted artificial damage (weighted blue-tack), LDV measurements were conducted. The relative position of the surface-mounted artificial damage for each panel was the same as reported in Figure 5.14. The LDV setup and the scanning densities for each panel can be referred to in 5.5.1.

During postprocessing, these chirp signals were reconstructed to five-cycle Hanning-windowed toneburst signals at 50 kHz and 250 kHz. Figure 6.15 plots UGW interactions with the surface-mounted artificial damage in the z-direction at 50 kHz (the A_0 mode) and 250 kHz (the S_0 mode) for the thickness of 2 mm, 4 mm and 9 mm panels. As can be seen in Figure 6.15, only the A_0 mode (50 kHz) interacted with the surface-mounted artificial damage for the thickness of 2mm, 4 mm and 9 mm panels. In conclusion, the A_0 mode is more appropriate for the surface-mounted artificial damage interaction. The next section will investigate the damage detection based on UGW response with embedded PZT transducers to validate this conclusion.

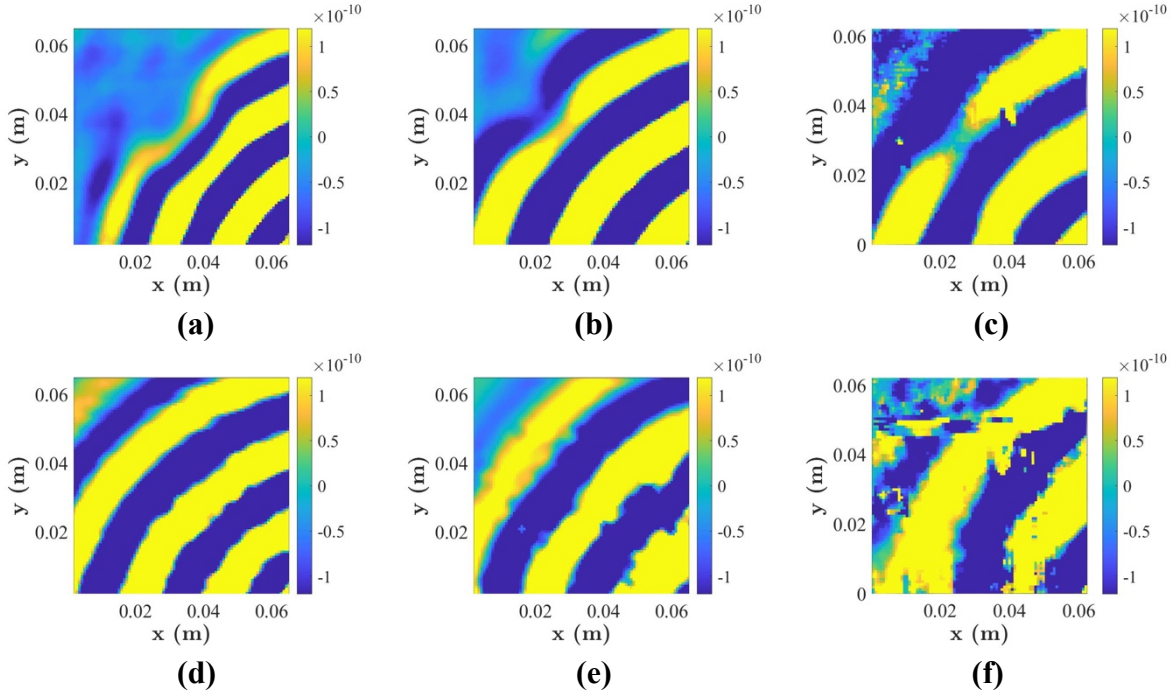

Figure 6.15. UGW interaction with the surface-mounted artificial damage at 50 kHz for the thickness of **(a)** 2 mm, **(b)** 4 mm and **(c)** 9 mm panels and at 250 kHz for the thickness of **(d)** 2 mm, **(e)** 4 mm and **(f)** 9 mm panels.

6.5.2. Damage Detection and Localization

In this section, the surface-mounted artificial damage was detected and located by the correlation coefficient and the DAS algorithm. The blue-tack was closely attached on a designated position (off-centre) of the surface of these composites.

Figure 6.16 to Figure 6.21 plot the results of damage detections and localizations for the thickness of 2 mm, 4 mm and 9 mm panels at 50 kHz and 250 kHz, respectively. For the 4 mm panel, the embedded circuits of the PZT transducer 1 (plate configuration is shown in Figure 6.2) disconnected after the manufacturing, so only three embedded PZT transducers were used for damage detections and localizations. For the 9 mm panel, the much higher amplitude of crosstalk affects the first wave packet of the measured signal to be distinguished for pair path 1-3/3-1 and 2-4/4-2 at 50 kHz, which caused the time-of-arrival (ToA) of the measured signals for above pair path cannot be identified, so it cannot be used for damage detection and localization based on the correlation coefficient and the DAS algorithm at 50 kHz.

As can be seen in Figure 6.16 and Figure 6.17, values of the damage index for the 2 mm and the 4 mm panels at 50 kHz are higher than those at 250 kHz. Therefore, the A_0 mode is more suitable for surface damage detection. Furthermore, damage localization results show that the surface-mounted artificial damage can be located accurately using the DAS algorithm even for the thick composite panel (9 mm). Although the results of LDV measurements have demonstrated the superiority of interaction of the A_0 mode with surface damage in section 6.5.1,

the results of the DAS algorithm show that 50 kHz and 250 kHz can both locate the damage accurately due to the high signal to noise ratio of the dynamical structure (plate + sensor) at 250 kHz. In addition, the previous experimental results (shown in Figure 5.22) have demonstrated that the S_0 mode cannot locate the surface-mounted artificial damage accurately for the thick composites (9 mm panel) at 250 kHz (S_0 mode) by surface-mounted PZT transducers. Therefore, embedded PZT transducers are more sensitive than surface-mounted PZT transducers for locating the surface-mounted artificial damage in thick composite laminates.

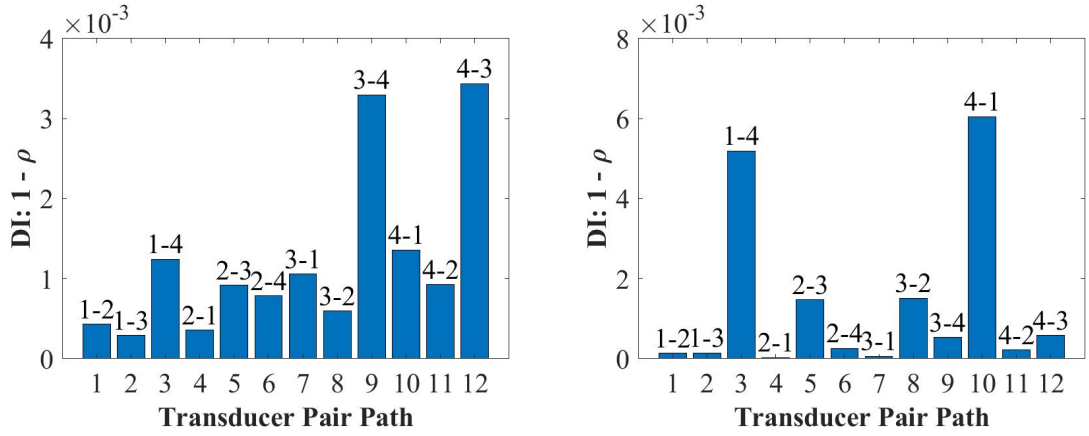

Figure 6.16. Damage detection for the 2 mm panel at **(a)** 50 kHz and **(b)** 250 kHz.

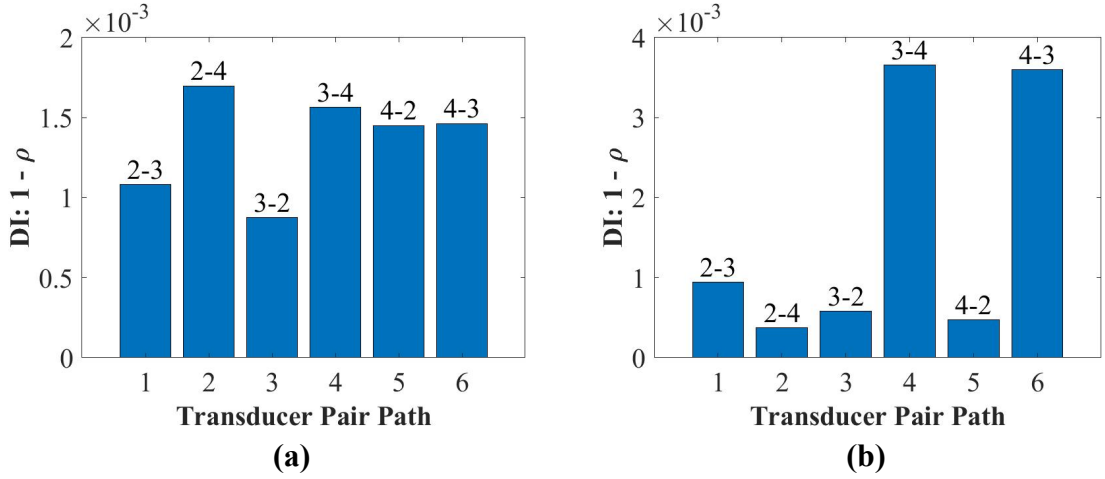

Figure 6.17. Damage detection for the 4 mm panel at **(a)** 50 kHz and **(b)** 250 kHz.

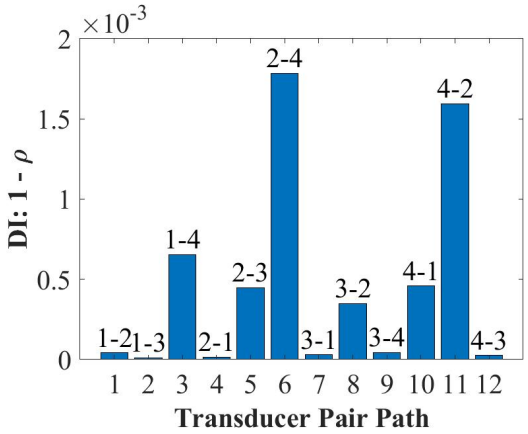

Figure 6.18. Damage detection for the 9 mm panel at 250 kHz.

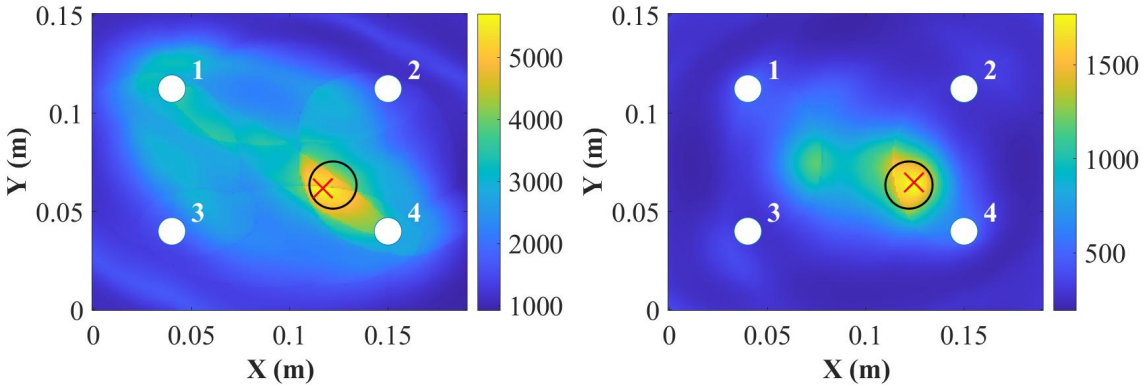

Figure 6.19. Damage localization for the 2 mm panel at **(a)** 50 kHz and **(b)** 250 kHz (where the "○" is the position for real damage and the "×" is the position for predicted damage).

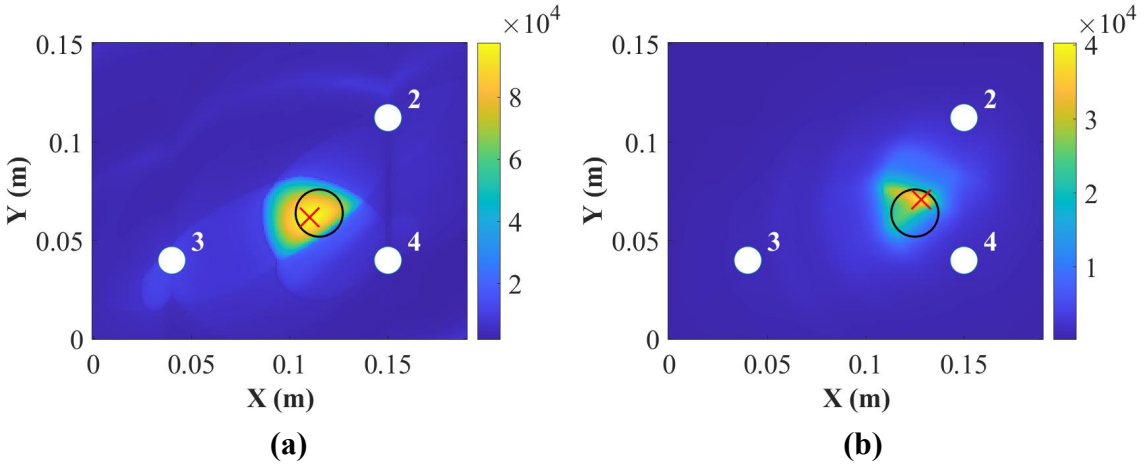

Figure 6.20. Damage localization for the 4 mm panel at **(a)** 50 kHz and **(b)** 250 kHz (where the "○" is the position for real damage and the "×" is the position for predicted damage).

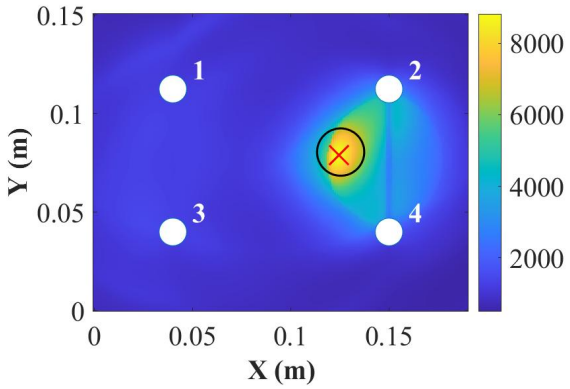

Figure 6.21. Damage localization for the 9 mm panel at 250 kHz (where the "○" is the position for real damage and the "×" is the position for predicted damage).

6.6. Impact Damage

The procedure of the impact tests and the C-scan results were the same as reported in section 5.6.1.

6.6.1. LDV Measurements

For LDV measurements, the scanning densities and spacing grid of each panel for the impact damage measurements can be referred to in 5.6.2. Figure 6.22 plots the results in the z-direction for the thickness of 2 mm, 4 mm and 9 mm panels at 50 kHz (A_0 mode) and 250 kHz (S_0 mode), respectively. As can be seen in Figure 6.22, both the A_0 and the S_0 modes show the reflection and refraction with impact damage for the thickness of 2 mm, 4 mm and 9 mm panels.

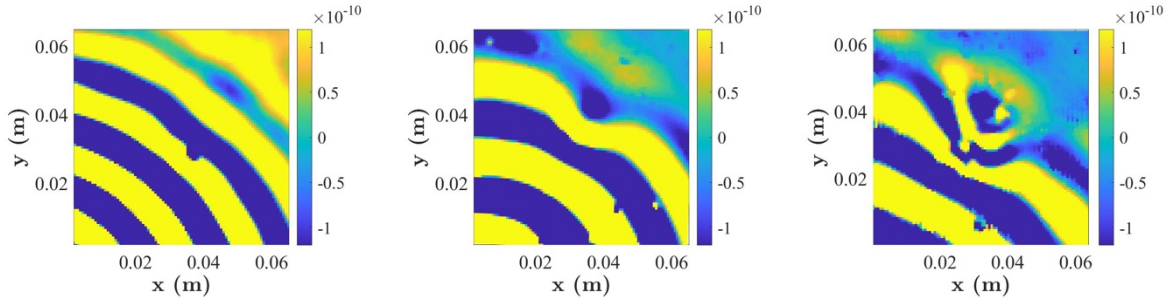

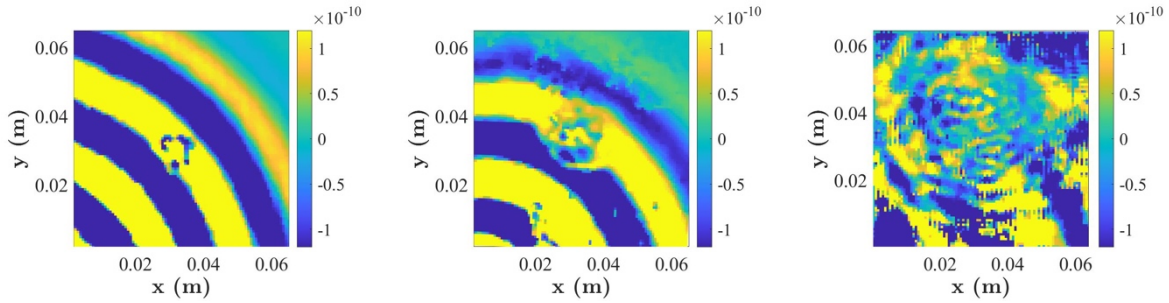

(d) **(e)** **(f)**

Figure 6.22. UGW interaction with the impact damage at 50 kHz for the thickness of **(a)** 2 mm, **(b)** 4 mm and **(c)** 9 mm panels and at 250 kHz for the thickness of **(d)** 2 mm, **(e)** 4 mm and **(f)** 9 mm panels.

6.6.2. Damage Detection and Localization

In this section, the correlation coefficient and the DAS algorithm were used to detect the impact damage for the thickness of 2 mm, 4 mm and 9 mm panels. Figure 6.23 to Figure 6.28 plot results of damage detections and localizations at 50 kHz and 250 kHz, respectively. As can be seen in the blow figures, the damage index can detect the damage. In addition, the DAS algorithm can locate the damage position accurately for the 2 mm and the 4 mm panels at 50 kHz, but not at 250 kHz for the thickness of 2 mm, 4 mm and 9 mm panels. The damage detection and location results show that the A_0 mode (50 kHz) is more suitable for detecting the impact damage. According to previous experimental results (Figure 5.29a and Figure 5.30a) using surface-mounted PZT transducers, the DAS algorithm cannot locate the impact damage accurately for both the A_0 and the S_0 modes. Therefore, embedded PZT transducers are more sensitive than surface-mounted PZT transducers for the impact damage at 50 kHz.

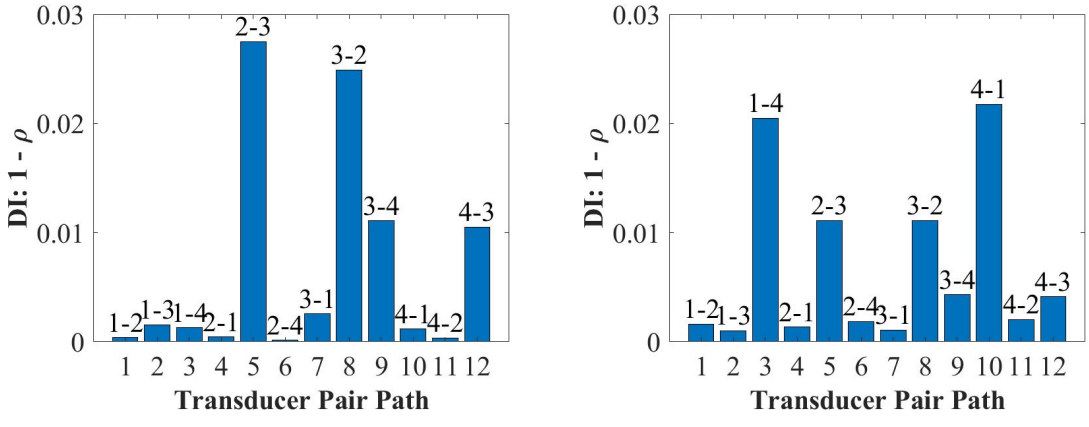

(a) **(b)**

Figure 6.23. Damage detection for the 2 mm panel at **(a)** 50 kHz and **(b)** 250 kHz.

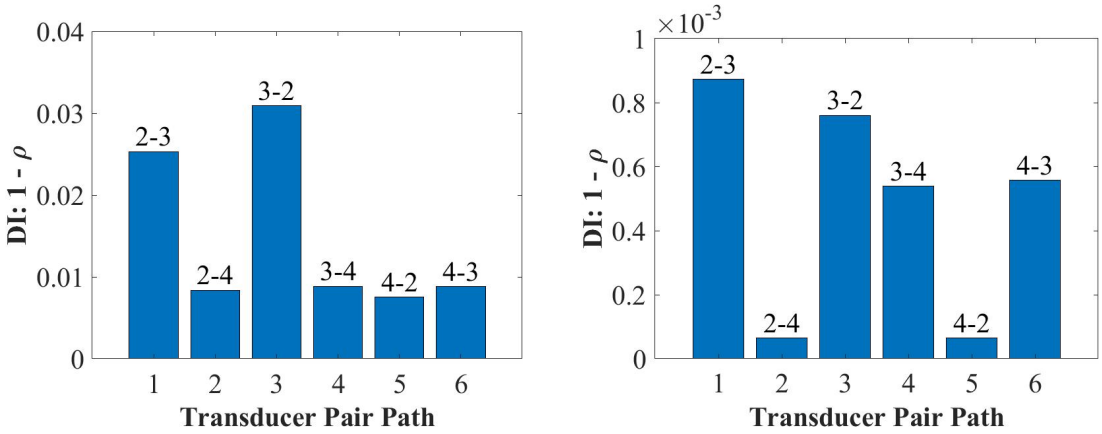

Figure 6.24. Damage detection for the 4 mm panel at **(a)** 50 kHz and **(b)** 250 kHz.

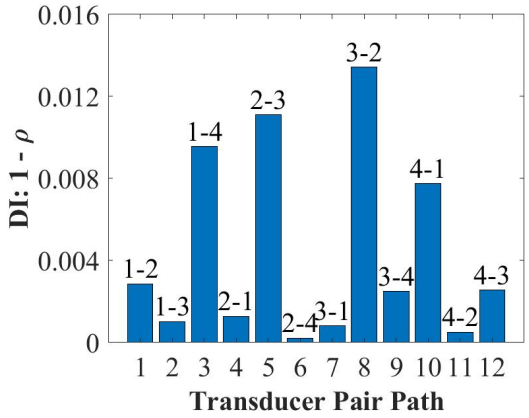

Figure 6.25. Damage detection for the 9 mm panel at 250 kHz.

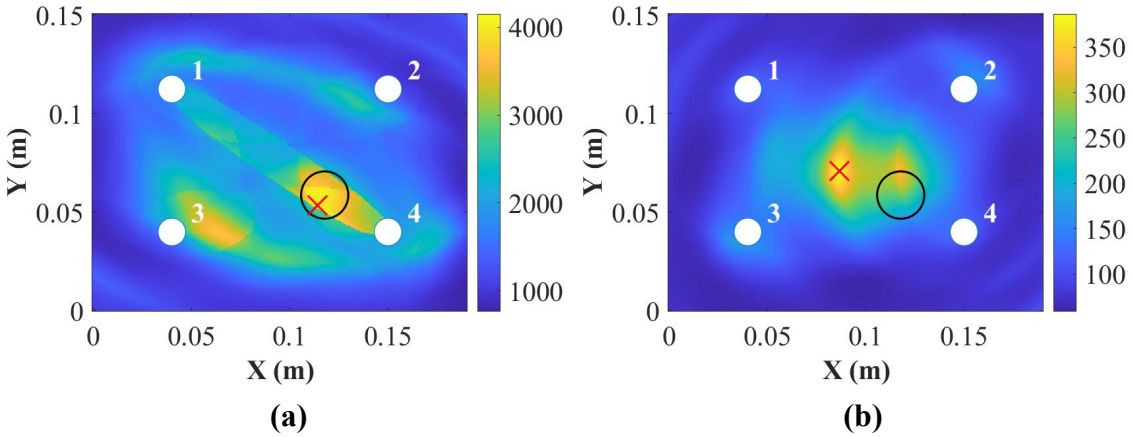

Figure 6.26. Damage localization for the 2 mm panel at **(a)** 50 kHz and **(b)** 250 kHz (where the "○" is the position for real damage and the "×" is the position for predicted damage).

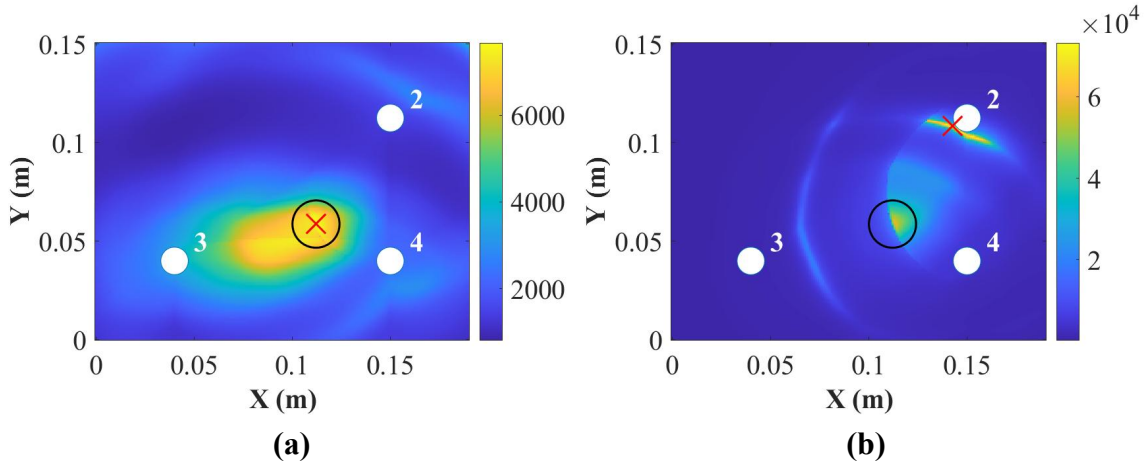

Figure 6.27. Damage localization for the 4 mm panel at **(a)** 50 kHz and **(b)** 250 kHz (where the "○" is the position for real damage and the "×" is the position for predicted damage).

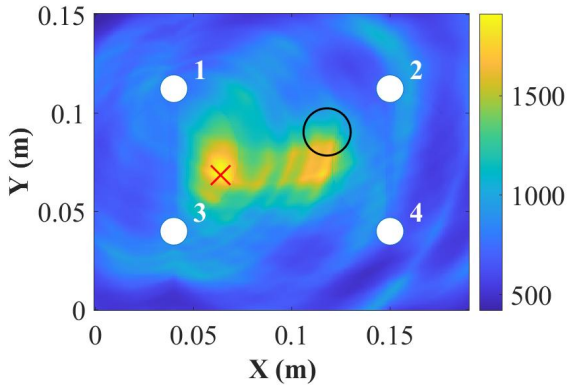

Figure 6.28. Damage localization for the 9 mm panel at 250 kHz (where the "○" is the position for real damage and the "×" is the position for predicted damage).

6.7. Influence of Embedded Position on UGW

6.7.1. Finite Element Modelling

To study the effect of different embedded positions on UGW, finite element modelling will be conducted to investigate relationships between the peak amplitude of the first wave packet, the time-of-arrival (ToA) and the time-of-flight (ToF) for the thicknesses of 2 mm, 4 mm and 9 mm panels. The material properties used in the modelling can be referred to in Table 4.1 in section 4.2. The size of the 3D model was 220 mm × 170 mm. The distance between two PZT transducers was 110 mm and the distances from the centre of the PZT transducer to the edge were 55 mm in the x-direction and 85 mm in the y-direction, respectively.

Figure 4.11 shows the schematic of the assembly relationships with embedded PZT transducers. For each model, two PZT transducers were either mounted on the surface or

embedded into the composite panel from the first layer to the middle layer. The model of composite panels with surface-mounted and embedded PZT transducers based on the implicit dynamic analysis (Abaqus/Standard) can be referred to in sections 4.2 and 4.3.

6.7.2. Modelling Results

6.7.2.1. The Summary of Envelop Signals

Figure 6.29 plots a summary of numerical envelope signals of UGW for the thicknesses of 2 mm, 4 mm and 9 mm panels in different placing positions at 50 kHz and 250 kHz, where the time-of-arrival (ToA) and the peak amplitude of the first wave packet for each signal were computed.

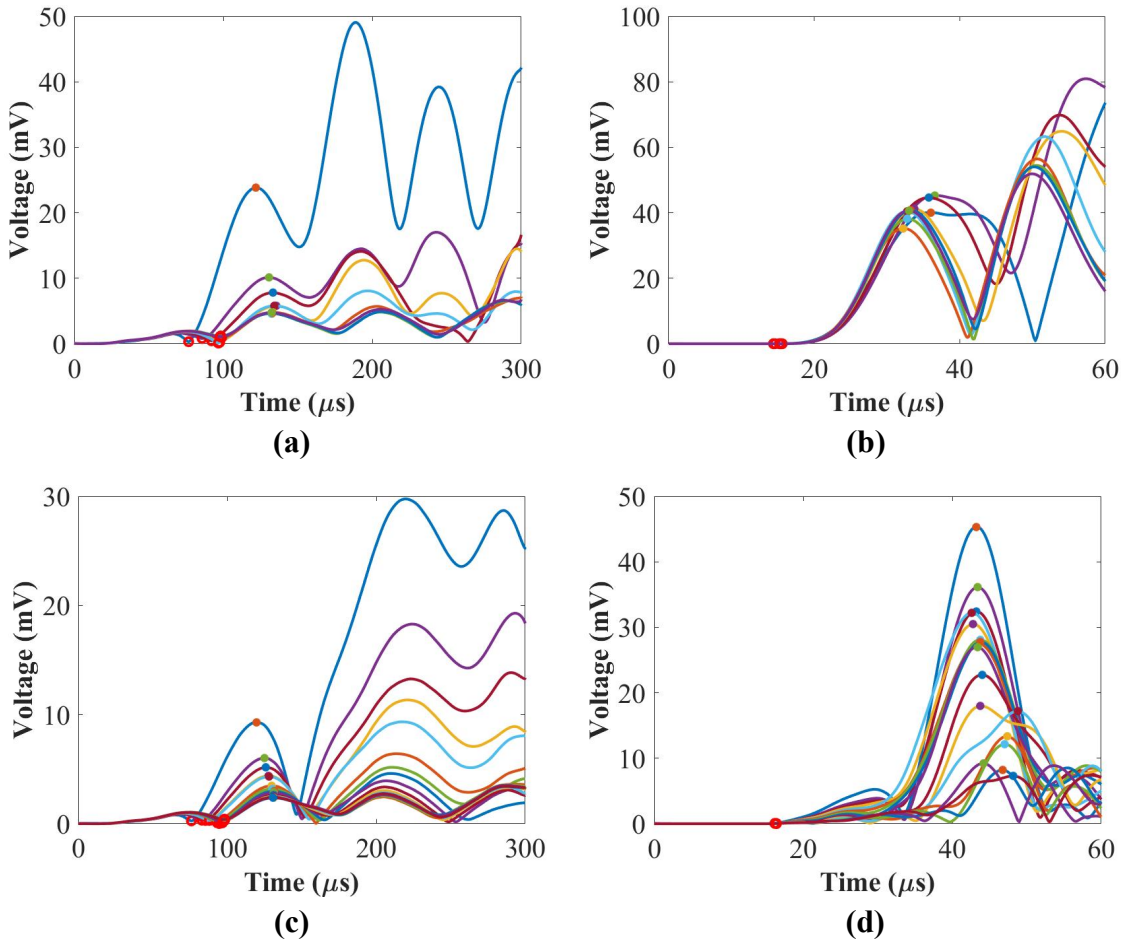

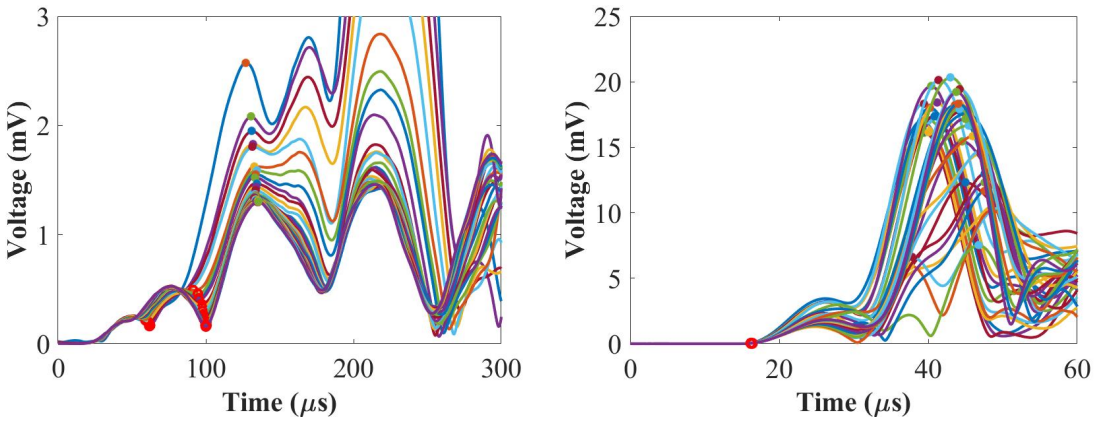

Figure 6.29. The summary of numerical envelope signals for the 2 mm panel at **(a)** 50 kHz and **(b)** 250 kHz; for the 4 mm panel at **(c)** 50 kHz and **(d)** 250 kHz; and for the 9 mm panel at **(e)** 50 kHz and **(f)** 250 kHz.

6.7.2.2. The Summary of the Time-of-Arrival (ToA)

Figure 6.30 plots relationships between the time-of-arrival (ToA) and different placing positions for the thicknesses of 2 mm, 4 mm and 9 mm panels at 50 kHz and 250 kHz, respectively. According to the rules of composite stacking sequences during modelling, the position 0 in the x-axis in Figure 6.30 means the PZT transducers were mounted on top of the composite panel (surface-mounting). When the PZT transducers were placed from the 1st layer to the end position (from 1st to 8th layer for the 2 mm panel in Figure 6.30), this means the PZT transducers were embedded from the 1st layer to the middle layer of the composite panel. As can be seen in Figure 6.30a, the ToA becomes slower when the PZT transducers were placed in a deeper position at 50 kHz except for the 9 mm panel when the PZT transducers were placed from the 2nd layer to the 5th layer. In Figure 6.30b, the ToA does not show an obvious difference when the PZT transducers were embedded in different layers at 250 kHz.

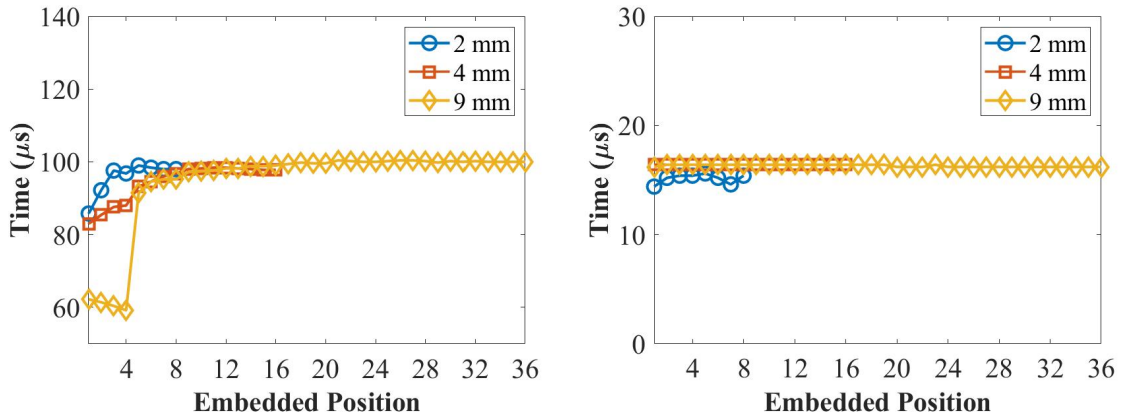

Figure 6.30. The summary of the ToA for all panels at **(a)** 50 kHz and **(b)** 250 kHz.

6.7.2.3. The Summary of the Time-of-Flight (ToF)

Figure 6.31 plots relationships between the time-of-flight (ToF) and different placing positions for the thicknesses of 2 mm, 4 mm and 9 mm panels at 50 kHz and 250 kHz, respectively. In Figure 6.31a, the ToF becomes slower when the PZT transducers were placed in a deeper position for the 4 mm and the 9 mm panel at 50 kHz. In Figure 6.31b, the ToF becomes faster for the 2 mm panel and slower at first then faster for the 9 mm panel at 250 kHz.

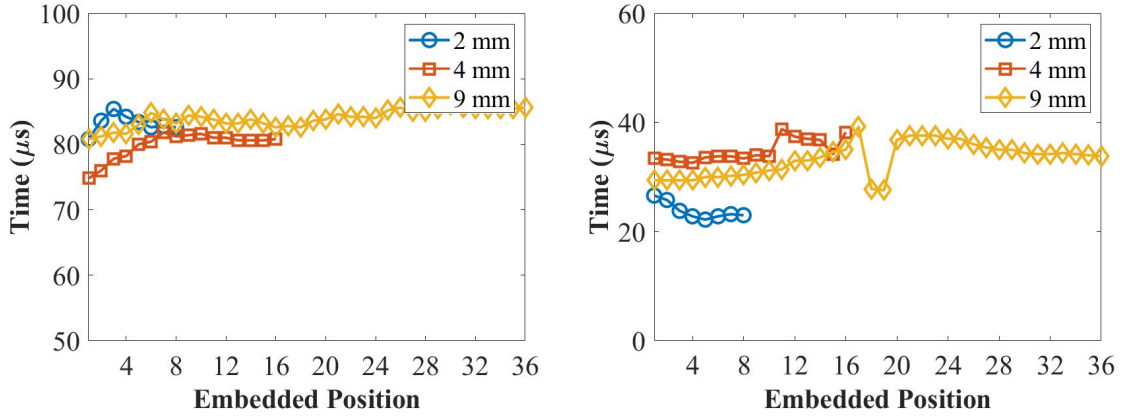

Figure 6.31. The summary of the ToF for all panels at **(a)** 50 kHz and **(b)** 250 kHz.

6.7.2.4. The Summary of the Peak Amplitude

Figure 6.32 plots relationships between the peak amplitude of the first wave packet and different placing positions for the thicknesses of 2 mm, 4 mm and 9 mm panels at 50 kHz and

250 kHz. As is shown in Figure 6.32, the peak amplitude of the first wave packet decreases when transducers were placed in a deeper position for the thicknesses of 2 mm, 4 mm and 9 mm panels at 50 kHz and the 4 mm panel at 250 kHz. For the 9 mm panel at 250 kHz, the peak amplitude depends on the lay-up angels and the placing positions from the 2nd layer to the 13th layer, then the peak amplitude decreases from the 14th layer to the 20th layer and then increased from the 21st layer to the middle layer for the 9 mm panel at 250 kHz.

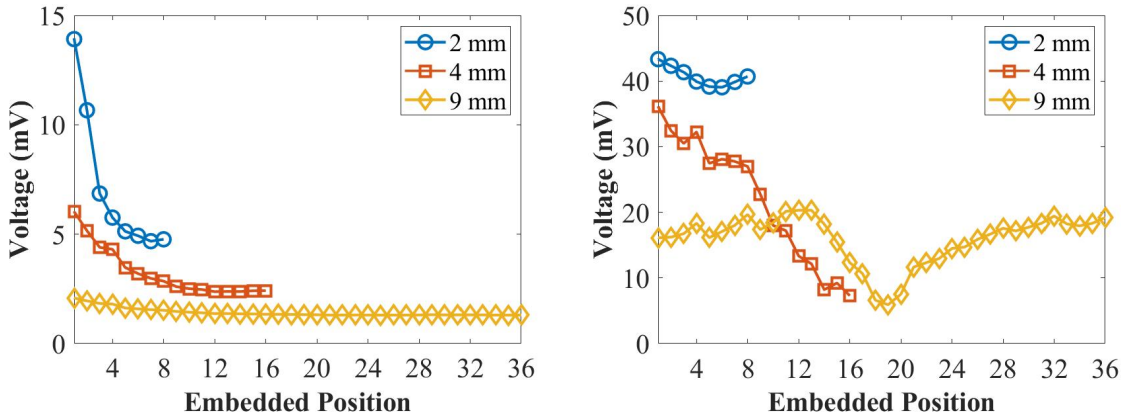

Figure 6.32. The summary of the peak amplitude of the first wave packet for all panels at **(a)** 50 kHz and **(b)** 250 kHz.

6.7.3. Experimental Setup

To experimentally study UGW between surface-mounted and embedded PZT transducers and the influence of the embedding position on UGW, composite coupons with the surface-mounted, the quarter- and the middle- embedded PZT transducers were fabricated. Unidirectional carbon fibre prepregs Hexply® IM7/8552 were used for the lay-up, and the stacking sequences were $[(0°/+45°/-45°/+90°)_n]_s$, where n was 2, 4 and 9 for the thicknesses of 2 mm, 4 mm and 9 mm panels respectively. The size of the coupon was 260 mm × 45 mm, and the distance between two PZT transducers was 180 mm to avoid the overlap between the crosstalk and the first wave packet of the embedded signals at 50 kHz. Distances from the centre of PZT transducers to the edge were 40 mm in the x-direction and 22.5 mm in the y-direction.

The fabrication of these coupons for the thickness of 2 mm, 4 mm and 9 mm panels can be referred to in section 3.3. Figure 6.33 shows the 9 mm trimmed coupon with the middle-embedded ending terminals and its connector. Figure 6.34 shows all three composite coupons with surface-mounted diagnostic films and PZT transducers, and the quarter-embedded ending terminals and connectors for the thicknesses of 2 mm, 4 mm and 9 mm, respectively.

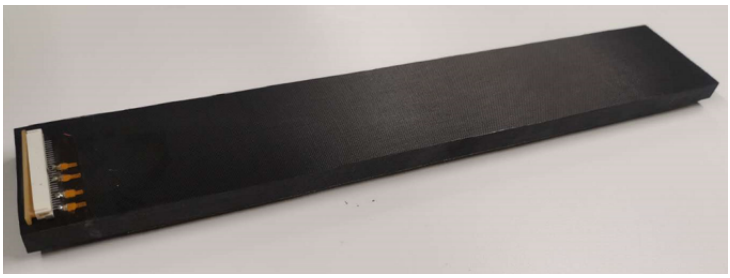

Figure 6.33. The 9 mm coupon with middle-embedded ending terminals and a connector.

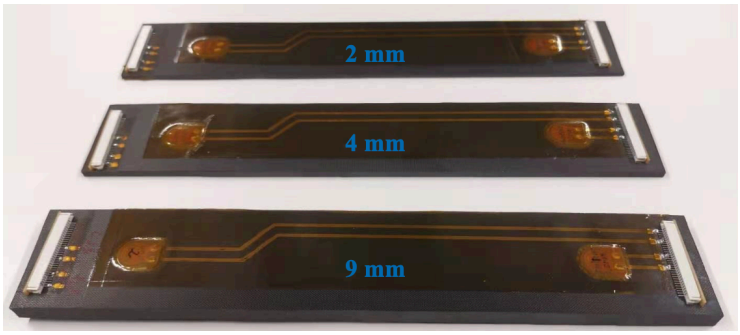

Figure 6.34. Coupons with surface-mounted diagnostic films and quarter-embedded ending terminals and connectors for the thickness of 2 mm, 4 mm and 9 mm panels.

6.7.4. Experimental Results

6.7.4.1. Electro-Mechanical Impedance (EMI) Methods

After fabrication, the electro-mechanical impedance (EMI) methods were used to verify the bonding properties of PZT transducers. In Figure 6.35, Figure 6.36 and Figure 6.37, slopes of the imaginary part of the admittance for PZT transducers in different positions (below 20 kHz) have no obvious difference for the thickness of 2 mm, 4 mm and 9 mm panels. Therefore, all the embedded and surface-mounted PZT transducers have good bonding properties and can be used for further guided wave measurements.

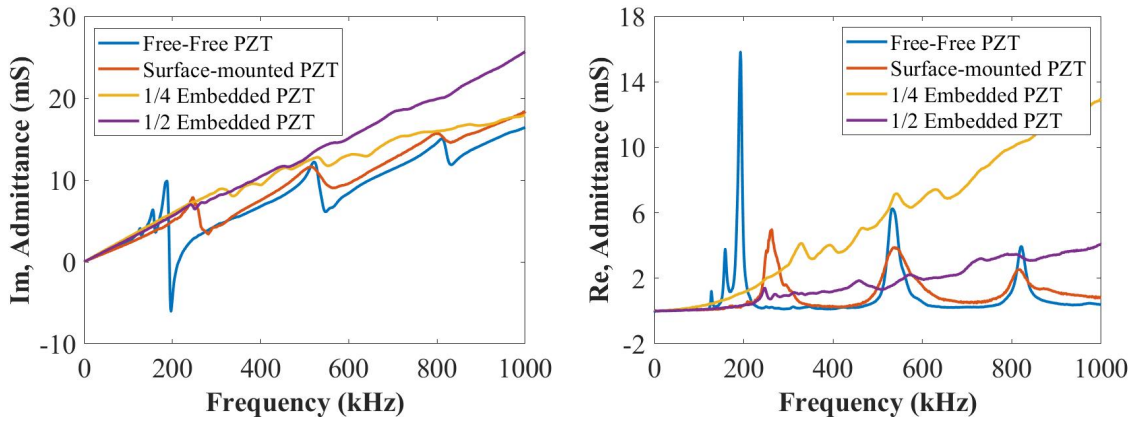

Figure 6.35. The EMI results of **(a)** the imaginary and **(b)** the real parts of the admittance for the thickness of the 2 mm coupon.

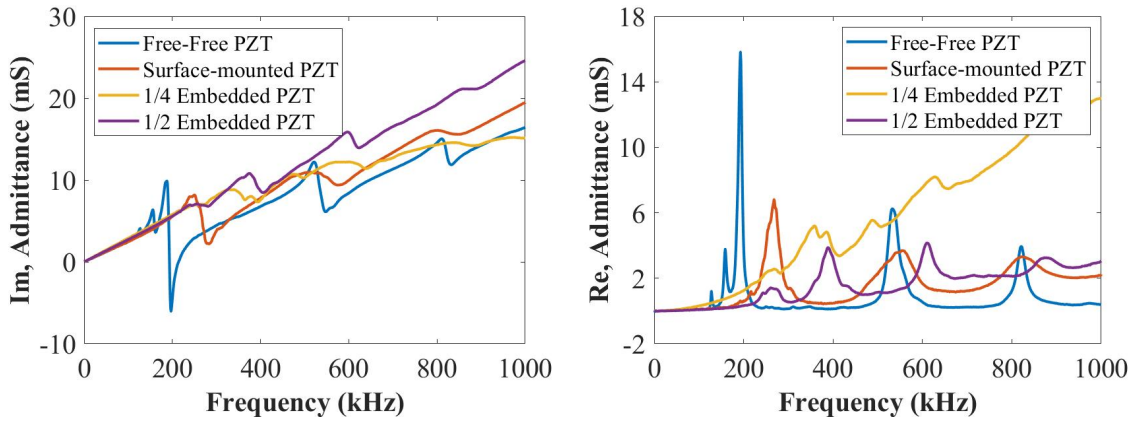

Figure 6.36. The EMI results of **(a)** the imaginary and **(b)** the real parts of the admittance for the thickness of the 4 mm coupon.

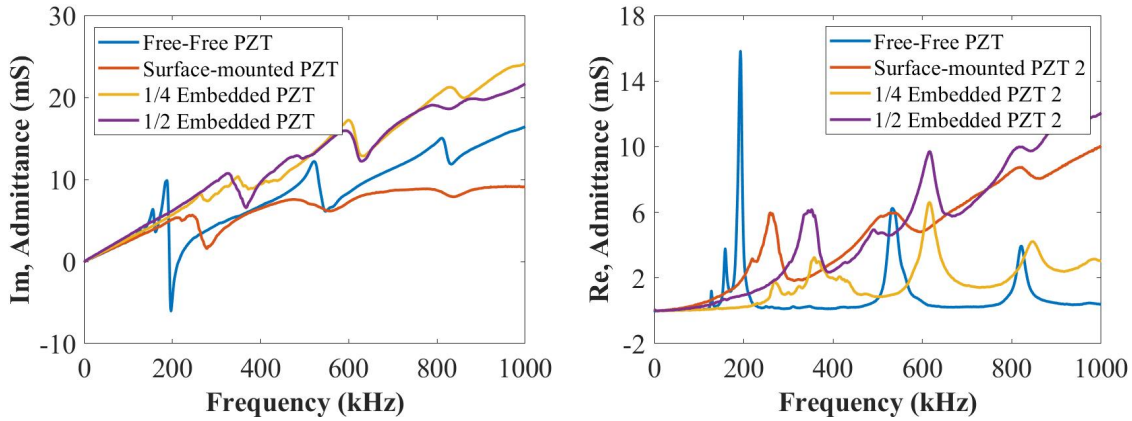

Figure 6.37. The EMI results of **(a)** the imaginary and **(b)** the real parts of the admittances for the thickness of the 9 mm coupon.

6.7.4.2. Effects of Transducers Placing Position on UGW

Figure 6.38 to Figure 6.40 plot UGW actuated by the PZT transducers in different placing positions for the thickness of 2 mm, 4 mm, and 9 mm coupons at 50 kHz and 250 kHz, respectively. After trimming, the connection of a quarter-embedded PZT transducer for the 9 mm coupon was disconnected due to the trimming issues, so the UGW of the quarter-embedded signals for the 9 mm coupon cannot be measured. As can be seen from Figure 6.40 to Figure 6.40, the peak amplitude of the first wave packet for the surface-mounted signal is higher than that of the quarter- and the middle- embedded signals at 50 kHz and 250 kHz except for the 4 mm panel at 250 kHz.

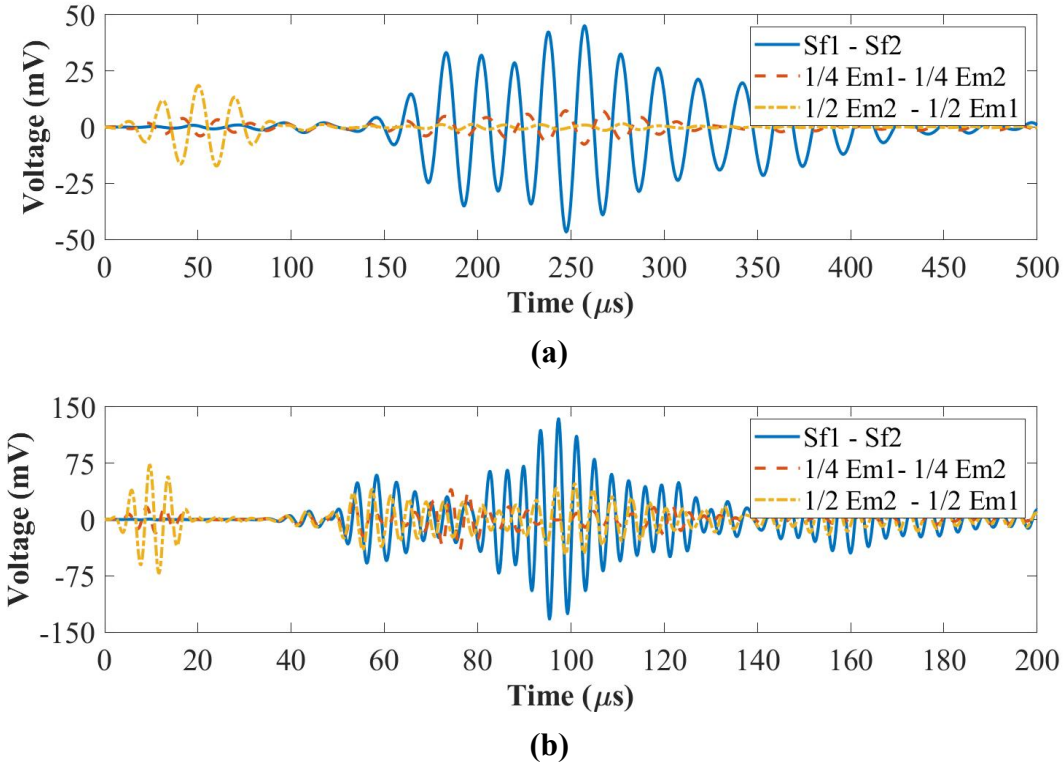

Figure 6.38. UGW actuated by the PZT transducers placed in different positions at **(a)** 50 kHz and **(b)** 250 kHz for the 2 mm coupon.

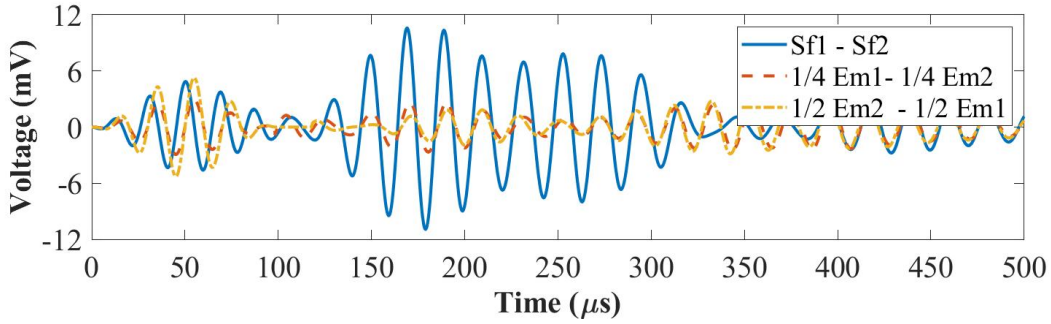

(a)

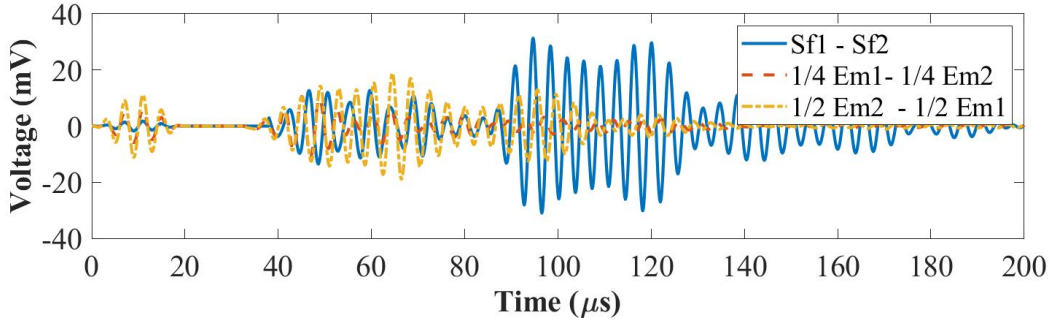

(b)

Figure 6.39. UGW actuated by the PZT transducers placed in different positions at **(a)** 50 kHz and **(b)** 250 kHz for the 4 mm coupon.

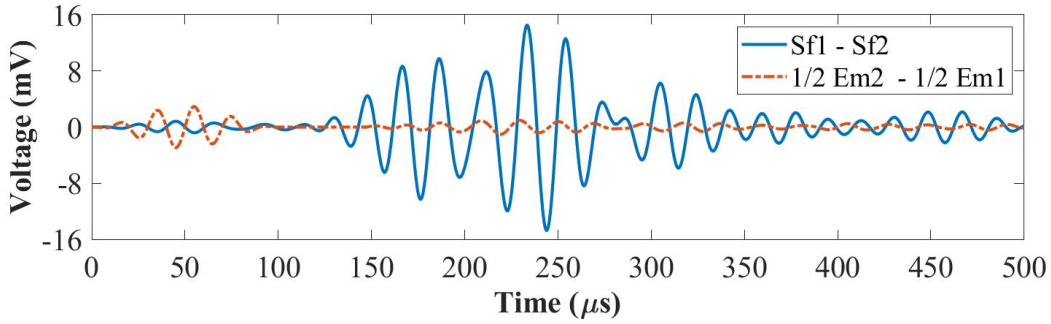

(a)

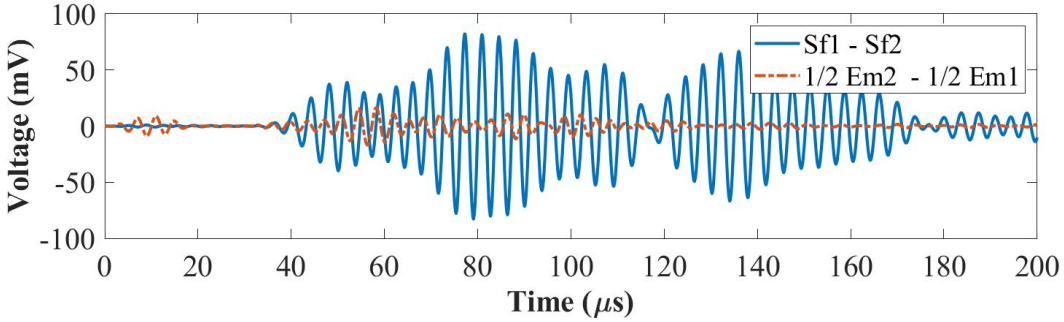

(b)

Figure 6.40. UGW actuated by the PZT transducers placed in different positions at **(a)** 50 kHz and **(b)** 250 kHz for the 9 mm coupon.

6.7.4.3. The Reversibility of UGW between Different Transducers for the 2 mm Coupon

Figure 6.41 and Figure 6.42 plot the reversibility of UGW between the surface-mounted, the quarter- and the middle- embedded PZT transducers for the 2 mm coupon at 50 kHz and 250 kHz, respectively. As can be seen in Figure 6.41 to Figure 6.42, amplitudes of the first wave packets actuated by the quarter- and the middle- embedded PZT transducers are higher than that of UGW actuated by the surface-mounted PZT transducer at 50 kHz and 250 kHz. In addition, the amplitude of the first wave packet actuated by the quarter-embedded PZT transducer is slightly higher than that of UGW actuated by the middle-embedded PZT transducer at 50 kHz and 250 kHz.

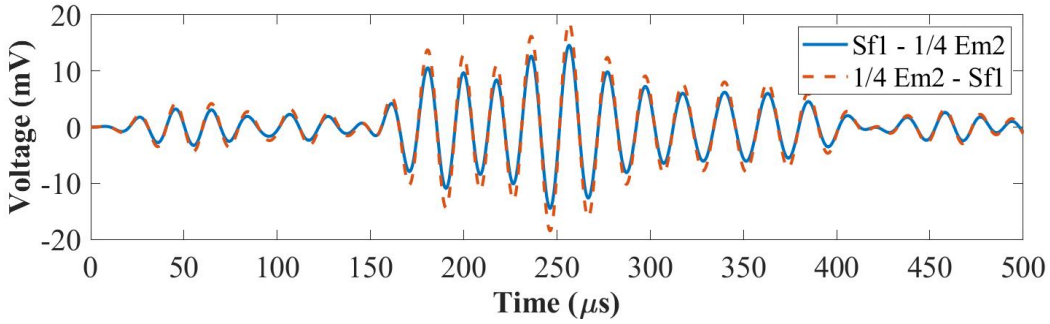

(a)

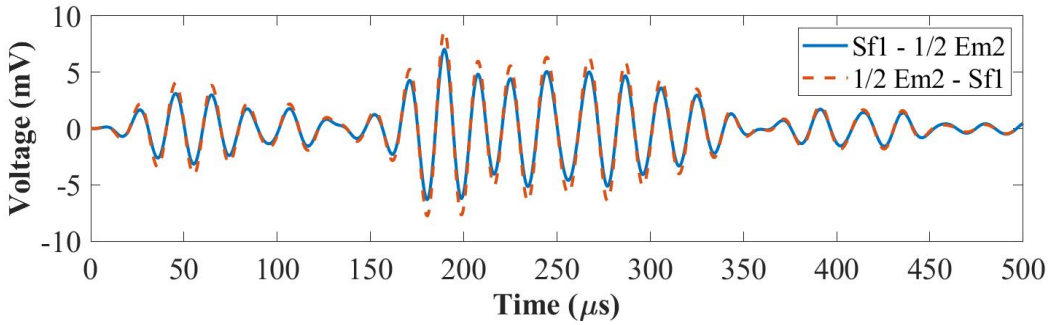

(b)

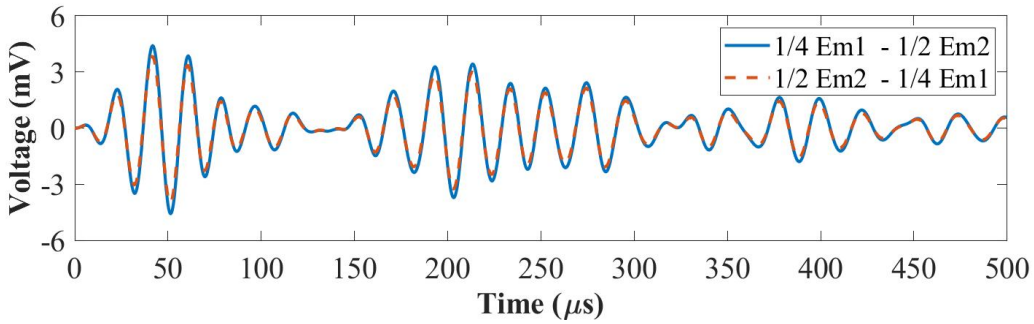

(c)

Figure 6.41. The reversibility of UGW between **(a)** the surface-mounted and the quarter-embedded transducers, **(b)** the surface-mounted and the middle-embedded transducers and **(c)** the quarter- and the middle-embedded transducers at 50 kHz for the 2 mm coupon.

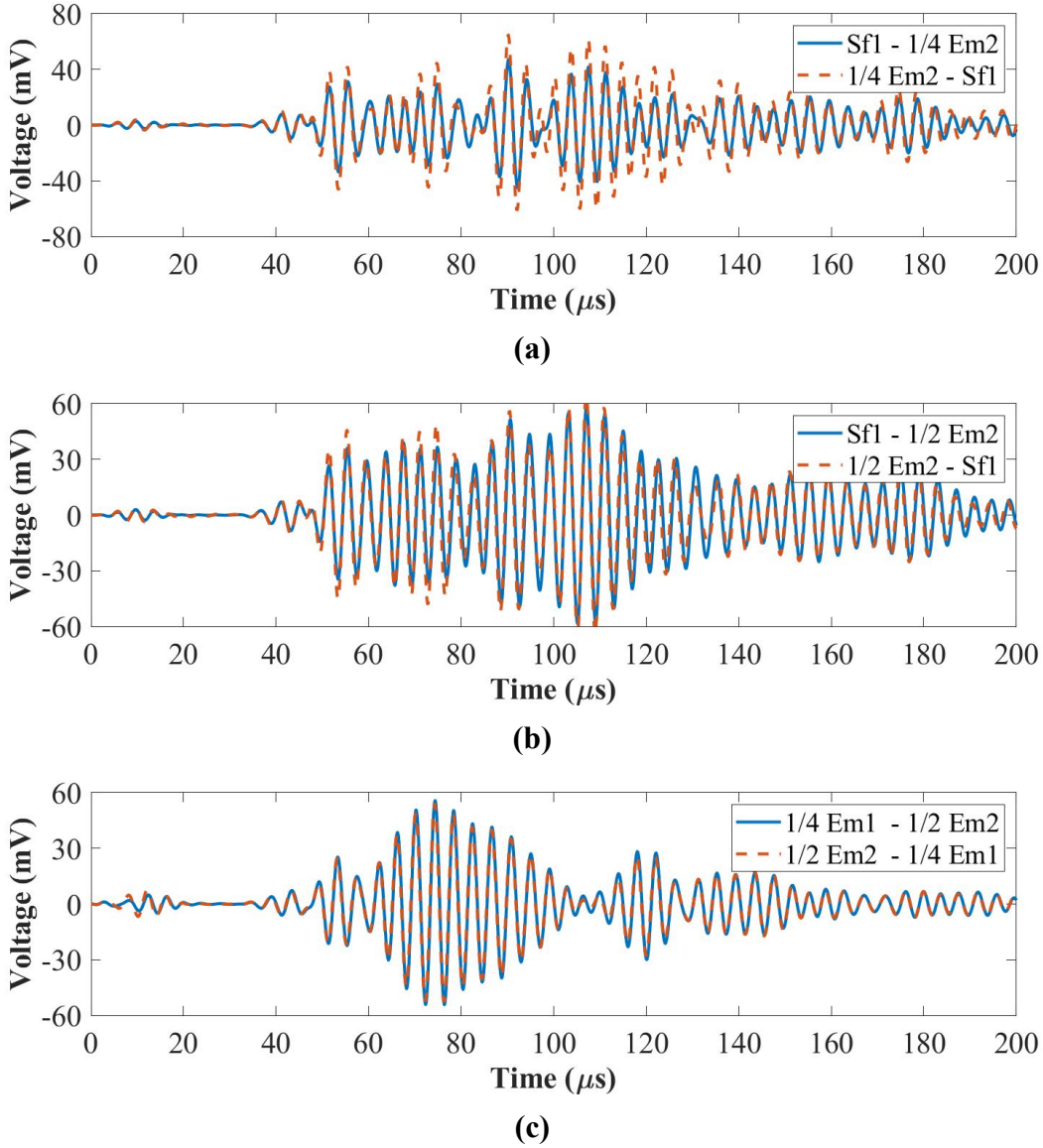

Figure 6.42. The reversibility of UGW between **(a)** the surface-mounted and the quarter-embedded transducers, **(b)** the surface-mounted and the middle-embedded transducers and **(c)** the quarter- and the middle-embedded transducers at 250 kHz for the 2 mm coupon.

6.7.4.4. The Reversibility of UGW between Different Transducers for the 4 mm Coupon

Figure 6.43 and Figure 6.44 plot the reversibility of UGW between the surface-mounted, the quarter- and the middle- embedded PZT transducers for the 4 mm coupon at 50 kHz and 250

kHz, respectively. As can be seen in Figure 6.43 and Figure 6.44, the amplitudes of the first wave packets actuated by the quarter- and the middle- embedded transducers are higher than that of the amplitude actuated by the surface-mounted transducer at 50 kHz and 250 kHz. In addition, the amplitude of the first wave packet actuated by the quarter-embedded PZT transducer is slightly higher than that of UGW actuated by the middle-embedded PZT transducer at 50 kHz and 250 kHz.

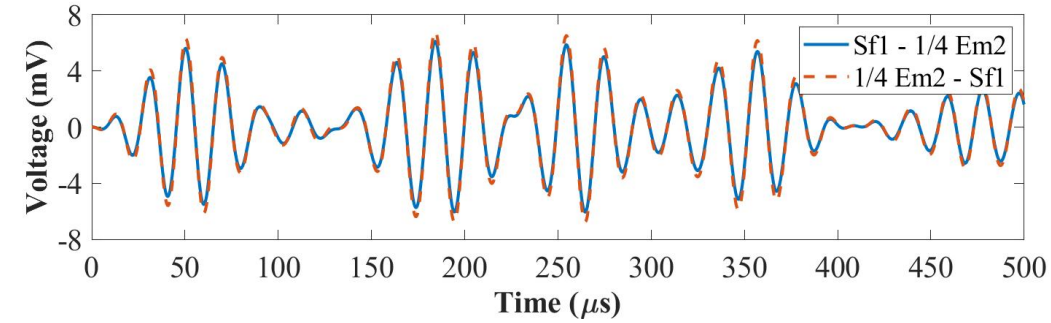

(a)

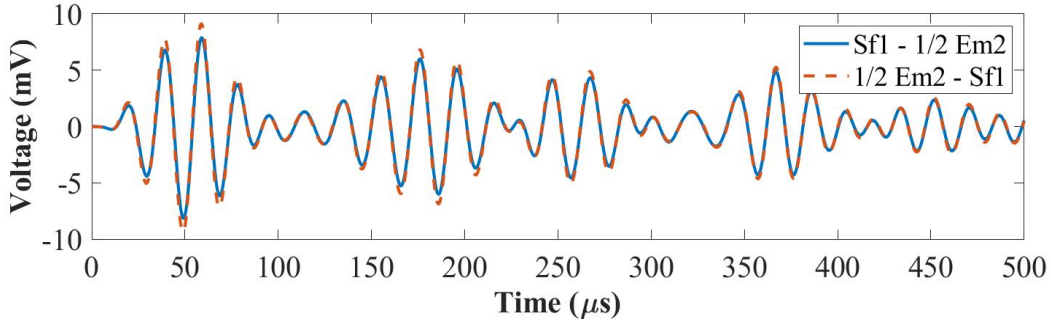

(b)

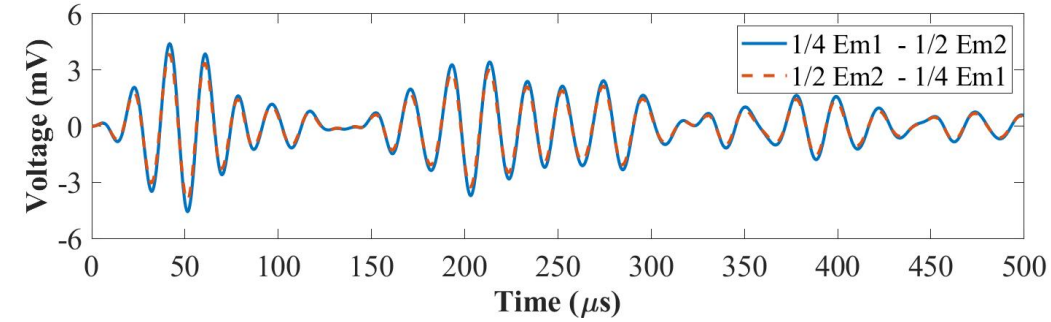

(c)

Figure 6.43. The reversibility of UGW between **(a)** the surface-mounted and the quarter-embedded transducers, **(b)** the surface-mounted and the middle-embedded transducers and **(c)** the quarter- and the middle-embedded transducers at 50 kHz for the 4 mm coupon.

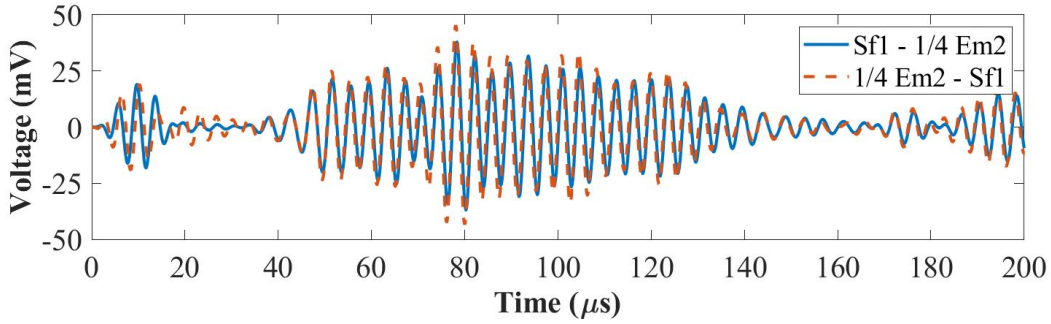

(a)

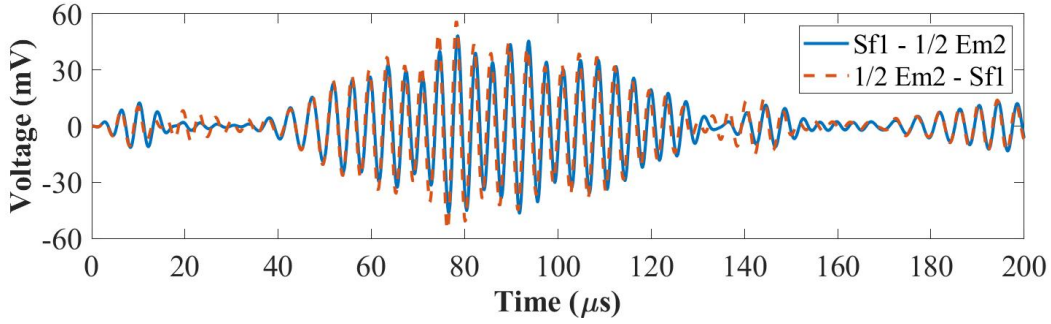

(b)

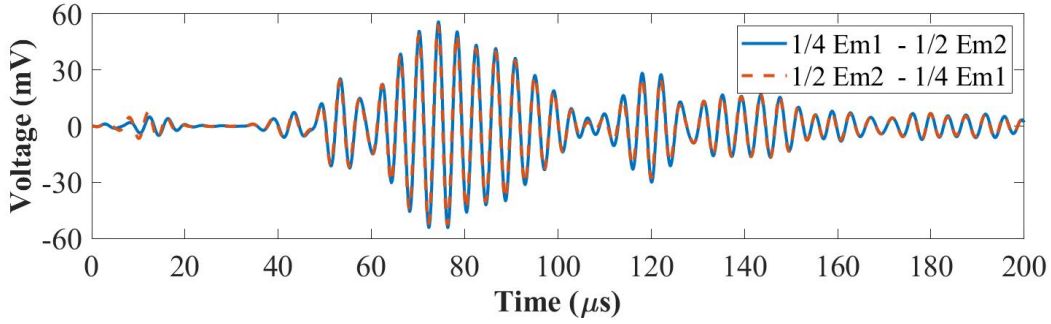

(c)

Figure 6.44. The reversibility of UGW between **(a)** the surface-mounted and the quarter-embedded transducers, **(b)** the surface-mounted and the middle-embedded transducers and **(c)** the quarter- and the middle-embedded transducers at 50 kHz for the 4 mm coupon.

6.7.4.5. The Reversibility of UGW between Different Transducers for the 9 mm Coupon

Figure 6.45 and Figure 6.46 plot the reversibility of UGW between the surface-mounted, the quarter- and the middle- embedded PZT transducers for the 9 mm coupon at 50 kHz and 250 kHz, respectively. As can be seen in Figure 6.45 and Figure 6.46, the peak amplitudes of first wave packets actuated by the quarter- and the middle- embedded PZT transducers are higher than that of the amplitude actuated by the surface-mounted PZT transducer at 50 kHz and 250

kHz. In addition, the peak amplitude of the first wave packet actuated by the middle-embedded transducer is higher than that of the amplitude actuated by the quarter-embedded transducer.

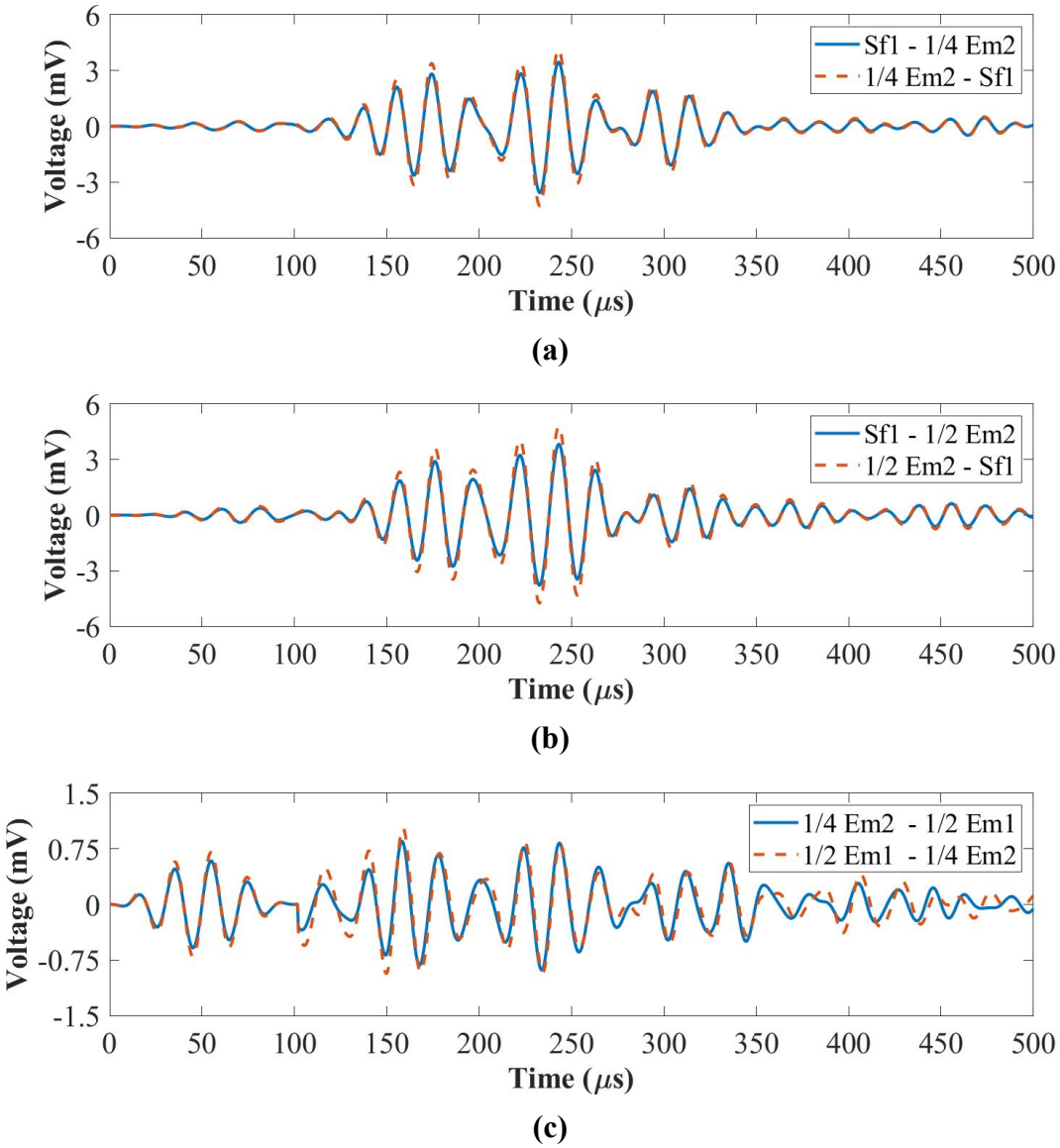

Figure 6.45. The reversibility of UGW between **(a)** the surface-mounted and the quarter-embedded transducers, **(b)** the surface-mounted and the middle-embedded transducers and **(c)** the quarter- and the middle-embedded transducers at 50 kHz for the 9 mm coupon.

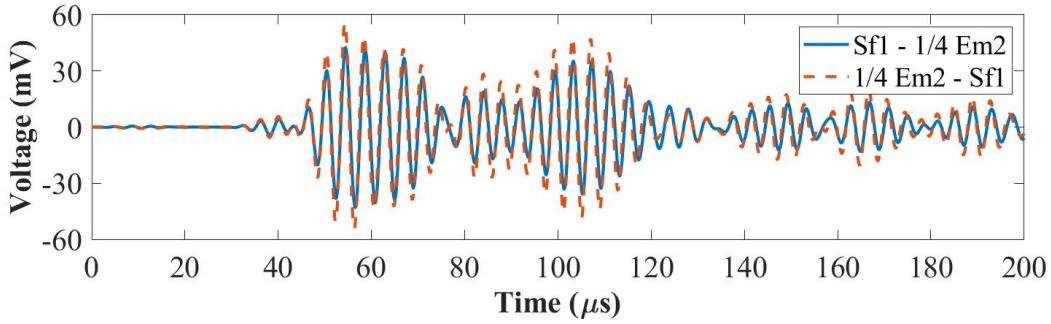

(a)

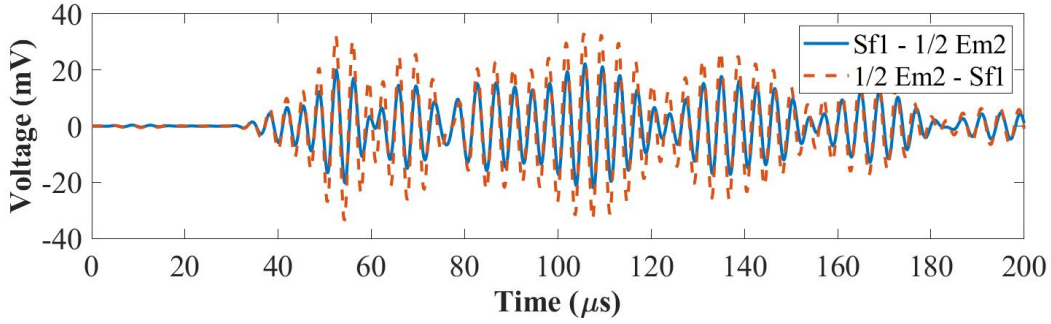

(b)

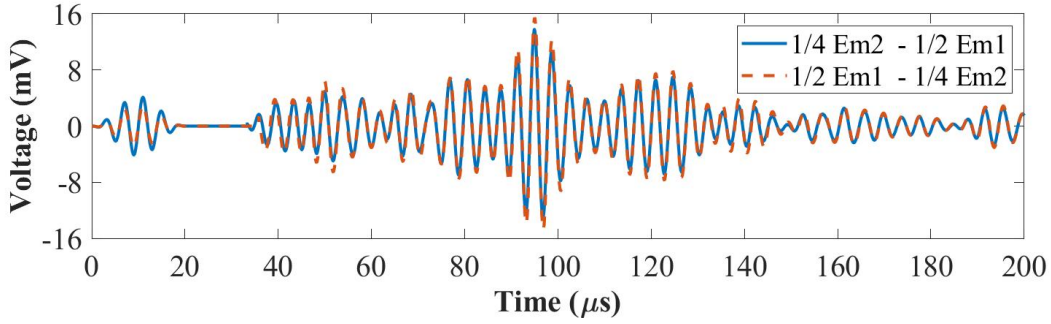

(c)

Figure 6.46. The reversibility of UGW between **(a)** the surface-mounted and the quarter-embedded transducers, **(b)** the surface-mounted and the middle-embedded transducers and **(c)** the quarter- and the middle-embedded transducers at 250 kHz for the 9 mm coupon.

6.8. Summary

In this chapter, the thickness effectiveness of composites on UGW excitation and propagation actuated by embedded PZT transducers with temperature influences, damage detection and localization were studied in detail.

The active sensing results (in-plane motion) show that the A_0 mode dominates at 50 kHz and the S_0 mode dominates at 250 kHz. Both the A_0 and the S_0 modes have a linear reduction with the increased thickness, which is not dependent on the thickness. The reason why conclusions are differences between LDV measurements and the active sensing results for the in-plane

motion is that LDV captures the surface wave propagation while the active sensing method is actuated/recorded by both embedded PZT transducers. The EMI results demonstrated that the thickness has no influence on the EMI properties and the higher actuation frequency (250 kHz) will amplify the amplitude of the A_0 and the S_0 modes significantly.

The temperature results show that the amplitude of the A_0 mode increases with the increased temperature at 50 kHz, which is not dependent on the thickness. The amplitude of the S_0 mode increases for the 2 mm and the 9 mm panels and reduces for the 4 mm panel at 250 kHz, which is not dependent on the thickness. In addition, the ToF results show that the group velocities become slow for the A_0 and the S_0 modes with the increased temperature except for the A_0 mode at 50 kHz for the 2 mm panel.

Comparing the embedded temperature results to the surface-mounted temperature results, the peak amplitude of the A_0 mode (50 kHz) reduces for surface-mounted PZT transducers but increases for embedded PZT transducers with the increased temperatures for the thickness of 2 mm, 4 mm and 9 mm panels. In addition, the peak amplitude of the S_0 mode (250 kHz) increases first and then reduces for the surface-mounted signals but increases only for the embedded signals for the 2 mm panel. The ToF of the A_0 mode (50 kHz) for the 2 mm panels increases for the surface-mounted signals but reduces first then increases for the embedded signals.

The results of LDV measurements show that only the A_0 mode interacted with the surface-mounted artificial damage at 50 kHz and it can be concluded that the A_0 mode is the more appropriate mode for the surface damage. The results of the damage index and the DAS algorithm show that both the A_0 and the S_0 modes can detect and locate the surface damage accurately due to the high signal to noise ratio at 250 kHz since the dynamical structure (plate + sensor). As it has been dementated previously that the S_0 mode cannot locate the surface damage accurately using surface-mounted PZT transducers at 250 kHz for the 9 mm panel, embedded PZT transducers are more sensitive and can have a better solution for locating the surface damage for thick composites.

Also presented were results for the impact damage. The results of LDV measurements show that both the A_0 and the S_0 modes show the reflection and refraction with the impact damage for the thickness of 2 mm, 4 mm and 9 mm panels. The damage index can detect the impact damage and the DAS algorithm can locate the impact damage accurately for the A_0 mode at 50 kHz while that of surface-mounted PZT transducers cannot. This also demonstrates the embedded PZT transducer can have better results than surface-mounted PZT transducers for locating the impact damage.

The experimental studies involved fabrications of composite coupons with thicknesses of 2 mm, 4 mm and 9 mm panels. The PZT transducers were mounted on the surface, embedded in the quarter and the middle of each composite coupon. First, the EMI results for all PZT transducers show that all PZT transducers have good bonding properties and can be used for further active sensing measurements. Second, UGW actuated by the PZT transducers in different placing positions were compared. It was found that the peak amplitude of the first wave packet for the surface-mounted signal is higher than that of the quarter- and the middle-

embedded signals at 50 kHz (A_0 mode dominates) and 250 kHz (S_0 mode dominates) except for the 4 mm coupon at 250 kHz (S_0 mode dominates). Therefore, the amplitude of the S_0 mode is dependent on thickness. Finally, the reversibility of UGW between the surface-mounted, the quarter- and the middle- embedded PZT transducers has been studied. It has been found that peak amplitudes of the first wave packet actuated by the quarter- and the middle- embedded PZT transducers are higher than that of the amplitude actuated by surface-mounted PZT transducers at 50 kHz and 250 kHz. Furthermore, the peak amplitude of the first wave packet actuated by the quarter-embedded transducer is higher than that amplitude actuated by the middle-embedded transducer for the 2 mm and the 4 mm coupons, but lower than that of the amplitude actuated by the middle-embedded transducers for the 9 mm coupon. Therefore, the embedded PZT transducer can actuate a higher amplitude of UGW for both the S_0 and the A_0 modes than that of the surface-mounted PZT transducer for comparing the reversible signals.

Chapter 7

7. Smart Repair Patch

7.1. Introduction

To meet the requirements of airworthiness certification, repair based on Structural Health Monitoring (SHM) system is an effective way to monitor the integrity of the bonded repair patch for aircrafts [66, 71, 75, 150]. Compared to traditional non-destructive inspection (NDI) techniques, SHM enables bondline inspection possible remotely and in real-time [75, 151]. It has been shown that the smart patch can detect the debonding, delamination of composite layers and the crack growth rate of the composite repairing area [71].

Many works were conducted on the SHM system for the smart repair patch. Rito R.L. *et al* [152] numerically and experimentally studied bondline monitoring using a composite repair patch with the embedded chirped fibre Bragg grating (CFBG) sensors. Both the experimental and the modelling results showed that the smart repair patch embedded with a CFBG sensor can be used to monitor the initial disbond. Lambinet F. *et al.* [75, 150] conducted bending fatigue and impact test for the step-sanded composite repair structures mounted with PZT transducers and used the scaling subtraction method (SSD) and reconstruction algorithm for probabilistic inspection of defects (RAPID) to detect and locate these damages. In addition, they [66] also proposed a novel Minimal Intersection Score (MIS) algorithm to detect and locate the damage to the smart repair patch under different environmental conditions. In their work, the results showed that the MIS algorithm was effective to detect and locate the damage under vibration and different temperatures. Roth W. *et al.* [153] used a smart patch with phased-array PZT transducers to numerically and experimentally monitor the artificial disbond. The Teflon tape was inserted in the edge between the patch and its host composite structure during the manufacturing. The results showed that disbond can be detected by using the electro-mechanical Impedance (EMI) method.

Furthermore, Qing X. et al. [154] used the smart patch combined with the SMART layer (Stanford Multi-Actuator-Receiver Transduction Layer) system to monitor the cure progress and disbond by using the active ultrasonic guided waved SHM technique. Their results showed that the combination of the SMART layer system for the smart repair patch can be used to monitor the cure progress and integrity of the bonding quality of the composite repair structure. In addition, Bekas D. G. *et al*. [155] used the inkjet-printed interdigital multifunctional sensor to monitor the curing and possible subsequent damage. Sánchez-Romate X.F. *et al.* [156] used the carbon nanotube (CNT) based adhesive films to investigate the crack sensing capabilities of adhesive film for composite bonded repair. They demonstrated that the use of the CNT

adhesive films for the bonded repair composite structures did not affect their mechanical performance and the electrometrical results showed they can be used for SHM purposes.

This chapter will assess embedded PZT transducers for detection of the damage along the bondline and on the surface of a composite repair patch. In previous work, PZT transducers were installed on the surface of the host structure to detect damage to the repair patch. This approach as shown in [66, 150] required the placement of many sensors surrounding the entire patch and the guided waves had to travel the entire length of the patch to detect possible damage. There was also scattering from the edge to the patch since the guided wave was generated from the host structure and not internally to the patch as with the approach proposed in this paper. Furthermore, the use of a hybrid PZT-FBG acquisition system has already been reported in [75]. Hence, a smart repair patch with the developed embedded diagnostic film and PZT transducers is the most innovative because it reduces the number of sensors.

In this chapter, the edge cut-out method is applied to manufacture a smart repair patch combined with an embedded diagnostic layer and PZT transducers. Then this patch will bond to the composite host structure together to simulate composite repair. Active sensing of UGW will be used for SHM purposes. The aim of this chapter is to investigate the monitoring ability of the smart repair patch using the diagnostic film for bondline inspection of the composite repair structure. First, the EMI method will be used to verify the bonding properties between PZT transducers and the repair patch. Second, the damage index (DI) correlation coefficient and the delay-and-sum (DAS) algorithm will be used to detect and locate the artificial delamination and the surface-mounted artificial damage.

7.2. Experimental Setup

Unidirectional carbon fibre prepregs Hexply® IM7/8552 were used in this experiment. For fabrication of the composite repair patch, the quasi-isotropic stacking sequence $[(0°/+45°/-45°/+90°)_2]_s$ was used during lay-up and the thickness of the repair patch was about 2 mm after curing. Figure 7.1 shows the general drawing of the smart repair patch with the configuration of PZT transducers and Figure 7.1 b shows the schematic of the embedding procedure during lay-up. The preparation of diagnostic films with PZT transducers and fabrication of the smart repair patch can be referred to in section 3.3. Figure 7.2a shows the picture of the embedded diagnostic film with PZT transducers during the lay-up and the trimmed repair patch after the fabrication is shown in Figure 7.2b. For manufacturing the host composite structure, a quasi-isotropic stacking sequence $(0°/+45°/-45°/+90°)_{4s}$ was used during the lay-up and the size was 300 mm × 260 mm, and the thickness of the host structure was about 4 mm after curing.

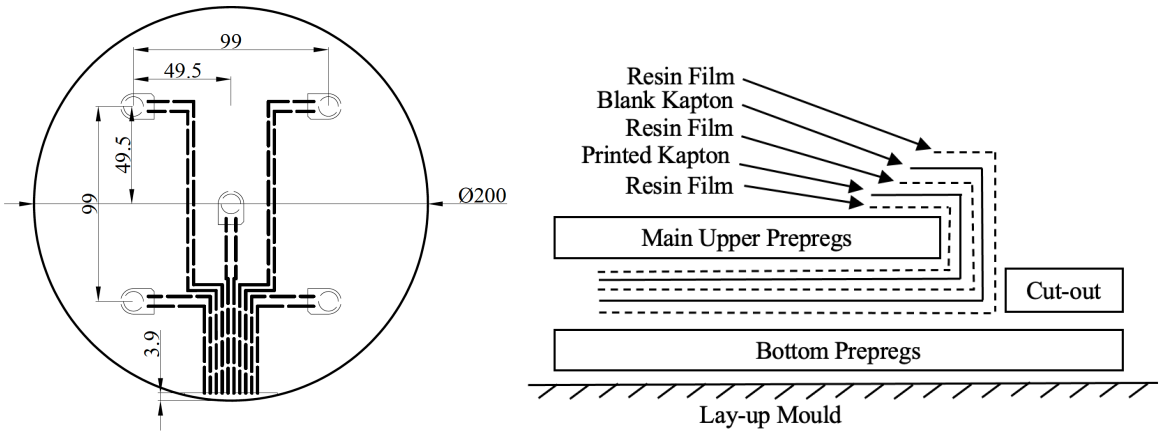

(a) **(b)**

Figure 7.1. **(a)** The general drawing of the repair patch; and **(b)** schematic of the embedding procedure during the lay-up.

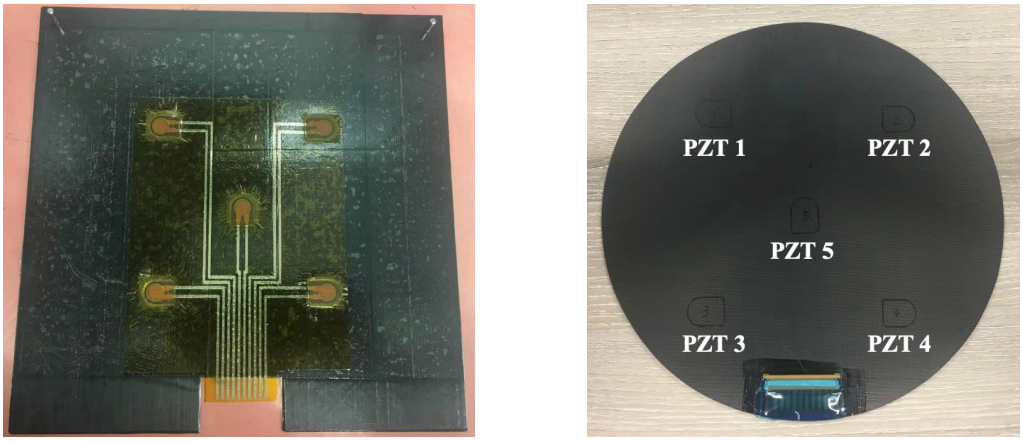

(a) **(b)**

Figure 7.2 Examples of **(a)** the embedded diagnostic film with PZT transducers and **(b)** the trimmed smart repair patch after manufacturing.

7.3. Electro-Mechanical Impedance (EMI) Methods

The EMI method was used to verify bonding qualities between embedded PZT transducers and their host structure. Figure 7.3 presents the EMI results for the imaginary and real parts of the admittance for different PZT transducers of the repair patch. As is shown in Figure 7.3a, the slope for the imaginary parts of the admittance for all embedded PZT transducers at the low-frequency range does not show an obvious difference. Hence, the bonding qualities were good for these embedded PZT transducers, and they can be further used for active sensing SHM purposes.

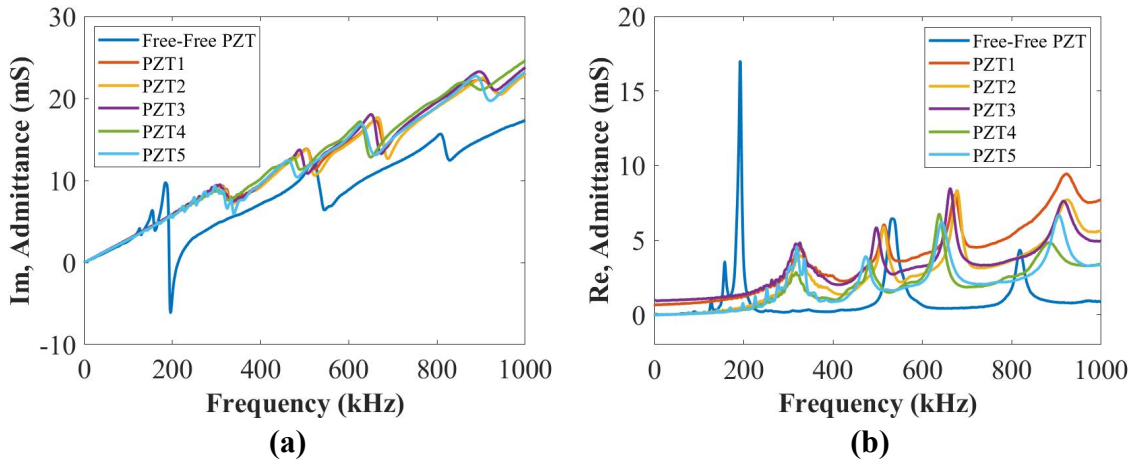

Figure 7.3. The EMI results of **(a)** the imaginary and **(b)** the real parts of the admittance for different PZT transducers.

7.4. Damage Detection and Localization

To verify if the smart repair patch embedded with the diagnostic film and PZT transducers can monitor the integrity of the bondline quality, the damage index (DI) correlation coefficient and the delay-and-sum (DAS) algorithm based on the active sensing method were used to detect and locate the bondline defects. In this section, two types of defects were studied, which were the artificial delamination and the surface-mounted artificial damage. In addition, the blue contact gel was fully applied to the repair patch to bond it with the composite host structure in this section as the baseline signals (as is shown in Figure 7.4a). Here, the contact gel was used in DolphiCam C-Scan to improve the coupling on rougher surfaces. The reason for using this contact gel was that the repair patch could be easily removed at room temperature and used for further measurements.

For simulating the delamination and measuring the current signals, the repair patch was removed and two layers of KAPTON® films were inserted in the designated positions of the repair patch (shown in Figure 7.4b). The repair patch was then put back to the original position as close as possible. To detect the surface-mounted artificial damage, a weighted blue-tack was placed in the designated positions on the surface of the repair patch and the bottom of the host structure as the current signals. During the measurements, the time-of-arrival (ToA) of the A_0 mode could not be distinguished at 50 kHz due to the overlap between the crosstalk and the first wave packet of each measured signal. Therefore, a five-cycle Hanning-windowed toneburst signal at 250 kHz was used as the actuation signal. The actuation amplitude and sampling frequency were 6 V and 100 MHz, respectively. Both the baseline and the current signals were measured at room temperature.

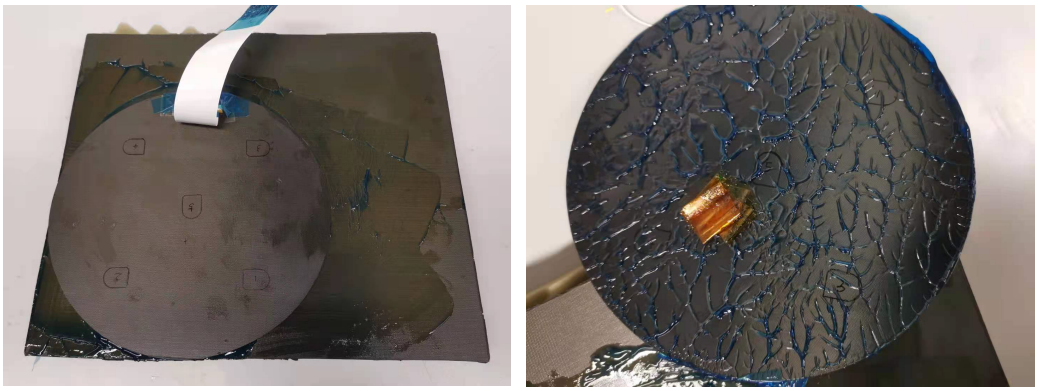

(a) **(b)**

Figure 7.4. Schematics of **(a)** a smart repair patch with the host structure and **(b)** the artificial delamination with blue contact gel.

7.4.1. Delamination

Figure 7.5 to Figure 7.6 compare the results of damage detections and localizations for two artificial delamination positions at 250 kHz by using three and four PZT transducers, respectively. The results show that both the DI results using three and four PZT transducers can detect the damage. The DAS results show that the artificial delamination can be located accurately using three PZT transducers but not using four PZT transducers. Two factors affected the detected results during the measurements. The repair patch cannot be placed in the same position as the baseline status after inserting the KAPTON® films into bondline positions. In addition, the thickness of the contact gel used to bond the repair patch and the host structure cannot be kept at the same value since the contact gel will come back again every time after pushing hardly the repair patch. Both above two factors would affect the measured signals. Therefore, using four PZT transducers cannot locate the damage accurately.

However, the smart repair patch will be bonded to the host structure permanently by the resin film for the actual situation. First, the repaired structure bonded by the resin film will make the patch maintain its original position when delamination happened and retain the same thickness of the bonding area. Furthermore, the selection of the contact glue to bond the patch and the host structure is a compromising way under laboratory conditions and no alternative material can be found to bond the repaired structure together and peel them after measuring. Hence, the above two factors would not affect the measuring results when using four PZT transducers, and it can be confirmed that the DAS results would be accurate when using four PZT transducers for the actual repair.

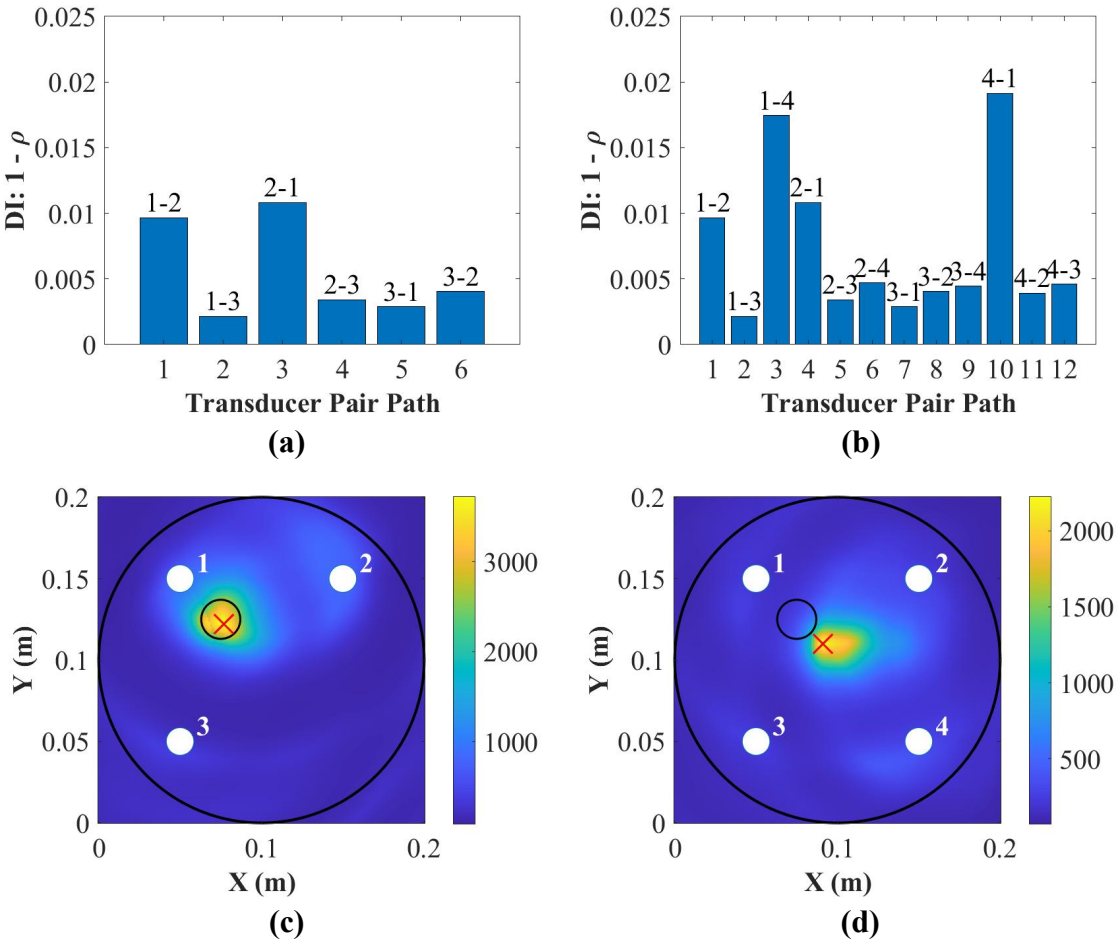

Figure 7.5. Damage detection using **(a)** three PZT and **(b)** four PZT transducers, and localization using **(c)** three PZT and **(d)** four PZT transducers at 250 kHz for the position 1 (where the "○" is the position for real damage and the "×" is the position for predicted damage).

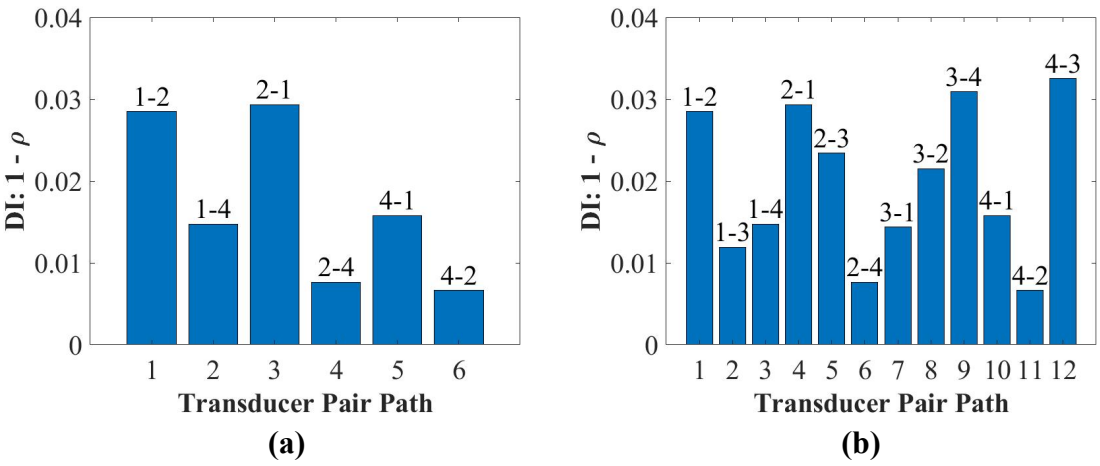

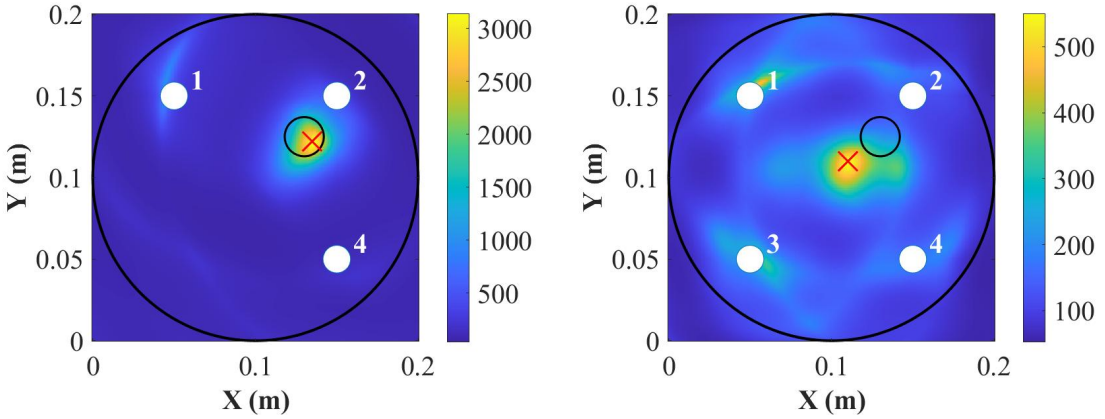

Figure 7.6. Damage detection using **(a)** three PZT and **(b)** four PZT transducers, and localization using **(c)** three PZT and **(d)** four PZT transducers at 250 kHz for the position 2 (where the "○" is the position for real damage and the "×" is the position for predicted damage).

7.4.2. Surface-mounted Artificial Damage – Top of the Repair Patch

To simulate the repair patch suffering the surface damage, a weighted blue-tack was attached on the top of the repair patch. Figure 7.7 to Figure 7.8 show the results of damage detection and localization for the surface-mounted artificial damage attached on the surface of the repair patch. As can be seen in Figure 7.7 to Figure 7.8, both using three and four PZT transducers can detect and locate the damage accurately. In this situation, the blue-tack was removed from the surface of the repair patch only, so the using of contact gel would not become the factor affecting the accuracy of localization results.

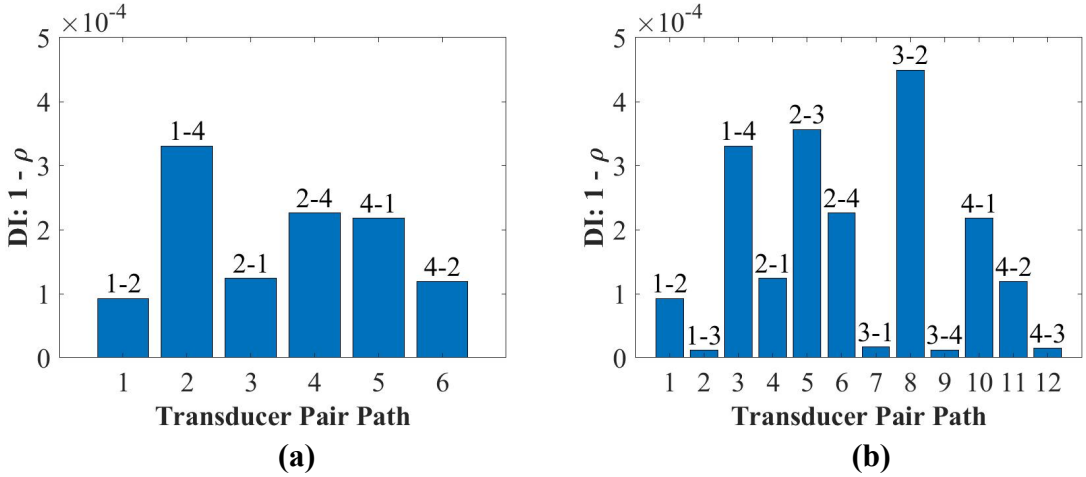

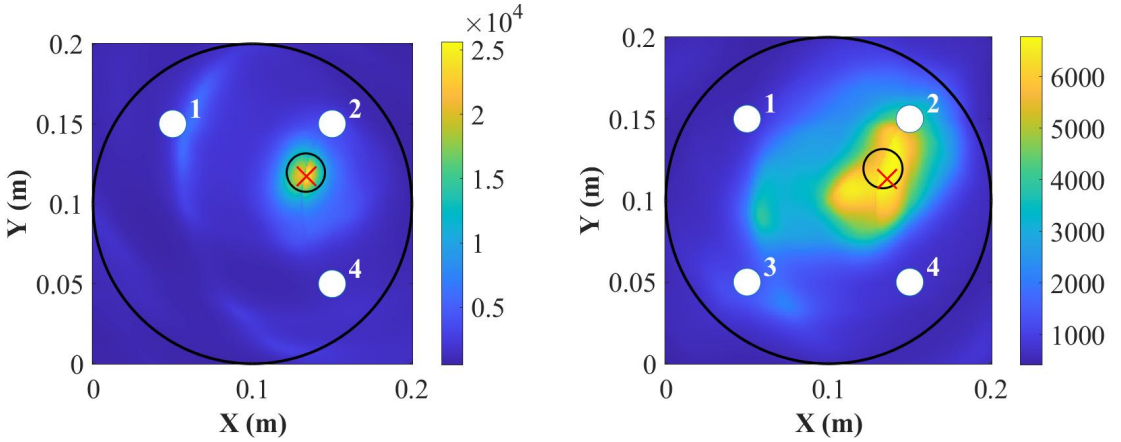

Figure 7.7. Damage detection using **(a)** three PZT and **(b)** four PZT transducers, and localization using **(c)** three PZT and **(d)** four PZT transducers at 250 kHz for the position 1 for the surface-mounted artificial damage on the surface of the repair patch (where the "○" is the position for real damage and the "×" is the position for predicted damage).

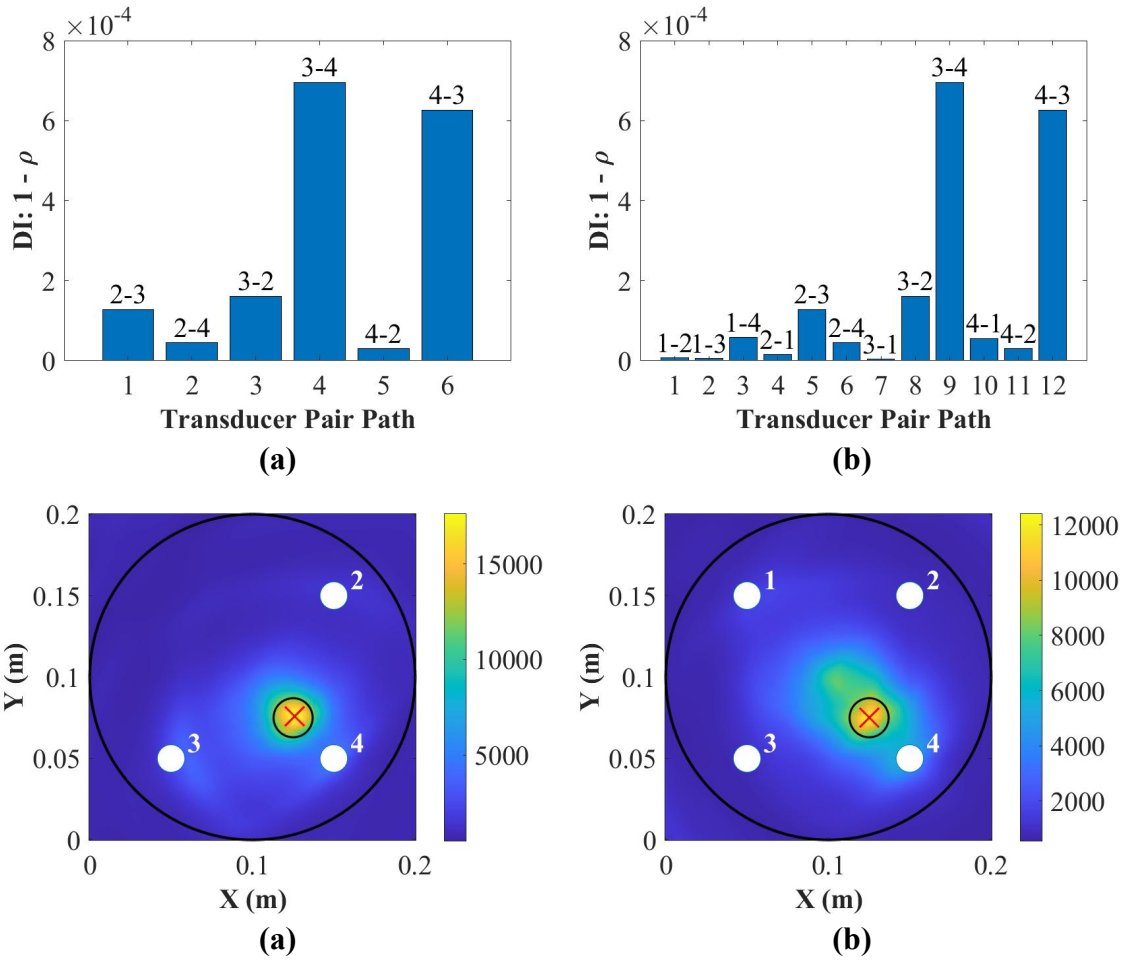

Figure 7.8. Damage detection using **(a)** three PZT and **(b)** four PZT transducers, and localization using **(c)** three PZT and **(d)** four PZT transducers at 250 kHz for the position 2

for the surface-mounted artificial damage on the surface of the repair patch (where the "○" is the position for real damage and the "×" is the position for predicted damage).

7.4.3. Surface-mounted Artificial Damage – Bottom of the Host Structure

To simulate the host structure suffering the surface damage, a weighted blue-tack was attached on the bottom of the host structure, which was the surface of the opposite side of the repair patch. Figure 7.9 to Figure 7.10 show the damage detection and localization for the surface-mounted artificial damage attached on the bottom of the host structure. As can be seen in Figure 7.9 to Figure 7.10, both using three and four PZT transducers can detect and locate the damage. However, the DAS algorithm can locate the damage more accurately using three PZT transducers. In addition, the reason why five PZT transducers were not used for damage localization in this chapter is that the repair patch is relatively small and having more sensors installed generate more noise in the signals. This can be seen with the results from using three and four PZT transducers that the noise in the signal was high enough to mask the scattering from the damage.

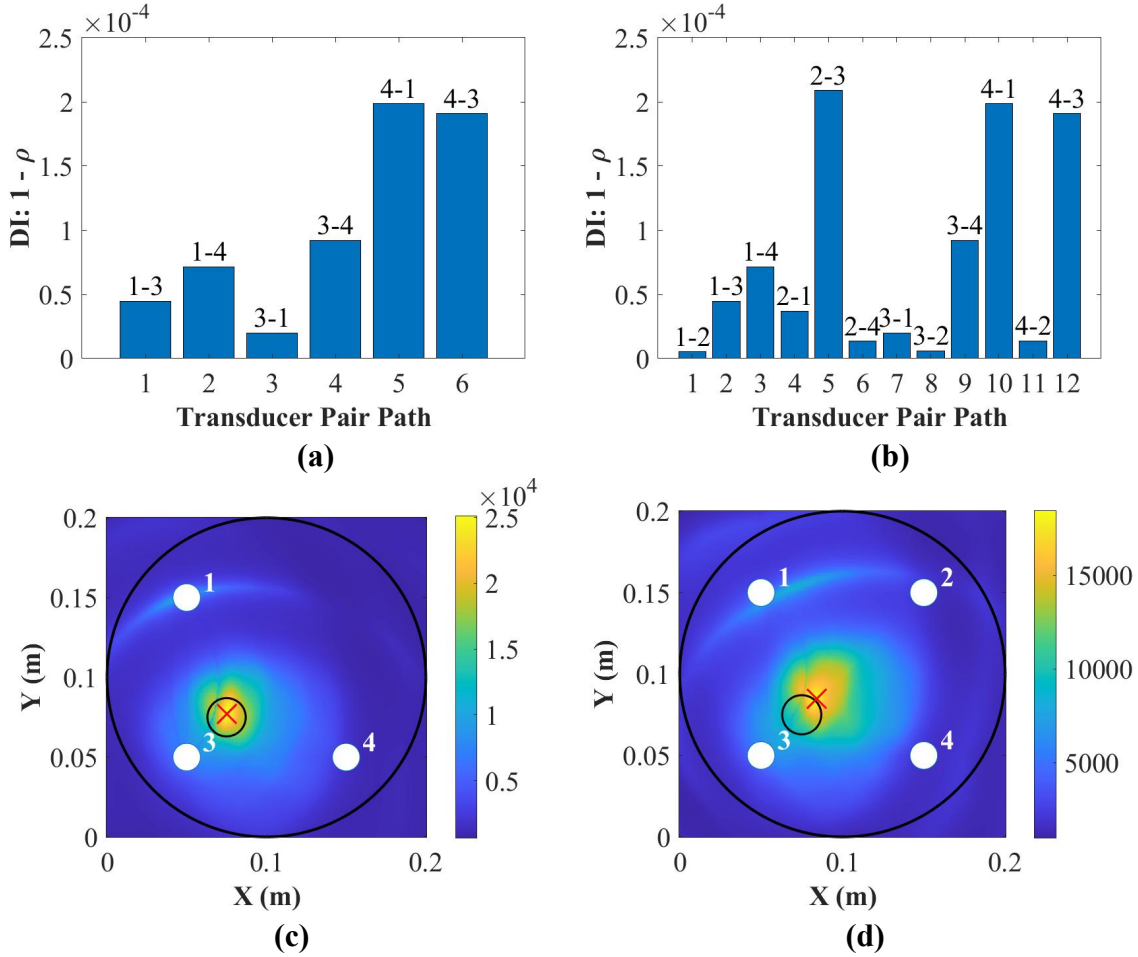

Figure 7.9. Damage detection using **(a)** three PZT and **(b)** four PZT transducers, and localization using **(c)** three PZT and **(d)** four PZT transducers at 250 kHz for the position 1 for the surface-mounted artificial damage on the bottom of the host structure (where the "○" is the position for real damage and the "×" is the position for predicted damage).

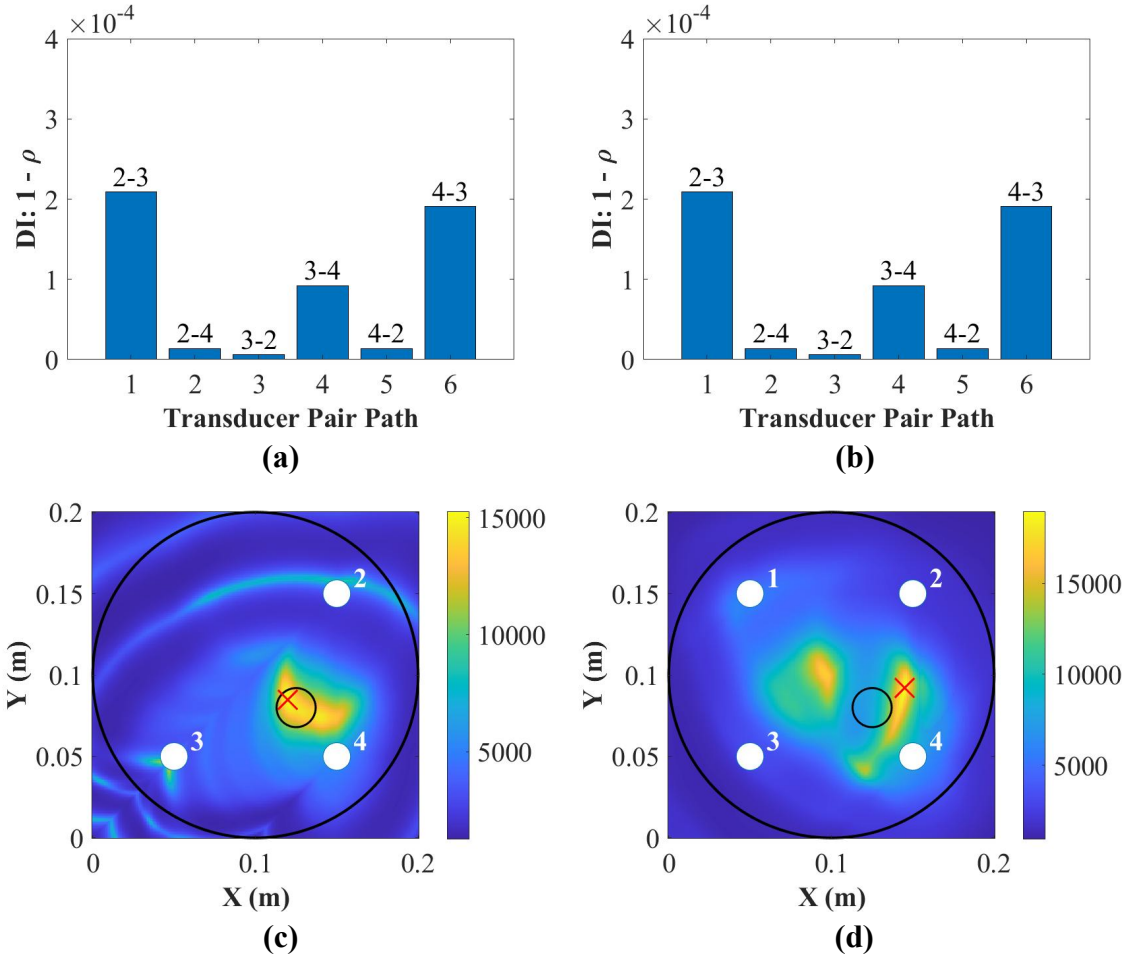

Figure 7.10. Damage detection using **(a)** three PZT and **(b)** four PZT transducers, and localization using **(c)** three PZT and **(d)** four PZT transducers at 250 kHz for the position 2 for the surface-mounted artificial damage on the bottom of the host structure (where the "○" is the position for real damage and the "×" is the position for predicted damage).

7.5. Summary

In this chapter, a smart repair patch was developed using the diagnostic film embedded into the patch using an edge cut-out method. The EMI results manifested that the bonding qualities of embedded PZT transducers were good after manufacturing. For damage detection and localization, the DI correlation coefficient and the DAS algorithm based on the active sensing technique were used. In addition, the blue contact gel was used to bond the repair patch and the host structure together for easier removing the patch and inserting KAPTON® films to

create artificial delamination. Furthermore, the A_0 mode at 50 kHz was not applicable due to the overlap between the crosstalk and the first wave packet of measured signals.

According to the DI results, the use of a smart repair patch can detect the artificial delamination and the surface-mounted artificial damage at 250 kHz using both three and four PZT transducers. Furthermore, the smart repair patch can locate the delamination using three PZT transducers and the surface-mounted artificial damage using four PZT transducers accurately. Since the resin film was replaced by blue contact gel for simulating the bonding and caused the inconsistency and uncertainty between the baseline and the current signals due to removing the patch and inserting the delamination, so the DAS results were not accurate when using four PZT transducers for the S_0 mode at 250 kHz. However, the use of the resin film will keep the composite repair structure consistent and it can be confirmed that using four PZT transducers will locate the delamination accurately using the DAS algorithm for actual composite repair. Therefore, the smart repair patch embedded with the developed diagnostic film and PZT transducers can be used to detect and locate the bondline defects of repaired composite structures based on SHM techniques.

Chapter 8

8. Conclusions and Future Work

8.1. Thesis Review

The aim of the thesis was to investigate the influence of ultrasonic guided waves (UGW) through the thickness of composite laminates under varying temperatures for damage detection and localization based on the active sensing of Structural Health Monitoring (SHM) techniques. To better understand the propagation properties of UGW for achieving above the purpose, UGW actuated by both surface-mounted and embedded lead zirconate titanate (PZT) transducers were evaluated.

To obtain stable signals of UGW actuated by embedded PZT transducers, a novel cut-out method for embedding diagnostic films with phased-array PZT transducers was proposed, which allowed edge trimming possible for the next higher assembly of industrial mass fabrication. The mechanical tests were conducted to evaluate the stabilities of the electro-mechanical impedance (EMI) properties and the active sensing behaviour, and the reductions of tensile and compressive moduli were also investigated for coupons with embedded PZT transducers.

After that, the amplitude and the group velocity of the S_0 and the A_0 modes of UGW and temperature influences through different thicknesses of composites actuated by both surface-mounted and embedded PZT transducers were systematically evaluated. The interactions of UGW with the surface-mounted artificial damage (weighted blue-tack) and the impact damage were studied using a laser Doppler vibrometer (LDV) by both surface-mounted and embedded PZT transducers. In addition, the thickness effects on damage detection and localization for the surface-mounted artificial damage and the impact damage were also investigated by surface-mounted and embedded PZT transducers.

Furthermore, the influence of the embedded position of PZT transducers on UGW was also numerically and experimentally studied. The reversibility of the peak amplitude of the first wave packet of UGW actuated/received by the PZT transducers in different positions was compared. Finally, the possibilities of monitoring the debonding and the artificial damage of the composite laminate bonded by a smart repair patch embedded with the diagnostic film and PZT transducers were also investigated. The results discussed from chapter 3 to chapter 7 have demonstrated that the aim of this research has been achieved.

8.2. Conclusions

In this thesis, the conclusions for each chapter can be drawn as below:

The developed embedding technique alleviates difficulties of the wires coming out of the edge of the composites which has proved so far to be a key impediment to embedding sensors into composites. The EMI technique was used to access the integrity of the bonding properties between the PZT transducers and their host structure. It was found the slope of the imaginary part of the admittance of the embedded PZT transducer is higher than that of the surface-mounted and the free-free PZT transducers at 0~20 kHz. In addition, the first resonance vibrations to the free-free, the embedded and the surface-mounted PZT transcoders are 192 kHz, 347 kHz and 254 kHz for the imaginary part of the admittance, and are 195 kHz, 328 kHz and 265 kHz for the real part of the admittance. Furthermore, the bonding integrity of embedded PZT transducers meets the double-side bonded requirement. The crosstalk issue for the printed circuits has been discussed. The crosstalk can be only eliminated by reducing the density of the printed circuits or adjusting the angles of the connecting wires. Furthermore, mechanical tests for composite coupons embedded with PZT transducers were investigated. First, fatigue tests for the force range of 0.5~5 kN and 1~10 kN with 1 million cycles were studied. The stability of the EMI properties and the active sensing behaviours of UGW remained good up to 1 million cycles at 50 kHz and 250 kHz. It has been demonstrated that the novel embedded circuits printed on the diagnostic film remain conductive and embedded PZT transducers remain active and intact after 1 million loading cycles, which indicates the embedded diagnostic film with networks of PZT transducers can withstand the mechanical loads applied to them. In addition, for the tensile and the compressive tests, the reduction of elastic moduli between standard coupons and coupons embedded with the diagnostic film and PZT transducers was compared. It was found that the embedded diagnostic film with PZT transducers made tensile modulus reduce by around 21% and made compressive modulus reduce by around 13%. Although the strength reduction was not ideal for this situation, the anticipated results would be significantly less when reducing the unprinted area of the diagnostic film during the lay-up. However, considering the benefits of this novel embedding technique, the embedded diagnostic film with the networks of PZT transducers can be applied as a layer (prepreg) during the lay-up. Moreover, this technique allows for embedding larger sensor networks with optimizing the design of connections. Therefore, this embedding technique would be a promising technique for SHM applications.

In ***chapter 4***, FEM explicit and implicit dynamic analyses were investigated for simulating UGW actuated by surface-mounted and embedded PZT transducers. Three strategies were proposed to model embedded PZT transducers into composite laminate for the implicit dynamic analysis. It was found that the result of the embedded strategy I was in good agreement with the experimental result. The influence of the structural damping on the group velocity of UGW was also investigated. It was found that values of the structural damping for composite damping cannot compensate for the group velocity of UGW very much. Finally, interactions

of UGW with the surface-mounted artificial damage and the impact damage have been investigated. It was found that UGW can successfully interact with both the surface-mounted artificial damage and the impact damage at 50 kHz and 250 kHz.

In ***chapter 5***, it was found that the amplitude of the A_0 mode is influenced more than that of the S_0 mode by the thickness variation because the A_0 mode (out-of-plane motion) needs more energy for the particles to move in the thicker composite laminates than the S_0 mode (in-plane motion). In addition, the group velocity of the A_0 mode increases with the increase of the thickness, while the group velocity of the S_0 mode for the 9 mm panel is faster than that of the 4 mm panel and slower than that of the 2 mm panel. This was later attributed to the dispersive nature of the S_0 mode at the frequency thickness product of 250 kHz and 9 mm plate. Overall, the amplitude of the A_0 mode is not dependent on the thickness that it reduces with the increased temperature for all panels, while that of the S_0 mode has different trends for panels of different thicknesses. In addition, the group velocities become slow for both the A_0 and the S_0 modes for all those panels with the increase of the temperature, which are not dependent on the thickness. Therefore, it is very important to define the relationship between the phase and the velocity change for composite panels, depending on their thickness, so that the compensation algorithm can be applied and damage detection can be carried out under different temperatures reliably. The LDV measurement results showed only the A_0 mode (50 kHz) interacted with the simulated damage for the thickness of 2mm, 4 mm and 9 mm panels and it was concluded as the more appropriate mode for the surface damage detection. The DI results showed that the A_0 mode has better detection of the surface simulated damage (added mass) for the 2 mm and the 4 mm panels and the DAS algorithm showed this type of damage could be located accurately excepted for the S_0 mode in the 9 mm panel at 250 kHz. As it had been demonstrated in the appendix in section 9.2 the damage could be located accurately at 250 kHz for the 9 mm panel when the surface-mounted artificial damage was attached on the same side of the PZT transducers. Hence, the S_0 mode became less sensitive when the thickness of the composite panel increased. Although the LDV results demonstrated the superiority of the A_0 mode for detecting surface damages, the results of the damage localization with the PZT recorded sensors showed that both 50 kHz and 250 kHz results were of good accuracy. This was due to the high signal to noise ratio at 250 kHz due to the dynamical structure (plate + sensor). The guided wave propagation and response with the PZTs for the detection of impact damage were also studied. The LDV results showed that both the A_0 mode (50 kHz) and the S_0 mode (250 kHz) had significant disturbance (reflection and refraction) with the impact damage (surface cracks and internal delamination) for the thickness of 2 mm, 4 mm and 9 mm panels. The damage index results showed the S_0 mode had better results for detection and localization for the 2 mm and the 4 mm panels which matched with the conclusion from the EMI results and hence higher reliability in damage detection. For the 9 mm panel, neither of the frequencies showed robust and reliable results in detection and localization which was attributed to the small severity of the damage in the C-scan result (hardly noticed through thickness). Therefore, the damage reflected waves were of small amplitude and falls mainly within the noise level and the damage should be extended for reliable detection. Another

important factor was that for the delay-and-sum results usually guided waves are chosen in their non-dispersive zone, but the dispersion curve results for the 9 mm panel at 250 kHz showed that the group velocities for the A_0 and the S_0 modes were too close to be distinguished from each other and the localization results would not be accurate.

In ***chapter 6***, the thickness effectiveness of composites on UGW excitation and propagation actuated by embedded PZT transducers with temperature influences, damage detection and localization were studied in detail. The active sensing results (in-plane motion) show that the A_0 mode dominates at 50 kHz and the S_0 mode dominates at 250 kHz. Both the A_0 and the S_0 modes have a linear reduction with the increase of the thickness, which is not dependent on the thickness. The reason why conclusions are differences between the LDV measurements and the active sensing results for the in-plane motion is that LDV captures the surface wave propagation while the active sensing method is actuated/recorded by both embedded PZT transducers. The EMI results demonstrated that the thickness has no influence on the EMI properties and the higher actuation frequency (250 kHz) will amplify the amplitude of the A_0 and the S_0 modes significantly. The temperature results show that the amplitude of the A_0 mode increases with the increased temperature at 50 kHz, which is not dependent on the thickness. The amplitude of the S_0 mode increases for the 2 mm and the 9 mm panels and reduces for the 4 mm panel at 250 kHz, which is not dependent on the thickness. In addition, the ToF results show that group velocities become slow for the A_0 and the S_0 modes with the increased temperature except for the A_0 mode at 50 kHz for the 2 mm panel. Comparing the embedded temperature results to the surface-mounted temperature results, the peak amplitude of the A_0 mode (50 kHz) reduces for surface-mounted PZT transducers but increases for embedded PZT transducers with the increased temperatures for the thickness of 2 mm, 4 mm and 9 mm panels. In addition, the peak amplitude of the S_0 mode (250 kHz) increases first and then reduces for the surface-mounted signals but increases only for the embedded signals for the 2 mm panel. The ToF of the A_0 mode (50 kHz) for the 2 mm panels increases for the surface-mounted signals but reduces first then increases for the embedded signals. The results of the LDV measurements show that only the A_0 mode interacted with the surface-mounted artificial damage at 50 kHz and it can be concluded that the A_0 mode is the more appropriate mode for the surface damage. The results of the damage index and the DAS algorithm show that both the A_0 and the S_0 modes can detect and locate the surface damage accurately due to the high signal to noise ratio at 250 kHz since the dynamical structure (plate + sensor). As it has been dementated previously that the S_0 mode cannot locate the surface damage accurately using surface-mounted PZT transducers at 250 kHz for the 9 mm panel, so embedded PZT transducers are more sensitive and can have a better solution for locating the surface damage for the thick composites. Also presented were results for impact damage. The results of the LDV measurements show that both the A_0 and the S_0 modes show the reflection and refraction with the impact damage for the thickness of 2 mm, 4 mm and 9 mm panels. The damage index can detect the impact damage and the DAS algorithm can locate the impact damage accurately for the A_0 mode at 50 kHz while that of surface-mounted PZT transducers cannot. This also demonstrates the embedded PZT transducer can have better results than surface-mounted PZT

transducers for locating the impact damage. The experimental studies involved fabrications of composite coupons with the thickness of 2 mm, 4 mm and 9 mm panels. PZT transducers were mounted on the surface, embedded in the quarter and the middle of each composite coupon. First, the EMI results for all PZT transducers show that all PZT transducers have good bonding properties and can be used for further active sensing measurements. Second, UGW actuated by the PZT transducers in different placing positions were compared. It was found that the peak amplitude of the first wave packet for the surface-mounted signal is higher than that of the quarter- and the middle- embedded signals at 50 kHz (A_0 mode dominates) and 250 kHz (S_0 mode dominates) except for the 4 mm coupon at 250 kHz (S_0 mode dominates). Therefore, the amplitude of the S_0 mode is dependent on thickness. Finally, the reversibility of UGW between the surface-mounted, the quarter- and the middle- embedded PZT transducers has been studied. It has been found that the peak amplitudes of the first wave packet actuated by the quarter- and the middle- embedded PZT transducers are higher than that of the amplitude actuated by surface-mounted PZT transducers at 50 kHz and 250 kHz. Furthermore, the peak amplitude of the first wave packet actuated by the quarter-embedded transducer is higher than that of the amplitude actuated by the middle-embedded transducer for the 2 mm and the 4 mm coupons, but lower than that of the amplitude actuated by the middle-embedded transducers for the 9 mm coupon. Therefore, the embedded PZT transducer can actuate a higher amplitude of UGW for both the S_0 and the A_0 modes than that of the surface-mounted PZT transducer for comparing the reversible signals.

In ***chapter 7***, a smart repair patch was developed using the diagnostic film embedded into the patch using an edge cut-out method. The EMI results manifested that the bonding qualities of embedded PZT transducers were good after manufacturing. For damage detection and localization, the DI correlation coefficient and the DAS algorithm based on the active sensing technique were used. In addition, blue contact gel was used to bond the repair patch and the host structure together for easier removing the patch and inserting KAPTON® films to create the artificial delamination. Furthermore, the A_0 mode at 50 kHz was not applicable due to the overlap between the crosstalk and the first wave packet of the measured signals. According to the DI results, the use of a smart repair patch can detect the artificial delamination and the surface-mounted artificial damage at 250 kHz using both three and four PZT transducers. Furthermore, the smart repair patch can locate the delamination using three PZT transducers and the surface-mounted-artificial damage using four PZT transducers accurately. Since the resin film was replaced by blue contact gel for simulating the bonding and caused the inconsistency and uncertainty between the baseline and the current signals due to removing the patch and inserting delamination, so the DAS results were not accurate when using four PZT transducers for the S_0 mode at 250 kHz. However, the use of the resin film will keep the composite repair structure consistent and it can be confirmed that using four PZT transducers will locate the delamination accurately using the DAS algorithm for actual composite repair. Therefore, the smart repair patch embedded with the developed diagnostic film and PZT transducers can be used to detect and locate the bondline defects of repaired composite structures based on SHM techniques.

8.3. Further Work Recommendations

In this research, the results of mechanical tests (tensile and compressive tests) in chapter 3 could be improved for the coupons using unidirectional carbon fibre prepregs Hexply® IM7/8552, so the author's first suggestion is to find an alternative unidirectional carbon fibre prepregs (for instance, Hexply® M21) to fabricate the coupons with the embedded diagnostic films and PZT transducers. During previous impact tests for the 9 mm panel, it was found that the composite panel made by Hexply® M21 took more energy to achieve a similar area of the impact damage, so the elastic properties of a composite panel made by Hexply® M21 may have less elastic reduction when doing tensile and compressive tests compared to the Hexply® IM7/8552.

In addition, the crosstalk issue can significantly affect the start of UGW signals especially actuated by embedded PZT transducers. The overlap between the crosstalk and the first wave packet of UGW will make temperature compensation and damage identification impossible, which has been deeply confusing to the author all the time during the period of PhD research. However, the author has found that the crosstalk disappeared sometimes when changing the angle of the external connected soldering cable (for instance, 90° to the panel) during the setup for the chamber measurements or using 2 more connectors (reported in section 3.5 in chapter 3). Therefore, it is highly suggested the following researchers to dig the reason, theoretically explain it (maybe due to electromagnetic induction) and experimentally solve the issue.

Furthermore, the implicit dynamic analysis (Abaqus/Standard) for simulating UGW with the embedded PZT transudes was extremely time-consuming (reported in section 4.2 in chapter 4). Therefore, it highly recommends proposing an analytical solution to simulate the equivalent radial deformation of the embedded PZT actuator and the output voltage of the embedded PZT sensor. Hence, the explicit dynamic analysis (Abaqus/Explicit) can be used for the models with embedded PZT transducers.

Finally, the algorithm for temperature compensation using the diagnostic film with phased-array PZT transducers for both surface-mounting and embedding shall be developed. The use of the resin film, the adhesive film and the diagnostic film have changed guided wave properties, and relationships of the temperature with the peak amplitude and the group velocity have been changed, which are different from the previous surface-mounted results. In addition, the relationships of the temperature with UGW actuated by surface-mounted and embedded PZT transducers were reversed for certain cases (reported in section 6.4 in chapter 6). Therefore, the algorithm for temperature compensation needs to be developed to adapt to the current situations for both surface-mounted and embedded PZT transducers.

9. Appendix

9.1. Dispersion Curves

In this appendix section, the dispersive curves based on the analytical method [32] are plotted to study the thickness influence on the group velocities of the S_0 and the A_0 modes. Figure 9.1 to Figure 9.3 plot the dispersion curves of quasi-isotropic composite panels for the thickness of 2 mm, 4 mm and 9 mm panels at 0° in the experiments, respectively. According to Figure 9.3a, the shapes of these curves look similar and the only difference is their frequency range. Figure 9.1b to Figure 9.3b shows the dispersion curves from 0~250 kHz, these figures clearly indicate the group velocity of the A_0 and the S_0 modes at 250 kHz are closer for increasing thickness. This means the thickness considerably affects the group velocity of the S_0 mode at 250 kHz. When the thickness is raised to 10 mm, the group velocities for the A_0 and the S_0 modes are almost identical (same time-of-arrival value) which will cause the signal to interact with each other, thus it is difficult for damage detection and localization of the S_0 mode at 250 kHz.

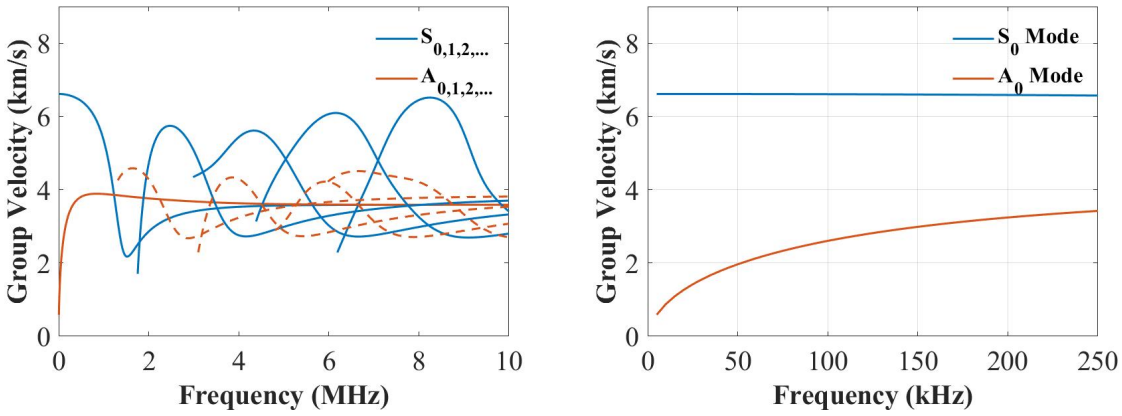

Figure 9.1. Dispersion Curves for the group velocity from **(a)** 0~10 MHz and **(b)** 0~250 kHz for the 2 mm panel.

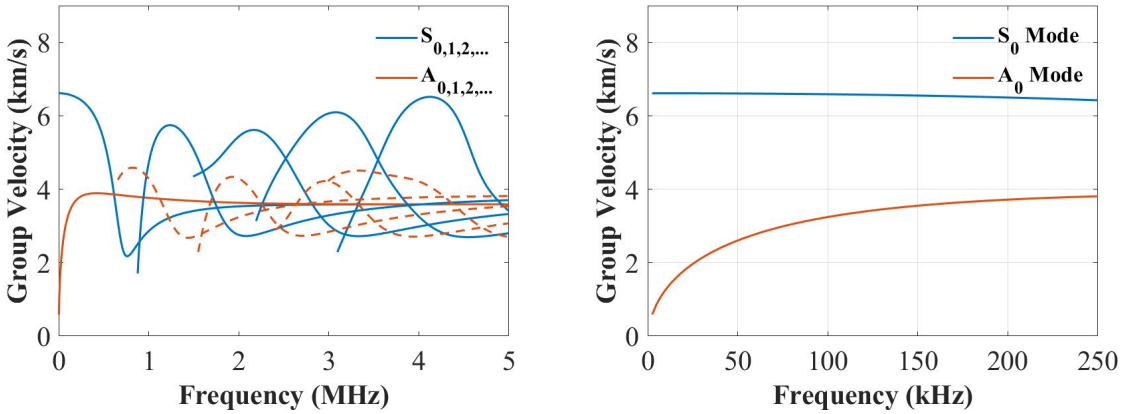

Figure 9.2. Dispersion Curves for the group velocity from **(a)** 0~5 MHz and **(b)** 0~250 kHz for the 4 mm panel.

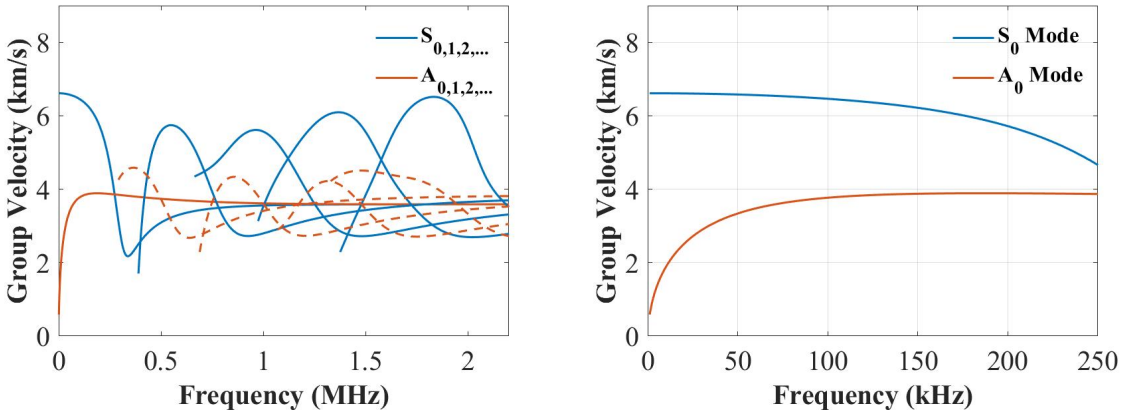

Figure 9.3. Dispersion Curves for the group velocity from **(a)** 0~2.5 MHz and **(b)** 0~250 kHz for the 9 mm panel.

9.2. Damage Detection and Localization

To demonstrate the thickness effect on thick composites, the surface-mounted artificial damage (blue-tack) was also attached to the composite surface on the same side of the PZT transducers to compare the those on the opposite side of the PZT transducers in section 5.5.2. As can be seen from Figure 9.4 to Figure 9.9, 50 kHz (A_0 mode) is more suitable for the surface damage due to the high DI value, and both 50 kHz (A_0 mode) and 250 kHz (S_0 mode) can locate the surface damage accurately.

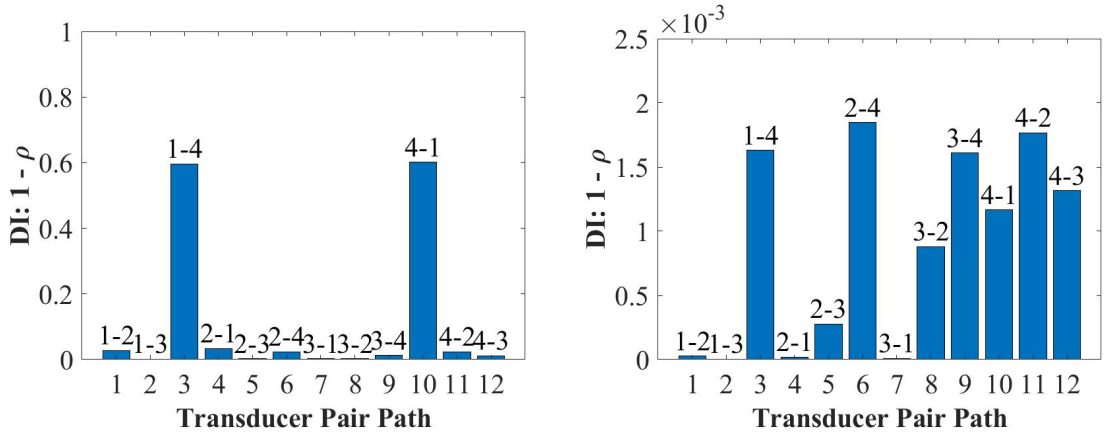

Figure 9.4. Damage detection for the 2 mm panel at **(a)** 50 kHz and **(b)** 250 kHz.

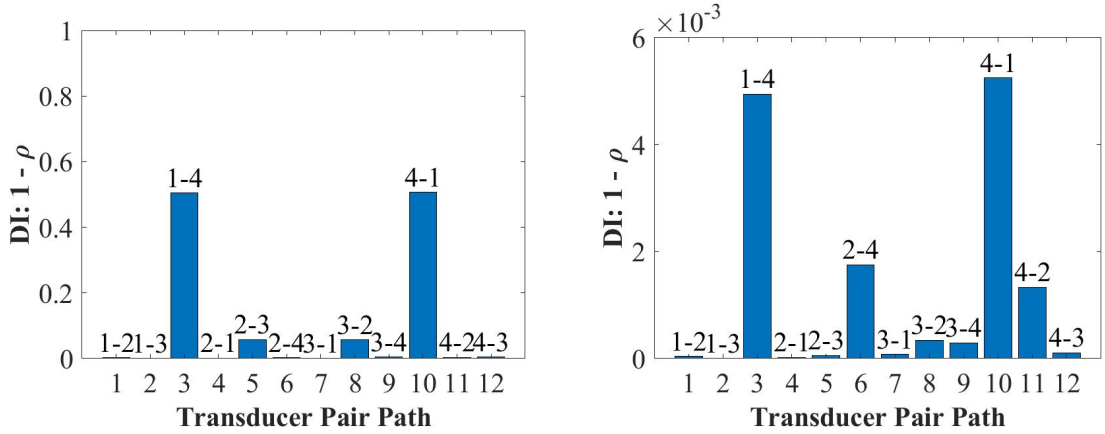

Figure 9.5. Damage detection for the 4 mm panel at **(a)** 50 kHz and **(b)** 250 kHz.

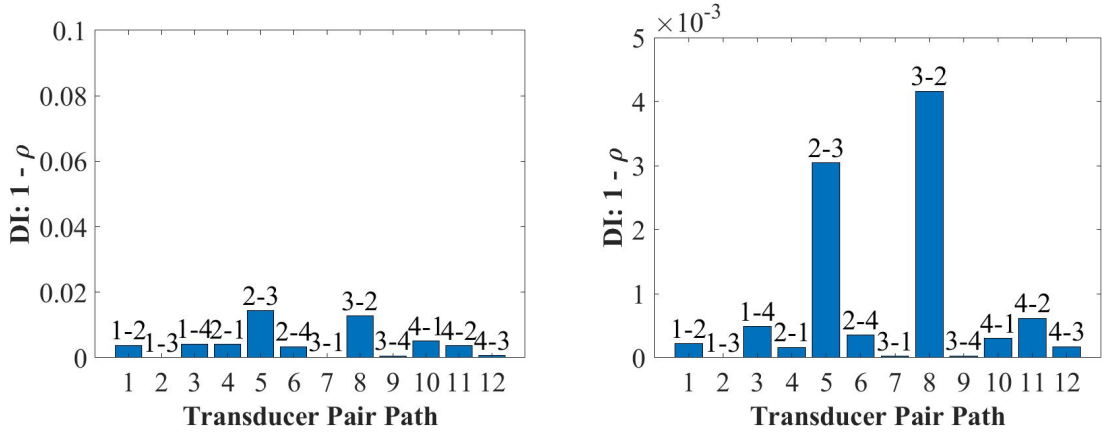

Figure 9.6. Damage detection for the 9 mm panel at **(a)** 50 kHz and **(b)** 250 kHz.

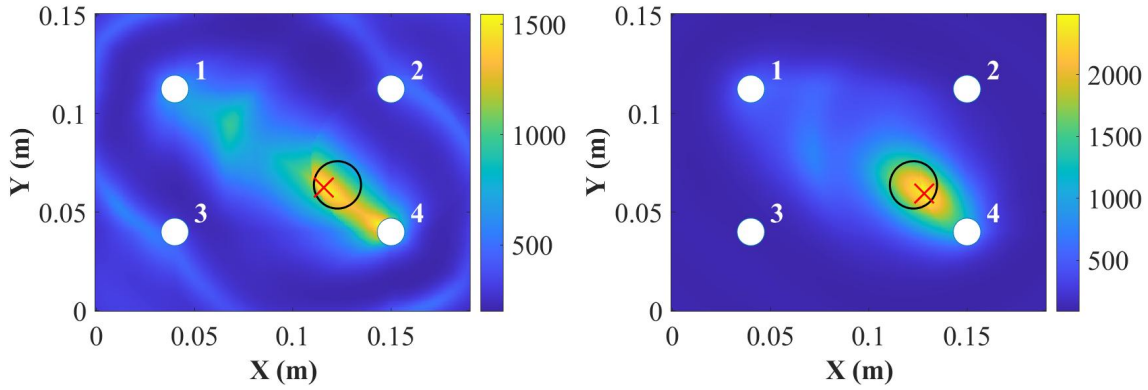

(a) **(b)**

Figure 9.7. Damage localization for the 2 mm panel at **(a)** 50 kHz and **(b)** 250 kHz (where the "○" is the position for real damage and the "×" is the position for predicted damage).

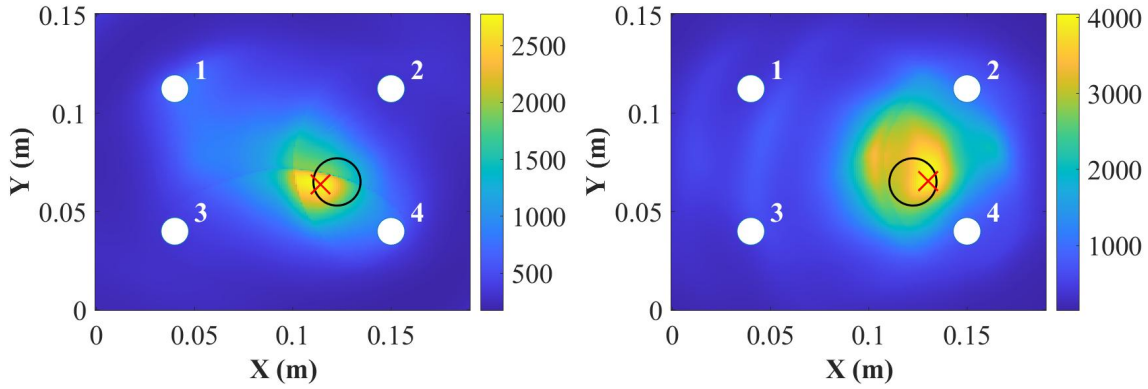

(a) **(b)**

Figure 9.8. Damage localization for the 4 mm panel at **(a)** 50 kHz and **(b)** 250 kHz (where the "○" is the position for real damage and the "×" is the position for predicted damage).

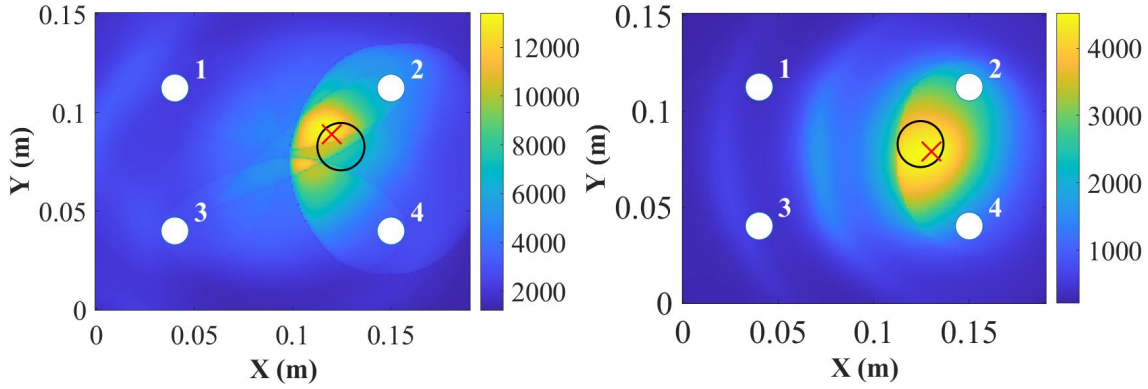

(a) **(b)**

Figure 9.9. Damage localization for the 9 mm panel at **(a)** 50 kHz and **(b)** 250 kHz (where the "○" is the position for real damage and the "×" is the position for predicted damage).

References

[1] G.C. Kahandawa, J. Epaarachchi, H. Wang, K. Lau, Use of FBG sensors for SHM in aerospace structures, Photonic Sensors 2(3) (2012) 203-214.
[2] V. Giurgiutiu, Structural health monitoring of aerospace composites, Academic Press2015.
[3] W.K. Chiu, L.R.F. Rose, N. Nadarajah, Scattering of the Fundamental Anti-symmetric Lamb Wave by a Mid-plane Edge Delamination in a Fiber-composite Laminate, Procedia Engineering 188 (2017) 317-324.
[4] L. Si, Z. Li, Online structural state assessment for aerospace composite structures using an acousto-ultrasonics-based multi-damage index identification approach, Structural Health Monitoring (2020) 1475921719899334.
[5] A.H. Orta, J. Vandendriessche, M. Kersemans, W. Van Paepegem, N.B. Roozen, K. Van Den Abeele, Modeling lamb wave propagation in visco-elastic composite plates using a fifth-order plate theory, Ultrasonics 116 (2021) 106482.
[6] A. Klepka, L. Pieczonka, W.J. Staszewski, F. Aymerich, Impact damage detection in laminated composites by non-linear vibro-acoustic wave modulations, Composites Part B: Engineering 65 (2014) 99-108.
[7] A. De Luca, F. Caputo, Z. Sharif Khodaei, M.H. Aliabadi, Damage characterization of composite plates under low velocity impact using ultrasonic guided waves, Composites Part B: Engineering 138 (2018) 168-180.
[8] M. Dziendzikowski, K. Dragan, A. Katunin, Localizing impact damage of composite structures with modified RAPID algorithm and non-circular PZT arrays, Archives of Civil and Mechanical Engineering 17 (2017) 178-187.
[9] R. James, V. Giurgiutiu, Towards the generation of controlled one-inch impact damage in thick CFRP composites for SHM and NDE validation, Composites Part B: Engineering 203 (2020) 108463.
[10] M. Dziendzikowski, A. Kurnyta, K. Dragan, S. Klysz, A. Leski, In situ Barely Visible Impact Damage detection and localization for composite structures using surface mounted and embedded PZT transducers: A comparative study, Mechanical Systems and Signal Processing 78 (2016) 91-106.
[11] M. Philibert, C. Soutis, M. Gresil, K. Yao, Damage detection in a composite T-joint using guided Lamb waves, Aerospace 5(2) (2018) 40.
[12] A. Coles, B.A. de Castro, C. Andreades, F.G. Baptista, M. Meo, F. Ciampa, Impact Localization in Composites Using Time Reversal, Embedded PZT Transducers, and Topological Algorithms, Frontiers in Built Environment 6 (2020) 27.
[13] H. Hsiao, I. Daniel, S. Wooh, A new compression test method for thick composites, Journal of Composite Materials 29(13) (1995) 1789-1806.

[14] R. Haj-Ali, R. El-Hajjar, A. Muliana, Cohesive fracture modeling of crack growth in thick-section composites, Engineering Fracture Mechanics 73(15) (2006) 2192-2209.
[15] M. Duan, Z. Yue, Q. Song, Investigation of damage to thick composite laminates under low-velocity impact and frequency-sweep vibration loading conditions, Advances in Mechanical Engineering 12(10) (2020).
[16] F. Hervin, L. Maio, P. Fromme, Guided wave scattering at a delamination in a quasi-isotropic composite laminate: Experiment and simulation, Composite Structures 275 (2021).
[17] V. Giurgiutiu, Structural Health Monitoring with Piezoelectric Wafer Active Sensors, Academic Press2014.
[18] F.-G. Yuan, Structural health monitoring (SHM) in aerospace structures, Woodhead Publishing2016.
[19] M.F. Aliabadi, Z.S. Khodaei, Structural health monitoring for advanced composite structures, World Scientific2017.
[20] D. Chronopoulos, Calculation of guided wave interaction with nonlinearities and generation of harmonics in composite structures through a wave finite element method, Composite Structures 186 (2018) 375-384.
[21] S. Carrino, A. Maffezzoli, G. Scarselli, Active SHM for composite pipes using piezoelectric sensors, Materials Today: Proceedings 34 (2021) 1-9.
[22] A.A.R. Broer, R. Benedictus, D. Zarouchas, The Need for Multi-Sensor Data Fusion in Structural Health Monitoring of Composite Aircraft Structures, Aerospace 9(4) (2022) 183.
[23] H. Rocha, C. Semprimoschnig, J.P. Nunes, Sensors for process and structural health monitoring of aerospace composites: A review, Engineering Structures 237 (2021) 112231.
[24] V. Memmolo, L. Maio, N.D. Boffa, E. Monaco, F. Ricci, Damage detection tomography based on guided waves in composite structures using a distributed sensor network, Optical Engineering 55(1) (2015) 011007.
[25] M.K. Malik, D. Chronopoulos, G. Tanner, Transient ultrasonic guided wave simulation in layered composite structures using a hybrid wave and finite element scheme, Composite Structures 246 (2020) 112376.
[26] I.N. Giannakeas, Z. Sharif Khodaei, M.H. Aliabadi, Digital clone testing platform for the assessment of SHM systems under uncertainty, Mechanical Systems and Signal Processing 163 (2022) 108150.
[27] C. Kexel, T. Maetz, M. Mälzer, J. Moll, Digital communication across orthotropic composite components using guided waves, Composite Structures 209 (2019) 481-489.
[28] A. Spada, M. Capriotti, F. Lanza di Scalea, Global-Local model for guided wave scattering problems with application to defect characterization in built-up composite structures, International Journal of Solids and Structures 182-183 (2020) 267-280.
[29] M.H. Aliabadi, Structural Health Monitoring for Life Management Of Composite Fuselage, (2021).
[30] A picture of health: Clean Sky's SHERLOC leaves no clue unturned. https://clean-aviation.eu/sites/default/files/2021-10/CLEAN_SKY_Article_Sherloc.pdf.

[31] H. Rocha, C. Semprimoschnig, J.P. Nunes, Sensors for process and structural health monitoring of aerospace composites: A review, Engineering Structures 237 (2021).
[32] Z. Su, L. Ye, Identification of damage using Lamb waves: from fundamentals to applications, Springer Science & Business Media2009.
[33] V. Giurgiutiu, A. Zagrai, J. Jing Bao, Piezoelectric wafer embedded active sensors for aging aircraft structural health monitoring, Structural Health Monitoring 1(1) (2002) 41-61.
[34] H.S. Kim, A. Ghoshal, A. Chattopadhyay, W.H. Prosser, Development of embedded sensor models in composite laminates for structural health monitoring, Journal of reinforced plastics and composites 23(11) (2004) 1207-1240.
[35] G. Dib, E. Koricho, O. Karpenko, M. Haq, L. Udpa, S.S. Udpa, Feasibility of PZT ceramics for impact damage detection in composite structures, AIP Conference Proceedings, AIP, 2015, pp. 1072-1080.
[36] A. Güemes, A. Fernandez-Lopez, A.R. Pozo, J. Sierra-Pérez, Structural health monitoring for advanced composite structures: A review, Journal of Composites Science 4(1) (2020).
[37] V. Giurgiutiu, Structural health monitoring of aerospace composites, 2015.
[38] S. Jinachandran, G. Rajan, Fibre bragg grating based acoustic emission measurement system for structural health monitoring applications, Materials 14(4) (2021) 1-16.
[39] A. Güemes, A. Fernández-López, P.F. Díaz-Maroto, A. Lozano, J. Sierra-Perez, Structural health monitoring in composite structures by fiber-optic sensors, Sensors (Switzerland) 18(4) (2018).
[40] Y. Qiu, Q.B. Wang, H.T. Zhao, J.A. Chen, Y.Y. Wang, Review on composite structural health monitoring based on fiber Bragg grating sensing principle, Journal of Shanghai Jiaotong University (Science) 18(2) (2013) 129-139.
[41] R. Soman, J. Wee, K. Peters, Optical Fiber Sensors for Ultrasonic Structural Health Monitoring: A Review, Sensors 21(21) (2021) 7345.
[42] S. Dong, M. Yuan, Q. Wang, Z. Liang, A Modified Empirical Wavelet Transform for Acoustic Emission Signal Decomposition in Structural Health Monitoring, Sensors 18(5) (2018) 1645.
[43] S.K. Al-Jumaili, M.R. Pearson, K.M. Holford, M.J. Eaton, R. Pullin, Acoustic emission source location in complex structures using full automatic delta T mapping technique, Mechanical Systems and Signal Processing 72-73 (2016) 513-524.
[44] P. Argus, M. Gurka, B. Kelkel, Development of a small-scale and low-cost SHM system for thin-walled CFRP structures based on acoustic emission analysis and neural networks, Proceedings of SPIE - The International Society for Optical Engineering, 2019.
[45] T. Fu, Y. Liu, Q. Li, J. Leng, Fiber optic acoustic emission sensor and its applications in the structural health monitoring of CFRP materials, Optics and Lasers in Engineering 47(10) (2009) 1056-1062.
[46] M.R. Pearson, M. Eaton, C. Featherston, R. Pullin, K. Holford, Improved acoustic emission source location during fatigue and impact events in metallic and composite structures, Structural Health Monitoring 16(4) (2017) 382-399.

[47] A. De Luca, D. Perfetto, A. De Fenza, G. Petrone, F. Caputo, Guided wave SHM system for damage detection in complex composite structure, Theoretical and Applied Fracture Mechanics 105 (2020).
[48] T. Wandowski, P. Kudela, W.M. Ostachowicz, Numerical analysis of elastic wave mode conversion on discontinuities, Composite Structures 215 (2019) 317-330.
[49] H. Mei, V. Giurgiutiu, Guided wave excitation and propagation in damped composite plates, Structural Health Monitoring 18(3) (2019) 690-714.
[50] H. Mei, M.F. Haider, R. James, V. Giurgiutiu, Pure S0 and SH0 detections of various damage types in aerospace composites, Composites Part B: Engineering 189 (2020).
[51] H. Mei, V. Giurgiutiu, Characterization of multilayer delaminations in composites using wavenumber analysis: numerical and experimental studies, Structural Health Monitoring 20(3) (2021) 1004-1029.
[52] P. Ochôa, V. Infante, J.M. Silva, R.M. Groves, Detection of multiple low-energy impact damage in composite plates using Lamb wave techniques, Composites Part B: Engineering 80 (2015) 291-298.
[53] O. Putkis, R.P. Dalton, A.J. Croxford, The anisotropic propagation of ultrasonic guided waves in composite materials and implications for practical applications, Ultrasonics 65 (2016) 390-399.
[54] C.A.C. Leckey, K.R. Wheeler, V.N. Hafiychuk, H. Hafiychuk, D.A. Timuçin, Simulation of guided-wave ultrasound propagation in composite laminates: Benchmark comparisons of numerical codes and experiment, Ultrasonics 84 (2018) 187-200.
[55] P.A. Ochôa, R.M. Groves, R. Benedictus, Effects of high-amplitude low-frequency structural vibrations and machinery sound waves on ultrasonic guided wave propagation for health monitoring of composite aircraft primary structures, Journal of Sound and Vibration 475 (2020).
[56] P. Deng, O. Saito, Y. Okabe, H. Soejima, Simplified modeling method of impact damage for numerical simulation of Lamb wave propagation in quasi-isotropic composite structures, Composite Structures 243 (2020) 112150.
[57] R. Xia, J. Zhu, J. Yi, S. Shao, Z. Li, Guided wave propagation in multilayered periodic piezoelectric plate with a mirror plane, International Journal of Mechanical Sciences 204 (2021) 106539.
[58] S. Guo, M. Rebillat, N. Mechbal, Dichotomy property of dispersion equation of guided waves propagating in anisotropic composite plates, Mechanical Systems and Signal Processing 164 (2022).
[59] R. James, V. Giurgiutiu, Towards the generation of controlled one-inch impact damage in thick CFRP composites for SHM and NDE validation, Composites Part B: Engineering 203 (2020).
[60] A.D. Abetew, T.C. Truong, S.C. Hong, J.R. Lee, J.B. Ihn, Parametric optimization of pulse-echo laser ultrasonic system for inspection of thick polymer matrix composites, Structural Health Monitoring 19(2) (2020) 443-453.

[61] C. Andreades, G.P. Malfense Fierro, M. Meo, A nonlinear ultrasonic SHM method for impact damage localisation in composite panels using a sparse array of piezoelectric PZT transducers, Ultrasonics 108 (2020).
[62] R. Gorgin, Y. Luo, Z. Wu, Environmental and operational conditions effects on Lamb wave based structural health monitoring systems: A review, Ultrasonics 105 (2020) 106114.
[63] N. Yue, M.H. Aliabadi, A scalable data-driven approach to temperature baseline reconstruction for guided wave structural health monitoring of anisotropic carbon-fibre-reinforced polymer structures, Structural Health Monitoring 19(5) (2020) 1487-1506.
[64] F.R. Flor, R. De Medeiros, V. Tita, Numerical and experimental damage identification in metal-composite bonded joint, Journal of Adhesion 91(10-11) (2015) 863-882.
[65] S. Sikdar, P. Fiborek, P. Malinowski, W. Ostachowicz, Ultrasonic guided wave propagation in a repaired stiffened composite panel, Proceedings of SPIE - The International Society for Optical Engineering, 2019.
[66] F. Lambinet, Z.S. Khodaei, Damage detection & localization on composite patch repair under different environmental effects, Engineering Research Express 2(4) (2020).
[67] K.B. Katnam, A.J. Comer, D. Roy, L.F.M. Da Silva, T.M. Young, Composite repair in wind turbine blades: An overview, Journal of Adhesion 91(1-2) (2015) 113-139.
[68] S.M. Spearing, P.A. Lagace, H.L.N. McManus, On the Role of Lengthscale in the Prediction of Failure of Composite Structures: Assessment and Needs, Applied Composite Materials 5(3) (1998) 139-149.
[69] J. Gryzagoridis, D. Findeis, Benchmarking shearographic NDT for composites, Insight: Non-Destructive Testing and Condition Monitoring 50(5) (2008) 249-252.
[70] K.B. Katnam, J.X. Dhôte, T.M. Young, Experimental analysis of the bondline stress concentrations to characterize the influence of adhesive ductility on the composite single lap joint strength, Journal of Adhesion 89(6) (2013) 486-506.
[71] H. Gharib, Structural Health Monitoring of Adhesive Bond in Aircraft Repair Patches.
[72] G.R. Sherwin, Non-autoclave processing of advanced composite repairs, International Journal of Adhesion and Adhesives 19(2) (1999) 155-159.
[73] W. Brostow, N.M. Glass, Cure progress in epoxy systems: Dependence on temperature and time, Materials Research Innovations 7(3) (2003) 125-132.
[74] K.B. Katnam, A.J. Comer, W.F. Stanley, M. Buggy, A.R. Ellingboe, T.M. Young, Characterising pre-preg and non-crimp-fabric composite single lap bonded joints, International Journal of Adhesion and Adhesives 31(7) (2011) 679-686.
[75] F. Lambinet, Z.S. Khodaei, Development of smart bonded composite patch repair solution, AIP Conference Proceedings, AIP Publishing LLC, 2020, p. 020009.
[76] E. Monaco, V. Memmolo, N. Boffa, L. Maio, F. Ricci, Guided waves based SHM systems: parameters selection for better identification and localisation of damages in composites stiffened plates, Health Monitoring of Structural and Biological Systems 2017, International Society for Optics and Photonics, 2017, p. 101701E.

[77] S. Cantero-Chinchilla, G. Aranguren, J.M. Royo, M. Chiachío, J. Etxaniz, A. Calvo-Echenique, Structural Health Monitoring Using Ultrasonic Guided-Waves and the Degree of Health Index, Sensors 21(3) (2021) 993.
[78] S. Torkamani, S. Roy, M.E. Barkey, E. Sazonov, S. Burkett, S. Kotru, A novel damage index for damage identification using guided waves with application in laminated composites, Smart Materials and Structures 23(9) (2014) 095015.
[79] K. Liu, S. Ma, Z. Wu, Y. Zheng, X. Qu, Y. Wang, W. Wu, A novel probability-based diagnostic imaging with weight compensation for damage localization using guided waves, Structural Health Monitoring 15(2) (2016) 162-173.
[80] T. Wandowski, P. Malinowski, W. Ostachowicz, Circular sensing networks for guided waves based structural health monitoring, Mechanical Systems and Signal Processing 66 (2016) 248-267.
[81] B. Yang, F.-Z. Xuan, S. Chen, S. Zhou, Y. Gao, B. Xiao, Damage localization and identification in WGF/epoxy composite laminates by using Lamb waves: Experiment and simulation, Composite Structures 165 (2017) 138-147.
[82] S. Cantero-Chinchilla, J. Chiachío, M. Chiachío, D. Chronopoulos, A. Jones, A robust Bayesian methodology for damage localization in plate-like structures using ultrasonic guided-waves, Mechanical Systems and Signal Processing 122 (2019) 192-205.
[83] I. Dafydd, Z. Sharif Khodaei, Analysis of barely visible impact damage severity with ultrasonic guided Lamb waves, Structural Health Monitoring 19(4) (2020) 1104-1122.
[84] B. Yang, F.Z. Xuan, P. Jin, C. Hu, B. Xiao, D. Li, Y. Xiang, H. Lei, Damage Localization in Composite Laminates by Building in PZT Wafer Transducers: A Comparative Study with Surface-Bonded PZT Strategy, Advanced Engineering Materials 21(3) (2019) 1801040.
[85] A. Muller, C. Soutis, M. Gresil, Image reconstruction and characterisation of defects in a carbon fibre/epoxy composite monitored with guided waves, Smart Materials and Structures 28(6) (2019) 065001.
[86] C. Paget, Active health monitoring of aerospace composite structures by embedded piezoceramic transducers, Institutionen för flygteknik, 2001.
[87] V. Giurgiutiu, A.N. Zagrai, Embedded self-sensing piezoelectric active sensors for on-line structural identification, Journal of Vibration and Acoustics 124(1) (2002) 116-125.
[88] Z. Su, L. Ye, Y. Lu, Guided Lamb waves for identification of damage in composite structures: A review, Journal of sound and vibration 295(3-5) (2006) 753-780.
[89] Z. Su, L. Ye, Lamb wave-based quantitative identification of delamination in composite laminates, Delamination Behaviour of Composites, Elsevier2008, pp. 169-216.
[90] J.L. Rose, Ultrasonic guided waves in solid media, Cambridge university press2014.
[91] V. Giurgiutiu, Structural Health Monitoring with Piezoelectric Wafer Active Sensors: with Piezoelectric Wafer Active Sensors, Elsevier2007.
[92] N. Hu, T. Shimomukai, H. Fukunaga, Z. Su, Damage identification of metallic structures using A0 mode of Lamb waves, Structural Health Monitoring 7(3) (2008) 271-285.
[93] Z. Su, L. Ye, Fundamental Lamb mode-based delamination detection for CF/EP composite laminates using distributed piezoelectrics, Structural Health Monitoring 3(1) (2004) 43-68.

[94] Q. Wang, S. Yuan, M. Hong, Z. Su, On time reversal-based signal enhancement for active lamb wave-based damage identification, Smart Structures and Systems 15(6) (2015) 1463-1479.
[95] Z. Su, L. Ye, Selective generation of Lamb wave modes and their propagation characteristics in defective composite laminates, Proceedings of the Institution of Mechanical Engineers, Part L: Journal of Materials: Design and Applications 218(2) (2004) 95-110.
[96] E. Balmes, A. Deraemaeker, Modeling structures with piezoelectric materials, SDT tutorial (2013).
[97] Z. Sharif-Khodaei, M. Ghajari, M. Aliabadi, Impact damage detection in composite plates using a self-diagnostic electro-mechanical impedance-based structural health monitoring system, Journal of Multiscale Modelling 6(04) (2015) 1550013.
[98] F. Zou, M. Aliabadi, On modelling three-dimensional piezoelectric smart structures with boundary spectral element method, Smart Materials and Structures 26(5) (2017) 055015.
[99] G. Park, C.R. Farrar, A.C. Rutherford, A.N. Robertson, Piezoelectric active sensor self-diagnostics using electrical admittance measurements, (2006).
[100] G. Park, C.R. Farrar, F.L. di Scalea, S. Coccia, Performance assessment and validation of piezoelectric active-sensors in structural health monitoring, Smart Materials and Structures 15(6) (2006) 1673.
[101] D. Wang, H. Song, H. Zhu, Embedded 3D electromechanical impedance model for strength monitoring of concrete using a PZT transducer, Smart materials and structures 23(11) (2014) 115019.
[102] Y.Y. Lim, W.Y.H. Liew, C.K. Soh, A parametric study on admittance signatures of a PZT transducer under free vibration, Mechanics of Advanced Materials and Structures 22(11) (2015) 877-884.
[103] M.E. Voutetaki, N.A. Papadopoulos, G.M. Angeli, C.P. Providakis, Investigation of a new experimental method for damage assessment of RC beams failing in shear using piezoelectric transducers, Engineering Structures 114 (2016) 226-240.
[104] R. Lammering, U. Gabbert, M. Sinapius, T. Schuster, P. Wierach, Lamb-wave based structural health monitoring in polymer composites, Springer2017.
[105] D. Systems, ABAQUS/CAE user's guide, Dassault Systemes Simulia. Providence, RI, 2014.
[106] J.E. Michaels, S.J. Lee, J.S. Hall, T.E. Michaels, Multi-mode and multi-frequency guided wave imaging via chirp excitations, Health Monitoring of Structural and Biological Systems 2011, International Society for Optics and Photonics, 2011, p. 79840I.
[107] I. Dafydd, Z.S. Khodaei, Damage severity assessment in composite structures using ultrasonic guided waves with chirp excitation, Sensors and Smart Structures Technologies for Civil, Mechanical, and Aerospace Systems 2018, International Society for Optics and Photonics, 2018, p. 105980D.
[108] N. Yue, M. Aliabadi, A scalable data-driven approach to temperature baseline reconstruction for guided wave structural health monitoring of anisotropic carbon-fibre-reinforced polymer structures, Structural Health Monitoring (2019) 1475921719887109.

[109] C. Xu, Z. Sharif Khodaei, A Novel Fabry-Pérot Optical Sensor for Guided Wave Signal Acquisition, Sensors 20(6) (2020) 1728.
[110] J.E. Michaels, Detection, localization and characterization of damage in plates with an in situ array of spatially distributed ultrasonic sensors, Smart Materials and Structures 17(3) (2008) 035035.
[111] Z. Sharif-Khodaei, M. Aliabadi, Assessment of delay-and-sum algorithms for damage detection in aluminium and composite plates, Smart materials and structures 23(7) (2014) 075007.
[112] A.M. Ferri, S.K. Zahra, Structural Health Monitoring for Advanced Composite Structures, World Scientific2017.
[113] Basic principles of laser Doppler vibrometry. https://www.polytec.com/uk/vibrometry/technology/laser-doppler-vibrometry.
[114] R.L. Mirko Nikolaj Neumann, Jochen Schell, Reinhard Behrendt, Structural Health Monitoring Using Lamb Wave Testing, 2017. https://www.polytec.com/fileadmin/website/vibrometry/pdf/OM_AN_VIB_G_020_Lamb_Wave_Testing_E_42438.pdf.
[115] P. Kudela, W. Ostachowicz, A. Żak, Damage detection in composite plates with embedded PZT transducers, Mechanical Systems and Signal Processing 22(6) (2008) 1327-1335.
[116] S. Mall, T. Hsu, Electromechanical fatigue behavior of graphite/epoxy laminate embedded with piezoelectric actuator, Smart Materials and Structures 9(1) (2000) 78.
[117] S. Mall, Integrity of graphite/epoxy laminate embedded with piezoelectric sensor/actuator under monotonic and fatigue loads, Smart Materials and Structures 11(4) (2002) 527.
[118] M. Yocum, H. Abramovich, A. Grunwald, S. Mall, Fully reversed electromechanical fatigue behavior of composite laminate with embedded piezoelectric actuator/sensor, Smart materials and structures 12(4) (2003) 556.
[119] M. Lin, X. Qing, A. Kumar, S.J. Beard, Smart layer and smart suitcase for structural health monitoring applications, Smart structures and materials 2001: industrial and commercial applications of smart structures technologies, International Society for Optics and Photonics, 2001, pp. 98-106.
[120] M. Lin, F.-K. Chang, The manufacture of composite structures with a built-in network of piezoceramics, Composites Science and Technology 62(7-8) (2002) 919-939.
[121] Z. Su, X. Wang, Z. Chen, L. Ye, D. Wang, A built-in active sensor network for health monitoring of composite structures, Smart Materials and Structures 15(6) (2006) 1939.
[122] M.S. Salmanpour, Z. Sharif Khodaei, M.H. Aliabadi, Airborne Transducer Integrity under Operational Environment for Structural Health Monitoring, Sensors 16(12) (2016) 2110.
[123] D. Bekas, Z. Sharif-Khodaei, M. Aliabadi, An innovative diagnostic film for structural health monitoring of metallic and composite structures, Sensors 18(7) (2018) 2084.

[124] T. Feng, D. Bekas, M. Aliabadi, Active Health Monitoring of Thick Composite Structures by Embedded and Surface-Mounted Piezo Diagnostic Layer, Sensors 20(12) (2020) 3410.
[125] M. Lin, f.-k. Chang, Composite structures with built-in diagnostics, Materials Today - MATER TODAY 2 (1999) 18-22.
[126] N. Yue, Z.S. Khodaei, M.H. Aliabadi, Damage detection in large composite stiffened panels based on a novel SHM building block philosophy, Smart Materials and Structures 30(4) (2021) 045004.
[127] S. Masmoudi, A. El Mahi, S. Turki, Fatigue behaviour and structural health monitoring by acoustic emission of E-glass/epoxy laminates with piezoelectric implant, Applied Acoustics 108 (2016) 50-58.
[128] S. Masmoudi, A. El Mahi, S. Turki, Use of piezoelectric as acoustic emission sensor for in situ monitoring of composite structures, Composites Part B: Engineering 80 (2015) 307-320.
[129] C. Tuloup, W. Harizi, Z. Aboura, Y. Meyer, Integration of piezoelectric transducers (PZT and PVDF) within polymer-matrix composites for structural health monitoring applications: new success and challenges, International Journal of Smart and Nano Materials 11(4) (2020) 343-369.
[130] C. Andreades, P. Mahmoodi, F. Ciampa, Characterisation of smart CFRP composites with embedded PZT transducers for nonlinear ultrasonic applications, Composite Structures 206 (2018) 456-466.
[131] C. Andreades, M. Meo, F. Ciampa, Fatigue testing and damage evaluation using smart CFRP composites with embedded PZT transducers, Materials Today: Proceedings 34 (2021) 260-265.
[132] H.M. Matt, Structural diagnostics of CFRP composite aircraft components by ultrasonic guided waves and built-in piezoelectric transducers, UC San Diego, 2007.
[133] S.-Y. Wu, C.E. Blevins, Method and structure for embedding piezoelectric transducers in thermoplastic composites, Google Patents, 1999.
[134] S. Mall, Integrity of graphite/epoxy laminate embedded with piezoelectric sensor/actuator under monotonic and fatigue loads, Smart Materials and Structures 11(4) (2002) 527-533.
[135] M. Lin, X. Qing, A. Kumar, S.J. Beard, Smart layer and smart suitcase for structural health monitoring applications, Smart Structures and Materials 2001: Industrial and Commercial Applications of Smart Structures Technologies, International Society for Optics and Photonics, 2001, pp. 98-107.
[136] R. Aoki, R. Higuchi, T. Yokozeki, K. Aoki, S. Uchiyama, T. Ogasawara, Damage-mechanics mesoscale modeling of composite laminates considering diffuse and discrete ply damages: Effects of ply thickness, Composite Structures 277 (2021) 114609.
[137] D.G. Bekas, Z. Sharif-Khodaei, M.H. Aliabadi, An innovative diagnostic film for structural health monitoring of metallic and composite structures, Sensors 18(7) (2018) 2084.
[138] What are the static and dynamic characteristics of the sensor?, (2020). https://www.allicdata.com/news/sensor/page/13.html.

[139] A. Raghavan, C.E. Cesnik, Effects of elevated temperature on guided-wave structural health monitoring, Journal of Intelligent Material Systems and Structures 19(12) (2008) 1383-1398.
[140] S. Roy, K. Lonkar, V. Janapati, F.-K. Chang, A novel physics-based temperature compensation model for structural health monitoring using ultrasonic guided waves, Structural Health Monitoring 13(3) (2014) 321-342.
[141] C. Fendzi, M. Rebillat, N. Mechbal, M. Guskov, G. Coffignal, A data-driven temperature compensation approach for Structural Health Monitoring using Lamb waves, Structural Health Monitoring 15(5) (2016) 525-540.
[142] C. Andreades, G.P. Malfense Fierro, M. Meo, F. Ciampa, Nonlinear ultrasonic inspection of smart carbon fibre reinforced plastic composites with embedded piezoelectric lead zirconate titanate transducers for space applications, Journal of Intelligent Material Systems and Structures 30(20) (2019) 2995-3007.
[143] M. Dziendzikowski, M. Heesch, J. Gorski, K. Dragan, Z. Dworakowski, Application of PZT Ceramic Sensors for Composite Structure Monitoring Using Harmonic Excitation Signals and Bayesian Classification Approach, Materials 14(19) (2021) 5468.
[144] S. Cenek, R. Mudit, H. Radek, Structural health monitoring of composite structures using embedded pzt sensors in space application, PHM Society European Conference, 2014.
[145] S.-C. Her, H.-Y. Chen, Deformation of Composite Laminates Induced by Surface Bonded and Embedded Piezoelectric Actuators, Materials 13(14) (2020) 3201.
[146] G. Konstantinidis, B. Drinkwater, P. Wilcox, The temperature stability of guided wave structural health monitoring systems, Smart Materials and Structures 15(4) (2006) 967.
[147] A. Croxford, P. Wilcox, B. Drinkwater, G. Konstantinidis, Strategies for guided-wave structural health monitoring, Proceedings of the Royal Society A: Mathematical, Physical and Engineering Sciences 463(2087) (2007) 2961-2981.
[148] M. Torres-Arredondo, C. Fritzen, Ultrasonic guided wave dispersive characteristics in composite structures under variable temperature and operational conditions, Proc. 6th European Workshop in Structural Health Monitoring, EWSHM 2012 (Dresden, Germany,), 2012, pp. 261-8.
[149] N. Yue, Z. Sharif Khodaei, F.M. Aliabadi, An innovative secondary bonding of sensors to composite structures for SHM application, Key Engineering Materials, Trans Tech Publ, 2018, pp. 516-522.
[150] F. Lambinet, Z.S. Khodaei, M.H. Aliabadi, Effectiveness of RAPID and SSM algorithms on composite scarf repair, Key Engineering Materials, 2018, pp. 535-540.
[151] J. Zhu, Y. Wang, X. Qing, A real-time electromechanical impedance-based active monitoring for composite patch bonded repair structure, Composite Structures 212 (2019) 513-523.
[152] R.L. Rito, A.D. Crocombe, S.L. Ogin, Health monitoring of composite patch repairs using CFBG sensors: Experimental study and numerical modelling, Composites Part A: Applied Science and Manufacturing 100 (2017) 255-268.

[153] W. Roth, V. Giurgiutiu, Structural health monitoring of an adhesive disbond through electromechanical impedance spectroscopy, International Journal of Adhesion and Adhesives 73 (2017) 109-117.
[154] X.P. Qing, S.J. Beard, A. Kumar, R. Hannum, A real-time active smart patch system for monitoring the integrity of bonded repair on an aircraft structure, Smart Materials and Structures 15(3) (2006) N66-N73.
[155] D.G. Bekas, Z. Sharif-Khodaei, D. Baltzis, M.H.F. Aliabadi, A.S. Paipetis, Quality assessment and damage detection in nanomodified adhesively-bonded composite joints using inkjet-printed interdigital sensors, Composite Structures 211 (2019) 557-563.
[156] X.F. Sánchez-Romate, C. García, J. Rams, M. Sánchez, A. Ureña, Structural health monitoring of a CFRP structural bonded repair by using a carbon nanotube modified adhesive film, Composite Structures 270 (2021).